12-2006

INVESTIGATION OF THE EFFECTS OF SUBGRID-SCALE TURBULENCE ON RESOLVABLE-SCALE STATISTICS

Qinglin Chen
Clemson University, qinglic@clemson.edu

INVESTIGATION OF THE EFFECTS OF SUBGRID-SCALE TURBULENCE ON RESOLVABLE-SCALE STATISTICS

A Dissertation
Presented to
the Graduate School of
Clemson University

In Partial Fulfillment
of the Requirements for the Degree
Doctor of Philosophy
Mechanical Engineering

---

by
Qinglin Chen
December 2006

Accepted by:
Dr. Chenning Tong, Committee Chair
Dr. Richard S. Figliola
Dr. James H. Leylek
Dr. Richard S. Miller

ABSTRACT

The effects of the subgrid-scale (SGS) turbulence on the resolvable-scale statistics as well as the effects of SGS models on large-eddy simulation (LES) are studied. It is shown that the SGS turbulence evolves the resolvable-scale joint probability density function (JPDF) through the conditional means of the SGS stress, the SGS scalar flux, and their production rate, which must be reproduced by the SGS model for LES to predict correctly the one-point resolvable-scale statistics, a primary goal of LES. This necessary condition is used as the basis for studying SGS physics and for testing SGS models. Theoretical predictions, measurements data, and numerical simulation results are combined to investigate the effects of filter size, the dependence of the SGS turbulence on the flow dynamics, and SGS models performance using new *a priori* and *a posteriori* tests developed in this research.

For inertial-range filter scales, LES statistics of the energy- and flux-containing scales are generally considered to be insensitive to the SGS model employed. To examine this premise, the effects of the subgrid-scale (SGS) velocity, scalar, and SGS models on the resolvable-scale velocity-scalar joint probability density function (JPDF) are studied. The mean SGS stress and SGS scalar flux production rate is predicted using Lumley's assumption (Lumley 1967), which is consistent with Kolmogorov's hypothesis. Analyses of these statistics using data obtained in a slightly heated turbulent jet show that the mean SGS stress, SGS scalar flux, and their production rates have filter-scale dependencies consistent with predictions, suggesting that the SGS turbulence has diminishing influence on the lower-order resolvable-scale statistics for inertial-range filter scales and supporting the premise of LES at the level of lower-order statistics. The measured conditional SGS stress and SGS flux as well as the conditional production rates have a strong dependence on the resolvable-scale velocity and scalar, indicating strong flow history effects, and decrease much slower than the predicted filter dependencies, indicating that the SGS turbulence has non-trivial effects on the high-order resolvable-scale statistics even for inertial-range filter scales.

For energy-containing filter scales, previous studies have shown that LES results depend strongly on the SGS models. To study the effects of the SGS turbulence on the resolvable-scale velocity statistics for such filter scales, the SGS stress in the atmospheric surface layer is studied using measurement data (HATS 2000). Analysis of the conditional SGS stress and the conditional stress production rate conditional on the resolvable-scale velocity show that both buoyancy and

shear play important roles in the physics of the SGS stress. Strong buoyancy and vertical shear associated with updrafts and positive streamwise velocity fluctuations cause conditional forward energy transfer and strong anisotropy in the conditional SGS stress. Downward returning flows associated with large convective eddies result in much less anisotropic SGS stress and conditional energy backscatter. Predictions of the conditional SGS stress and the conditional stress production rate predicted using several SGS models are compared with measurements. None of the models tested are able to predict correctly the trends of both statistics. The deficiencies of the SGS models that cause inaccurate LES statistics, such as the over-prediction of the mean shear and under-prediction of the vertical velocity skewness, are identified.

To study the effects of the SGS turbulence on the resolvable-scale velocity-scalar statistics for energy-containing filter scales, the SGS scalar flux in the atmospheric surface layer is studied using field measurements data. The results show that the conditional scalar flux and its production rate depend on the resolvable-scale velocity and temperature fluctuations, suggesting that these conditional variables have strong influences on the resolvable-scale statistics. The dependencies are argued to be due to the effects of buoyancy and flow history. The results show that the conditional vertical scalar flux affects the conditional horizontal scalar flux production rate. However, the conditional horizontal scalar flux has no direct effect on the conditional vertical scalar production rate. Therefore, the correct modeling of the conditional vertical scalar flux components is crucial. Predictions of the conditional scalar flux and its production rate predicted using several SGS models are compared with measurements. The current SGS models have varying levels of performance in predicting different SGS flux components. As a results, the poor prediction of one SGS component often affects the prediction of the production rate of another SGS component, thereby resulting in errors in the LES statistics. Therefore, efforts to improve SGS models need to ensure that all the relevant SGS fluxes related to the LES statistics of interests or of importance to the intended applications are correct predicted. The present study shows that analysis of the conditional statistics can serve as an important guide in studying the SGS physics, identifying model deficiencies, and developing improved SGS models.

To understand the model performance, a new *a posteriori* test is employed to study SGS model performance. Unlike traditional *a posteriori* tests of SGS models, which often compare LES profiles of various statistics with measurements, the new approach compares the conditional means of the LES-generated SGS stress and the conditional stress production rate conditional on the resolvable-scale velocity with measurements. The Smagorinsky model, the split model, and the Kosović model are tested. The LES results for convective atmospheric boundary layers show that

the level of the anisotropy of the SGS stress represented in the Lumley triangle is under-predicted by both the Smagorinsky model and the Kosović model. The magnitudes of the conditional SGS stress and the conditional SGS stress production rate are generally under-predicted by both models as well. The trends of the conditional SGS stress and the conditional SGS stress production rate are generally better predicted by the Kosović model than that of the Smagorinsky model. The model strengths and deficiencies observed here were also identified in previous statistical *a priori* tests analyzing the conditional statistics. The remarkable consistency between the two types of tests suggests that statistical tests analyzing the conditional SGS stress and its production rate are capable of identifying specific model deficiencies and for evaluating SGS model performance in simulations.

ACKNOWLEDGMENTS

I deeply thank Dr. Chenning Tong for his invaluable guidance and support not only as my research advisor but also a wonderful teacher. His steadfast support and incessant encouragement proved to be extremely important in my research work and in preparing my dissertation. I would like to thank Dr. Richard S. Figliola, Dr. James H. Leylek, and Dr. Richard S. Miller for serving on my advisory committee.

I thank my colleagues Danhong Wang, Hengbin Zhang, Jian Cai, Xingshi Wang, and Matthew J. Dinger for their fruitful discussions and valuable advices. Special thanks to my labmates Brian Jones and Paul Wright for their enthusiastic support that help me greatly in my research work.

TABLE OF CONTENTS

Table of Contents (Continued)

Page

LIST OF TABLES

LIST OF FIGURES

List of Figures (Continued)

List of Figures (Continued)

List of Figures (Continued)

List of Figures (Continued)

List of Figures (Continued)

CHAPTER 1

Introduction

Large-eddy simulation (LES) has become a very important approach for computing engineering and environmental turbulent flows [1, 2, 3, 4, 5, 6, 7, 8, 9, 10, 11, 12], for example, atmospheric boundary layers. Large-eddy simulation(LES) computes the large, or resolvable-scale and models the effects of the small, or subgrid-scales (SGS). For nonreacting incompressible turbulent flow LES, models are required for SGS stress and SGS scalar flux. The resolvable-scales contain most of the energy and fluxes and depend on the flow environments, while the subgrid-scales are less energetic and are considered to be more universal. When the filter size is sufficiently small to resolve most of the turbulent energy and fluxes, LES statistics of the energy- and flux-containing scales are generally expected to be insensitive to the SGS model employed. This premise is based on Kolmogorov's hypothesis of statistical independence of distant-scales.

However, in many cases the highest resolution of LES are often at the beginning of the inertial range or even larger due to the limitation of computer resources or the inherent scale inhomogeneity, such as the atmospheric surface layer. The LES results employing current SGS models, such as the Smagorinsky model, the similarity model, and the nonlinear model, have shown varying degrees of accuracy [13, 7, 14, 11, 15, 16, 17, 18, 19, 12, 20]. There is also evidence that energy-containing statistics such as mean and variance in the outer-regions of high-Reynolds-number boundary layers are to some extent insensitive to the details of the SGS model employed [21]. While these studies provided useful empirical information for evaluating the effects of SGS models on LES results, it is important to examine more rigorously the dependencies of the resolvable-scale statistics on the SGS stress and those of LES results on the SGS models.

Traditionally SGS models are studied primarily in two ways: *a priori* and *a posteriori* tests (e.g. [22, 23, 24, 6, 25, 26, 8, 27, 28, 29, 30, 21, 31, 32, 33, 19, 34, 35, 36]). Traditional tests have contributed greatly to the understanding of the current SGS models. However, they also have their limitations. For *a priori* tests, it is difficult to predict the effects of model behaviors on LES results. For example, the correlation between the modeled and measured SGS stress components provides little information about model performance in a simulation. For *a posteriori* tests, it is difficult to

relate deficiencies of LES results to specific aspects of the model behaviors. This is not only because the SGS stress evolves LES fields through dynamic equations, but also because the equations are chaotic with many degrees of freedom, making it difficult to relate the properties of the solutions to the behaviors of the SGS terms in the equation.

In view of the difficulties in directly assessing the model effects on LES results, it is important to use a more systematic approach for analyzing SGS models. While SGS models affect the predicted instantaneous flow fields and structures, their impact on flow statistics is arguably most important and should first be understood. In fact, Pope (2000) [37] argues that the best LES that can be achieved is one that statistically corresponds to the true resolvable-scale fields. Although it is not practical to expect an SGS model to predict all the statistics of the resolvable-scale fields, it should at least be able to predict those important for specific applications (e.g. mean and r.m.s. profile, spectra, vertical velocity skewness, etc.). Because flow statistics are often strongly influenced by large-scale flow structures, their correct prediction will also benefit the predicted flow structures. Therefore, an important task in improving an SGS stress model is to understand how the SGS stress influences the resolvable-scale statistics and how the influences vary with the filter scale. The former is important for understanding SGS model strengths and deficiencies, therefore is essential to developing improved models. The latter is important for understanding the extent to which LES depends on the SGS model as the filter scale decreases, i.e., the extent to which the premise of LES is valid.

To accomplish this task, an analysis method relating the SGS model to LES statistics is needed. Dynamic equations for the statistics of the resolvable-scale velocity are a very useful choice. Chen *et al.* [38] studied the effects of the SGS turbulence on the resolvable-scale statistics using the transport equation of the resolvable-scale velocity joint probability density function (JPDF). They showed that the SGS stress affects the resolvable-scale velocity JPDF directly through the conditional SGS stress and the conditional stress production rate conditional on the resolvable-scale velocity and indirectly through the conditional pressure and conditional pressure-strain correlation. Their study is extended to the velocity-scale JPDF equation and provide theoretical predictions of the filter-scale dependencies in Chapter 2. These conditional statistics are further studied using data obtained in the surface layer of the atmospheric boundary layer in Chapters 3 and 4. A new JPDF based *a posteriori* test for SGS stress models is given in Chapter 5, followed by conclusions.

CHAPTER 2

Effects of subgrid scales on resolvable-scale velocity-scalar JPDF and their filter-scale dependencies

Chen *et al.* (2003) [38] studied the conditional SGS stress and the conditional SGS stress production rate using the resolvable-scale velocity JPDF, and gave the necessary conditions for LES to correctly predict the resolvable-scale velocity JPDF as that the SGS model must reproduce the conditional SGS stress and conditional SGS stress production. To understand the extent to which LES premise is valid, Chen *et al.* [38] also examined the filter-scale dependencies of these conditional means using experimental data obtained in a turbulent jet. Their results show that while the conditional SGS stress decreased with the filter scale, the conditional SGS stress production is nearly independent of the filter scale, suggesting that the SGS turbulence might influence the resolvable-scale statistics even with inertial-range filter scales. Therefore certain effects of the SGS model on LES statistics might not diminish with filter scale. In this chapter, The effects of SGS stress and SGS scalar flux on the resolvable-scale velocity-scalar JPDF are examined using the JPDF transport equation and the filter-scale dependence of these effects. Correct prediction of the velocity-scalar JPDF by LES is important because in addition to mean and r.m.s. it also contains all higher-order single-point statistics, some of which are of practical importance. For example, several third-order statistics represent turbulent transport while the scalar PDF is key to describe pollutant dispersion.

The velocity-scalar JPDF equation can be obtained following the method given by Pope (1985) [39]. Differentiating the definition of the JPDF:

$$f = \left\langle \delta[\phi^r - \psi] \prod_{i=1}^{3} \delta[u_i^r - v_i] \right\rangle \tag{2.1}$$

we obtain

$$\frac{\partial f}{\partial t} = -\frac{\partial}{\partial v_i}\left\{\left\langle \frac{\partial u_i^r}{\partial t}\middle| \mathbf{u^r} = \mathbf{v}, \phi^r = \psi \right\rangle f\right\} - \frac{\partial}{\partial \psi}\left\{\left\langle \frac{\partial \phi^r}{\partial t}\middle| \mathbf{u^r} = \mathbf{v}, \phi^r = \psi \right\rangle f\right\} \tag{2.2}$$

where $\mathbf{v}$ and ψ are the sample-space variables for the resolvable-scale velocity $\mathbf{u}^r$ and the resolvable-scale scalar ϕ^r, respectively. The Dirac delta function and the filtering operation are denoted by δ and a superscript r, respectively. Substituting the time derivative term $\frac{\partial u_i^r}{\partial t}$ and $\frac{\partial \phi^r}{\partial t}$ in equation (2.2) with the right-hand-side (RHS) of the equation for the resolvable-scale velocity:

$$\frac{\partial u_i^r}{\partial t} = -\frac{\partial u_j^r u_i^r}{\partial x_j} - \frac{\partial \tau_{ij}}{\partial x_j} - \frac{\partial L_{ij}}{\partial x_j} - \frac{\partial p^r}{\partial x_i} + \nu \frac{\partial^2 u_i^r}{\partial x_j \partial x_j} \tag{2.3}$$

where $\tau_{ij} = (u_i u_j)^r - (u_i^r u_j^r)^r, L_{ij} = (u_i^r u_j^r)^r - u_i^r u_j^r$, p^r, and ν are the SGS stress, Leonard stress, filtered pressure, and molecular viscosity, respectively, and the filtered equation for the resolvable-scale scalar:

$$\frac{\partial \phi^r}{\partial t} = -\frac{\partial \phi^r u_i^r}{\partial x_i} - \frac{\partial F_i}{\partial x_i} - \frac{\partial G_i}{\partial x_i} + \Gamma \frac{\partial^2 \phi^r}{\partial x_i^2} \tag{2.4}$$

where $F_i = (u_i \phi)^r - (u_i^r \phi^r)^r, G_i = (u_i^r \phi^r)^r - u_i^r \phi^r$ and Γ are the SGS scalar flux, Leonard part of the SGS scalar flux, and molecular diffusivity, respectively, we obtain the transport equation of the JPDF of the resolvable-scale velocity and scalar

$$\begin{aligned}\frac{\partial f}{\partial t} + v_j \frac{\partial f}{\partial x_j} = &\frac{\partial}{\partial v_i}\left\{\left\langle \frac{\partial \tau_{ij}}{\partial x_j}\middle| \mathbf{u^r} = \mathbf{v}, \phi^r = \psi \right\rangle f\right\} + \frac{\partial}{\partial v_i}\left\{\left\langle \frac{\partial L_{ij}}{\partial x_j}\middle| \mathbf{u^r} = \mathbf{v}, \phi^r = \psi \right\rangle f\right\} \\ &+ \frac{\partial}{\partial \psi}\left\{\left\langle \frac{\partial F_i}{\partial x_i}\middle| \mathbf{u^r} = \mathbf{v}, \phi^r = \psi \right\rangle f\right\} + \frac{\partial}{\partial \psi}\left\{\left\langle \frac{\partial G_i}{\partial x_i}\middle| \mathbf{u^r} = \mathbf{v}, \phi^r = \psi \right\rangle f\right\} \\ &+ \frac{\partial}{\partial v_i}\left\{\left\langle \frac{\partial p^r}{\partial x_i}\middle| \mathbf{u^r} = \mathbf{v}, \phi^r = \psi \right\rangle f\right\}. \end{aligned} \tag{2.5}$$

The two terms on the left-hand-side are the time rate of change and advection in physical space. The first two terms on the RHS are transport of the JPDF in velocity space by the SGS stress divergence and the Leonard stress divergence, respectively. The third and forth terms are transport in scalar space by the SGS scalar flux divergence and the Leonard scalar flux divergence, respectively. The last term is transport in velocity space by the filtered pressure gradient. The viscous and scalar diffusion terms are small and are omitted at high Reynolds numbers.

Traditionally, SGS turbulence are studied by analyzing the SGS stress and flux rather than their divergences. Therefore, an alternative form of the equation similar to that given by Chen *et*

al. [38] is derived

$$\begin{aligned}
\frac{\partial f}{\partial t}+v_j\frac{\partial f}{\partial x_j} &= \frac{\partial^2}{\partial v_i\partial x_j}\left\{\langle \tau_{ij}|\,\mathbf{u^r}=\mathbf{v},\phi^r=\psi\rangle\, f\right\}+\frac{\partial^2}{\partial v_i\partial x_j}\left\{\langle L_{ij}|\,\mathbf{u^r}=\mathbf{v},\phi^r=\psi\rangle\, f\right\}\\
&+\frac{\partial^2}{\partial v_i\partial v_j}\left\{\langle -P_{ij}|\,\mathbf{u^r}=\mathbf{v},\phi^r=\psi\rangle\, f\right\}+\frac{\partial^2}{\partial v_i\partial v_j}\left\{\left\langle L_{ik}\frac{\partial u_j^r}{\partial x_k}\right|\mathbf{u^r}=\mathbf{v},\phi^r=\psi\right\rangle f\right\}\\
&+\frac{\partial^2}{\partial\psi\partial x_i}\left\{\langle F_i|\,\mathbf{u^r}=\mathbf{v},\phi^r=\psi\rangle\, f\right\}+\frac{\partial^2}{\partial\psi\partial x_i}\left\{\langle G_i|\,\mathbf{u^r}=\mathbf{v},\phi^r=\psi\rangle\, f\right\}\\
&+\frac{\partial^2}{\partial\psi\partial v_i}\left\{\langle -P_{Fi}|\,\mathbf{u^r}=\mathbf{v},\phi^r=\psi\rangle\, f\right\}+\frac{\partial^2}{\partial\psi\partial v_i}\left\{\left\langle L_{ik}\frac{\partial\phi^r}{\partial x_k}+G_k\frac{\partial u_i^r}{\partial x_k}\right|\mathbf{u^r}=\mathbf{v},\phi^r=\psi\right\rangle f\right\}\\
&+\frac{\partial^2}{\partial\psi\partial\psi}\left\{\langle -P_{\phi}|\,\mathbf{u^r}=\mathbf{v},\phi^r=\psi\rangle\, f\right\}+\frac{\partial^2}{\partial v_i\partial x_i}\left\{\langle p^r|\,\mathbf{u^r}=\mathbf{v},\phi^r=\psi\rangle\, f\right\}\\
&+\frac{\partial^2}{\partial v_i\partial v_k}\left\{\left\langle p^r\frac{\partial u_k^r}{\partial x_i}\right|\mathbf{u^r}=\mathbf{v},\phi^r=\psi\right\rangle f\right\}+\frac{\partial^2}{\partial v_i\partial\psi}\left\{\left\langle p^r\frac{\partial\phi^r}{\partial x_i}\right|\mathbf{u^r}=\mathbf{v},\phi^r=\psi\right\rangle f\right\} \qquad (2.6)
\end{aligned}$$

where $P_{ij}=-\frac{1}{2}\left\{\tau_{ik}\frac{\partial u_j^r}{\partial x_k}+\tau_{jk}\frac{\partial u_i^r}{\partial x_k}\right\}$, $P_{Fi}=-\left\{\tau_{ik}\frac{\partial\phi^r}{\partial x_k}+F_k\frac{\partial u_i^r}{\partial x_k}\right\}$, and $P_\phi=-F_k\frac{\partial\phi^r}{\partial x_k}$ are the SGS stress production rate, the SGS scalar flux production rate, and the SGS scalar variance production rate, respectively. Therefore, the SGS stress and the SGS scalar flux evolve the JPDF directly through their conditional means and their conditional production rates. The terms in equation (2.6) have familiar physical interpretations: the first two terms on the RHS are mixed transport in both velocity and physical spaces due to the SGS stress and the Leonard stress, followed by transport in velocity space due to the SGS stress production rate and the Leonard stress production rate. The next two terms are mixed transport in both scalar and physical spaces due to the SGS scalar flux and the Leonard scalar flux. The fifth and the sixth terms are mixed transport in scalar and velocity spaces due to the SGS scalar flux production rate and the Leonard scalar flux production rate. The next term is transport in scalar space due to the SGS scalar variance production rate. The last three terms are mixed transport in velocity and physical spaces, transport in velocity space, and mixed transport in velocity and scalar spaces due to the resolvable pressure, the pressure-strain correlation, and the pressure-scalar-gradient correlation, respectively.

From equation (2.6) The necessary conditions for LES to correctly predict the resolvable-scale velocity-scalar JPDF is obtained as that SGS models reproduce the conditional SGS stress, the conditional SGS scalar flux, the SGS stress production rate, the conditional SGS scalar flux production rate, and the SGS scalar variance production rate. These statistics have physical meanings similar to those of Reynolds stress and Reynolds stress production rate, therefore can be interpreted more clearly in the context of the flow dynamics than those in equation (2.5). Compared to the LES equations which deal with random variables, the JPDF equation contains only statistics; therefore

it relates the SGS statistics much more closely to the resolvable-scale statistics (Chapter 3). Furthermore, analytical results (Sabelnikov (1998) [40]) can be used to understand the effects of these conditional statistics (the SGS turbulence) on the JPDF. Correct predictions of these conditional SGS statistics by SGS models will also be essential for LES predictions of time correlation (Adrian (1990) [41]), which are important for predicting acoustic radiation [42, 43].

In the present work, The above conditional statistics are analyzed using experimental data obtained in a turbulent axisymmetric jet to investigate the effects of SGS turbulence and SGS models on the resolvable-scale and LES statistics. The filter-scale dependencies of the conditional statistics is also predicted using Lumley's assumption [44], which is consistent with Kolmogorov's hypothesis of independence of distant scales. The predictions are compared with measurements and Smagorinsky model results. It is found that the conditional statistics depend strongly on the dynamics of the jet and that the dependencies of some SGS production rates decrease slower with filter scale than predicted using Lumley's assumption, suggesting non-diminishing effects of SGS models on the JPDF. Therefore, in applications where the JPDF (or higher-order statistics) is important, the SGS model needs to be tested against these conditional statistics. The rest of the chapter is organized as follows. The filter-scale dependencies of the mean SGS stress production rate and SGS flux production rate are considered in Section 2.1. In Section 2.2 the experimental facility and flow conditions are described. Section 2.3 examines the conditional statistics, their dependencies on the filter scale, and the Smagorinsky predictions using data obtained in an axisymmetric turbulent jet. The conclusions are given in Section 2.4.

2.1 Predictions of inertial-range dependencies

In this section, the filter-scale dependencies of the mean production rates for SGS stress and the production rate for scalar fluxes is considered. Without loss of generality, a homogenous shear flow with a crossstream mean scalar gradient is considered because this flow possesses the two scalar flux production mechanisms found in a more general flow. At off-centerline positions in a jet it is expected the SGS production rates to be similar to those in a homogenous shear flow except that turbulent transport may be important in the SGS stress and flux transport equation. the SGS shear stress production rate $\langle P_{12} \rangle$ is first considered. Following Lumley [44], It is assumed that in the inertial range $\langle P_{12} \rangle$ is determined by ϵ, k, and $U' = \frac{\partial \langle u_1 \rangle}{\partial x_2}$, where ϵ is the mean energy transfer rate and k is the wavenumber magnitude. The equation for $\langle P_{12} \rangle$ is

$$\frac{\partial \langle P_{12} \rangle}{\partial k} = \left\langle \widehat{u_1 \frac{\partial p}{\partial x_2}} \right\rangle + \left\langle \widehat{u_2 \frac{\partial p}{\partial x_1}} \right\rangle . \tag{2.7}$$

Here $\left\langle \widehat{u_1 \frac{\partial p}{\partial x_2}} \right\rangle$ denote the spherically averaged co-spectrum of u_1 and $\frac{\partial p}{\partial x_2}$. It is noted that $\langle P_{12} \rangle$ includes both the production rate due to the mean gradient and the spectral transfer rate due to turbulent fluctuations because the resolvable scales include the mean flow. Therefore, under quasi-equilibrium conditions, $\langle P_{12} \rangle$ varies due to pressure destruction. Because the pressure term must be odd in U', the RHS of (7) has the form

$$\epsilon^{2/3} k^{-5/3} U' \psi \left[\left(\frac{U'}{(\epsilon k^2)^{1/3}} \right)^2 \right], \tag{2.8}$$

where the function ψ represents the departure from the inertial-range form as the integral scales are approached. Following Lumley's analyses, we let $x = (k/k_0)^{-4/3}$ and $\frac{(U')^2}{(\epsilon k_0^2)^{2/3}} = 1$. Using the boundary condition $\frac{\langle P_{12} \rangle}{\epsilon} \to 0$ as $x \to 0$ (the high wavenumber limit), we obtain

$$\frac{\langle P_{12} \rangle}{\epsilon} = x^{1/2} \psi(0) = \left(\frac{k}{k_0} \right)^{-2/3} \psi(0), \text{ for } x \ll 1. \tag{2.9}$$

Therefore $\langle P_{12} \rangle$ falls off as $k^{-2/3}$ ($\Delta^{2/3}$), which is slower than the $k^{-4/3}$ prediction [44] for the anisotropy of the energy transfer rate to each velocity component. This is because the latter requires existing anisotropy whereas $\langle P_{12} \rangle$ can result from straining of isotropic turbulence.

The predictions of the SGS flux production will be considered separately for F_1 and F_2 because they have different production mechanisms: the former is primarily caused by straining and rotation of scalar flux, $\left\langle F_2 \frac{\partial u_1^r}{\partial x_2} \right\rangle$, whereas the latter is due to the scalar gradient production, $\left\langle \tau_{22} \frac{\partial \phi^r}{\partial x_2} \right\rangle$. Lumley's assumption is extended to $\langle P_{F2} \rangle$ as that it is determined by ϵ, χ, k and ϕ' where χ and $\phi' = \frac{\langle \partial \phi \rangle}{\partial x_2}$ are the mean scalar variance transfer rate and the mean scalar gradient, respectively. We then have

$$\frac{\partial \langle P_{F2} \rangle}{\partial k} = \left\langle \widehat{\phi \frac{\partial p}{\partial x_2}} \right\rangle, \tag{2.10}$$

where $\left\langle \widehat{\phi \frac{\partial p}{\partial x_2}} \right\rangle$ denotes the spherically averaged co-spectrum of ϕ and $\frac{\partial p}{\partial x_2}$, which must be odd in ϕ' and therefore has the form

$$\epsilon^{2/3} k^{-5/3} \phi' \psi_2 \left(\frac{(\phi')^2}{\chi \epsilon^{-1/3} k^{4/3}} \frac{(U')^2}{(\epsilon k^2)^{2/3}} \right). \tag{2.11}$$

Again ψ_2 represents the departure from the inertial-range scaling and is even in ϕ'. We have

$$\frac{\langle P_{F2} \rangle}{(\chi \epsilon)^{1/2}} = x^{1/2} \psi_2(0) \sim k^{-2/3}, \text{ for } x \ll 1. \tag{2.12}$$

Therefore, $\langle P_{F2} \rangle$ falls off at the same rate as the mean SGS stress production rate $\langle P_{12} \rangle$. The production rate $\langle P_{F1} \rangle$ is different from $\langle P_{F2} \rangle$ as it is odd in both U' and ϕ'. Therefore

$$\frac{\partial \langle P_{F1} \rangle}{\partial k} = \left\langle \widehat{\phi \frac{\partial p}{\partial x_1}} \right\rangle = \epsilon^{1/3} k^{-7/3} \phi' U' \psi_1 \left(\frac{(\phi')^2}{\chi \epsilon^{-1/3}} \frac{(U')^2}{(\epsilon k^2)^{2/3}} \right). \tag{2.13}$$

We then have

$$\frac{\langle P_{F1} \rangle}{(\chi \epsilon)^{1/2}} = x \psi_2(0) \sim k^{-4/3}, \text{ for } x \ll 1 \tag{2.14}$$

Therefore $\langle P_{F1} \rangle$ falls off faster than $\langle P_{F2} \rangle$ and $\langle P_{12} \rangle$.

These predicted production rates will be compared with experimental results in Section 2.3.2 to examine the filter-scale dependencies of the conditional SGS flux and the conditional SGS flux production rate. These theoretical predictions are consistent with Kolmogorov's hypothesis of statistical independence between large and small scales, therefore agreement between measurements and predictions would indicate that the SGS turbulence (other than the energy and scalar variance transfer rates) has diminishing effects on the JPDF for sufficiently small filter scales. On the other hand, fall-offs slower than the predictions would suggest that the SGS stress and fluxes have lasting influences on the resolvable-scale JPDF. The Smagorinsky model predictions of the filter-scale dependencies will also be compared with the theoretic predictions and the experimental results.

2.2 Experimental apparatus and flow conditions

The jet facility was housed in a large, air conditioned room. The jet flow was produced with an assembly of a nozzle and a plenum chamber (Figure 2.1) with a section of flow-straightening honeycomb and three stages of damping screens. The assembly was mounted vertically on a 5×5 ft^2 grill portion of the floor to allow the flow of entrainment air. The flow downstream of the nozzle was surrounded by a circular screen ($1/16''$ mesh size) of 6 ft in diameter to reduce the disturbances in the room. A collection hood connected to an exhaust duct was installed at a downstream distance of 260 nozzle diameters (3.9 m) to minimize the effects of the ceiling on the jet. Jet air supply was heated with a pipe heater before entering the plenum chamber, producing an excess (above the ambient) temperature of 20°C at the nozzle exit. The jet nozzle had a fifth-order polynomial profile with a large contraction ratio (≈ 100), producing a nearly top-hat velocity profile at the nozzle exit.

All measurements were made for a jet exit velocity U_j of 40 m/s. The jet Reynolds number Re_j based on the nozzle diameter D_j and the jet exit velocity ($U_j D_j / \nu$) was 40000 where ν is the

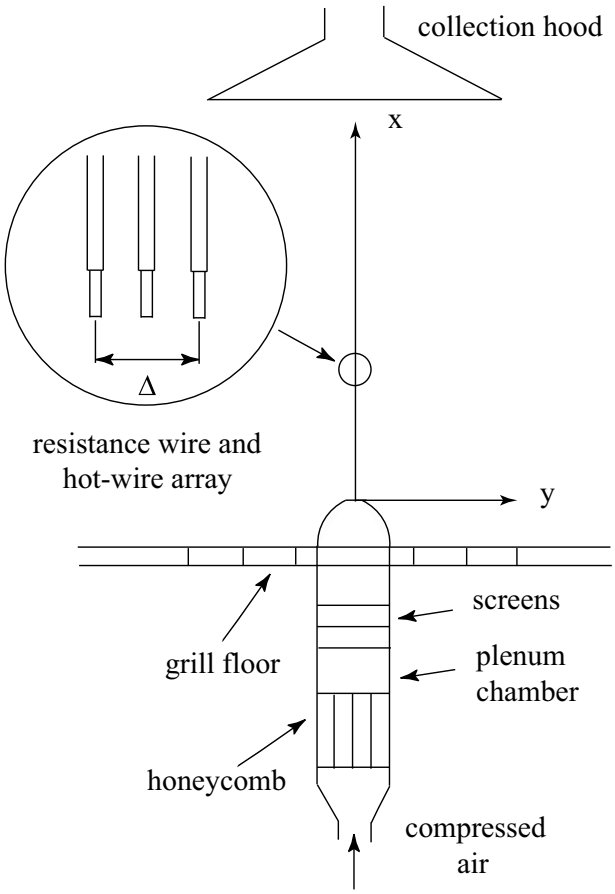

Figure 2.1 A schematic of the experimental set-up including a magnified view of the velocity and temperature sensor arrays. The arrays are used to perform filtering in the transverse direction in addition to the streamwise filtering performed by invoking Taylor's hypothesis.

Table 2.1 Flow parameters on the jet centerline at $x/D_j = 80$

$\langle U \rangle$	$\langle u_1^2 \rangle^{1/2}$	$\langle u_2^2 \rangle^{1/2}$	R_λ	ϵ	χ	η	η_ϕ
3.07 (m/s)	0.73 (m/s)	0.61 (m/s)	233	5.22 (m^2/s^3)	5.54 (K^2/s)	0.16 (mm)	0.22 (mm)

kinematic viscosity. The corresponding Taylor microscale Reynolds number $R_\lambda = \langle u^2 \rangle^{1/2} \lambda/\nu$ was approximately 233 (Table. 2.1), where $\langle u^2 \rangle^{1/2}$ is the r.m.s. streamwise velocity fluctuation and λ is the Taylor microscale. Data were collected at $x/D_j = 80$, well into the self-similar (fully developed) region of the jet. Jet off-centerline measurements is limited to $y/x = 0.1$ to avoid flow reversal and to minimize errors associated with employing Taylor's hypothesis. The mean axial velocity on the jet centerline U_c at this downstream location was 3.08 m/s and the resulting U_j/U_c value was comparable to previous results [45, 46, 47]. The Kolmogorov scale $\eta = (\nu^3/\epsilon)^{1/4}$ was 0.16 mm, where $\epsilon = 15\nu \left\langle (\frac{\partial u_1}{\partial x_1})^2 \right\rangle$ was the energy dissipation rate. The scalar dissipation length scale $\eta_\phi = (\gamma^3/\epsilon)^{1/4}$ was 0.22 mm, where γ is the thermal diffusivity. Under these flow conditions the Kolmogorov frequency of the signals ($U_c/(2\pi\eta) = 2.5$kHz) can be fully resolved by the sensors.

Measurements of filtered variables require spatial filtering of scalar fields. Due to the difficulties in obtaining three-dimensional data experimentally, two-dimensional (streamwise and radial directions) filtering as well as one-dimensional (streamwise direction only) were employed in the present study. Streamwise filtering was performed by invoking Taylor's hypothesis and the cross-stream filtering was realized with three hot-wire sensors aligned in the cross-stream direction (Figure 2.1). This filtering technique was studied by Tong *et al.* [48] and has been used by a number of authors to study the SGS stress [48, 49, 50, 51, 52, 38] and conditional SGS PDF [53, 54, 55]. Two-dimensional filtering has been demonstrated to provide a very good approximation of three-dimensional filtering, with errors of approximately 5% for the r.m.s. of the resolvable-scale variables [48]. In the present study three filter width: 10, 20, and 40 mm were used, corresponding to $\Delta/\eta = 63$, 125, and 250, respectively. Box filters were used here because it allows the resolvable-scale velocity derivatives in the cross-stream direction to be computed from the sensor array data.

To obtain the Leonard stresses, the SGS stress, the Leonard part of the SGS scalar flux, and the SGS scalar flux defined in Section 2.1, which are different from the definition $\tau_{ij} = (u_i u_j)^r - u_i^r u_j^r$ and $F_i = (u_i \phi)^r - u_i^r \phi^r$ in some literature, one-dimensional filters are also employed. For example, the SGS stress $\tau_{ij} = (u_i u_j)^r - (u_i^r u_j^r)^r$ is computed by filtering $u_i u_j$ and u_i with a two-dimensional filter

and then filtering $u_i^r u_j^r$ with a one-dimensional filter. Meneveau [31] has used one-dimensional filter to study the SGS stress and argued that the trends obtained should be similar to those using two- and three-dimensional filters. Wang and Tong [54] have also used one- and two-dimensional filters to compute statistics of conditionally filtered scalar dissipation and qualitatively comparable results were obtained. Thus it is argued here that for computations of the statistics of filtered variables, a one-dimensional filter is expected to yield qualitatively similar results as two- and three-dimensional filters.

Temperature fluctuations were measured with platinum resistance wires of 0.625μm in diameter with a maximum frequency response approximately 5 kHz. This response was determined by analyzing the heat transfer to (or from) the wire [56]. The wires were connected to dc bridges with ultra-low noise amplifiers. The probe current was set at 100μA so that the velocity contamination of the temperature signal was negligible. Details of the devices are given in Rajagopalan and Tong [55]. Velocity measurements were made with three X-wire probes operated by TSI IFA 100 hot-wire anemometers with an overheat ratio of 1.8. The X-wire probes are placed approximately 0.75 mm from their resistance wires. The probes were calibrated using a method developed by Browne *et al.* [57] in which a velocity-voltage relation was obtained at zero yaw angle and a single effective wire angle for each wire was determined using yaw-angle calibration. The angles were then used as "geometric" wire angles in computing two velocity components. Due to the high signal-to-noise ratio of the resistance-wire temperature device, a very low excess temperature (1.25°C at the measurement location) can be used, rendering the temperature contamination of hot wires negligible. For the statistics consideration, the differences between the corrected and uncorrected results are within 2%. Therefore, the uncorrelated results are given. The outputs from the hot-wire and resistance wires anemometers were low-pass filtered at 5 kHz and amplified by Krohn-Hite 3364 filters. The signals were digitized at 10 k samples/second by a 12-bit National Instrument A/D converter (PCI-6071E) which has a maximum sampling rate of 1.25×10^6 samples/second so that the inter channel delay is much shorter than the sample interval.

In the present study most of the statistics computed are conditional statistics with three conditioning variables. To obtain these conditional statistics at a reasonable level of convergence, a large amount of data is needed. The precise number of samples to achieve a given confidence level, however, is difficult to estimate because of the complex statistical characteristics of the conditional samples. Therefore, an empirical method (see ref. Chapter 3) is used in which a series of computations are performed with increasing sample sizes until satisfactory convergence for all the statistics concerned is achieved. It is found that typically 2×10^8 data samples are sufficient.

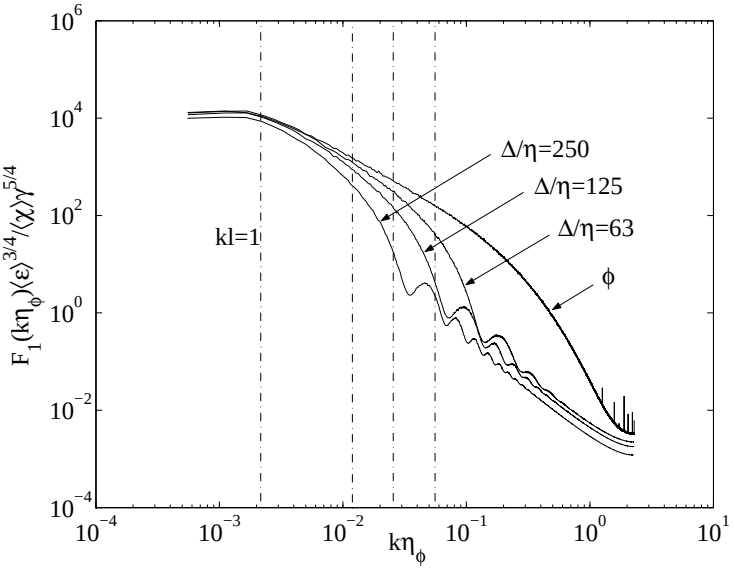

Figure 2.2 Spectra of the full and resolvable-scale scalar fluctuations on the jet centerline. The wavenumber and the spectra are normalized by scalar dissipation length scale and scalar scale. The filter wavenumber $\kappa_\Delta = \pi/\Delta$ for each filter width is marked by a dashed vertical line. The lobes at higher wavenumbers are due to the inherent leakage in spectral space of box filters. The left most dashed vertical line marks the integral-scale wavenumber.

2.3 Experimental results

In the present study three filter scales, $\Delta/\eta = 63$, 125, and 250 were used. Figure 2.2 shows the streamwise spectra of the full and the resolvable-scale scalar spectra normalized by dissipation-scale scalar and length scales. The lower spectral values for the resolvable-scale velocity at wavenumbers below $\kappa\Delta = \pi$ is due to the removal of cross-streamwise wavenumbers that would be aliased into the resolvable scales if only streamwise filtering is performed.

2.3.1 Conditional SGS statistics

Conditional SGS scalar flux and its production rate

The results for conditional SGS scalar flux are normalized by the r.m.s. streamwise velocity and scalar fluctuations. The normalized conditional SGS scalar flux components $\langle F_1|\mathbf{u}^r, \phi^r\rangle$ and $\langle F_2|\mathbf{u}^r, \phi^r\rangle$ for $\Delta/\eta = 125$ are shown in Figure 2.3(b) and (e), respectively. For convenience, The sample-space variables ψ and $\mathbf{v}$ are omitted from the conditional means hereafter. In addition, only the fluctuating parts of ϕ^r and $\mathbf{u^r}$ are plotted. The results for the conditional SGS scalar flux production rate are normalized by the mean scalar dissipation rate. The normalized conditional SGS scalar flux components $\langle P_{F1}|\mathbf{u}^r, \phi^r\rangle$ and $\langle P_{F2}|\mathbf{u}^r, \phi^r\rangle$ for $\Delta/\eta = 125$ are shown in Figure 2.4(b) and 2.4(e), respectively.

The figures show that both $\langle F_1|\mathbf{u}^r, \phi^r\rangle$ and $\langle F_2|\mathbf{u}^r, \phi^r\rangle$ depend on both $\mathbf{u}^r$ and ϕ^r. For positive ϕ^r fluctuations, $\langle F_1|\mathbf{u}^r, \phi^r\rangle$ increases with u_1^r, and the dependence is stronger for larger u_2^r fluctuations. The cross-stream SGS flux, $\langle F_2|\mathbf{u}^r, \phi^r\rangle$, increases with u_2^r while the dependence on u_1^r is generally weak. For negative ϕ^r fluctuations, $\langle F_1|\mathbf{u}^r, \phi^r\rangle$ decreases and becomes negative with increasing u_1^r. The magnitude of $\langle F_2|\mathbf{u}^r, \phi^r\rangle$ increases with $|u_2^r|$, and the dependence is stronger for positive u_1^r. For small ϕ^r fluctuations (≈ 0), both $\langle F_1|\mathbf{u}^r, \phi^r\rangle$ and $\langle F_2|\mathbf{u}^r, \phi^r\rangle$ have saddle shapes with $\langle F_2|\mathbf{u}^r, \phi^r\rangle$ having as the same sign $-u_1^r u_2^r$.

The SGS flux production $\langle P_{F1}|\mathbf{u}^r, \phi^r\rangle$ (Figure 2.4(b)) has saddle-shaped isocontours with the saddle point moving toward positive u_1^r for positive ϕ^r and vice versa. Large positive and negative production values tend to occur for large $|u_2^r|$ values. The isocontours of $\langle P_{F2}|\mathbf{u}^r, \phi^r\rangle$ has a saddle shape for positive ϕ^r and has the same sign as $-u_1^r u_2^r$. For small ϕ^r, both $\langle P_{F1}|\mathbf{u}^r, \phi^r\rangle$ and $\langle P_{F2}|\mathbf{u}^r, \phi^r\rangle$ have trends similar to $\langle F_1|\mathbf{u}^r, \phi^r\rangle$ and $\langle F_2|\mathbf{u}^r, \phi^r\rangle$ respectively, suggesting local balance of conditional SGS scalar flux production and destruction under this condition. Comparing the three cases of different ϕ^r values, the saddle point of the $\langle P_{F1}|\mathbf{u}^r, \phi^r\rangle$ contours appears to shift toward positive u_1^r for positive ϕ^r, and toward negative u_1^r for negative ϕ^r. The zero point for $\langle F_1|\mathbf{u}^r, \phi^r\rangle$ also appears to shift in the same direction by a larger amount, however, suggesting that the balance between production and destruction may also have shifted.

The trends of the conditional SGS scalar flux generally can be understood from their production rates. For small ϕ^r fluctuations, the SGS eddies are more likely to be well mixed. For positive ϕ^r fluctuations, they are likely to have come from upstream positions near the centerline. In both cases they are in equilibrium with the local conditions. In Chapter 3, it is found that when SGS turbulence is in local equilibrium, the conditional SGS stress and conditional SGS stress production

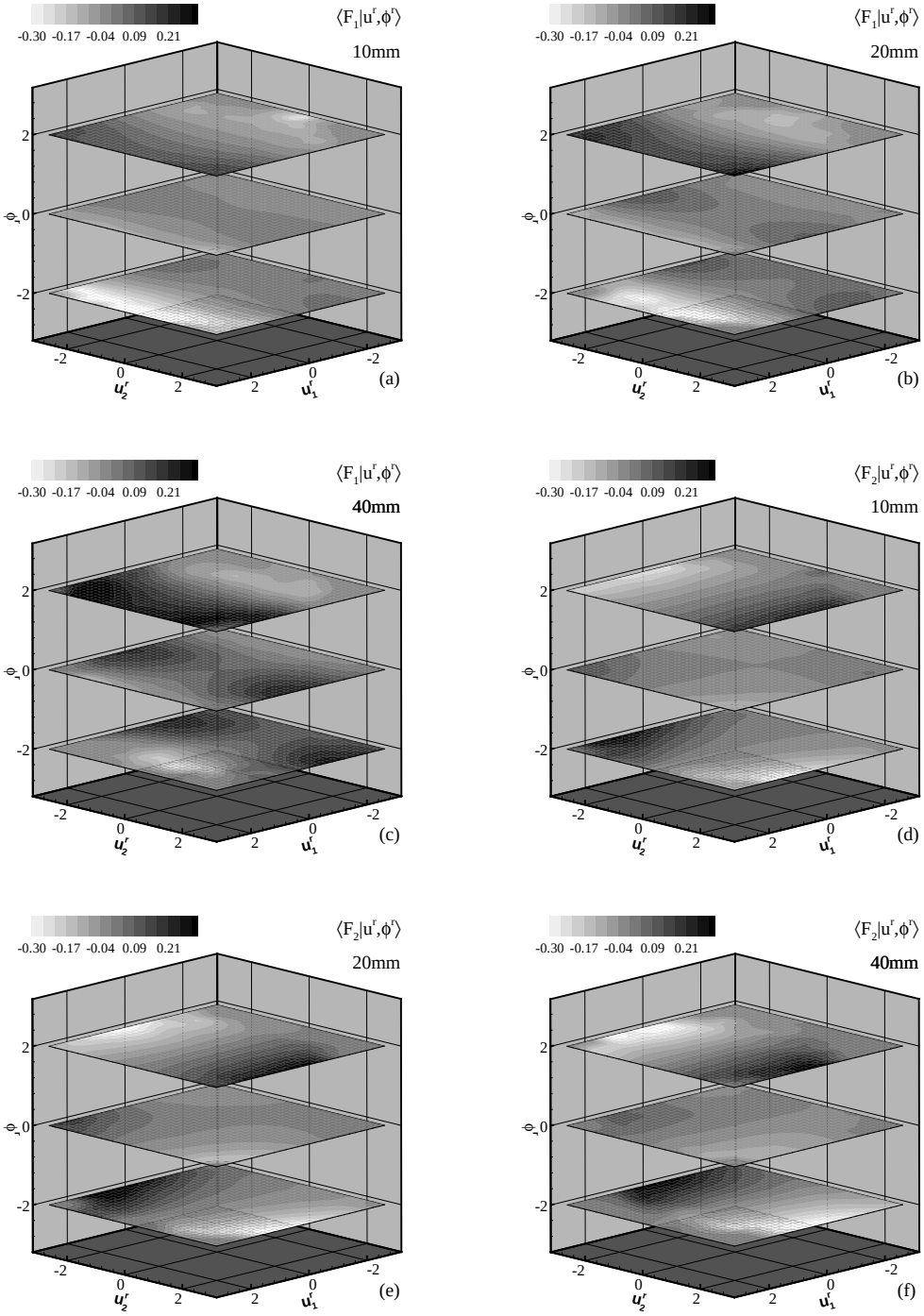

Figure 2.3 Conditional SGS scalar flux, $\langle F_1|\mathbf{u}^r,\phi^r\rangle$ (a)-(c), and $\langle F_2|\mathbf{u}^r,\phi^r\rangle$ (d)-(f) for $\Delta/\eta = 63, 125$ and 250, respectively. Both $\langle F_1|\mathbf{u}^r,\phi^r\rangle$ and $\langle F_2|\mathbf{u}^r,\phi^r\rangle$ depend on the resolvable-scale velocity and scalar, and fall-off slower with filter scale than the predictions.

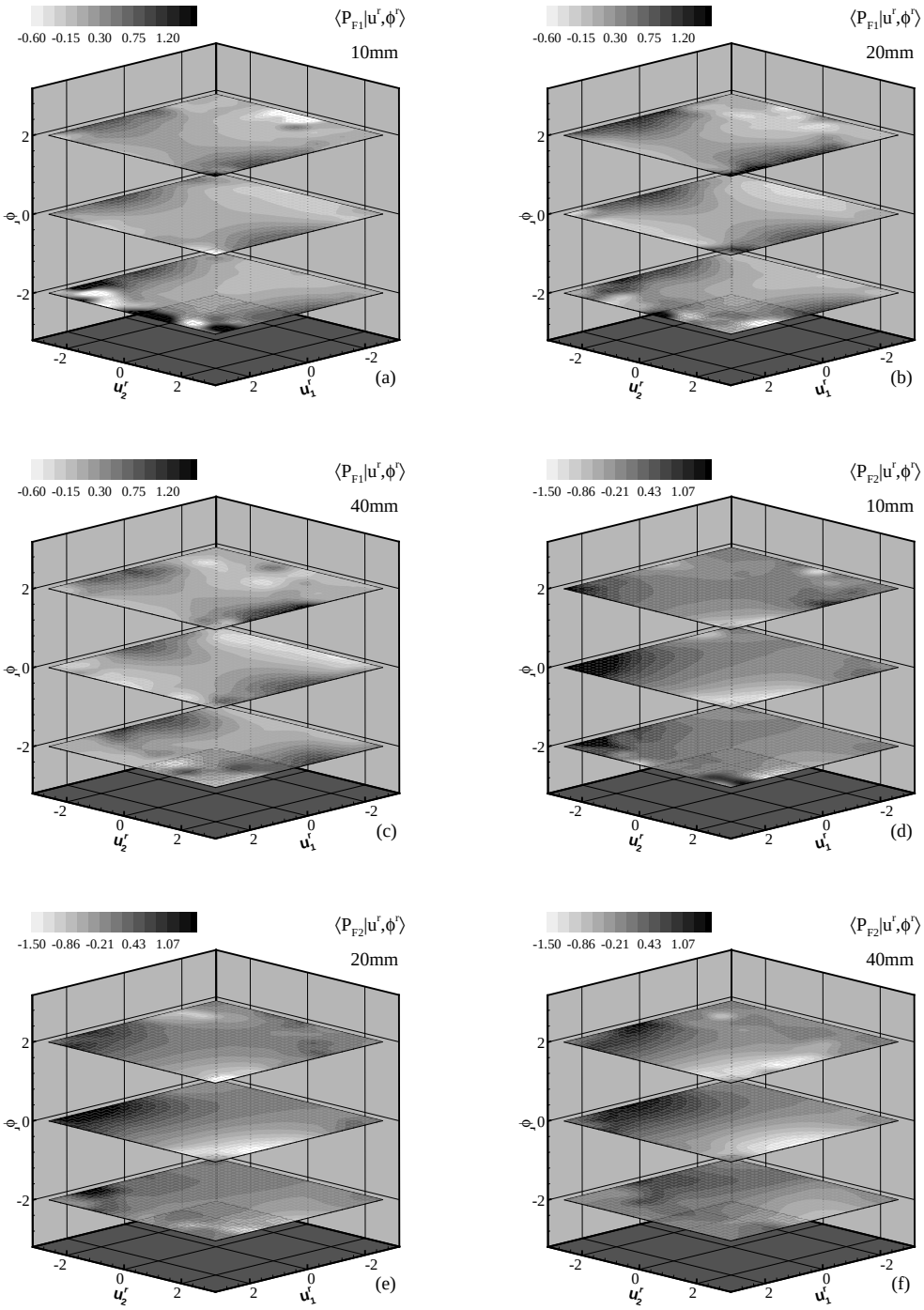

Figure 2.4 Conditional SGS scalar flux production rate, $\langle P_{F1}|\mathbf{u}^r, \phi^r\rangle$ (a)-(c), and $\langle P_{F2}|\mathbf{u}^r, \phi^r\rangle$ (d)-(f) for $\Delta/\eta = 63, 125$ and 250, respectively. Both $\langle P_{F1}|\mathbf{u}^r, \phi^r\rangle$ and $\langle P_{F2}|\mathbf{u}^r, \phi^r\rangle$ depend on the resolvable-scale velocity and scalar and fall-off slower with filter scale than the predictions.

have similar trends. Consequently, $\langle F_1|\mathbf{u}^r,\phi^r\rangle$ and $\langle F_2|\mathbf{u}^r,\phi^r\rangle$ have dependencies similar to those of $\langle P_{F1}|\mathbf{u}^r,\phi^r\rangle$ and $\langle P_{F2}|\mathbf{u}^r,\phi^r\rangle$ for positive ϕ^r.

For negative ϕ^r, the dependence of $\langle F_1|\mathbf{u}^r,\phi^r\rangle$ on u_2^r is stronger for negative u_1^r. Because the SGS eddies experienced strong shear and rotation, therefore may contain strong non-local (history) effects compared to those with small or positive ϕ^r values. The dominant term in its production rate, $\langle P_{F1}|\mathbf{u}^r,\phi^r\rangle$, is $\left\langle -F_2\frac{\partial u_1^r}{\partial x_2}\middle|\,\mathbf{u}^r,\phi^r\right\rangle$, which is due to the dominant resolvable-scale velocity gradient $\partial u_1^r/\partial x_2$. It can be rewritten as:

$$\left\langle -F_2\frac{\partial u_1^r}{\partial x_2}\middle|\,\mathbf{u}^r,\phi^r\right\rangle = \langle -F_2S_{12}|\mathbf{u}^r,\phi^r\rangle + \langle -F_2\Omega_{12}|\mathbf{u}^r,\phi^r\rangle \tag{2.15}$$

where S_{12} and Ω_{12} are components of the resolvable-scale strain rate tensor and the rotation rate tensor, respectively. The terms on the RHS of equation (2.15) are the production of $\langle F_1|\mathbf{u}^r,\phi^r\rangle$ due to straining and rotation of the SGS turbulence, respectively. Figures 2.5(a) and (b) show that the SGS eddies experience stronger shear and rotation when they enter the centerline (large $|u_2^r|$) with large negative u_1^r than those with large positive u_1^r, thereby resulting in larger magnitudes of the conditional $\langle F_1|\mathbf{u}^r,\phi^r\rangle$ for negative u_1^r. The dependence of the conditional $\langle F_2|\mathbf{u}^r,\phi^r\rangle$ on u_2^r is stronger for positive u_1^r. The dominant term in $\langle P_{F2}|\mathbf{u}^r,\phi^r\rangle$ is $\left\langle -\tau_{22}\frac{\partial\phi^r}{\partial x_2}\middle|\,\mathbf{u}^r,\phi^r\right\rangle$, due to the dominant resolvable-scale scalar gradient $\partial\phi^r/\partial x_2$. (The production rates of F_2 due to the straining S_{12} and rotation Ω_{12} approximately cancel each other.) Because the SGS eddies entering the jet centerline with positive u_1^r generally have a larger SGS stress τ_{22} (Figure 2.7(b)). Therefore, $\langle F_2|\mathbf{u}^r,\phi^r\rangle$ is larger for positive u_1^r.

Conditional SGS scalar variance production rate

The conditional SGS scalar variance production rate, $\langle P_\phi|\mathbf{u}^r,\phi^r\rangle$, for $\Delta/\eta = 125$, normalized by the mean scalar dissipation rate, is shown in Figure 2.6. The isocontours generally have saddle shapes, and the dependence on the resolvable-scale velocity is stronger for negative ϕ^r. For negative ϕ^r, $\langle P_\phi|\mathbf{u}^r,\phi^r\rangle$ generally has stronger dependence on u_2^r for small magnitude of the u_1^r, indicating that the eddies from the edge of the jet carry a larger SGS scalar variance transfer rate when entering the centerline with large crossstream velocity and average streamwise velocity. For positive ϕ^r, the dependence of $\langle P_\phi|\mathbf{u}^r,\phi^r\rangle$ on the resolvable-scale velocity is weaker, and the magnitude is smaller, suggesting that the eddies from upstream positions near the centerline, which are likely already well-mixed, have smaller SGS scalar variance transfer rate.

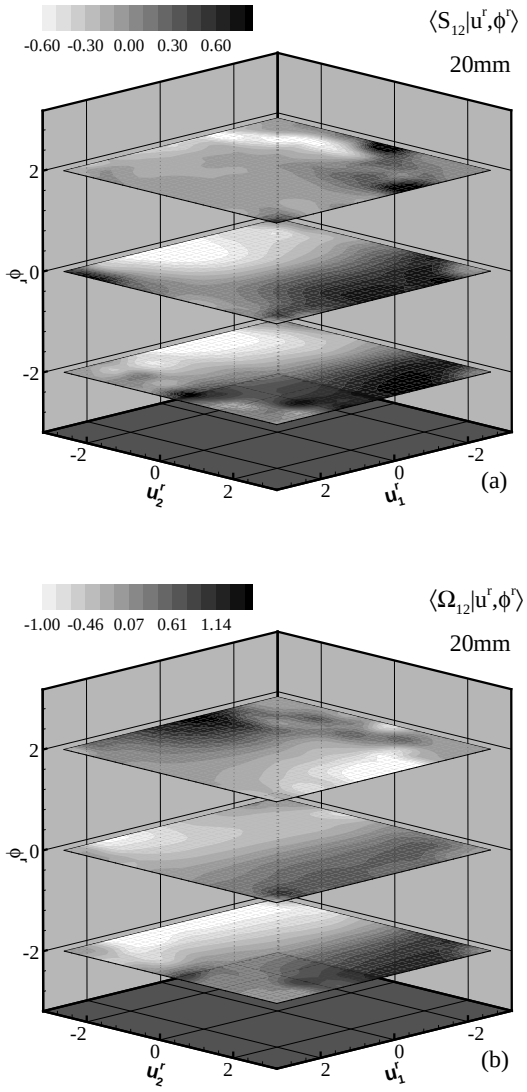

Figure 2.5 Conditional strain rate S_{12} (a) and rotation Ω_{12} (b) for $\Delta/\eta = 125$ on the jet centerline.

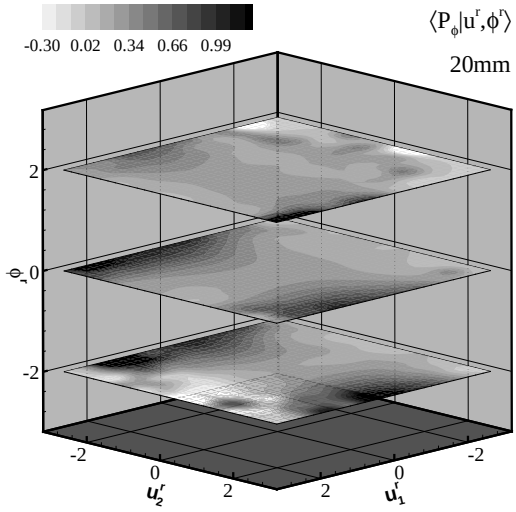

Figure 2.6 Conditional scalar variance production rate, $\langle P_\phi | \mathbf{u}^r, \phi^r \rangle$ for $\Delta/\eta = 125$ on the jet centerline.

Conditional SGS stress and its production rate

The results for the conditional SGS stress and its production rate shown in Figures (2.7) and (2.8) are normalized by the variance of the streamwise velocity and the total energy dissipation rate, respectively. The dependencies of the SGS stress and its production rate on the resolvable-scale velocity are generally less influenced by ϕ^r than those of SGS scalar flux and SGS scalar flux variance transfer rate. The results are generally similar to those in Chen *et al.* [38] and have slightly stronger dependencies on the resolvable-scale velocity for small and positive ϕ^r fluctuations, indicating that well-mixed eddies have stronger dependence on the resolvable-scale velocity.

The results in this section show that the conditional SGS stress, scalar flux, and their production rates are closely related to the dynamics of the jet. Specifically, for eddies in equilibrium (small and positive ϕ^r on the jet centerline) the conditional SGS flux and stress have similar dependencies on u_1^r and u_2^r to those of the conditional SGS production rates. For eddies in non-equilibrium (negative ϕ^r from the edge of the jet) the similarity is much less evident. The different dependencies on the resolvable-scale velocity for positive and negative ϕ^r fluctuations reflect the different histories of the SGS turbulence since eddies at a given location with the same velocity but different scalar values must have experienced different histories (e.g. came from different locations). Therefore, inclusion of ϕ^r can provide some information on the flow history to SGS models that are based on single-point modeling approach.

As equation (2.6) shows, the conditional SGS production rates affect the JPDF. Previous analytical results (e.g. ref. Sabelnikov [40]) on scalar PDF have shown that concave and convex shapes for conditional scalar dissipation, which plays a similar role as the SGS scalar variance production, correspond to super- and sub-Gaussian PDFs, respectively. While there have been no analytical results on the conditional SGS production rates, they will likely influence the JPDF in similar ways. For example, higher magnitudes for larger $\mathbf{u}^r$ or ϕ^r fluctuations would result in higher JPDF values compared to a joint-Gaussian JPDF and vice versa. Therefore, the conditional SGS production rates can be used to test SGS model predictions. Furthermore, it is important to know whether the dependencies of the conditional production rates diminish according to the theoretical predictions (or Kolmogorov's hypothesis), which is examined below. It is noted that while the results here are obtained in a turbulent jet, some of the behaviors of the conditional statistics for equilibrium eddies are similar to those observed in the atmospheric boundary layer (Chapter 3). Specifically, the conditional SGS stress and flux have functional forms similar to their production rates, suggesting that the similarity might be a universal behavior regardless of the large-scale geometry. This provides

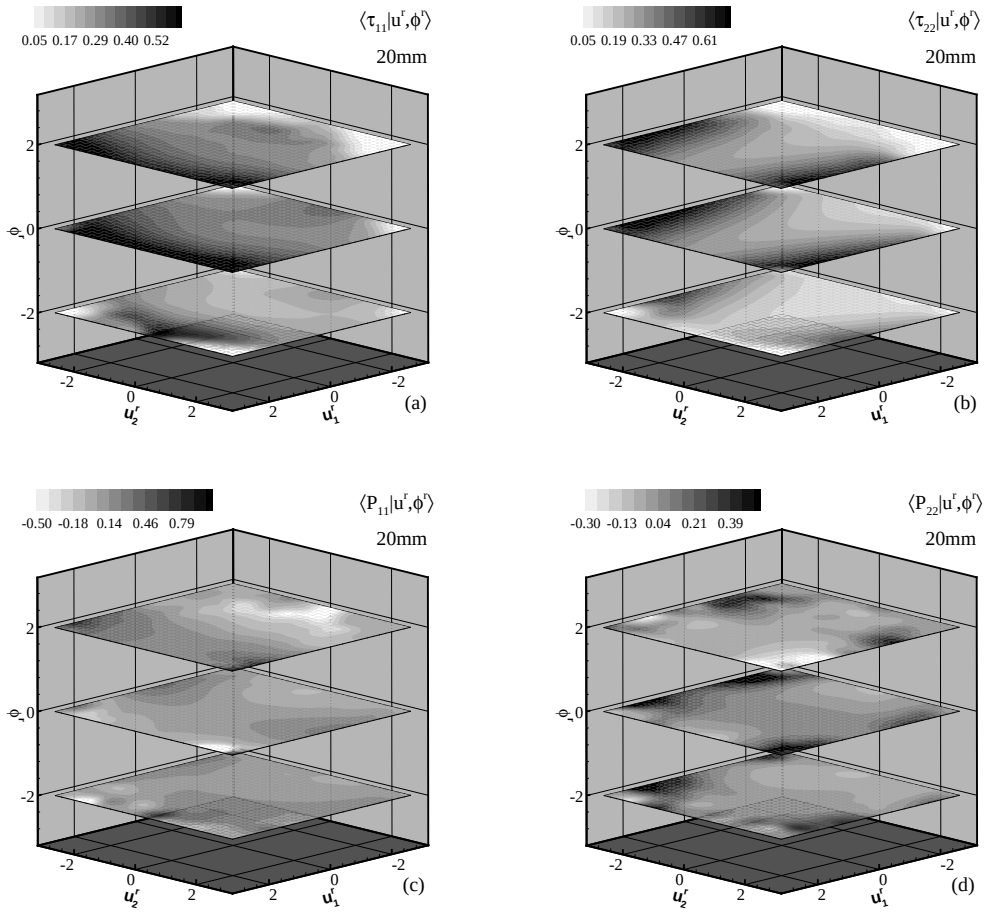

Figure 2.7 Normal components of the conditional SGS stress, $\langle \tau_{11} | \mathbf{u}^r, \phi^r \rangle$ and $\langle \tau_{22} | \mathbf{u}^r, \phi^r \rangle$, and their production rates for $\Delta/\eta = 125$ on the jet centerline.

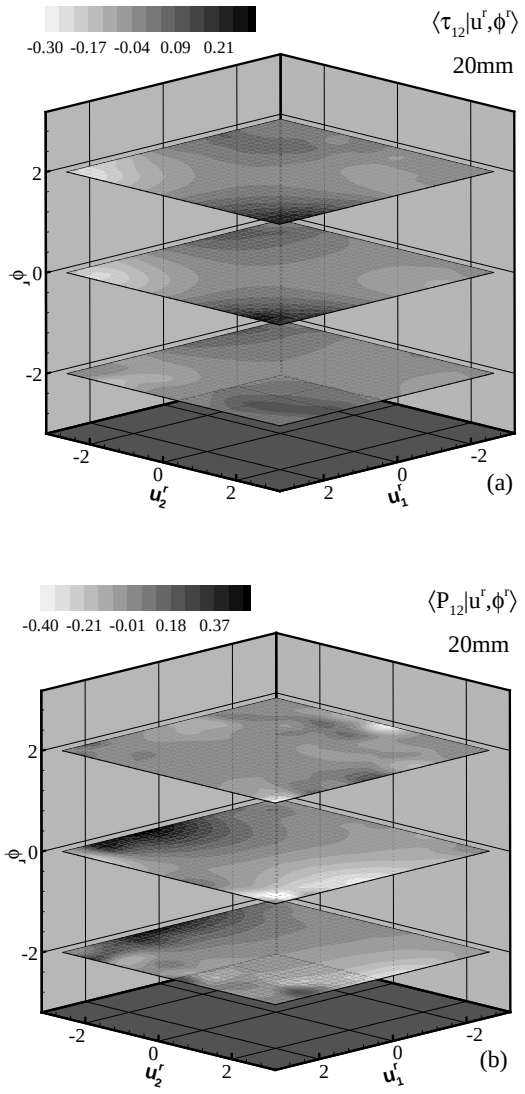

Figure 2.8 Shear component of the conditional SGS stress $\langle \tau_{12} | \mathbf{u}^r, \phi^r \rangle$ and its production rate for $\Delta/\eta = 125$ on the jet centerline.

further support in using the production rates as models for SGS stress and flux for quasi-equilibrium eddies [58].

2.3.2 Filter-scale dependence

The mean SGS flux, SGS flux production rate, and SGS shear stress for the centerline and off-centerline positions is first considered, which are given in Figure 2.9 for the three filter scales. The SGS statistics generally decrease with the filter scale, except the scalar variance transfer rate (not shown), which should be constant for all filter scales in the inertial range. The cross-stream SGS scalar $\langle F_2 \rangle$ (at the off-centerline position) is close to the $\Delta^{4/3}$ dependence, consistent with Lumley's $k^{-7/3}$ prediction for the scalar-flux co-spectrum. The mean streamwise SGS flux, $\langle F_1 \rangle$, is close to Δ^2 on the jet centerline and is between $\Delta^{4/3}$ and Δ^2 at the off-centerline position. Wyngaard [59] predicted the k^{-3} dependence for the streamwise scalar-flux co-spectrum in a horizontally homogenous atmospheric boundary layer. The prediction also holds for a homogenous shear flow with a cross-stream mean scalar gradient. The observed approximate Δ^2 dependence of $\langle F_1 \rangle$ is not inconsistent with this prediction but suggests that inhomogeneity and turbulent transport might play important roles in any deviation from the Δ^2 dependence.

The mean SGS flux production rate $\langle P_{F2} \rangle$ (Figure 2.9(b)) is close to the $\Delta^{2/3}$ scaling given in Section 2.1, indicating that it is consistent with Lumley's assumption and Kolmogorov's hypothesis. The mean production rate $\langle P_{F1} \rangle$ is close to the predicted $\Delta^{4/3}$ scaling at the off centerline position, again indicating consistency with the hypothesis. The measured dependence on the jet centerline is close to $\Delta^{2/3}$, a slower fall-off with filter scales. This is perhaps because the production mechanism on the jet centerline is different from that off the centerline: the former is primarily due to the streamwise stretching of F_1 whereas the latter is dominated by straining and rotation of F_2. Because the mean SGS flux and SGS flux production rates evolve the mean scalar and scalar flux, the consistency of measurements with predictions suggests that they are likely to have diminishing influences on the lower-order resolvable-scale statistics (mean profiles, mean stress and fluxes) for inertial-range filter scales because the assumption used in the predictions are consistent with Kolmogorov's hypothesis of statistical independence of distinct scales.

The mean SGS shear stress production rate $\langle P_{12} \rangle$ (Figure 2.10) decreases somewhat faster (Δ) than the predicted $\Delta^{2/3}$ dependence. However, the filter-scale dependence appear to be changing and is weaker between $\Delta = 20$ and 40 mm ($\approx \Delta^{2/3}$). Therefore, the results are not inconsistent with Kolmogorov's hypothesis.

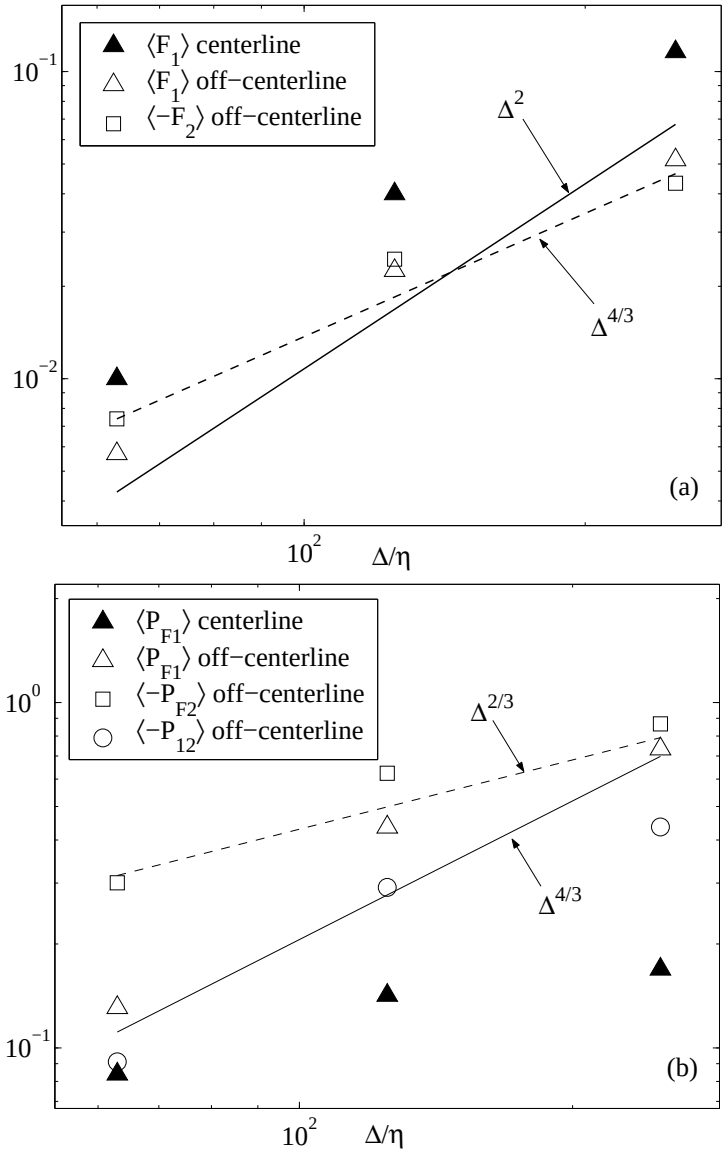

Figure 2.9 Filter-scale dependencies of the mean SGS scalar fluxes (a) and their production rate (b) for both the centerline and off-centerline positions. The cross-stream SGS scalar flux $\langle F_2 \rangle$ and its production rate (at the off-centerline position) have dependencies close to the $\Delta^{4/3}$ and $\Delta^{2/3}$ predictions, respectively.

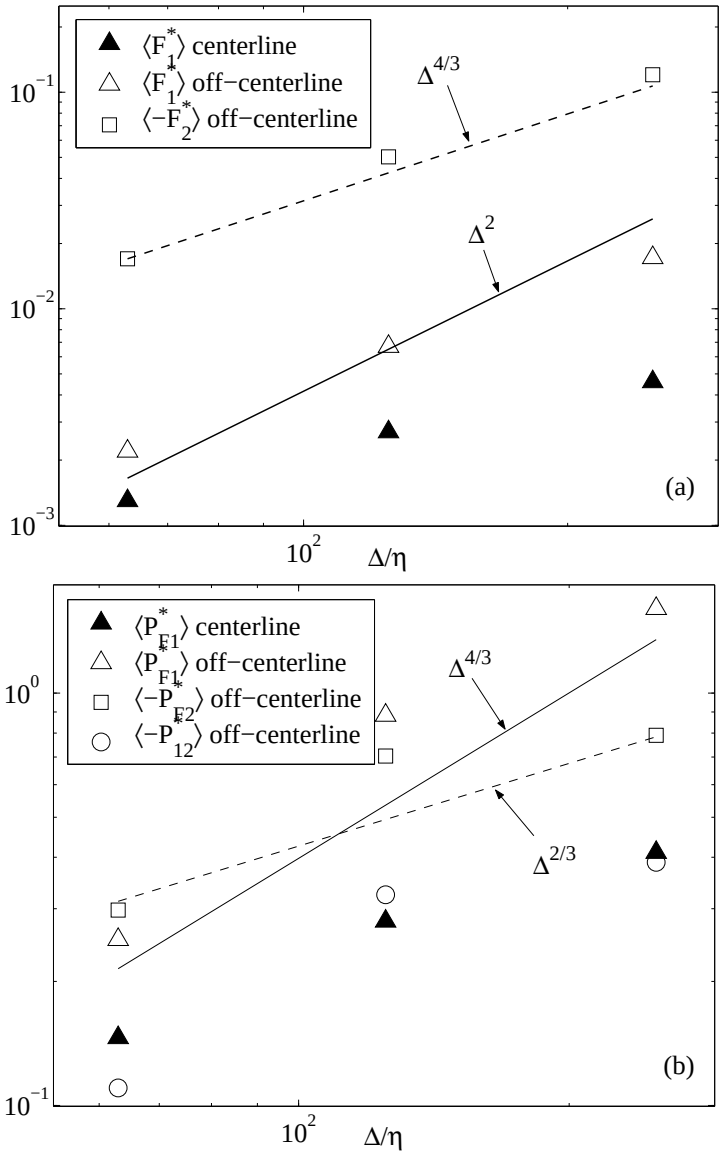

Figure 2.10 Filter-scale dependencies of the mean SGS scalar fluxes (a) and their production rate (b) predicted using the Smagorinsky models for both centerline and off-centerline positions. The scale dependencies are generally consistent with measurements.

While the lower-order resolvable-scale statistics depend on the mean SGS flux and SGS flux production rate, the shape of the JPDF depends primarily on the conditional SGS flux and conditional SGS flux production rate. Furthermore, consistency of their dependencies on the filter scale with Kolmogorov's hypothesis would indicate that the JPDF will be invariant to the SGS turbulence as the filter scale becomes small. Figure 2.3 shows the conditional SGS scalar fluxes for the three filter scales. While $\langle F_1 \rangle$ decreases by a factor of more than 10 from $\Delta = 40$mm to $\Delta = 10$mm, the largest values of $\langle F_1 | \mathbf{u}^r, \phi^r \rangle$ only fall by a factor of two. The largest values of the cross-stream flux $\langle F_2 | \mathbf{u}^r, \phi^r \rangle$ decrease by only 20%, much slower than the mean flux $\langle F_2 \rangle$ (for the off-centerline position). The slower fall-off of the conditional SGS fluxes shows that while the mean SGS fluxes follow the theoretical predictions, the large fluctuations (conditional averages) do not. This suggests that the relatively rare events that contribute to large conditional SGS fluxes have "anomalous" behaviors.

The conditional production rates (Figure 2.4) also fall off much slower than the mean production rates: the reductions are approximately $10\% - 20\%$ from $\Delta = 40$mm to $\Delta = 10$mm for $\langle P_{F1} | \mathbf{u}^r, \phi^r \rangle$ and $\langle P_{F2} | \mathbf{u}^r, \phi^r \rangle$, respectively, while the mean SGS flux production rates, $\langle P_{F1} \rangle$ and $\langle P_{F2} \rangle$, (Figure 2.9(b)) follow the predictions using Lumley's assumption. The results again suggest that large deviations from the mean production rates also have "anomalous" behaviors.

The slower fall-offs of the conditional SGS flux, the conditional SGS stress, and the conditional production rates compared to the predictions suggest that the SGS stress and fluxes have non-diminishing influences on the resolvable-scale JPDF (especially its shape). Consequently, while it is expected that lower-order LES statistics (mean, variance, covariance), which depend primarily on the mean SGS flux and the mean SGS flux production rate, to become insensitive to the SGS models employed as the filter scale decreases, these models can potentially have a strong impact on LES predictions of the JPDF even for inertial-range filter scales. Therefore, in applications where higher-order statistics are important (e.g. turbulent transport or scalar PDF), SGS models need to correctly predict the conditional SGS statistics. It is emphasized that these understandings are based on the dynamic terms in the JPDF equation, therefore are on more solid physical grounds than the previous arguments supporting the LES premise (see the introduction).

2.3.3 Smagorinsky model predictions

To examine the effects of SGS models on LES statistics and their filter-scale dependencies, the Smagorinsky model is used to the predict conditional SGS scalar flux and its production rate. Other models such as the Bardina model require a test filter, which can only be achieved in one

dimension in the present measurements, therefore tests of these models are not attempted here. To predict the conditional SGS scalar flux production rate, the modeled SGS stress is needed. The method given in Chen *et al.* [38] is used to compute the SGS stress. The Smagorinsky model [60, 1] for SGS scalar flux is given by

$$F_i^* = -Pr_T^{-1}(C_S\Delta)^2(2S_{ij}S_{ij})^{1/2}\frac{\partial\phi^r}{\partial x_i} \tag{2.16}$$

where $C_s = 0.154$ is the Smagorinsky model constant for a box filter, and a value of 0.5 for the turbulent Prandtl number, Pr_T, was suggested by Lilly [1]. Here $S_{ij}S_{ij}$ is computed with the available components of the resolvable-scale strain rate tensor as $S_{11}^2 + S_{22}^2 + S_{33}^2 + 2S_{12}^2$ (the incompressibility condition is used to obtain S_{33}), thus a factor of $(15/7)^{1/2}$ obtained for isotropic turbulence is used in computing F_i.

The mean streamwise scalar flux $\langle F_1\rangle$ (Figure 2.10) is under-predicted. This is perhaps because the Smagorinsky model uses only the resolvable-scale scalar gradient to predict F_1 whereas the true flux production is primarily due to straining and rotation of the SGS scalar fluxes. The filter-scale dependence of $\langle F_1\rangle$ (Δ^2) at the off-centerline position is well predicted but not on the centerline. The scale dependence of the mean flux production $\langle P_{F1}\rangle$ off the centerline ($\Delta^{4/3}$) is also quite well predicted, although its magnitude is not because not all the components of $\langle P_{F1}\rangle$ are measured. The scale dependence on the centerline is consistent with measurements (less than $\Delta^{4/3}$). The mean cross-stream flux $\langle F_2\rangle$ is over-predicted by the model, but its scale dependence of $\Delta^{4/3}$ is very well predicted. The flux production rate $\langle P_{F2}\rangle$ is also well predicted, showing a $\Delta^{2/3}$ dependence. The more accurate predictions for $\langle F_2\rangle$ and $\langle P_{F2}\rangle$ are because the cross-stream resolvable-scale scalar gradient plays an important role in the production of $\langle F_2\rangle$, which is also used in the Smagorinsky model. The Smagorinsky model prediction of $\langle P_{12}\rangle$ has a similar scale dependence to measurements, indicating that model the behavior, at the level of the mean SGS shear stress production rate, is consistent with Kolmogorov's hypothesis and that of the SGS turbulence.

The predicted conditional SGS scalar fluxes $\langle F_1^*|\mathbf{u}^r, \phi^r\rangle$ (Figure 2.11(a)-(c)) and $\langle F_2^*|\mathbf{u}^r, \phi^r\rangle$ (Figure 2.11(d)-(f)) have smaller magnitudes compared with the measured $\langle F_1|\mathbf{u}^r, \phi^r\rangle$ (Figure 2.3(a)-(c)) and $\langle F_2|\mathbf{u}^r, \phi^r\rangle$ (Figure 2.3(d)-(f)). The trends are better predicted for small ϕ^r fluctuations than those for large fluctuations. The conditional means $\langle F_1^*|\mathbf{u}^r, \phi^r\rangle$ and $\langle F_2^*|\mathbf{u}^r, \phi^r\rangle$ decrease faster with the filter scale than measurements but slower than the predictions; therefore the dependencies are not consistent with Kolmogorov's hypothesis. Chen *et al.* (2003) also observed slower fall-off of the conditional SGS shear stress production rate $\langle P_{12}|\mathbf{u}^r, \phi^r\rangle$.

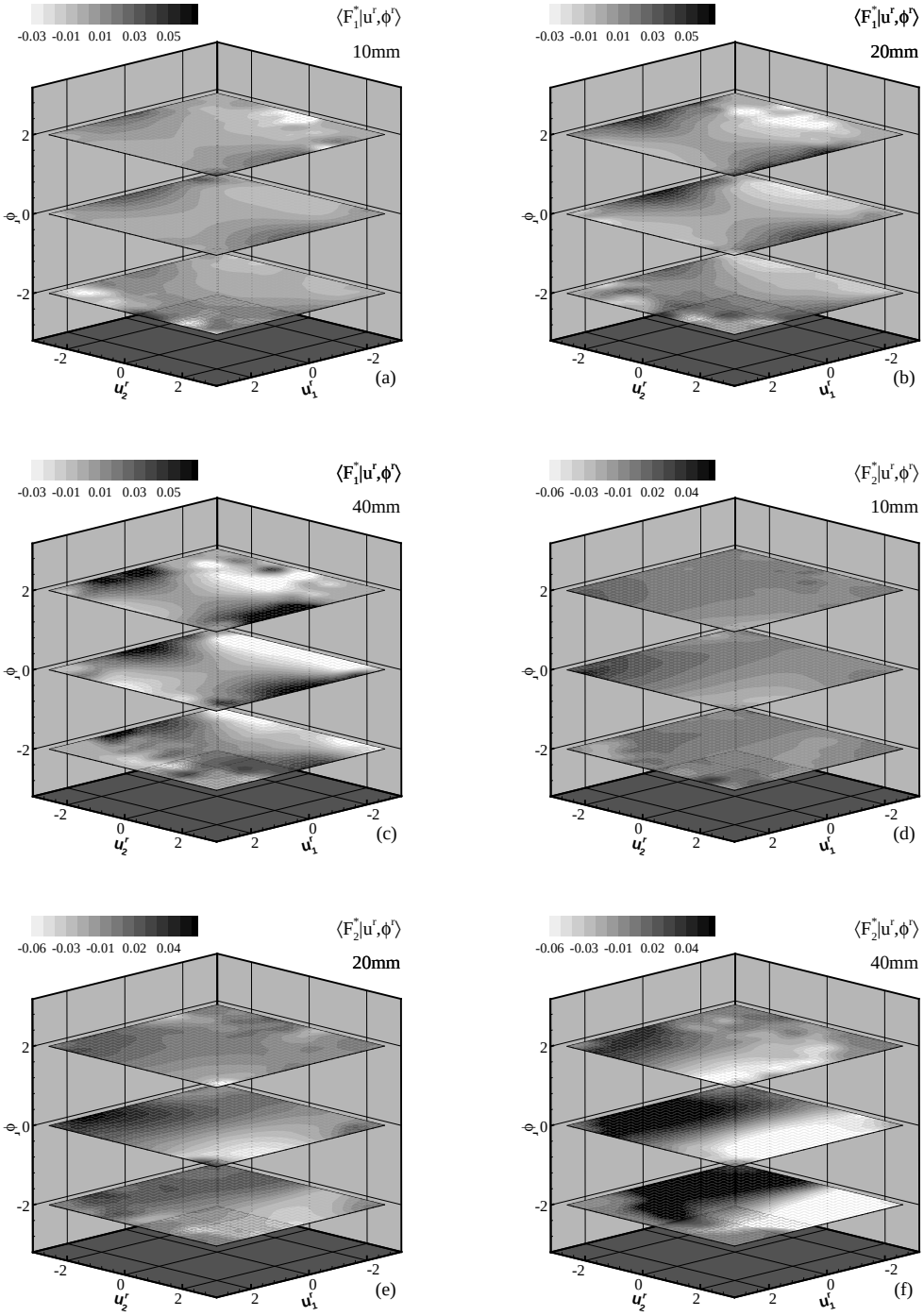

Figure 2.11 Conditional SGS scalar flux, $\langle F_1^* | \mathbf{u}^r, \phi^r \rangle$ (a)-(c), and $\langle F_2^* | \mathbf{u}^r, \phi^r \rangle$ (d)-(f) for $\Delta/\eta = 63, 125$ and 250 predicted using the Smagorinsky models. Both predicted conditional SGS scalar fluxes fall off with the filter scale slower than the unconditional means.

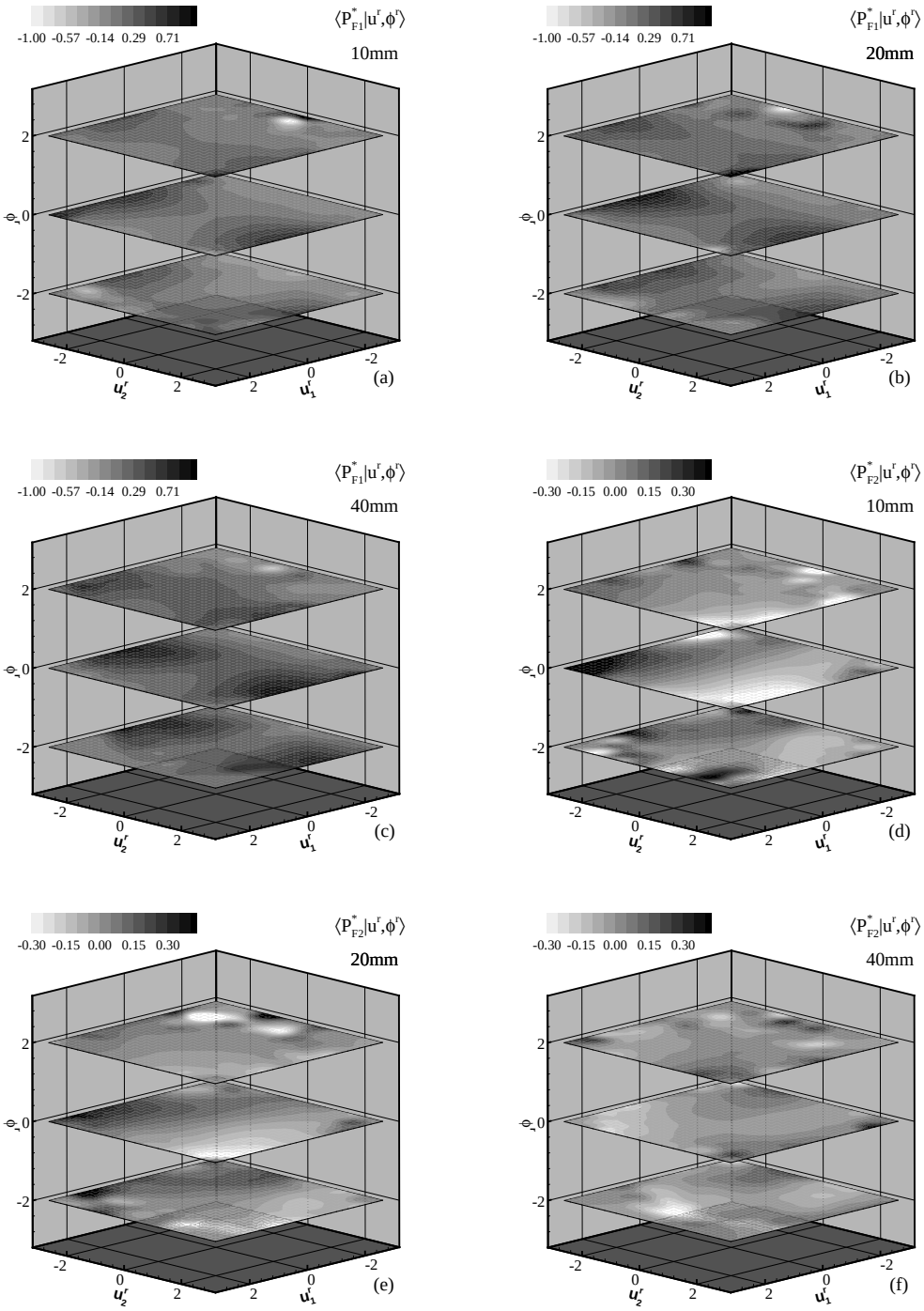

Figure 2.12 Conditional SGS scalar flux production rate, $\langle P^*_{F1}|\mathbf{u}^r, \phi^r\rangle$ (a)-(c), and $\langle P^*_{F2}|\mathbf{u}^r, \phi^r\rangle$ (d)-(f) for $\Delta/\eta = 63, 125$ and 250 predicted using the Smagorinsky models. While $\langle P^*_{F1}|\mathbf{u}^r, \phi^r\rangle$ fall off with the filter scale, $\langle P^*_{F2}|\mathbf{u}^r, \phi^r\rangle$ appear to increase with the filter scale.

The isocontours of $\langle P^*_{F1}|\mathbf{u}^r, \phi^r\rangle$ (Figure 2.12(a)-(c)) and $\langle P^*_{F2}|\mathbf{u}^r, \phi^r\rangle$ (Figure 2.12(d)-(f)) are also better predicted for small ϕ^r fluctuations than those for large $|\phi^r|$ suggesting that the SGS flux and its production rate associated with the well-mixed eddies, which are in better local equilibrium than the un-mixed eddies, can be better predicted. The predicted magnitudes of $\langle P^*_{F1}|\mathbf{u}^r, \phi^r\rangle$ and $\langle P^*_{F2}|\mathbf{u}^r, \phi^r\rangle$ are in closer agreement with the measurements than the predicted SGS scalar fluxes. In addition, the largest values of $\langle P^*_{F2}|\mathbf{u}^r, \phi^r\rangle$ appear to increase with decreasing filter scale. The cause for this model behavior is unclear at this point.

The predicted conditional SGS scalar variance transfer rate, $\left\langle P^*_\phi \middle| \mathbf{u}^r, \phi^r \right\rangle$, is shown in Figure 2.13. Similar to the results for the flux production rate, the trend of $\left\langle P^*_\phi \middle| \mathbf{u}^r, \phi^r \right\rangle$ for small ϕ^r fluctuations is better predicted than those for large $|\phi^r|$. The model over-predicts the magnitude besides not capable of predicting the conditional backscatter observed (Figure 2.6). In addition, $\left\langle P^*_\phi \middle| \mathbf{u}^r, \phi^r \right\rangle$ also appears to increase with decreasing filter scale, inconsistent with the measurements.

The model results show that in general the Smagorinsky models correctly predicts the scale dependencies of the mean SGS fluxes and its production rates and the predictions are consistent with the theoretical predictions using Lumley's assumption, which is based on Kolmogorov's hypothesis. Therefore, the modeled mean fluxes and production rates are expected to have diminishing influences on LES results as the filter scale becomes smaller, consistent with Kolmogorov's hypothesis of statistical independence of distance scales. On the other hand, the model predictions of the conditional production rates are at variance with Kolmogorov's hypothesis, therefore may have lasting influences on these statistics. However, they will influence the resolvable-scales in ways different from that of the SGS turbulence because the conditional SGS scalar flux and the conditional SGS scalar flux production rates obtained from the model have different filter-scale dependencies than measurements.

It is noted in the introduction that simulations have suggested that lower-order LES statistics are somewhat insensitive to the model details when the energy-containing scales are well resolved. However, such an observation is entirely empirical and generally cannot point to the specific model behaviors that are responsible for this insensitivity. By contrast, the present study analyzes the behaviors of the statistics that evolve the JPDF through the JPDF equation, therefore can establish a much closer link between SGS model behaviors and LES results. Specifically, the results show that the mean SGS stress, the mean SGS flux, and their production rates predicted by the Smagorinsky model, which evolve the lower-order LES statistics, are consistent with the Kolmogorov's hypothesis. Consequently, the model will have diminishing effects on the LES statistics for inertial-range filter

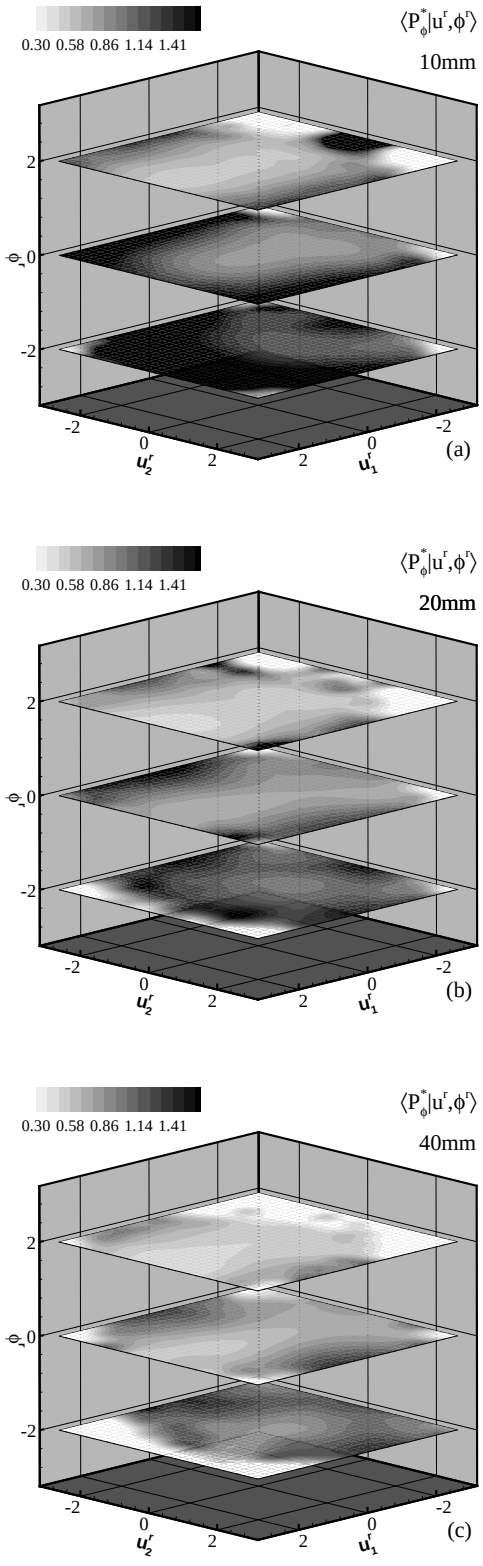

Figure 2.13 Conditional SGS scalar variance production rate, $\left\langle P_\phi^* \middle| \mathbf{u}^r, \phi^r \right\rangle$ (a)-(c) for $\Delta/\eta = 63, 125$ and 250 predicted using the Smagorinsky model. It appears to increase with the filter scale.

scales. Therefore, the previously observed insensitivity of the LES results to model details is largely due to the consistency of the model predictions of the mean SGS stress, the mean SGS flux, and their production rates with Kolmogorov's hypothesis. The results also suggest that SGS models should be evaluated based on the applications. The requirements on SGS models are more stringent where higher-order statistics, such as turbulent transport and PDF, are needed.

2.4 Summary

In the present work the issue of the influences of the SGS stress and SGS scalar flux on the resolvable-scale velocity-scalar JPDF is examined. The necessary conditions for LES to correctly predict the JPDF are given as that the SGS models reproduce the conditional means of the SGS stress and fluxes and their production rates conditional on the resolvable-scale velocity and scalar. The filter-scale dependencies of the mean production rates are predicted using Lumley's assumption. Experimental data obtained in a slightly heated turbulent jet are used to analyze the conditional SGS stress and scalar flux, their filter-scale dependencies, and the SGS model predictions.

The conditional SGS flux and the conditional SGS flux production rates are found to strongly depend on the resolvable-scale velocity and scalar and have similar functional forms for eddies that are likely in quasi-equilibrium. This is also observed in the atmospheric surface layer (Chapter 3), suggesting that the similarity exists whenever SGS eddies are in quasi-equilibrium regardless of the larger-scale flow geometry. It is also found that the dependencies on the resolvable-scale velocity have qualitatively different forms for positive and negative resolvable-scale scalar fluctuations, indicating strong flow history effects. This suggests that it might be beneficial to include a passive scalar in LES even when only velocity statistics are interested.

The predicted mean streamwise and crossstream SGS scalar flux production rates vary with filter scale as $\Delta^{4/3}$ and $\Delta^{2/3}$, respectively. The predicted mean SGS shear stress components $\langle P_{12} \rangle$ vary as $\Delta^{2/3}$. The measured mean SGS scalar flux, the mean SGS scalar flux production rate, and the mean SGS shear stress production rate are generally consistent with the predictions based on Lumley's assumption, which is consistent with Kolmogorov's hypothesis of statistical independence of distant scales, suggesting that the SGS flux, its production rate and the SGS shear stress production have diminishing effects on the lower-order resolvable-scale velocity-scalar statistics. However, It is found that the conditional SGS scalar flux and SGS scalar flux production rate fall-off much slower with the filter scale than the mean SGS scalar flux and SGS scalar flux production rate, a behavior similar to the conditional SGS shear stress production rate Chen *et al.* [38]. The slower fall-offs

of these conditional statistics suggest that they have non-diminishing influences on the JPDF and the high-order statistics of the resolvable-scale velocity and scalar, such as turbulent transport and scalar PDF.

The Smagorinsky model predictions of the filter-scale dependencies of the mean SGS fluxes and the mean SGS flux production rate are consistent with predictions and experimental results; therefore, the models are likely to have diminishing effects on lower-order LES statistics (e.g. mean and r.m.s.). The model predictions of the conditional SGS flux decrease faster with the filter scale than measurements whereas those of the conditional SGS flux production do not decrease. Therefore, the model is likely to have effects on the high-order LES statistics even for inertial-range filter scales. It is emphasized that the results here are based on the dynamics terms in the JPDF equation (Chapter 3) and provide an understanding of the specific model behaviors that cause the previously observed insensitivities of LES lower-order statistics to model details.

The present study shows that even for inertial-range filter scales the SGS stress and flux have strong influences on the higher-order resolvable-scale velocity-scalar statistics, which are important for many practical applications. A SGS model needs to correctly predict the modeled conditional SGS stress, conditional SGS scalar flux, and the conditional production rates to reproduce the higher-order resolvable-scale statistics. Therefore, in applications where higher-order statistics (e.g. turbulent transport and scalar PDF) are important, SGS predictions of these conditional statistics should be an essential part of model tests. On the other hand, the mean SGS stress and flux as well as their production rates have diminishing effects on the lower-order resolvable-scale statistics for inertial-range filter scales. Therefore, a SGS model that satisfies the inertial-range scaling of the mean SGS flux and SGS flux production rate is likely to be able to correctly predict the lower-order statistics with an inertial-range filter scale, thereby supporting the premise of LES at the level of lower-order statistics.

CHAPTER 3

On the subgrid-scale stress and its production rate in a convective atmospheric boundary layer

In this chapter, the subgrid-scale (SGS) stress and its production rate are studied using field measurements data in the unstable atmospheric surface-layer. When the filter scale is in the inertial range, as is often the case in the interior of a turbulent boundary layer or in the fully developed region of a free shear flow, the energy-containing scales are well resolved and most of the turbulent stress is carried by the resolvable scales. Under such conditions, the LES result is to some extent insensitive to the subgrid-scale model employed ([6, 21]). The role of the subgrid scales is considered to be limited to extracting energy from the resolvable scales at the correct rate ([1, 27, 61]).

However, in LES of high-Reynolds-number turbulent boundary layers, such as the atmospheric boundary layer (ABL), the filter scale in the near-wall region is inevitably in the energy-containing scales because the latter scale with the distance from the surface ([62, 21, 32, 48, 49]). Consequently, a significant portion of the turbulent stress in LES must be carried by the SGS model, thereby causing strong dependence of the results on the SGS model ([49]). The deficiencies in the SGS model are therefore more likely to lead to errors in LES results in the near-wall region. For example, LES of the unstable ABL using the Smagorinsky model over-predicts the mean shear and the streamwise velocity variance ([6, 21, 10, 63]) in the surface layer, and at the same time under-predicts the vertical velocity skewness. On the other hand, the standard dynamic Smagorinsky model, which generally performs better than the Smagorinsky model, under-predicts the mean shear ([64]). The under resolution and the strong dependence of the LES results on SGS models are an inherent problem in high-Reynolds-number boundary layers and cannot be solved by reducing the filter size ([21, 32, 48, 49]).

These deficiencies in LES results have been argued to be related to the Smagorinsky model's being too dissipative ([21, 10]) and the dynamic model's being not dissipative enough ([64]). Various

methods for improving LES results have been developed, including stochastic backscatter ([65, 66, 8]), the split model of Schumann ([65, 10]), a nonlinear model ([67]), and the scale-dependent dynamic Smagorinsky model ([64]). Mason *et al.* (1992) [8] argued that the problem could be addressed by simply changing the length scale in the Smagorinsky model. They included a stochastic forcing term in the LES equation to represent the energy backscatter process, which was absent in the Smagorinsky model. Significant improvements in the mean velocity profile and the streamwise velocity variance profiles were achieved. Sullivan (1994) *et al.* [10] modified the split model of Schumann ([65]), which consisted of an isotropic part and an anisotropic part for the model SGS stress. The latter is produced only by the mean shear strain rate. Such a formulation reduced the impact of the Smagorinsky model on the fluctuating fields and the energy dissipation, making the smallest resolved scales more energetic. Improvements similar to those obtained by Mason *et al.* (1992) [8] were achieved. Kosović (1997) [67] constructed a nonlinear model that includes both the strain rate and the rotation tensors based on the argument that the SGS stress is not frame indifferent. The model yielded an improved mean velocity profile, but also resulted in redistribution of the energy among the normal SGS stress components. Porté-Agel (2000) *et al.* [64] argued that in the surface layer the coefficients in the dynamic Smagorinsky model were not equal at the LES and test filters. They used a second test filter and an assumption of power-law variations to account for this scale dependence. The results for the mean velocity profile, velocity variance profiles, and the velocity spectra showed improvements over the standard dynamic model. The improvements achieved by these methods demonstrated the importance of incorporating surface-layer SGS physics into SGS models and of systematically understanding the effects of model behaviors on LES results.

Recent studies ([37] and [68]) have provided the necessary and sufficient conditions for LES to predict correctly all one-time multi-point joint probability density function (JPDF) of the resolvable-scale velocity: the conditional mean of the SGS stress conditional on the entire resolvable-scale velocity field must be reproduced by the modeled SGS stress. A model that satisfies this condition will yield the optimal LES. This condition is an extension of that given by Adrian (1990) [41]. However, in practice, it is not feasible to obtain this conditional SGS stress as it requires a large number of resolvable-scale velocity fields to cover the functional space. In the present work, the influence of the SGS motions on the resolvable-scale statistics is studied by analysing the transport equation of the one-time, one-point JPDF of the resolvable-scale velocity components.

The JPDF equation can be derived following the method given by Pope ([39, 31]) using the equation for the resolvable-scale velocity

$$\frac{\partial u_i^r}{\partial t} = -\frac{\partial u_j^r u_i^r}{\partial x_j} - \frac{\partial \tau_{ij}}{\partial x_j} - \frac{\partial p^r}{\partial x_i} + \frac{g}{\Theta}\theta^r \delta_{i3} + \nu \frac{\partial^2 u_i^r}{\partial x_j \partial x_j} \tag{3.1}$$

where

$$\tau_{ij} = (u_i u_j)^r - u_i^r u_j^r$$

is the SGS stress (the Leonard stress $L_{ij} = (u_i^r u_j^r)^r - u_i^r u_j^r$ has been included in τ_{ij}), a superscript r denotes a resolvable-scale variable, and Θ and θ are the mean and fluctuation potential temperatures, respectively. Taking the time derivative of the JPDF, $f = \langle f' \rangle = \left\langle \prod_{i=1}^{3} \delta(u_i^r - v_i) \right\rangle$, where f' is the fine-grained JPDF and the angle brackets denote an ensemble mean, we obtain

$$\frac{\partial f}{\partial t} = \left\langle \frac{\partial f'}{\partial u_i^r} \frac{\partial u_i^r}{\partial t} \right\rangle = -\frac{\partial}{\partial v_i} \left\langle \frac{\partial u_i^r}{\partial t} f' \right\rangle \tag{3.2}$$

Substituting $\frac{\partial u_i^r}{\partial t}$ in the right-hand side of (3.2) leads to the JPDF equation

$$\begin{aligned} \frac{\partial f}{\partial t} + v_j \frac{\partial f}{\partial x_j} = & \frac{\partial}{\partial v_i} \left\{ \left\langle \frac{\partial \tau_{ij}}{\partial x_j} \middle| \mathbf{u}^r = \mathbf{v} \right\rangle f \right\} \\ & + \frac{\partial}{\partial v_i} \left\{ \left\langle \frac{\partial p^r}{\partial x_i} \middle| \mathbf{u}^r = \mathbf{v} \right\rangle f \right\} \\ & - \frac{g}{\Theta} \frac{\partial}{\partial v_3} \left\{ \langle \theta^r | \, \mathbf{u}^r = \mathbf{v} \rangle \, f \right\}. \end{aligned} \tag{3.3}$$

The left-hand side of the equation is the time derivative and the advection in physical space. The right-hand side is transport in velocity space of the JPDF by the SGS stress divergence, the resolvable-scale pressure gradient, and the buoyancy force. Transport due to viscous force is generally small at high Reynolds numbers and is omitted from the equation. Galilean invariance of the velocity JPDF equation has been proven by Tong ([69]).

An alternative form of the equation was given by Chen *et al.* [38]

$$\begin{aligned} \frac{\partial f}{\partial t} + v_j \frac{\partial f}{\partial x_j} = & \frac{\partial^2}{\partial v_i \partial x_j} \left\{ \langle \tau_{ij} | \, \mathbf{u}^r = \mathbf{v} \rangle \, f \right\} + \frac{\partial^2}{\partial v_i \partial v_j} \left\{ \left\langle -\frac{1}{2} P_{ij} \middle| \mathbf{u}^r = \mathbf{v} \right\rangle f \right\} \\ & + \frac{\partial^2}{\partial v_i \partial x_i} \left\{ \langle p^r | \, \mathbf{u}^r = \mathbf{v} \rangle \, f \right\} + \frac{\partial^2}{\partial v_i \partial v_j} \left\{ \left\langle p^r \frac{\partial u_j^r}{\partial x_i} \middle| \mathbf{u}^r = \mathbf{v} \right\rangle f \right\} \\ & - \frac{g}{\Theta} \frac{\partial}{\partial v_3} \left\{ \langle \theta^r | \, \mathbf{u}^r = \mathbf{v} \rangle \, f \right\} \end{aligned} \tag{3.4}$$

The right-hand side now represents mixed transport in physical and velocity spaces by the conditional SGS stress and the resolvable-scale pressure and transport in velocity space by the conditional SGS stress production rate, $\left\langle -\frac{1}{2} P_{ij} | \mathbf{u}^r = \mathbf{v} \right\rangle$, the conditional resolvable-scale pressure-strain correlation,

and the conditional buoyancy force, where

$$P_{ij} = -\left\{\tau_{ik}\frac{\partial u_j^r}{\partial x_k} + \tau_{jk}\frac{\partial u_i^r}{\partial x_k}\right\}. \tag{3.5}$$

Equation (3.4) shows that the SGS stress directly affects the resolvable-scale velocity JPDF through the conditional SGS stress and the conditional SGS stress production and indirectly through the pressure terms. Therefore, the necessary conditions for LES to correctly predict the velocity JPDF are that the conditional means of SGS stress and SGS stress production rate must be reproduced by the SGS model ([38]). The conditions show that the modeled and true SGS stress should be compared statistically, not instantaneously, because a modeled SGS stress field can satisfy these conditions but does not correlate well with the true SGS stress. It is noted that although in LES equation (3.1) is solved, the SGS model evolves the JPDF according to equation (3.3) or (3.4).

Equation (3.4) provides a link between the SGS stress and the resolvable-scale velocity JPDF and can be used to study the effects of the SGS stress on the JPDF. It also reveals two important effects of the SGS turbulence on the resolvable scales. First, the trace of $\langle P_{ij}|\mathbf{u}^r = \mathbf{v}\rangle$ is the conditional energy transfer rate from the resolvable to the subgrid scales. Therefore, equation (3.4) provides an analytical proof that the (conditional) energy transfer is essential for the evolution of the JPDF ([38]), while previous studies have only argued its importance based on its role in the inertial-range turbulence. In addition, conditional forward transfer and conditional backscatter have qualitatively different effects on the evolution of the JPDF because the conditional energy transfer in equation (3.4) plays a role similar to the diffusion coefficient in a diffusion equation. Second, previous studies focused primarily on the SGS stress whereas equation (3.4) also points to the importance of the SGS stress production rate. Because the SGS stress and the SGS stress production are important for the SGS dynamics and have clear physical meanings; their results can be interpreted better than those for the SGS stress divergence in equation (3.3).

In the present study, the necessary conditions for LES to reproduce the JPDF and the dependencies of the terms in the JPDF equation on the surface layer dynamics are investigated to gain an understanding of the SGS physics that are important for SGS modeling and to examine SGS models. Although analyses of the terms in the JPDF equation using experimental data are still *a priori* in nature, they differ qualitatively from previous *a priori* analyses in several aspects. First, the JPDF-based analyses deal with the conditional averages of the SGS stress and its production rate, which evolve the JPDF. Consequently, there exists a close link between the conditional statistics and the JPDF in the present analyses. On the other hand, the traditional model tests often compute the correlation coefficient between the modeled and true SGS stress, which generally cannot be related to

LES statistics because the correlation in general cannot be used to measure the model performance for predicting the conditional SGS stress (and more so for the conditional SGS stress production rate). Second, the system described by the JPDF equation is not chaotic. The solution of the JPDF equation is a statistic (a deterministic field) and is generally stable to small perturbations in initial and boundary conditions as well as the modeled terms. Therefore, an SGS model that provides close approximations of the conditional SGS stress and the conditional SGS stress production is consistent with the above mentioned necessary conditions, thereby having the potential to predict the JPDF well and vice versa. Such *a priori* analyses are in contrast with the traditional tests: because the LES equation (3.1) is chaotic, i.e. its solution exhibits stochastic behaviors, any imperfection in the correlation between the modeled and true SGS stress will cause the LES field to diverge exponentially from the true resolvable-scale field, making it practically impossible to relate the modeled instantaneous SGS stress to LES results. Third, for the analyses based on the JPDF equation there are analytical results (e.g., [70]; [40]) that can be used as a basis to investigate the relationship between the SGS terms and the JPDF whereas no such analyses can be performed for the LES equation. Therefore, *a priori* tests based on the JPDF equation are fundamentally different from the traditional *a priori* tests and JPDF equations of the resolvable-scale velocity provide a more rational approach for studying the effects of the SGS stress and SGS models on the resolvable-scale statistics.

In LES employing certain SGS models, such as the Smagorinsky model, only the deviatoric part of the SGS stress, $\tau_{ij}^d = \tau_{ij} - \frac{1}{3}\tau_{kk}\delta_{ij}$, is modeled. Therefore, it is also useful to examine the corresponding production term P_{ij}^d defined as

$$P_{ij}^d = -\left\{\tau_{ik}^d \frac{\partial u_j^r}{\partial x_k} + \tau_{jk}^d \frac{\partial u_i^r}{\partial x_k}\right\}. \tag{3.6}$$

Thus, P_{ij} can be written as

$$P_{ij} = P_{ij}^d - \frac{2}{3}\tau_{kk}S_{ij}, \tag{3.7}$$

where S_{ij} is the resolvable-scale strain rate tensor. Equation (3.6) shows that P_{ij}^d is the production rate due to the interaction between the deviatoric (anisotropic) part of the SGS stress and the resolvable-scale velocity gradient, and $-\frac{2}{3}\tau_{kk}S_{ij}$ is the production rate due to straining of the isotropic part of the SGS stress by the resolvable-scale strain rate. Therefore, the normal components of P_{ij} contain the energy transfer from the resolvable to the subgrid scales, $P_{\alpha\alpha}^d$ ($\alpha = 1, 2, 3$), and the redistribution among three normal components of the SGS stress (inter-component exchange), $-\frac{2}{3}\tau_{kk}S_{\alpha\alpha}$, respectively. Note that the summation of inter-component exchange $-\frac{2}{3}\tau_{kk}S_{ll}$ is zero,

indicating that this term redistributes energy among the three normal components of the SGS stress. Therefore, the anisotropy of the normal SGS stress components is important for the evolution of the JPDF. The shear components of P_{ij}^d represent the production of SGS shear stress in anisotropic turbulence owing to both straining and rotation by the resolvable-scale velocity field. The shear components $-\frac{2}{3}\tau_{kk}S_{ij}, (i \neq j)$, represent the production of shear stress due to straining of isotropic SGS turbulence. Therefore the decomposition in (3.7) is useful for further understanding the physics of P_{ij}.

The dynamics of the SGS stress can also be examined using the SGS stress transport equation

$$\frac{\partial \tau_{ij}}{\partial t} + u_k^r \frac{\partial \tau_{ij}}{\partial x_k} = \frac{\partial}{\partial x_k}\left\{u_k^r (u_i u_j)^r - (u_i u_j u_k)^r + (\tau_{ik} u_j^r + \tau_{jk} u_i^r)\right\} + P_{ij} + P_{Bij} - \left(u_j \frac{\partial p}{\partial x_i}\right)^r - \left(u_i \frac{\partial p}{\partial x_j}\right)^r + u_i^r \frac{\partial p^r}{\partial x_j} + u_j^r \frac{\partial p^r}{\partial x_i} - \epsilon_{ij}. \tag{3.8}$$

The left-hand side is the time rate of change and advection. The right-hand side is the turbulent transport, turbulent production, buoyancy production and pressure transport and destruction and molecular dissipation $(2\nu(\partial u_i/\partial x_k)(\partial u_j/\partial x_k))$. The buoyancy production rate

$$P_{Bij} = \frac{g}{\Theta}\left\{\delta_{i3}[(\theta u_j)^r - \theta^r u_j^r] + \delta_{j3}[(\theta u_i)^r - \theta^r u_i^r]\right\} \tag{3.9}$$

has only three non-zero components P_{Bi3}; therefore, it affects only the τ_{i3} components. Wyngaard *et al.* [71] showed that the shear production of the Reynolds shear stress exceeds that of energy under all stability conditions, whereas the buoyancy production of shear stress is larger than that of energy under neutral and stable conditions, but falls off as the surface layer becomes more unstable. These results suggest that the magnitude of shear to buoyancy production of the SGS stress is also important for the behavior of the SGS stress.

Pope (2004) [72] discussed the issue of LES statistics and argued that the perfect LES should correctly predict all statistics of the total velocity, not those of the resolvable-scale velocity. He showed that the dynamic Smagorinsky model, in fact, minimized the dependence of the predicted total stress on the filter scale, thereby improving the predictions when the filter scale is larger than the inertial-range scales. While the perfect LES is desirable, in many cases, the SGS model has no direct contribution to the higher-order statistics of the total velocity. For example, an SGS stress model only contributes to the vertical velocity skewness through its correlation with the resolvable-scale vertical velocity, while the contribution from the SGS vertical velocity is not predicted. More generally, the one-point PDF of the total velocity cannot be estimated using models for SGS stress. To predict the total velocity PDF, a different approach that models the SGS velocity distribution

is needed, e.g., the filtered density function methods ([73, 74]). Therefore, for LES employing SGS stress models, the optimal LES can only be expected to reproduce the true resolvable-scale statistics, which approach the total velocity statistics as the filter scale is asymptotically small compared to the energy-containing scales.

In the present study, the SGS stress and its production rate in the unstable atmospheric surface layer are studied using field measurements data. The rest of the chapter is organized as follows. Section 3.1 outlines the field program and the array filter technique for measuring resolvable- and subgrid-scale variables. The measured conditional SGS stress and the conditional SGS stress production are discussed in Sections 3.2. Sections 3.3 and 3.4 present the SGS model predictions and their implications for SGS modeling. Some further discussions on the relationships between the conditional SGS stress and the conditional SGS stress production are given in Section 3.5, followed by the conclusions.

3.1 Field measurements and data analysis procedures

The field measurements for this study, named the horizontal array turbulence study, or HATS field program, were conducted at a field site 5.6 km east-northeast of Kettleman City, California, in the summer of 2000 as a collaboration primarily among the National Center for Atmospheric Research, Johns Hopkins University and Penn State University (CT was part of the Penn State group). Horst *et al.* (2004) [75] describe the field site and the data collection procedures in detail.

The field measurement design is based on the transverse array technique proposed, studied, and first used by the Penn State group ([76, 77, 48, 49]) for surface-layer measurements in the ABL. It has subsequently been used by several groups in the ABL over land ([77, 49, 35, 78, 75]) and ocean (the recent ocean HATS program) as well as in engineering flows ([52, 53, 54, 55, 38, 74]). The technique uses horizontal sensor arrays (Figure 3.1) to perform two-dimensional filtering to obtain resolvable- and subgrid-scale variables. Two arrays are vertically spaced to obtain vertical derivatives. The primary horizontal array consists of nine equally spaced sonic anemometers (Campbell Scientific SAT3) and the secondary array has five sonics at a second height. The arrays are aligned perpendicular to the prevailing wind direction.

The filter operation in the streamwise direction is performed by invoking Taylor's hypothesis. Filtering in the transverse direction is realized by averaging the output of the signals from the sensor array ([48]). For example, the transversely filtered resolvable-scale velocity (denoted by a superscript

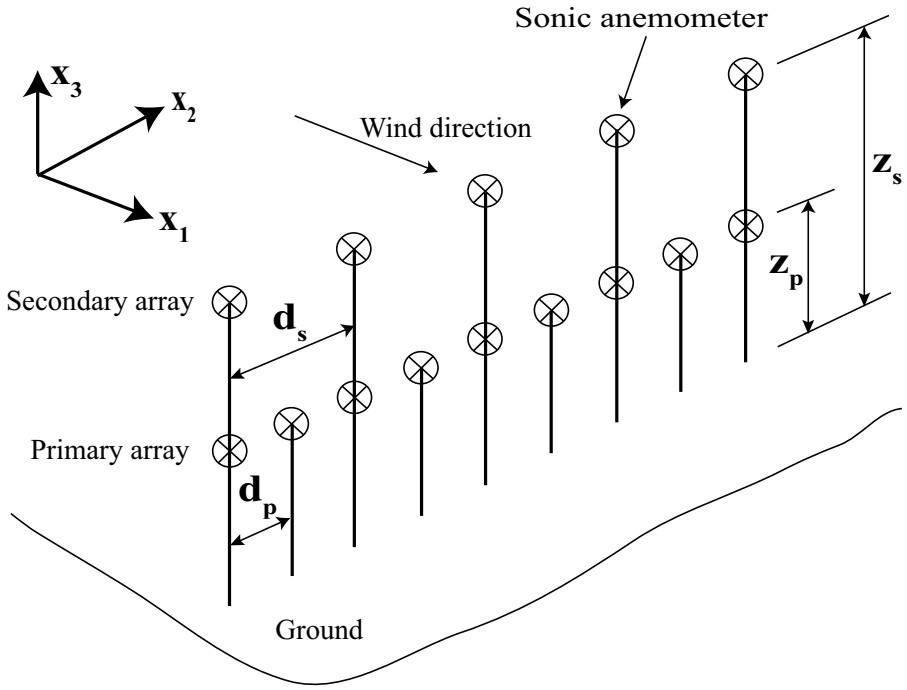

Figure 3.1 Schematic of the array setup. The secondary array (denoted by a subscript s) is used to obtain derivatives in the vertical direction.

t) is obtained as

$$u_i^t(\mathbf{x},t) = \sum_{j=-N}^{N} C_j u_i(x_1, x_2 + j\times, d, x_3, t) \tag{3.10}$$

where $2N+1, C_j$ and d are the number of sensors on an array, the weighting coefficient for the j^{th} sensor and the spacing between adjacent sensors, respectively. $2N+1=5$ is used and 3 for filtering at the heights of the primary and secondary arrays, respectively, to maintain the same filter size. The subgrid-scale velocity is obtained by subtracting the resolvable-scale part from the total velocity. In the present study, the arrays to approximate top-hat filters is used, which are the most compact type in physical space. Because derivatives are computed using finite differencing (with a spacing of $4d_p$ in the horizontal directions), which is effectively a top-hat filter, top-hat filters provide consistency among the resolvable-scale velocity and its derivatives.

The issues in applying the array filtering technique, including the accuracy of the array filter and the use of Taylor's hypothesis, have been systematically studied by Tong *et al.* [48]. They showed that a two-dimensional filter is a good approximation of a three-dimensional filter. They demonstrated that among the mechanisms that could affect the accuracy of Taylor's hypothesis ([79]), including the effect of different convection velocity for different wavenumber components,

Table 3.1 Configurations of the four arrays (lengths in meter).

Array	Δ/z_p	z_p	d_p	z_s	d_s
1	3.88	3.45	3.35	6.90	6.70
2	2.00	4.33	2.167	8.66	4.33
3	1.00	8.66	2.167	4.33	1.08
4	0.48	4.15	0.50	5.15	0.625

temporal changes in the reference moving with the mean velocity, and the fluctuating convecting velocity, only the last one is significant. Their analyses of the accuracy of a spectral cutoff array filter as an approximation of a true two-dimensional filter showed that the r.m.s. values of the filtered variables differ by less than 10%. Because the spectral cutoff filter has the slowest decay in physical space, it is the most difficult to approximate by the array. Therefore, the accuracy of the top-hat filter array filter is expected to be higher. The error associated with one-sided finite differencing in the vertical direction is examined by Kleissl *et al.* (2003) [78]. They evaluated the divergence-free condition for the filter velocity field and concluded that reasonable accuracy can be achieved in computing derivatives of filtered velocity. Horst *et al.* (2004) [75] further studied various issues of using the array technique including the aliasing errors associated with evaluating derivatives using finite diffferencing and also demonstrated sufficient accuracy of the technique.

Four different array configurations, shown in Table 3.1, are employed in the HATS program. The filter (grid) aspect ratio (Δ/z) ranges from 0.48 to 3.88, allowing the effects of grid anisotropy to be examined. z is referred as the height of the primary array z_p here and hereafter. Array 3 is at a much higher z, therefore the effects of the stability parameter $-z/L$ can be examined, where $L = -\frac{u_*^3 \Theta}{k_a g \langle u_3' \theta' \rangle}$, $u_*^2 = -\langle u_1' u_3' \rangle$ (a prime denotes fluctuations), $k_a = 0.41$, and g are the Monin-Obukov length, friction velocity, von Kármán constant and acceleration due to gravity, respectively. The surface layer parameters for the data sets collected using the four arrays are given in Tables 3.2 and 3. The results in Section 3.2.3 show that the SGS stress for array 1, which has the largest Δ/z, is the most anisotropic and most difficult for SGS models to predict, therefore discussions of results are focused on array 1. All array 1 data used in the present study were collected during daytime under clear conditions and the boundary layer was convective with a Monin-Obukov length of approximately -15 m.

Although the arrays were arranged to be perpendicular to the prevailing wind direction, the mean wind direction for a given data section might not be exactly perpendicular to the array. Therefore, the coordinate system is rotated and the velocity and temperature are interpolated in

Table 3.2 Surface-layer parameters for array 1 ($\Delta/z = 3.88$) under unstable conditions. The primary array height z_p is used for z.

Data	$\langle u \rangle$ (m s^{-1})	$-z/L$	u_* (m s^{-1})	ϵ (m^2 s^{-3})	H (K m s^{-1})	Duration (min)
a	1.42	0.34	0.15	0.003	0.02	35
b	3.56	0.22	0.33	0.031	0.17	30
c	3.65	0.21	0.36	0.039	0.20	83
d	3.25	0.24	0.36	0.041	0.24	33

the Cartesian coordinate system defined by mean wind and cross-wind directions ([75]). The interpolation is performed in spectral space to avoid attenuating the high-frequency (wavenumber) fluctuations.

In the present work, the unstable surface layer, i.e. $z/L < 0$ is studied. Data sections that are quasi-stationary are generally 30-90 min in length. In order to achieve reasonable statistical convergence, the results of selected data sections collected under similar stability conditions using each array configuration must be combined. Four data sections collected using array 1 (Table 3.2) are focused. The conditional statistics obtained using the individual data sets (not shown) are very similar, but with varying degrees of uncertainty. Therefore, the results for each data set are normalized using its parameters, then weight-average them according to the number of conditional samples in each bin.

Because of the complexity of the variables of interest and of the conditional sampling procedure, a precise level of statistical uncertainty are not able to be provided. However, by monitoring the statistical scatter while increasing the data size, it is concluded that reasonable statistical convergence is achieved. An example of the convergence process is given in Figure 3.3. In addition, comparisons between model predictions and measurements require only the relative magnitude of the results and are less affected by the uncertainty. Therefore, the data size is sufficient for obtaining reliable statistics for the analyses.

3.2 Results

In this section, discussions on results obtained using data from array are focused. The stability parameter $-z/L$ has an average value of 0.24. Therefore, it is expected both buoyancy and shear to affect the surface-layer turbulence. Top-hat filters in both streamwise and cross-stream directions are used to obtain the resolvable-scale and subgrid-scale variables with a filter size $\Delta = 3.88z$, which is in the energy-containing range. The results for the other array configurations, i.e. different Δ/z, and $-z/L$ (Table 3.3), are also obtained. The results are generally similar to

Table 3.3 Surface-layer parameters for the other arrays under unstable conditions. The primary array height z_p is used for z.

Array	Δ/z ($\approx$)	$\langle u \rangle$ (m s^{-1})	$-z/L$	u_* (m s^{-1})	ϵ (m^2 s^{-3})	Total duration (min)
2	2.00	3.09	0.36	0.30	0.020	257
3	1.00	4.22	0.60	0.34	0.018	591
4	0.48	2.73	0.35	0.30	0.021	60

Table 3.4 Measured Reynolds stress and mean SGS stress for the four arrays.

Array	σ_u^2/u_*^2	σ_v^2/u_*^2	σ_w^2/u_*^2	$\langle \tau_{11} \rangle / \sigma_u^2$	$\langle \tau_{22} \rangle / \sigma_v^2$	$\langle \tau_{33} \rangle / \sigma_w^2$	$\langle -\tau_{13} \rangle / u_*^2$
1	8.17	9.55	1.52	0.35	0.21	0.89	0.73
2	12.12	13.19	1.86	0.20	0.14	0.76	0.57
3	9.53	13.58	2.19	0.17	0.09	0.54	0.34
4	10.98	10.57	1.69	0.07	0.06	0.35	0.11

those for array 1. Therefore, their differences with those of array 1 and the influence of Δ/z and $-z/L$ are only briefly discuss. Table 3.4 gives the normalized Reynolds stress and the ratios of the mean SGS stress components to the Reynolds stress components. Array 1 has the highest fraction of the vertical shear stress carried by the subgrid scales. The deviatoric part of the measured and modeled SGS stress components are given in Table 3.5 and discussed in Section 3.3.

The results for conditional SGS stress $\langle \tau_{ij} | \mathbf{u}^r \rangle$ are normalized by the friction velocity u_*^2. The results for the conditional SGS stress production $\langle P_{ij} | \mathbf{u}^r \rangle$, the buoyancy production $\langle P_{Bij} | \mathbf{u}^r \rangle$ and the advection term $\left\langle -u_3^r \frac{\partial \tau_{ij}}{\partial x_3} \middle| \mathbf{u}^r \right\rangle$ are normalized by the estimated energy dissipation rate $\epsilon = \phi_\epsilon \frac{u_*^3}{k_a z}$, where $\phi_\epsilon = 1 - z/L$ for $z/L \leq 0$ as suggested by Kaimal *et al.* (1972) [62].

3.2.1 Normal components of $\langle \tau_{ij} | \mathbf{u}^r \rangle$ and $\langle P_{ij} | \mathbf{u}^r \rangle$

The results for the conditional normal SGS stress components are plotted against the horizontal resolvable-scale velocity, u_1^r, for different values of the vertical resolvable-scale velocity, u_3^r (Figure 3.2). Owing to the limited data size, the third velocity component in the conditional SGS stress are not able to be included. The data bin for the first conditioning variable [e.g. u_1^r in Figure 3.2(a)] have the width shown in the Figures (12 bins between ± 2 standard deviations whereas that for the second conditioning variable is twice as wide). Figure 3.3 gives a representative case (τ_{11}) of the convergence of the conditional SGS stress as the sample size is increased from one fifth to the full data set. Based on such tests it is concluded that reasonable statistical convergence is achieved. Figures 3.2(a) and 2(c) show that $\langle \tau_{11} | u_1^r, u_3^r \rangle$ and $\langle \tau_{33} | u_1^r, u_3^r \rangle$ generally increase with u_3^r. They also increase with u_1^r when u_3^r is positive, and depend weakly on u_1^r when u_3^r is negative, indicating that

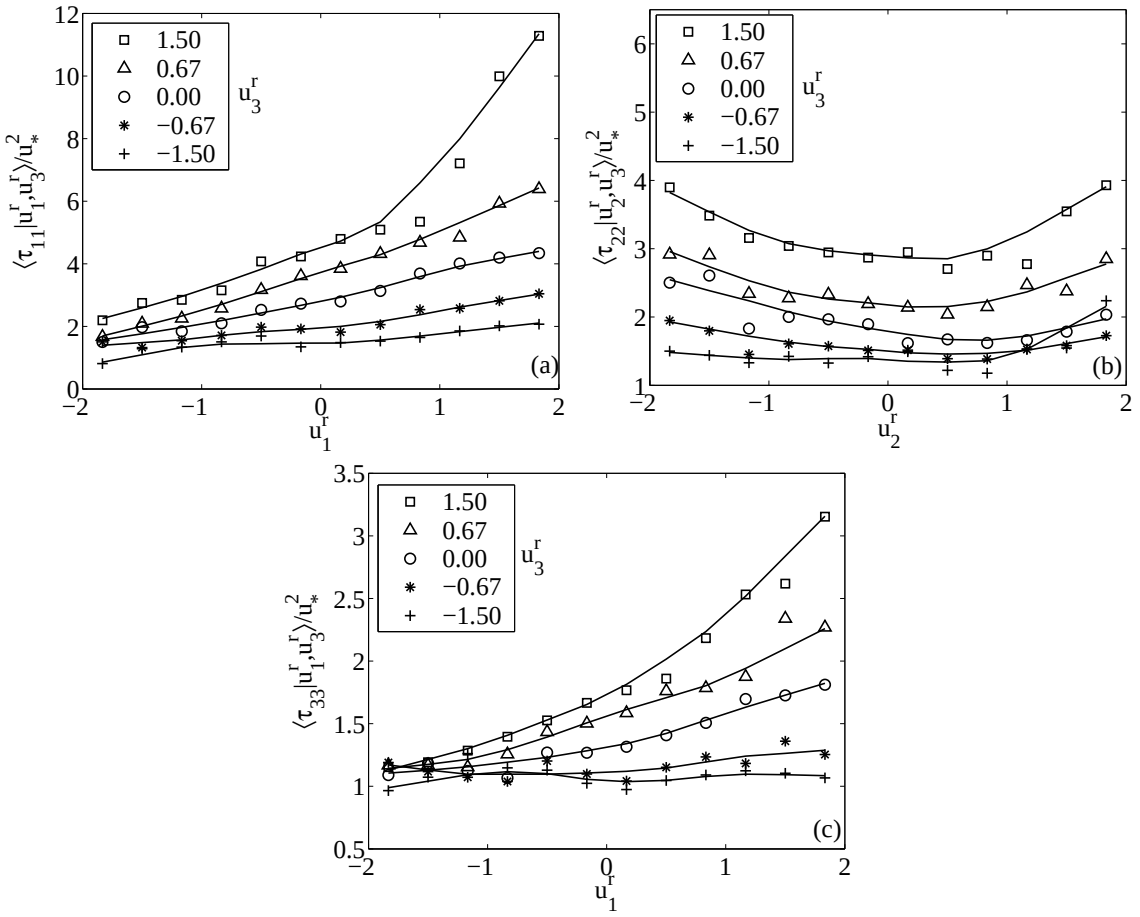

Figure 3.2 Conditional means of the measured normal SGS stress components conditional on the resolvable-scale velocity components. The dependence on the horizontal velocity components is stronger for positive u_3^r. Here and thereafter u_i^r is normalized by the r.m.s. fluctuations of the total velocity σ_{u_i}.

the dependence on u_1^r is enhanced by positive u_3^r. Figure 3.2(b) shows that $\langle \tau_{22} | u_2^r, u_3^r \rangle$ increases with u_3^r and $|u_2^r|$, but its dependence on $|u_2^r|$ is generally weaker than that of $\langle \tau_{11} | u_1^r, u_3^r \rangle$ on u_1^r. The dependence of $\langle \tau_{11} | u_1^r, u_3^r \rangle$ (and $\langle \tau_{22} | u_2^r, u_3^r \rangle$) on u_3^r can be attributed partly to the vertical advection ([49]). The measured advection (not shown) is generally positive for positive u_3^r and vice versa. This is because in the surface-layer, the velocity variance varies slowly with the distance from the ground whereas the length scale is proportional to the distance; therefore, the SGS eddies brought up from near the ground generally contain a larger magnitude of SGS stress.

The anisotropic part of the conditional SGS stress, $\left\langle \tau_{ij}^d | \mathbf{u}^r \right\rangle$, which is predicted by some SGS stress models, is also computed. The diagonal components $\left\langle \tau_{\alpha\alpha}^d | \mathbf{u}^r \right\rangle$ (no summation) are shown in Figure 3.4. The off-diagonal components of $\left\langle \tau_{ij}^d | \mathbf{u}^r \right\rangle$ are identical to those of $\langle \tau_{ij} | \mathbf{u}^r \rangle$. The trends of

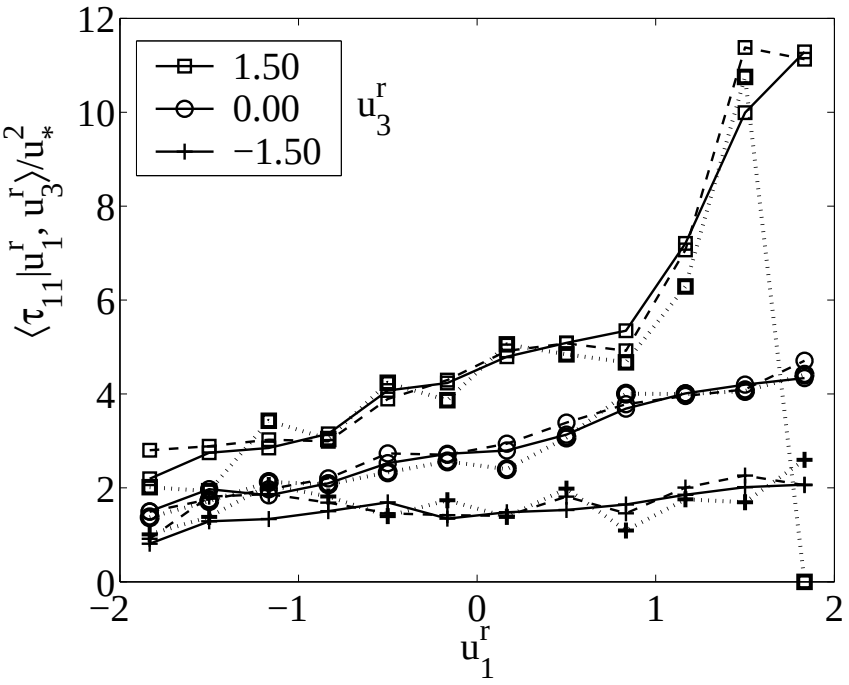

Figure 3.3 Convergence of the conditional SGS stress component $\langle \tau_{11}|u_1^r, u_3^r\rangle$. The dotted, dashed, and solid lines represent the results obtained using one fifth, one half, and the full data set, respectively.

$\langle \tau_{\alpha\alpha}^d|\mathbf{u}^r\rangle$ are similar to those in Figure 3.2. The magnitudes of $\langle \tau_{11}^d|u_1^r, u_3^r\rangle$ and $\langle \tau_{22}^d|u_2^r, u_3^r\rangle$ become smaller compared to $\langle \tau_{11}|u_1^r, u_3^r\rangle$ and $\langle \tau_{22}|u_2^r, u_3^r\rangle$, and $\langle \tau_{33}^d|u_1^r, u_3^r\rangle$ becomes negative owing to the strong anisotropy of the surface layer ($\langle \tau_{11}\rangle > \langle \tau_{33}\rangle$). The anisotropy of $\langle \tau_{ij}|\mathbf{u}^r\rangle$ is further discussed in Section 3.2.3. Further understanding of the trends for the conditional SGS normal stress can be gained from the results for the SGS stress production discussed in the following.

The results for the normal components of the conditional production rate $\langle P_{\alpha\alpha}|\mathbf{u}^r\rangle$ (no summation), which contains the energy transfer terms, are shown in Figure 3.5. Similar to $\langle \tau_{11}|u_1^r, u_3^r\rangle$, $\langle P_{11}|u_1^r, u_3^r\rangle$ also increases with u_3^r. It also increases with u_1^r and the dependence on u_1^r is enhanced by positive u_3^r and weakened by negative u_3^r. Figure 3.5(c) shows that $\langle P_{33}|u_1^r, u_3^r\rangle$ decreases with u_3^r and its dependence on u_1^r is generally weak, especially for negative u_3^r. Similar to $\langle \tau_{22}|u_2^r, u_3^r\rangle$, $\langle P_{22}|u_2^r, u_3^r\rangle$ also increases with $|u_2^r|$. These trends can be understood in terms of the dynamics of the unstable surface layer and are discussed below.

The decomposition of $\langle P_{ij}|\mathbf{u}^r\rangle$ into $\langle P_{ij}^d|\mathbf{u}^r\rangle$ and $\langle -\frac{2}{3}\tau_{kk}S_{ij}|\mathbf{u}^r\rangle$ is first examined. Figure 3.6(a) shows that the trend and magnitude of $\langle P_{11}^d|u_1^r, u_3^r\rangle$ are similar to those of $\langle P_{11}|u_1^r, u_3^r\rangle$ (Figure

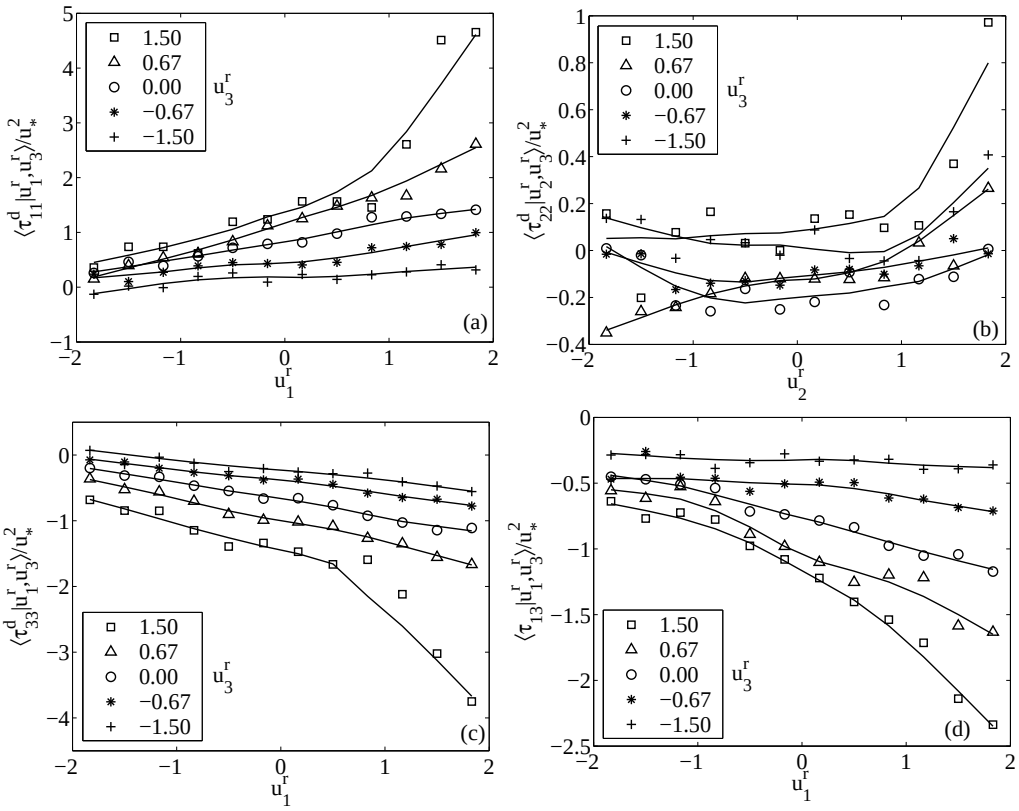

Figure 3.4 Conditional means of the measured deviatoric SGS stress components conditional on the resolvable-scale velocity components. The normal component $\langle \tau_{33}^d | u_1^r, u_3^r \rangle$ generally has the opposite sign as $\langle \tau_{33} | u_1^r, u_3^r \rangle$ due to the strong anisotropy of the SGS stress.

3.5a), indicating that the conditional spectral transfer part of $\langle P_{11} | \mathbf{u}^r \rangle$ dominates over the redistribution part. Figure 3.6(b) shows that $\langle P_{33}^d | u_1^r, u_3^r \rangle$ weakly depends on u_1^r and increases with u_3^r. For negative u_3^r ($u_3^r < -0.5$), $\langle P_{33}^d | u_1^r, u_3^r \rangle$ is negative, indicating conditional backscatter. Notice that the dependence of $\langle P_{33}^d | u_1^r, u_3^r \rangle$ has the opposite trend to that of $\langle P_{33} | u_1^r, u_3^r \rangle$ owing to the redistribution term $\langle -\frac{2}{3} \tau_{kk} S_{33} | u_1^r, u_3^r \rangle$ (see below). The conditional energy transfer rate (Figure 3.6e) shows a similar trend to $\langle P_{11}^d | u_1^r, u_3^r \rangle$ and is forward for $u_3^r > 0$. It decreases monotonically as u_3^r moves toward negative values. It is probable that for large negative u_3^r values, the conditional energy transfer will reverse direction (conditional backscatter). These observations are somewhat similar to those of Piomelli *et al.* (1996) [80] in DNS of a plane channel flow that forward transfer and backscatter are associated with ejections and sweeps, respectively. Sullivan *et al.* (2003) [36] showed that the average amount of backscatter increased with the ratio of the vertical-velocity integral length scale to the filter scale. The results shown here are for the most anisotropic filter in the present study, i.e. for the smallest length scale ratio; therefore, for the data collected using the other

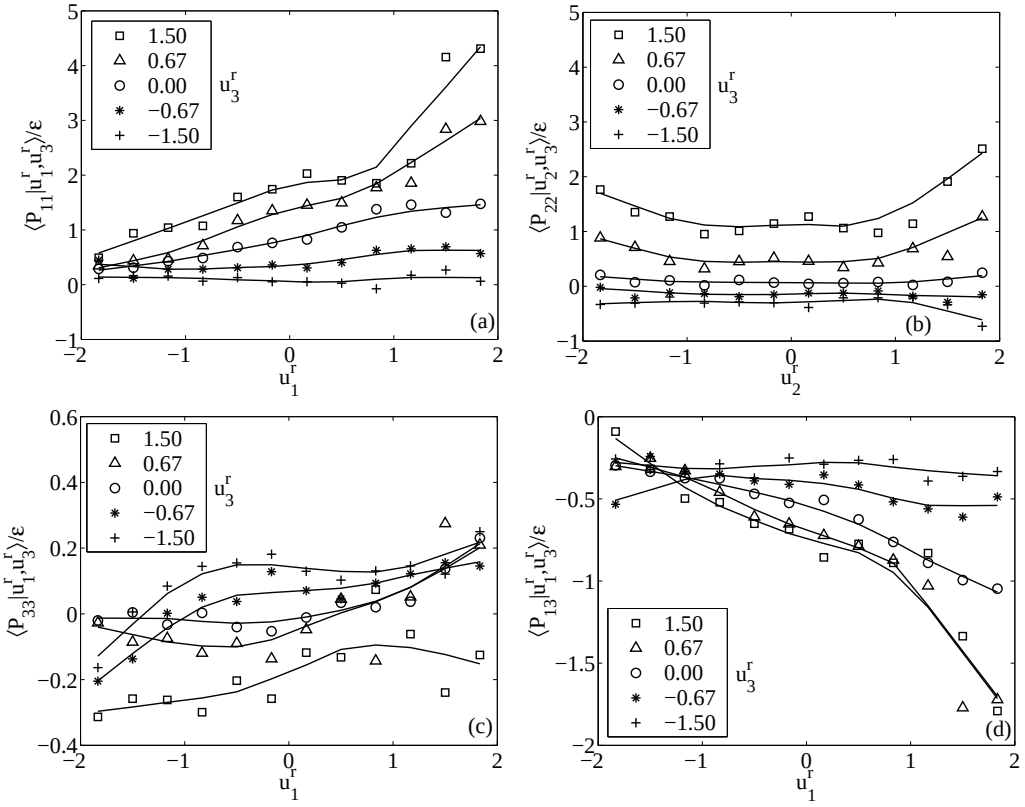

Figure 3.5 Conditional means of the measured SGS stress production components conditional on the resolvable-scale velocity components.

array configurations under similar stability conditions, it is expected larger amounts of conditional backscatter. Because conditional backscatter has qualitatively different effects on the evolution of the JPDF than conditional forward transfer, it is important for SGS models to predict conditional backscatter. Therefore, stochastic backscatter models will not be sufficient if they do not predict correctly the conditional backscatter.

The redistribution terms $\left\langle -\frac{2}{3}\tau_{kk}S_{11}|u_1^r, u_3^r\right\rangle$ and $\left\langle -\frac{2}{3}\tau_{kk}S_{33}|u_1^r, u_3^r\right\rangle$ are shown in Figures 3.6(c) and 6(d), respectively. Figure 3.6(c) shows that $\left\langle -\frac{2}{3}\tau_{kk}S_{11}|u_1^r, u_3^r\right\rangle$ depends weakly on u_1^r, but increases with u_3^r. It has the same sign as u_3^r, indicating that τ_{11} loses energy to τ_{33} for negative u_3^r and gains energy for positive u_3^r owing to redistribution. Figure 3.6(d) shows that $\left\langle -\frac{2}{3}\tau_{kk}S_{33}|u_1^r, u_3^r\right\rangle$ has a similar trend and magnitude to $\left\langle -\frac{2}{3}\tau_{kk}S_{11}|u_1^r, u_3^r\right\rangle$ but has the opposite sign to u_3^r, indicating that τ_{33} gains energy for negative u_3^r and loses energy for positive u_3^r.

To further understand the conditional SGS stress production rate and its relationship to the surface-layer dynamics, $\langle P_{11}|\mathbf{u}^r\rangle$ and $\langle P_{33}|\mathbf{u}^r\rangle$ is expanded into individual SGS stress and velocity gradient terms and examine their relative contributions. Such analyses are useful for identifying

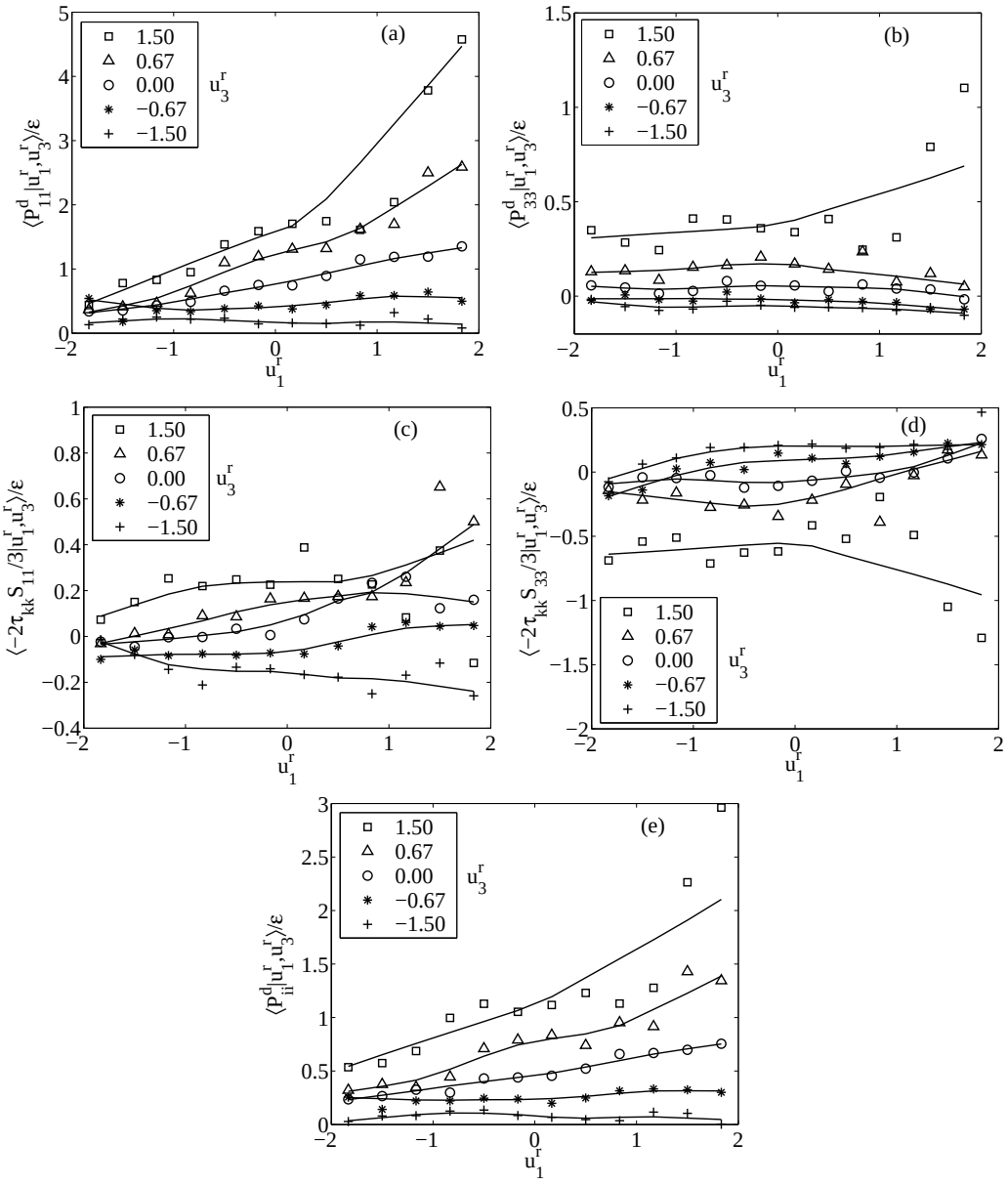

Figure 3.6 Conditional means of the measured production rates of the normal SGS stress components due to: (a) and (b), the deviatoric part of the SGS stress (τ_{ij}^d); (c) and (d), the isotropic part ($\frac{1}{3}\tau_{kk}s_{ij}$, the redistribution term); (e), the conditional energy transfer rate. Conditional backscatter is evident in (b).

the surface-layer processes that contribute to these statistics to guide SGS modeling. From (3.5), $\langle P_{11}|\mathbf{u}^r\rangle$ can be expanded as:

$$\langle P_{11}|\mathbf{u}^r\rangle = -2\left\langle \tau_{11}^d \frac{\partial u_1^r}{\partial x_1} + \frac{1}{3}\tau_{kk}\frac{\partial u_1^r}{\partial x_1} + \tau_{12}\frac{\partial u_1^r}{\partial x_2} + \tau_{13}\frac{\partial u_1^r}{\partial x_3}\middle| \mathbf{u}^r \right\rangle. \tag{3.11}$$

The first term on the right-hand side of (3.11) is the conditional energy transfer from resolvable to subgrid-scales associated with the normal strain rate and the normal SGS stress. The second is the conditional inter-component exchange (redistribution). The last two terms are the conditional energy transfer associated with the SGS shear stress and strain components. The results obtained from the data show that all the terms on the right-hand side of (3.11) are of the same order of magnitude; therefore, the results for each of them will be discussed. Similarly, $\langle P_{33}|\mathbf{u}^r\rangle$ can be expanded as:

$$\langle P_{33}|\mathbf{u}^r\rangle = -2\left\langle \tau_{33}^d \frac{\partial u_3^r}{\partial x_3} + \frac{1}{3}\tau_{kk}\frac{\partial u_3^r}{\partial x_3} + \tau_{31}\frac{\partial u_3^r}{\partial x_1} + \tau_{32}\frac{\partial u_3^r}{\partial x_2}\middle| \mathbf{u}^r \right\rangle. \tag{3.12}$$

The terms on the right-hand side of (3.12) are similar to those in (3.11). However, the results (not shown) indicate that the spectral transfer associated with the shear stress is much smaller than that associated with the normal stress and the inter-component exchange. This is because the derivatives of u_3^r in the horizontal directions ($\partial u_3^r/\partial x_1$ and $\partial u_3^r/\partial x_2$) are small compared to its vertical derivative. Therefore, two parts of $\langle P_{33}|\mathbf{u}^r\rangle$, $\left\langle -2\tau_{33}^d \frac{\partial u_3^r}{\partial x_3}\middle| \mathbf{u}^r \right\rangle$ and $\left\langle -\frac{2}{3}\tau_{kk}\frac{\partial u_3^r}{\partial x_3}\middle| \mathbf{u}^r \right\rangle$ will be focused, which are an energy transfer term and the inter-component exchange term, respectively.

The results for the components of $\langle P_{11}|u_1^r, u_3^r\rangle$ and $\langle P_{33}|u_1^r, u_3^r\rangle$ are discussed now. The results for positive and negative u_3^r will be discussed separately because these components have qualitatively different characteristics owing to the different surface-layer dynamics associated with updrafts and downdrafts. When u_3^r is positive, vertical-velocity energy-containing eddies move upward and are, on average, stretched in the vertical direction due to buoyancy acceleration, i.e. $\partial u_3^r/\partial x_3 > 0$. At the same time, continuity requires the eddies, on average, to be compressed in the horizontal direction, i.e. $\partial u_1^r/\partial x_1 < 0$ and $\partial u_2^r/\partial x_2 < 0$. Therefore, the spectral transfer terms associated with the normal strain, $\left\langle -2\tau_{33}^d \frac{\partial u_3^r}{\partial x_3}\middle| u_1^r, u_3^r \right\rangle$ and $\left\langle -2\tau_{11}^d \frac{\partial u_1^r}{\partial x_1}\middle| u_1^r, u_3^r \right\rangle$ (not shown) are positive because $\tau_{33}^d < 0$ and $\tau_{11}^d > 0$ owing to the strong anisotropy in the surface layer ($\langle\tau_{11}\rangle > \langle\tau_{33}\rangle$), indicating that both τ_{11} and τ_{33} gain energy (forward transfer) through the spectral transfer associated with the normal strain rates. The inter-component exchange terms, however, have opposite signs with $\left\langle -\frac{2}{3}\tau_{kk}\frac{\partial u_3^r}{\partial x_3}\middle| u_1^r, u_3^r \right\rangle$ being negative and $\left\langle -\frac{2}{3}\tau_{kk}\frac{\partial u_1^r}{\partial x_1}\middle| u_1^r, u_3^r \right\rangle$ being positive, indicating that τ_{33} loses energy to τ_{11} through inter-component exchange. Because $\left\langle -\frac{2}{3}\tau_{kk}\frac{\partial u_3^r}{\partial x_3}\middle| u_1^r, u_3^r \right\rangle$ has a larger

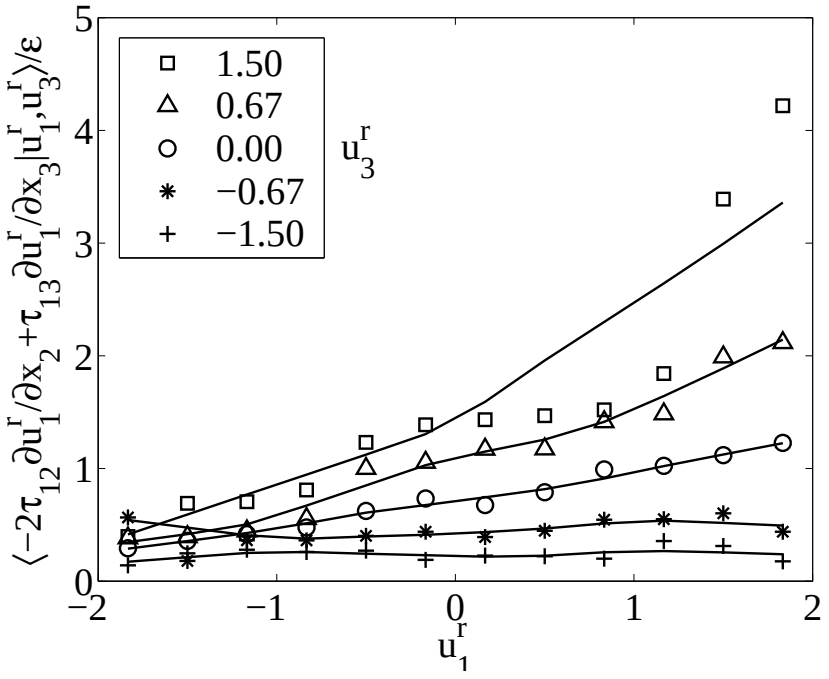

Figure 3.7 Components of $\langle P_{11}|u_1^r, u_2^r\rangle$ due to the shear stress components conditional on the resolvable-scale velocity, which are responsible for the dependence of $\langle P_{11}|u_1^r, u_2^r\rangle$ on u_1^r.

magnitude than $\left\langle -2\tau_{33}^d \frac{\partial u_3^r}{\partial x_3}\middle| u_1^r, u_3^r\right\rangle$, τ_{33} loses more energy owing to the inter-component exchange than it gains from the spectral transfer, resulting in negative $\langle P_{33}|u_1^r, u_3^r\rangle$ values.

The processes described above are enhanced with increasing u_3^r, making the magnitudes of $\left\langle -\frac{2}{3}\tau_{kk}\frac{\partial u_1^r}{\partial x_1}\middle| u_1^r, u_3^r\right\rangle$ and $\left\langle -2\tau_{11}^d \frac{\partial u_1^r}{\partial x_1}\middle| u_1^r, u_3^r\right\rangle$ (components of $\langle P_{11}|u_1^r, u_3^r\rangle$) and $\langle P_{33}|u_1^r, u_3^r\rangle$ larger. This is owing to two aspects of the surface-layer dynamics. First, a larger u_3^r generally corresponds to stronger buoyancy acceleration, therefore larger vertical stretching and larger magnitudes of $\partial u_3^r/\partial x_3$ and $\partial u_1^r/\partial x_1$ (not shown). Second, the local SGS stress is generally enhanced by positive u_3^r owing to eddies with a larger amount of SGS energy brought up from near the ground. This is an advection effect discussed above. Therefore, $\left\langle -\frac{2}{3}\tau_{kk}\frac{\partial u_1^r}{\partial x_1}\middle| u_1^r, u_3^r\right\rangle$ and $\left\langle -2\tau_{11}^d \frac{\partial u_1^r}{\partial x_1}\middle| u_1^r, u_3^r\right\rangle$ (components of $\langle P_{11}|u_1^r, u_3^r\rangle$) and the magnitude of $\langle P_{33}|u_1^r, u_3^r\rangle$ generally increase with positive u_3^r.

The spectral transfer terms $\left\langle -2\tau_{33}^d \frac{\partial u_3^r}{\partial x_3}\middle| u_1^r, u_3^r\right\rangle$ and $\left\langle -2\tau_{11}^d \frac{\partial u_1^r}{\partial x_1}\middle| u_1^r, u_3^r\right\rangle$ depend only weakly on u_1^r. The inter-component-exchange terms also have similar dependencies (not shown). This is because $\partial u_3^r/\partial x_3$ and $\partial u_1^r/\partial x_1$ have weak dependencies on u_1^r. Consequently, $\langle P_{33}|u_1^r, u_3^r\rangle$, $\left\langle -\frac{2}{3}\tau_{kk}\frac{\partial u_1^r}{\partial x_1}\middle| u_1^r, u_3^r\right\rangle$, and $\left\langle -2\tau_{11}^d \frac{\partial u_1^r}{\partial x_1}\middle| u_1^r, u_3^r\right\rangle$ (components of $\langle P_{11}|u_1^r, u_3^r\rangle$) generally depend weakly on u_1^r. This indicates

that the dependence of $\langle P_{11}|u_1^r, u_3^r\rangle$ on u_1^r shown in Figure 3.5(a) is due to the shear production components $-2\left\langle \tau_{12}\frac{\partial u_1^r}{\partial x_2} + \tau_{13}\frac{\partial u_1^r}{\partial x_3}\middle| u_1^r, u_3^r\right\rangle$ (Figure 3.7), which have positive contributions to $\langle P_{11}|\mathbf{u}^r\rangle$. Both terms depend on u_1^r because when u_3^r is positive, a larger u_1^r on average results in a larger shear strain rate, $\partial u_1^r/\partial x_3$, and at the same time enhances the SGS shear stress component τ_{13}. Thus, $\langle P_{11}|u_1^r, u_3^r\rangle$ is positive and generally depends on u_1^r. Increasing u_3^r on average enhances the SGS shear stress components τ_{13} due to the advection effect, and enhances $\partial u_1^r/\partial x_3$ due to the large horizontal velocity deficit carried by fluid brought up from near the ground, making the shear production of the $\langle P_{11}|u_1^r, u_3^r\rangle$ larger. Therefore, $\langle P_{11}|u_1^r, u_3^r\rangle$ generally increases with u_3^r.

The results for negative u_3^r can also be understood in terms of the surface layer dynamics. When u_3^r is negative, the vertical-velocity energy-containing eddies associated with the returning flow of large convective eddies move downward and are on average compressed in the vertical direction due to the presence of the ground, resulting in negative $\partial u_3^r/\partial x_3$ and positive $\partial u_1^r/\partial x_1$ and $\partial u_2^r/\partial x_2$. Therefore, the spectral transfer associated with both the normal strain $\left\langle -2\tau_{33}^d\frac{\partial u_3^r}{\partial x_3}\middle| u_1^r, u_3^r\right\rangle$ and $\left\langle -2\tau_{11}^d\frac{\partial u_1^r}{\partial x_1}\middle| u_1^r, u_3^r\right\rangle$ are negative, indicating that both τ_{11} and τ_{33} lose energy through spectral transfer associated with the normal strain (conditional backscatter). Similar to the case of $u_3^r > 0$, the inter-component-exchange terms still have opposite signs, but with $\left\langle -\frac{2}{3}\tau_{kk}\frac{\partial u_3^r}{\partial x_3}\middle| u_1^r, u_3^r\right\rangle$ being positive and $\left\langle -\frac{2}{3}\tau_{kk}\frac{\partial u_1^r}{\partial x_1}\middle| u_1^r, u_3^r\right\rangle$ being negative, indicating that τ_{33} gains energy from τ_{11} through inter-component exchange. Because $\left\langle -\frac{2}{3}\tau_{kk}\frac{\partial u_3^r}{\partial x_3}\middle| u_1^r, u_3^r\right\rangle$ has a larger magnitude than $\left\langle -2\tau_{33}^d\frac{\partial u_3^r}{\partial x_3}\middle| u_1^r, u_3^r\right\rangle$, τ_{33} gains more energy than it loses due to conditional backscatter, resulting in positive $\langle P_{33}|u_1^r, u_3^r\rangle$ values.

These processes are also somewhat enhanced by larger (negative) u_3^r, although to a much lesser extent than positive u_3^r, resulting in larger magnitudes of $\left\langle -\frac{2}{3}\tau_{kk}\frac{\partial u_1^r}{\partial x_1}\middle| u_1^r, u_3^r\right\rangle$ and $\left\langle -2\tau_{11}^d\frac{\partial u_1^r}{\partial x_1}\middle| u_1^r, u_3^r\right\rangle$ (components of $\langle P_{11}|u_1^r, u_3^r\rangle$) and $\langle P_{33}|u_1^r, u_3^r\rangle$. This is because a stronger downdraft (returning flow of large convective eddies) generally produces larger vertical compression, i.e., larger magnitudes of $\partial u_3^r/\partial x_3$ and $\partial u_1^r/\partial x_1$. However, since the eddies carried by returning flow generally have larger length scales, they contain smaller SGS stress (τ_{11}^d, τ_{33}^d and τ_{kk}). Therefore, although the magnitudes of $\left\langle -\frac{2}{3}\tau_{kk}\frac{\partial u_1^r}{\partial x_1}\middle| u_1^r, u_3^r\right\rangle$ and $\left\langle -2\tau_{11}^d\frac{\partial u_1^r}{\partial x_1}\middle| u_1^r, u_3^r\right\rangle$ (components of $\langle P_{11}|u_1^r, u_3^r\rangle$) and $\langle P_{33}|u_1^r, u_3^r\rangle$ generally increase with magnitude of u_3^r, the dependence is not as strong as for the case of positive u_3^r because of these competing effects, and because of the milder vertical compression due to the downdrafts than that due to updrafts (buoyancy acceleration).

When u_3^r is negative, $\langle P_{33}|u_1^r, u_3^r\rangle$, $\left\langle -\frac{2}{3}\tau_{kk}\frac{\partial u_1^r}{\partial x_1}\middle| u_1^r, u_3^r\right\rangle$ and $\left\langle -2\tau_{11}^d\frac{\partial u_1^r}{\partial x_1}\middle| u_1^r, u_3^r\right\rangle$ (components of $\langle P_{11}|u_1^r, u_3^r\rangle$) generally depend weakly on u_1^r for reasons similar to those for the case of positive u_3^r.

In contrast to the case of positive u_3^r, the shear production components $-2\left\langle \tau_{12}\frac{\partial u_1^r}{\partial x_2}+\tau_{13}\frac{\partial u_1^r}{\partial x_3}\middle| u_1^r, u_3^r\right\rangle$ (Figure 3.7) also depend weakly on u_1^r. This is because both the horizontal shear strain rate component, $\partial u_1^r/\partial x_3$, and the SGS shear stress component, τ_{13}, depend weakly on u_1^r as the vertical shear is weakened by the returning flow. Therefore, $\langle P_{11}|u_1^r, u_3^r\rangle$ also depends weakly on u_1^r. The shear production has a positive contribution, which is larger than the backscatter associated with the normal strain rates and the loss due to inter-component exchange, resulting in positive $\langle P_{11}|u_1^r, u_3^r\rangle$. Increasing the magnitude of u_3^r causes the shear stress components τ_{13} and shear strain rate component $\partial u_1^r/\partial x_3$ to decrease owing to the advection effect and the horizontal velocity deficit carried by the returning eddies. Therefore, $\langle P_{11}|u_1^r, u_3^r\rangle$ generally decreases with u_3^r.

The trends for $\langle P_{22}|u_2^r, u_3^r\rangle$ (Figure 3.5*b*) are generally similar to those of $\langle P_{11}|u_1^r, u_3^r\rangle$. However, there are several differences. One is that $\langle P_{22}|u_2^r, u_3^r\rangle$ increases with $|u_2^r|$, because the flow is symmetric in the lateral direction. Another difference is that the magnitude of $\langle P_{22}|u_2^r, u_3^r\rangle$ is smaller than that of $\langle P_{11}|u_1^r, u_3^r\rangle$ and is negative when u_3^r has large negative values ($u_3^r < -0.6$) because the shear strain rate $\partial u_2^r/\partial x_3$ is smaller than $\partial u_1^r/\partial x_3$, resulting in smaller spectral transfer associated with shear compared to the case for $\langle P_{11}|u_1^r, u_3^r\rangle$. Thus, $\langle P_{22}|u_2^r, u_3^r\rangle$ is smaller than $\langle P_{11}|u_1^r, u_3^r\rangle$ when u_3^r is positive and becomes negative when u_3^r is strongly negative. Therefore, when u_3^r is negative, τ_{22} loses more energy due to the spectral transfer associated with normal strain and inter-component-exchange than it gains due to spectral transfer associated with shear.

With the above discussions on $\langle P_{\alpha\alpha}|\mathbf{u}^r\rangle$, the trends for $\langle \tau_{\alpha\alpha}|\mathbf{u}^r\rangle$ become clearer. Because the evolution of $\langle \tau_{11}|u_1^r, u_3^r\rangle$ is dominated by $\langle P_{11}|u_1^r, u_3^r\rangle$, $\langle \tau_{11}|u_1^r, u_3^r\rangle$ has similar trends to $\langle P_{11}|u_1^r, u_3^r\rangle$. For the same reason, $\langle \tau_{22}|u_2^r, u_3^r\rangle$ has similar trends to $\langle P_{22}|u_2^r, u_3^r\rangle$. However, the trends for $\langle \tau_{33}|u_1^r, u_3^r\rangle$ are different from those of $\langle P_{33}|u_1^r, u_3^r\rangle$, because buoyancy production dominates the evolution of τ_{33}. Thus, $\langle \tau_{33}|u_1^r, u_3^r\rangle$ has similar trends to the buoyancy production rate $\langle P_{B33}|u_1^r, u_3^r\rangle$ (Figure 3.8), instead of $\langle P_{33}|u_1^r, u_3^r\rangle$. This suggests that buoyancy effects can potentially play an important role in models of the SGS stress.

To summarize this part of the results, when u_3^r is positive, the energy transfer rates due to both normal and shear strain rates are positive (forward). The former depends strongly on u_3^r, but weakly on u_1^r, whereas the latter depends on both. The inter-component exchange is positive for τ_{11} and τ_{22} and is negative for τ_{33}. When u_3^r is negative, the energy transfer due to the normal strain is negative, whereas that due to shear strain is positive. The dependence on both u_1^r and u_3^r is weaker. The inter-component-exchange terms have opposite signs to those for positive u_3^r. These are closely related to the surface-layer dynamics.

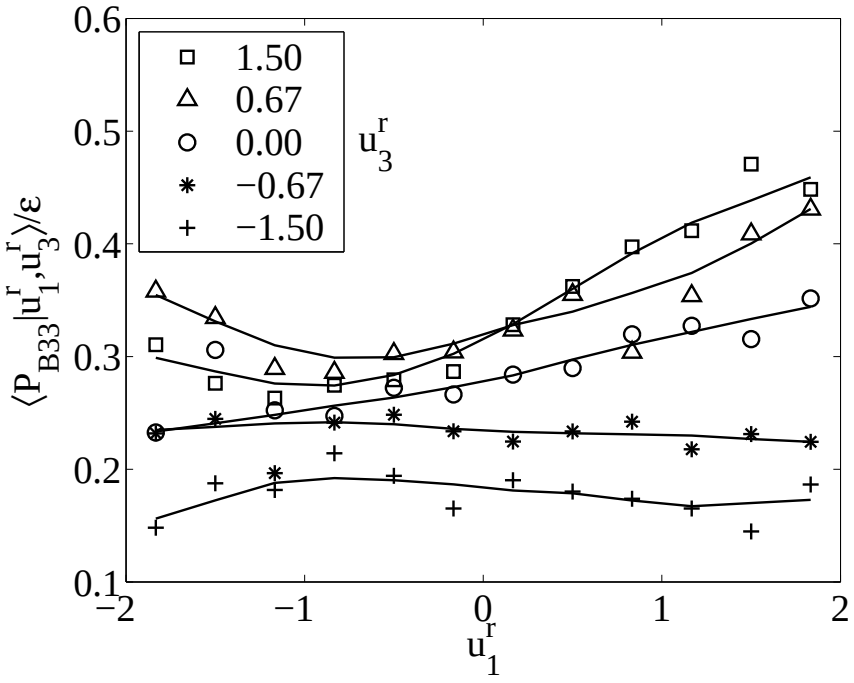

Figure 3.8 The conditional mean of the buoyancy production P_{B33} conditional on the resolvable-scale velocity.

3.2.2 Shear components of $\langle \tau_{ij}|\mathbf{u}^r\rangle$ and $\langle P_{ij}|\mathbf{u}^r\rangle$

The results for the conditional shear stress component $\langle \tau_{13}|u_1^r, u_3^r\rangle$ are shown in Figure 3.4(d). The magnitude of $\langle \tau_{13}|u_1^r, u_3^r\rangle$ generally increases with u_3^r. It also increases with u_1^r and the dependence is enhanced by positive u_3^r and weakened by negative u_3^r. To further understand the result of $\langle \tau_{13}|u_1^r, u_3^r\rangle$, the result of $\langle P_{13}|u_1^r, u_3^r\rangle$ is first discussed. Figure 3.5(d) shows that the trends of $\langle P_{13}|u_1^r, u_3^r\rangle$ are similar to those of $\langle \tau_{13}|u_1^r, u_3^r\rangle$. The results of $\langle P_{13}|u_1^r, u_3^r\rangle$ can also be understood in terms of the dynamics of the unstable surface layer. The results of $\left\langle P_{13}^d|u_1^r, u_3^r\right\rangle$ and $\left\langle -\frac{2}{3}\tau_{kk}S_{13}|u_1^r, u_3^r\right\rangle$ which are due to deviatoric and isotropic parts of the SGS stress, respectively (Figures 3.9(a) and 9(b)) are examined. Their magnitudes depend on u_1^r and are enhanced by positive u_3^r. The former is positive, indicating destruction of the shear stress, which has negative values, owing to straining and rotation of the anisotropic part of the SGS turbulence. The latter is negative and has about twice the magnitude of the former, indicating production due to straining of the isotropic part of the SGS turbulence.

To understand $\langle P_{13}|\mathbf{u}^r\rangle$ in more detail, it is expanded as

$$\langle P_{13}|\mathbf{u}^r\rangle = -\left\langle \tau_{11}\frac{\partial u_3^r}{\partial x_1} + \tau_{12}\frac{\partial u_3^r}{\partial x_2} + \tau_{13}\frac{\partial u_3^r}{\partial x_3} + \tau_{31}\frac{\partial u_1^r}{\partial x_1} + \tau_{32}\frac{\partial u_1^r}{\partial x_2} + \tau_{33}\frac{\partial u_1^r}{\partial x_3}\middle| \mathbf{u}^r\right\rangle. \tag{3.13}$$

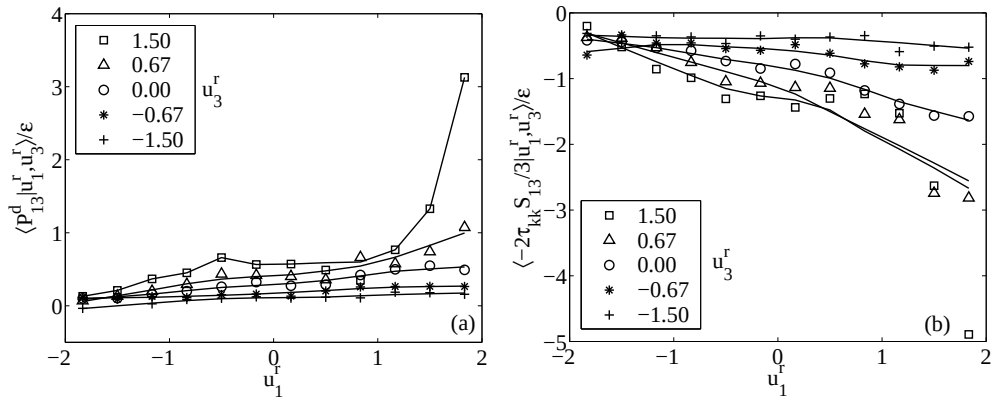

Figure 3.9 Conditional mean of the measured production rate of the shear SGS stress component τ_{13} due to: (a), the deviatoric part of the SGS stress (τ_{ij}^d); (b), the isotropic part ($\frac{1}{3}\tau_{kk}s_{ij}$, the redistribution term). The deviatoric part is generally positive, therefore reduces the SGS shear stress.

The results obtained from the data show that the first five terms on the right-hand side of (3.13) are small compared to the last term. This is because the derivatives of u_1^r in the horizontal directions and the derivatives of u_3^r are relatively small compared to $\partial u_1^r/\partial x_3$. Therefore, the last term $\left\langle -\tau_{33}\frac{\partial u_1^r}{\partial x_3}\middle|\,\mathbf{u}^r\right\rangle$ is focused.

The results in Section 3.2.1 have shown that the SGS normal stress τ_{33} and the shear strain rate component $\partial u_1^r/\partial x_3$ increase with u_3^r. They also increase with u_1^r, but the dependence is enhanced by positive u_3^r and weakened by negative u_3^r. Therefore, the magnitude of $\langle P_{13}|\mathbf{u}^r\rangle$ also has similar trends. To further understand the trends of $\langle P_{13}|\mathbf{u}^r\rangle$, $\left\langle -\tau_{33}\frac{\partial u_1^r}{\partial x_3}\middle|\,\mathbf{u}^r\right\rangle$ is rewritten as:

$$\left\langle -\tau_{33}\frac{\partial u_1^r}{\partial x_3}\middle|\,\mathbf{u}^r\right\rangle = \left\langle -\frac{1}{2}\tau_{33}^d S_{13}\middle|\,\mathbf{u}^r\right\rangle + \left\langle -\frac{1}{2}\tau_{33}^d \Omega_{13}\middle|\,\mathbf{u}^r\right\rangle + \left\langle -\frac{1}{3}\tau_{kk}\frac{\partial u_1^r}{\partial x_3}\middle|\,\mathbf{u}^r\right\rangle \tag{3.14}$$

where Ω_{ij} is the rotation tensor of resolvable-scale velocity. The first two terms on the right-hand side of (3.14) are the conditional shear stress production due to straining and rotation of the anisotropic part of the SGS turbulence. The third is the conditional shear stress production due to the straining of the isotropic part of the SGS turbulence. The trends of $\left\langle -\frac{1}{2}\tau_{33}^d S_{13}\middle|\,u_1^r, u_3^r\right\rangle$ and $\left\langle -\frac{1}{2}\tau_{33}^d \Omega_{13}\middle|\,u_1^r, u_3^r\right\rangle$ (not shown) are similar to that of $\left\langle P_{13}^d|\mathbf{u}^r\right\rangle$. Their magnitudes are nearly equal and are approximately half of that of $\left\langle P_{13}^d|u_1^r, u_3^r\right\rangle$, indicating that the destruction of the conditional shear stress due to rotation, and straining of the anisotropic part of the SGS turbulence are almost equal. Therefore, $\left\langle P_{13}^d|u_1^r, u_3^r\right\rangle$ comes primarily from the interactions of τ_{33}^d with the shear strain rate, S_{13}, and the rotation sensor component, Ω_{13}. The trend and magnitude of $\left\langle -\frac{1}{3}\tau_{kk}\frac{\partial u_1^r}{\partial x_3}\middle|\,u_1^r, u_3^r\right\rangle$ (not shown) are

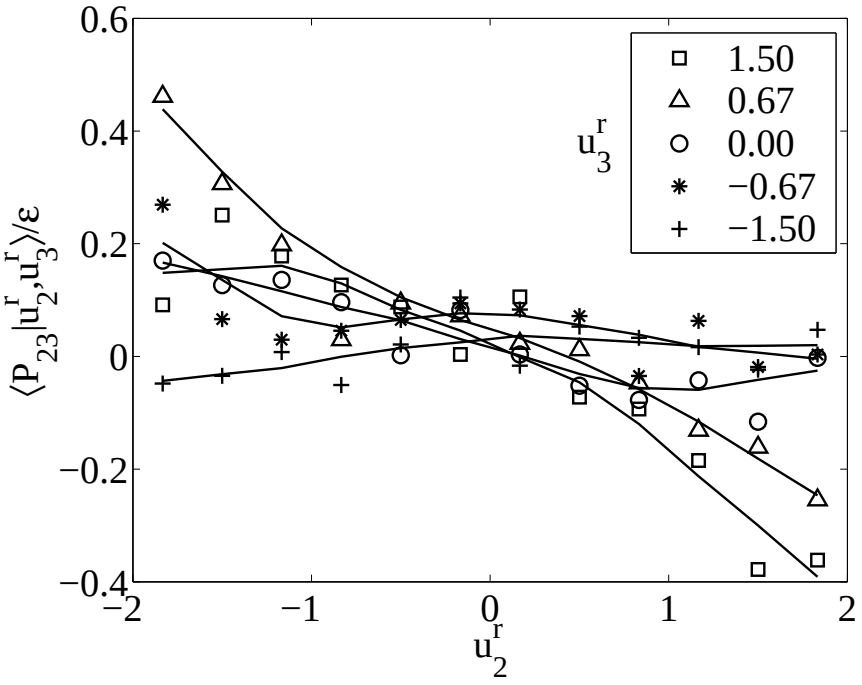

Figure 3.10 Conditional mean of P_{23} conditional on the resolvable-scale velocity components (u_2^r, u_3^r).

close to that of $\langle -\frac{2}{3}\tau_{kk}S_{13}|u_1^r, u_3^r\rangle$, indicating that the conditional shear stress production due to straining of isotropic turbulence comes mainly from the interaction of τ_{kk} with the shear strain, S_{13}.

Similarly to $\langle P_{13}|u_1^r, u_3^r\rangle$, $\langle P_{23}|u_2^r, u_3^r\rangle$ comes mainly from the interaction between the normal SGS stress τ_{33} and the horizontal shear $\partial u_2^r/\partial x_3$. The results for $\langle P_{23}|u_2^r, u_3^r\rangle$ are shown in Figure 3.10 and are similar to those of $\langle P_{13}|u_1^r, u_3^r\rangle$. The differences are that the magnitude of $\langle P_{23}|u_2^r, u_3^r\rangle$ increases with $|u_2^r|$ because the flow is symmetric in the lateral direction, and that the magnitude of $\langle P_{23}|u_2^r, u_3^r\rangle$ is smaller than that of $\langle P_{13}|u_1^r, u_3^r\rangle$ because the shear due to u_2^r is smaller than that due to u_1^r.

The evolution of $\langle \tau_{13}|u_1^r, u_3^r\rangle$ is dominated by both $\langle P_{13}|u_1^r, u_3^r\rangle$ and conditional buoyancy production $\langle P_{B13}|u_1^r, u_3^r\rangle$ (Figure 3.11). The conditional buoyancy production $\langle P_{B13}|u_1^r, u_3^r\rangle$ has similar trends and magnitudes to $\langle P_{13}|u_1^r, u_3^r\rangle$. Therefore, $\langle \tau_{13}|u_1^r, u_3^r\rangle$ also has similar trends. Similarly, the evolution of $\langle \tau_{23}|u_2^r, u_3^r\rangle$ (Figure 3.12*a*) is dominated by both $\langle P_{23}|u_2^r, u_3^r\rangle$ and buoyancy production $\langle P_{B23}|u_2^r, u_3^r\rangle$ (Figure 3.12*b*), which $\langle P_{B23}|u_2^r, u_3^r\rangle$ has similar trends and magnitudes to $\langle P_{23}|u_2^r, u_3^r\rangle$. Therefore, $\langle \tau_{23}|u_2^r, u_3^r\rangle$ also has similar trends.

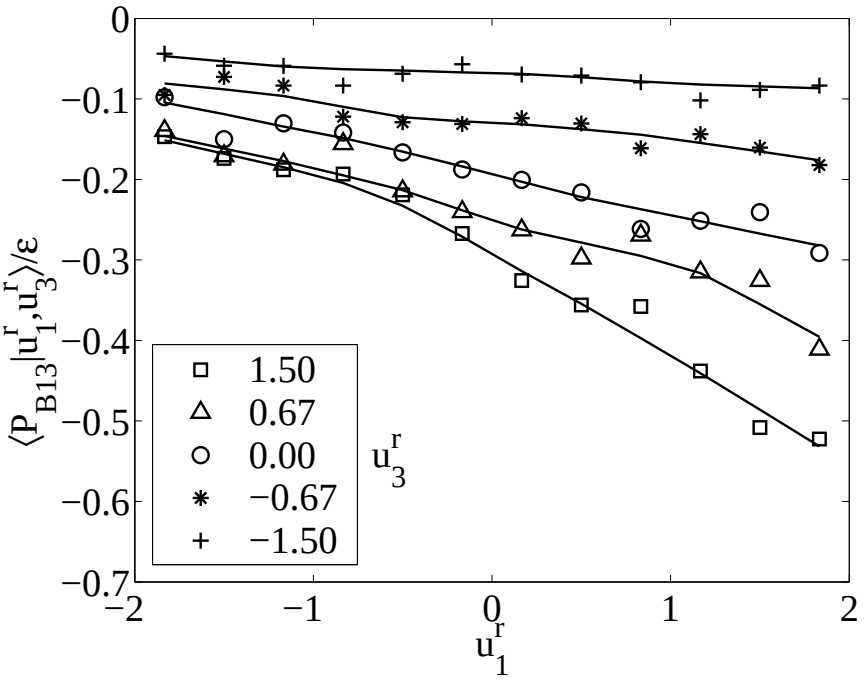

Figure 3.11 Conditional mean of the buoyancy production P_{B13} conditional on the resolvable-scale velocity, which has the similar trend to that of $\langle \tau_{13}|u_1^r, u_3^r\rangle$.

3.2.3 Anisotropy of the conditional SGS stress

An important property of the SGS stress is its level of anisotropy. Sullivan *et al.* (2003) [36] found that the mean SGS stress in the surface layer is generally close to axisymmetric with one large eigenvalue, similar to the Reynolds stress in turbulent boundary layers. It has been argued that the Smagorinsky model under-predicts the anisotropy (redistribution of SGS energy among the normal components) ([67]).

The level of anisotropy of the conditional SGS stress can be characterized by the representation in the Lumley triangle ([81]). The normalized anisotropy tensor for $\langle \tau_{ij}|\mathbf{u}^r\rangle$,

$$\left\langle \tau_{ij}^d|\mathbf{u}^r\right\rangle / \left\langle \tau_{kk}|\mathbf{u}^r\right\rangle = \left\langle \tau_{ij}|\mathbf{u}^r\right\rangle / \left\langle \tau_{kk}|\mathbf{u}^r\right\rangle - \frac{1}{3}\delta_{ij}, \tag{3.15}$$

can be determined by two variables ξ and η defined in terms of its invariants ([37])

$$6\eta^2 = -2II = \left\langle \tau_{ij}^d|\mathbf{u}^r\right\rangle \left\langle \tau_{ij}^d|\mathbf{u}^r\right\rangle / \left\langle \tau_{kk}|\mathbf{u}^r\right\rangle^2, \tag{3.16}$$

$$6\xi^3 = 3III = \left\langle \tau_{ij}^d|\mathbf{u}^r\right\rangle \left\langle \tau_{jk}^d|\mathbf{u}^r\right\rangle \left\langle \tau_{ki}^d|\mathbf{u}^r\right\rangle / \left\langle \tau_{kk}|\mathbf{u}^r\right\rangle^3, \tag{3.17}$$

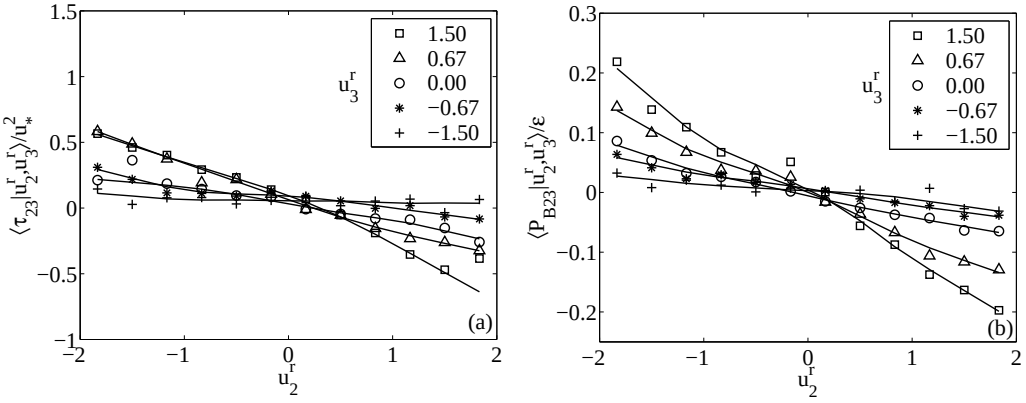

Figure 3.12 Conditional means of (a), the measured SGS stress τ_{23}, and (b), the conditional buoyancy production P_{B23}, which has the similar trend to that of $\langle \tau_{23}|u_2^r, u_3^r\rangle$.

where II and III are the second and third invariants of the anisotropy tensor. If $\langle \tau_{ij}|\mathbf{u}^r\rangle$ is isotropic, both ξ and η are zero. (The first invariant or trace of $\langle \tau_{ij}^d|\mathbf{u}^r\rangle$ is always zero by definition). The representation for the conditional SGS stress results in Figures 3.2 and 3.4 is shown in Figure 3.13. There is a clear dependence of the anisotropy on the resolvable-scale velocity. When u_3^r is positive, $\langle \tau_{ij}|u_1^r, u_3^r\rangle$ is quite anisotropic. For negative u_1^r (and positive u_3^r), the points representing the anisotropy are not far from $\eta = -\xi$, indicating that $\langle \tau_{ij}|u_1^r, u_3^r\rangle$ is close to axisymmetric with one small eigenvalue. Such a SGS stress structure is probably a result of the strong buoyancy effects causing τ_{33} to lose energy to the horizontal components τ_{11} and τ_{22}. As u_1^r increases, the points move toward $\eta = \xi$, indicating that $\langle \tau_{ij}|u_1^r, u_3^r\rangle$ is close to axisymmetric with one large eigenvalue. In addition, as u_1^r and u_3^r both increase, the points appear to move toward the upper right-hand corner, indicating that the conditional SGS stress is approaching the one-component limit. This is probably caused by the strong vertical shear generating an elongated structure under such conditions. For negative u_3^r, the points are closer to the origin, indicating that $\langle \tau_{ij}|u_1^r, u_3^r\rangle$ is much less anisotropic. The dependence on u_1^r is also weak, consistent with the results on the conditional SGS stress in Figure 3.4. These results show that not only is there significant anisotropy in $\langle \tau_{ij}|u_1^r, u_3^r\rangle$, but also there are significant variations in the level of anisotropy, which depends on the resolvable-scale velocity. The implications of the anisotropy on LES are discussed in Section 3.4.

It is noted that the measured invariants, ξ and η, contain statistical uncertainties due to the uncertainties in the measured conditional SGS stress. While the results for $(\xi, \eta) = F(u_1^r, u_3^r)$ are well behaved (surfaces with bumps due to uncertainties), data points with large but similar (u_1^r, u_3^r) can appear at quite different places in the invariant map. This is a manifestation of the uncertainties

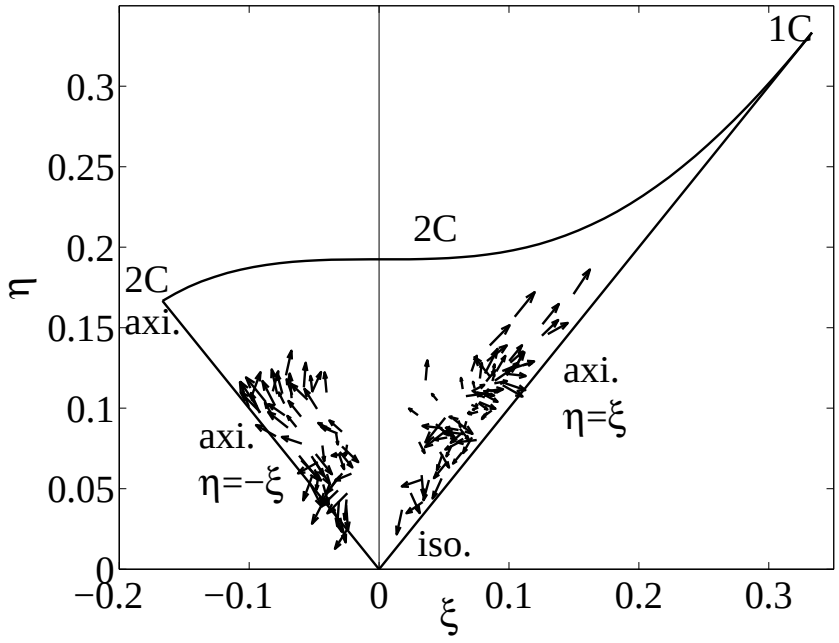

Figure 3.13 Representation of the anisotropy tensor in the Lumley triangle for the conditional SGS stress $\langle \tau_{ij} | u_1^r, u_3^r \rangle$ for array 1 ($\Delta/z = 3.88, -z/L = 0.24$). The arrows represent the conditioning vector (u_1^r, u_3^r). The anisotropy is stronger for $u_3^r > 0$. The SGS stress is close to axisymmetric with one large and small eigenvalue for $u_1^r > 0$ and $u_1^r < 0$, respectively.

because the inverse relationship of $(\xi, \eta) = F(u_1^r, u_3^r)$ is shown in the map, suggesting that the results of the invariants for large u_1^r and u_3^r fluctuations are sensitive to the uncertainties in the conditional SGS stress. The sensitivity appears to be higher when u_3^r is negative, at which the magnitude of the conditional SGS stress is small (larger relative uncertainties). Nonetheless, the general trends of the dependence of the anisotropy on the velocity fluctuations are clear on the map.

The results discussed above are for $\Delta/z = 3.88$ and $-z/L = 0.24$ (array 1). Sullivan *et al.* (2003) [36] show that the non-dimensional SGS stress results collapse when plotted as a function of the ratio of the vertical-velocity length scale to the filter size. To examine the effects of Δ/z and $-z/L$ the results for the other array configurations are also obtained. The results for $\langle \tau_{ij} | u_1^r, u_3^r \rangle$ are qualitatively similar to those for array 1, with the dependence on u_3^r generally stronger and the dependence on u_1^r generally weaker. The level of the anisotropy of $\langle \tau_{ij} | u_1^r, u_3^r \rangle$ for different array configurations are shown in Figure 3.14. When $-z/L$ is fixed, reducing Δ/z (from 2.00 for array 2 to 0.48 for array 4) has essentially no effects on shear and buoyancy. However, an anisotropic grid inherently trends to result in anisotropic SGS stress through anisotropic filtering. Therefore, there is a slight decease in anisotropy in $\langle \tau_{ij} | u_1^r, u_3^r \rangle$ associated with the filter anisotropy. Furthermore,

near the surface, anisotropic SGS eddies are affected more strongly by the presence of surface, i.e. the vertical compression due to the returning flows ($u_3^r < 0$) associated with the large convective eddies. The compression effects for array 4 are weaker than those for array 2, resulting in fewer points for the axisymmetric SGS stress with one small eigenvalue ($\eta = -\xi$). A comparison of the levels of anisotropy for array 2 ($\Delta/z = 2.00, -z/L = 0.36$) and array 3 ($\Delta/z = 1.00, -z/L = 0.60$) shows that $\langle \tau_{ij} | u_1^r, u_3^r \rangle$ for array 3 is less anisotropic than that for array 2, and has very few points near the line of axisymmetric SGS stress with one small eigenvalue ($\eta = -\xi$). The height of array 3 is larger than that of the array 2 (Table 3.1), corresponding to a larger $-z/L$ and a smaller Δ/z. With a larger $-z/L$, the effects of buoyancy are enhanced, but the effects of shear are weakened. These competing effects result in more points for axisymmetric SGS stress with one large eigenvalue ($\eta = \xi$). A smaller Δ/z for array 3 slightly reduces the level of anisotropy in $\langle \tau_{ij} | \mathbf{u}^r \rangle$ and the compression effects ($u_3^r < 0$), resulting in fewer points for axisymmetric SGS stress with one small eigenvalue ($\eta = -\xi$). Among the four arrays, array 1 has the largest Δ/z and the smallest $-z/L$, and consequently has the highest level of anisotropy and the strongest compression effects associated with the returning flow of large convective eddies. Therefore, it is expected that the SGS stress and its production rate for array 1 are the most challenging to predict by SGS models. Anisotropic grids (refined in the vertical direction), which are often used near the surface to match the flow interior with the surface (e.g., [21]), are therefore of importance. In the following section, SGS stress models are tested using data obtained using array 1.

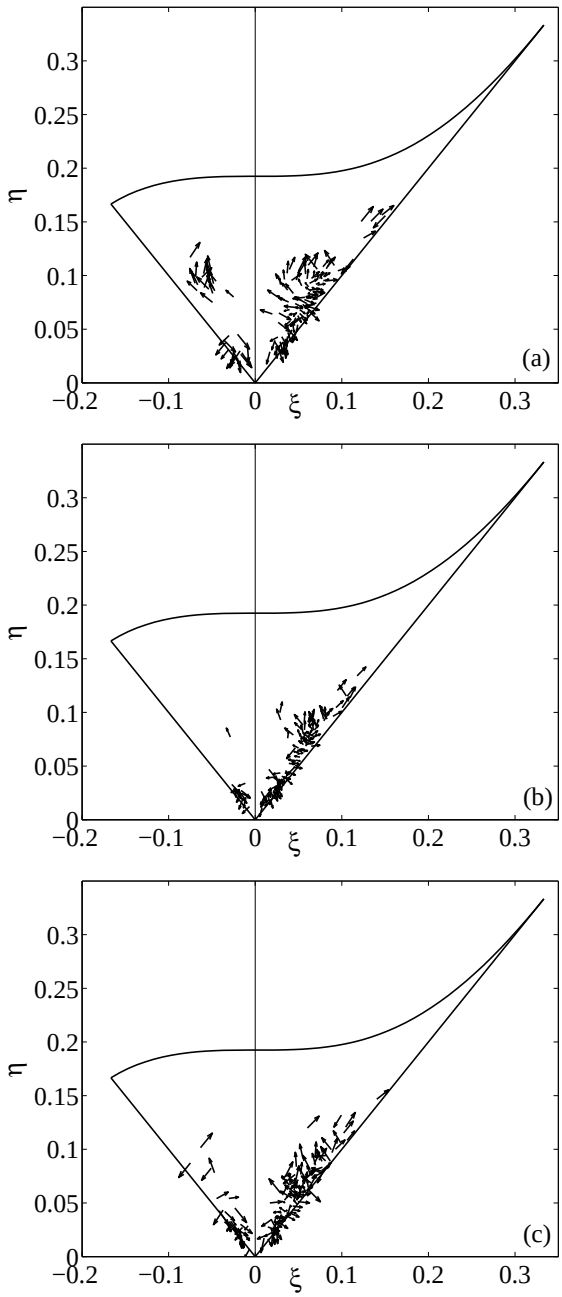

Figure 3.14 The Lumley triangle representation of the conditional SGS stress from other array configurations: (a) array 2 ($\Delta/z = 2.00, -z/L = 0.36$); (b) array 3 ($\Delta/z = 1.00, -z/L = 0.60$); (c) array 4 ($\Delta/z = 0.48, -z/L = 0.35$). The arrows represent the conditioning vector (u_1^r, u_3^r).

Table 3.5 Measured and modeled deviatoric SGS stress for array 1.

	$\langle\tau_{11}^d\rangle/u_*^2$	$\langle\tau_{12}\rangle/u_*^2$	$\langle\tau_{13}\rangle/u_*^2$	$\langle\tau_{22}^d\rangle/u_*^2$	$\langle\tau_{23}\rangle/u_*^2$	$\langle\tau_{33}^d\rangle/u_*^2$
τ_{ij}^d	0.79	-0.02	-0.73	-0.04	-0.06	-0.74
τ_{ij}^{smg}	0.02	-0.01	-0.34	0.02	0.01	-0.02
τ_{ij}^{n1}	1.15	-0.04	-0.13	-0.05	0.03	-1.10
τ_{ij}^{mix}	1.16	-0.04	-0.34	-0.03	0.04	-1.12
τ_{ij}^{n2}	0.39	-0.01	-0.33	0.17	0.01	-0.54

3.3 SGS stress model predictions

The necessary conditions for predicting the JPDF can be used to test SGS models. In this section, the model predictions of $\langle\tau_{ij}|\mathbf{u}^r\rangle$ and $\langle P_{ij}|\mathbf{u}^r\rangle$ are computed and compared to the experimental results for array 1 ($\Delta/z = 3.88, -z/L = 0.24$) presented in Section 3.2. The Smagorinsky model, the nonlinear model of Leonard (1974) [82], the mixed model ([18]), and the nonlinear model of Kosović (1997) [67] are considered. The average values of the measured and modeled mean deviatoric SGS stress components are given in Table 3.5.

3.3.1 Smagorinsky model

The Smagorinsky model is given by Smagorinsky (1963) [60], and Lilly (1967) [1].

$$\tau_{ij}^{smg} = -2\nu_T S_{ij} = -2(C_s\Delta)^2(2S_{mn}S_{mn})^{1/2}S_{ij}, \tag{3.18}$$

where $C_s = 0.154$ is the Smagorinsky constant for a box filter. In this work, C_s is determined by matching the mean energy transfer rate, i.e. $C_s = \langle P_{ii}^d\rangle / \langle P_{ii}^{smg}\rangle$.

The mean normal SGS stress components are severely under-predicted by the Smagorinsky model and the mean shear stress $\langle\tau_{13}^{smg}\rangle$ is under-predicted by a factor of two. The conditional mean of the model predictions, $\langle\tau_{ij}^{smg}|\mathbf{u}^r\rangle$ and $\langle P_{ij}^{smg}|\mathbf{u}^r\rangle$ is compared with the conditional mean of the deviatoric part of the SGS stress $\langle\tau_{ij}^d|\mathbf{u}^r\rangle$ obtained from the data, because the Smagorinsky model predicts only this part. The predicted normal components of the conditional SGS stress, $\langle\tau_{11}^{smg}|u_1^r, u_3^r\rangle$ (Figure 3.15 *a*) and $\langle\tau_{33}^{smg}|u_1^r, u_3^r\rangle$ (Figure 3.15 *c*) have weaker trends and smaller magnitudes compared with the measured $\langle\tau_{11}^d|u_1^r, u_3^r\rangle$ (Figure 3.4*a*) $\langle\tau_{33}^d|u_1^r, u_3^r\rangle$ (Figure 3.4*c*). The trends of the production term $\langle P_{11}^{smg}|u_1^r, u_3^r\rangle$ (Figures 3.16*a* vs. 3.6*a*) are predicted better than those of $\langle\tau_{11}|u_1^r, u_3^r\rangle$. However, the magnitudes are under-predicted (in addition to no conditional backscatter). Since correct prediction of $\langle P_{33}^d|\mathbf{u}^r\rangle$ is essential to reproduce the PDF of vertical resolvable-scale velocity, the results are plotted using u_3^r as the independent variable (Figure 3.17*a*). The magnitudes of $\langle P_{33}^d|u_1^r, u_3^r\rangle$ are under-predicted by a factor of two compared with measurements (Figure 3.17*b*), probably because the magnitude of the $\langle\tau_{33}^d|u_3^r\rangle$ is under-predicted by the model.

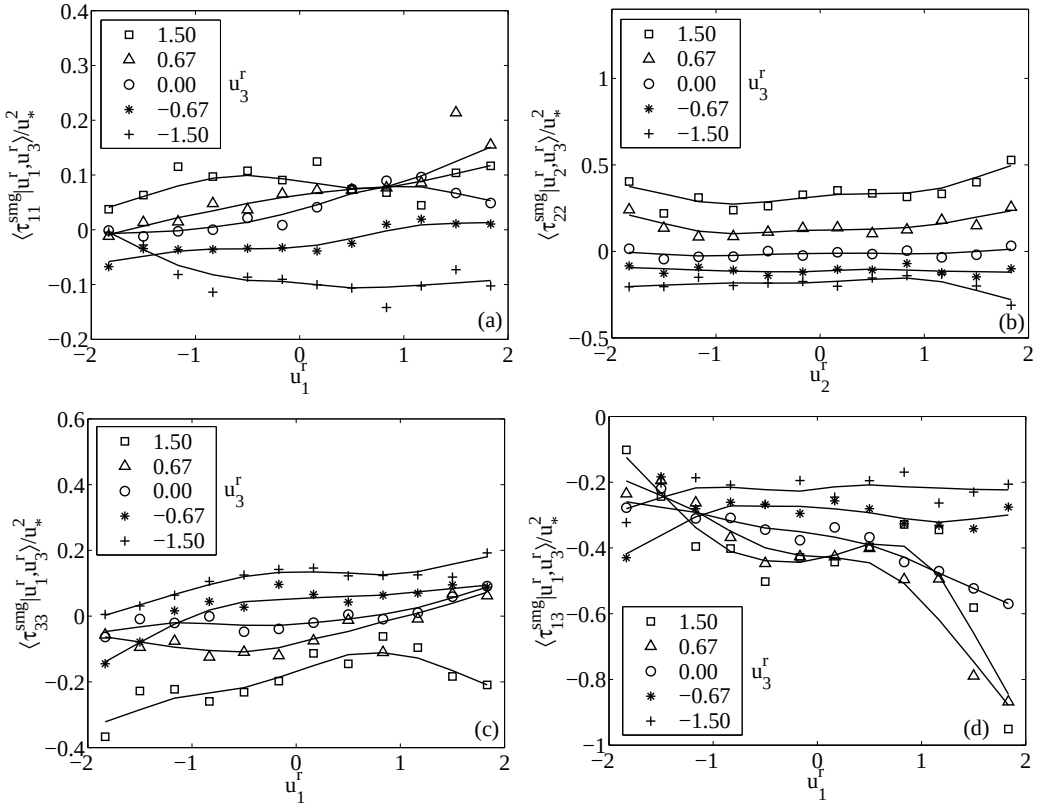

Figure 3.15 Predicted conditional SGS stress using the Smagorinsky model conditional on the resolvable-scale velocity. Only the trend of $\langle \tau_{13} | u_1^r, u_3^r \rangle$ is reasonably well predicted.

The trend of the SGS shear stress component $\langle \tau_{13}^{smg} | u_1^r, u_3^r \rangle$ (Figure 3.15*d*) compares reasonably well with $\langle \tau_{13} | u_1^r, u_3^r \rangle$ (Figure 3.4*d*). However, the magnitude is under-predicted by a factor of two. The corresponding production rate $\langle P_{13}^{smg} | u_1^r, u_3^r \rangle$ (Figures 3.16*b* vs. 9*a*) is poorly predicted both in terms of magnitude and trend. Therefore, it appears that the standard Smagorinsky model can predict the trends of some SGS shear stress components, but not the normal components, and can predict the trends of some normal components of conditional SGS stress production, but not the shear components. The magnitudes of these components are generally poorly predicted.

The Smagorinsky model predictions can be understood in terms of the surface-layer dynamics and the model ingredients. The results in Section 3.2 show that although the evolution (production) of $\langle \tau_{11}^d | u_1^r, u_3^r \rangle$ involves $\partial u_1^r/\partial x_1, \partial u_1^r/\partial x_2$ and $\partial u_1^r/\partial x_3$, the shear strain rate component $\partial u_1^r/\partial x_3$ has the most important contribution. However, $\langle \tau_{11}^{smg} | u_1^r, u_3^r \rangle$ is modeled using only $\partial u_1^r/\partial x_1$. Because $\partial u_1^r/\partial x_1$ and $\partial u_1^r/\partial x_3$ have very different behaviors in the surface-layer (not shown), neither the magnitude nor trend of $\langle \tau_{11}^{smg} | u_1^r, u_3^r \rangle$ are well predicted. The situation is similar

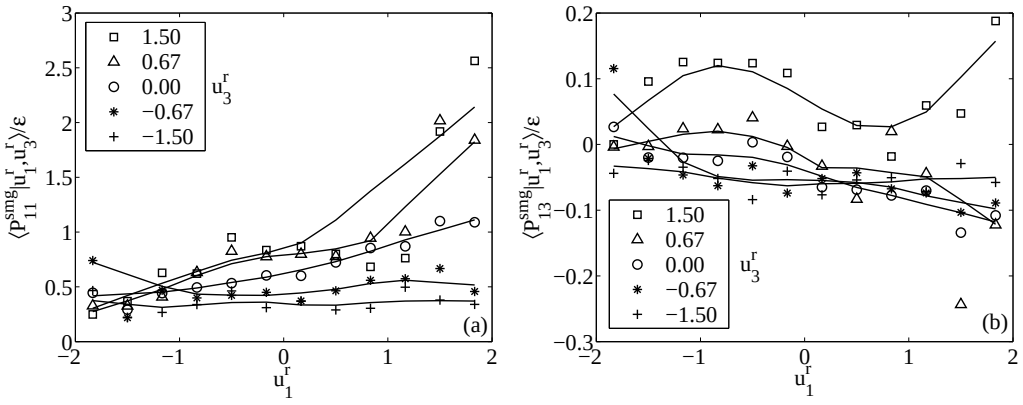

Figure 3.16 Predicted conditional SGS stress production using the Smagorinsky model conditional on the resolvable-scale velocity. Only the trend of $\langle P_{11}^d|u_1^r,u_3^r\rangle$ is reasonably well predicted.

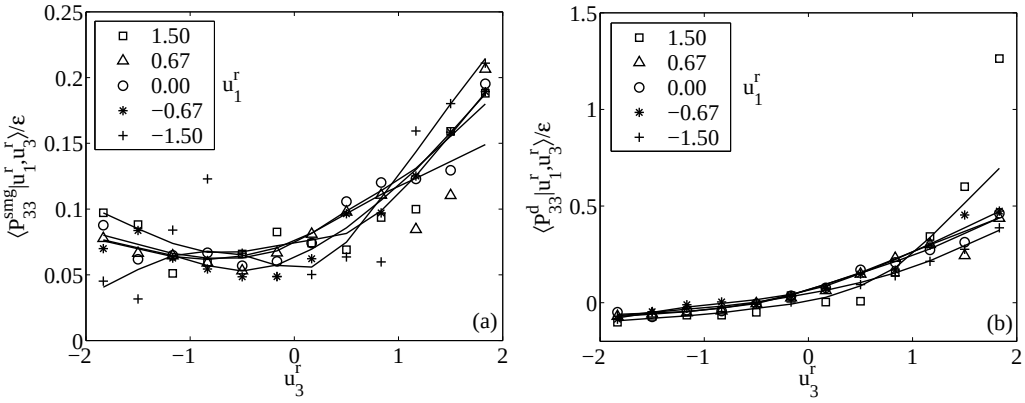

Figure 3.17 Predicted conditional SGS stress production of τ_{33} using the Smagorinsky model conditional on the resolvable-scale velocity.

for $\langle \tau_{22}^{smg}|u_2^r,u_3^r\rangle$. The normal component $\langle \tau_{33}^{smg}|u_1^r,u_3^r\rangle$ is also not predicted correctly because the model does not take into account of the influence of buoyancy. The predicted trend of $\langle \tau_{13}|u_1^r,u_3^r\rangle$ is somewhat better because the model uses $\partial u_1^r/\partial x_3$, which is also contained in P_{13}; however, because $\langle \tau_{13}^{smg}|\mathbf{u}^r\rangle$ does not include the effect of buoyancy, the magnitude is not predicted well.

The Smagorinsky model prediction of the anisotropy tensor is obtained by using the modeled $\langle \tau_{ij}^d|\mathbf{u}^r\rangle$ and the measured conditional SGS energy, i.e. it is assumed that the model for the SGS energy used in combination with the Smagorinsky model is accurate. The data points in Figure 3.18(a) are much closer to the origin than the results in Figure 3.13, indicating that the level of anisotropy is severely under-predicted. This is perhaps a reflection of the properties of the resolvable-scale strain rate tensor.

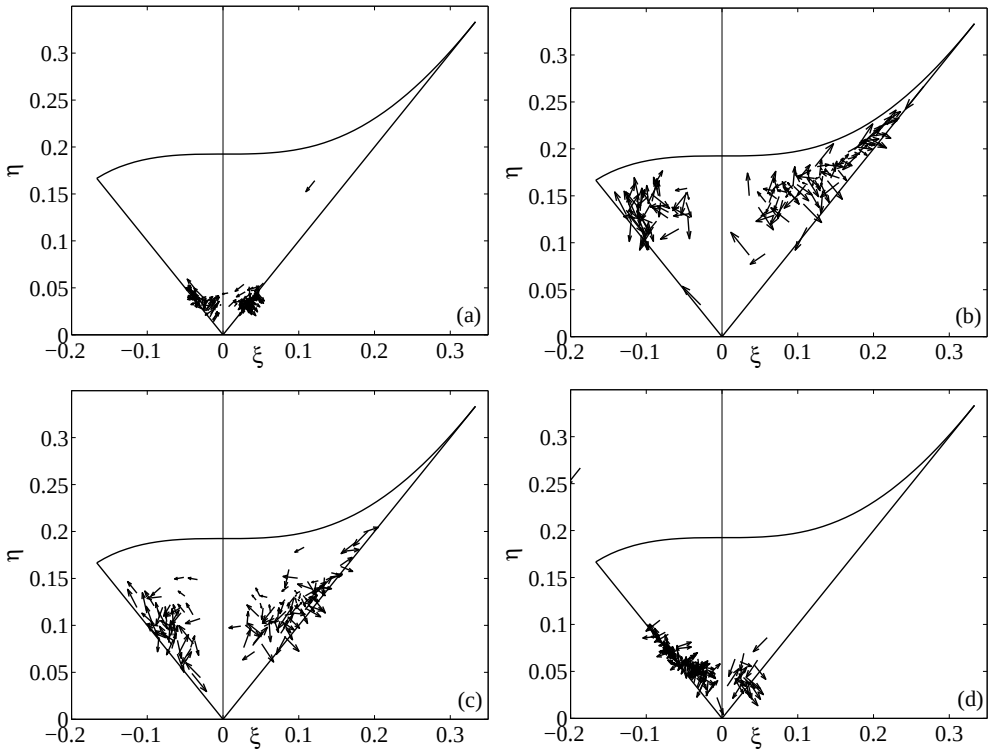

Figure 3.18 The Lumley triangle representation of the conditional SGS stress from SGS models: (a), the Smagorinsky model; (b), the Nonlinear model; (c), the deviatoric mixed model; (d), Kosović's nonlinear model. The arrows represent the conditioning vector (u_1^r, u_3^r)**.**

Another variation of the Smagorinsky model uses the SGS kinetic energy to obtain eddy viscosity ([65]), $\nu_T = C_e \Delta e^{1/2}$ (e is the SGS kinetic energy). This model has been used extensively in large-eddy simulation of the atmospheric boundary layer ([83, 84, 21]). The predictions of $\langle \tau_{ij} | \mathbf{u}^r \rangle$ and $\langle P_{ij} | \mathbf{u}^r \rangle$ are also computed using this model. The results are close to those given by (3.18), probably because they both use eddy viscosity and the resolvable-scale strain rate.

3.3.2 Nonlinear model

Bardina *et al.* (1980) [24] proposed a similarity model, which is based on the scale invariance of inertial-range turbulence. It assumes that the instantaneous SGS stress has similar structures at different scales. The model involves two filters with different filter sizes. Owing to the limitation of the array configuration, this double filtering cannot be performed to test the model. However, the data set allows to test the nonlinear model, which is the first-order approximation of the similarity

model ([82, 22]).

$$\tau_{ij}^{n1} = \frac{1}{12}\Delta^2 \frac{\partial u_i^r}{\partial x_k}\frac{\partial u_j^r}{\partial x_k}, \tag{3.19}$$

The nonlinear model under-predicts the energy transfer rate by a factor of two and the SGS kinetic energy by 23% ($\langle \tau_{kk}^{n1} \rangle / u_*^2 = 4.29$ vs. $\langle \tau_{kk} \rangle / u_*^2 = 6.27$). The normal mean SGS stress components are generally under-predicted (can be obtained from Table 3.5), but their deviatoric parts are over-predicted (Table 3.5). The conditional SGS stress component $\langle \tau_{11}^{n1} | u_1^r, u_3^r \rangle$ (Figure 3.19(a) and $\langle \tau_{22}^{n1} | u_2^r, u_3^r \rangle$ (not shown) are only slightly under-predicted whereas $\langle \tau_{33}^{n1} | u_1^r, u_3^r \rangle$ (not shown) are under-predicted by a factor of two. The model also predicts the SGS shear stress $\langle \tau_{13}^{n1} | u_1^r, u_3^r \rangle$ poorly both in terms of the trend and magnitude. On the other hand, the trends for the conditional SGS stress production rate components are predicted quite well ($\langle P_{11}^{n1} | u_1^r, u_3^r \rangle$ is shown in Figure 3.19(b)). Their magnitudes are under-predicted by a factor of two except that of $\langle P_{22}^{n1} | u_2^r, u_3^r \rangle$. Matching the mean energy transfer rate by changing the model coefficient improves the predictions for $\langle P_{ij} | \mathbf{u}^r \rangle$, but causes the magnitude of the conditional SGS stress to be over-predicted. Therefore, the nonlinear model also cannot predict the conditional SGS stress and its production rate at the same time.

The nonlinear model predictions can also be understood in terms of the model ingredients and the production of the SGS stress. Because $\langle \tau_{11}^{n1} | \mathbf{u}^r \rangle$ involves $\partial u_1^r/\partial x_1, \partial u_1^r/\partial x_2$, and $\partial u_1^r/\partial x_3$, which also appear in $\langle P_{11} | u_1^r, u_3^r \rangle$, its trend is better predicted. The situation is similar for $\langle \tau_{22}^{n1} | u_2^r, u_3^r \rangle$. The modeled component $\langle \tau_{33}^{n1} | u_1^r, u_3^r \rangle$ does not include the dominant influence of buoyancy, thus, $\langle \tau_{33} | u_1^r, u_3^r \rangle$ is poorly predicted. Although $\langle \tau_{13}^{n1} | u_1^r, u_3^r \rangle$ involves $\partial u_1^r/\partial x_3$, it is also related to $\partial u_1^r/\partial x_1$ and $\partial u_3^r/\partial x_3$ which are likely to introduce spurious dependence on $\mathbf{u}^r$, therefore, $\langle \tau_{13} | u_1^r, u_3^r \rangle$ is also poorly predicted (Figure 3.19c).

Unlike the Smagorinsky model, the nonlinear model (Figure 3.18b) over-predicts the level of anisotropy. The results are still close to either $\eta = -\xi$ or $\eta = \xi$, i.e. axisymmetric with one small or large eigenvalue, but are much closer to the two-component axisymmetric or the one-component limits. The lowest predicted level of anisotropy is comparable to the highest measured level. These trends perhaps occur because the nonlinear model contains the resolvable-scale rotation tensor, and therefore contains the effects of the mean rotation.

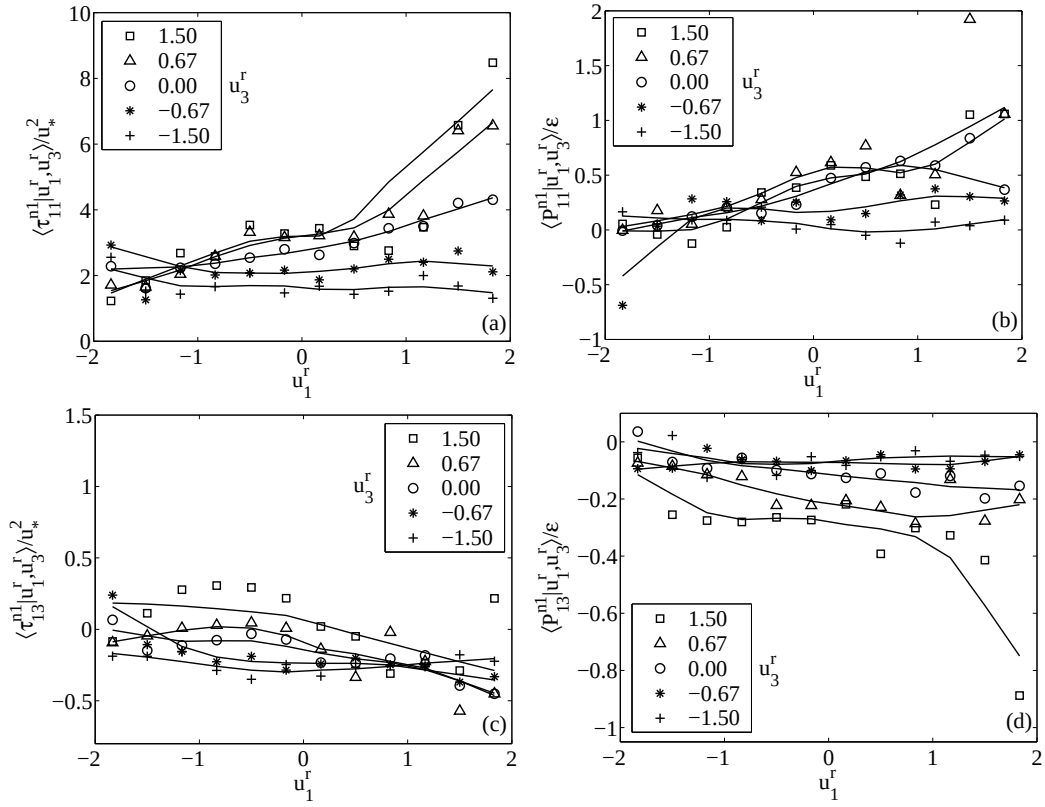

Figure 3.19 Predicted conditional SGS stress and conditional SGS stress production using the nonlinear model conditional on the resolvable-scale velocity. Both $\langle \tau_{11} | u_1^r, u_3^r \rangle$ and $\langle P_{11} | u_1^r, u_3^r \rangle$ are reasonably well predicted.

3.3.3 The mixed model

The above results show that the Smagorinsky model and the nonlinear model under- and over-predict the anisotropy of the conditional SGS stress, respectively. Thus, a mixed model combining these two models (the term, mixed model, is originally used as the combination of the similarity model and Smagorinsky model):

$$\tau_{ij}^{mix} = \frac{1}{12}\Delta^2 \frac{\partial u_i^r}{\partial x_k}\frac{\partial u_j^r}{\partial x_k} - 2(C_s\Delta)^2(2S_{mn}S_{mn})^{1/2}S_{ij} \tag{3.20}$$

can potentially provide improved predictions. The results of Vreman *et al.* (1997) [18] show that this model is better than that of the nonlinear model or Smagorinsky model alone in the large-eddy simulation of a turbulent mixing layer. Here this model are also tested. The model coefficient C_s is determined by matching the mean energy transfer rate, i.e. letting $\langle P_{ii} \rangle = \langle P_{ii}^{mix} \rangle$. The results show that the normal components of SGS stress, $\langle \tau_{11} | u_1^r, u_3^r \rangle$ and $\langle \tau_{22} | u_2^r, u_3^r \rangle$, and their production rate, $\langle P_{11} | u_2^r, u_3^r \rangle$ and $\langle P_{22} | u_2^r, u_3^r \rangle$, are generally predicted well. However, the vertical components of

$\langle \tau_{ij}|u_1^r, u_3^r\rangle$ and $\langle P_{ij}|u_1^r, u_3^r\rangle$ are under-predicted. For example, comparisons between Figures 3.20(a) and 4(d) and between Figures 3.20(b) and 3.5(d) show that $\langle \tau_{13}|u_1^r, u_3^r\rangle$ and $\langle P_{13}|u_1^r, u_3^r\rangle$ are under-predicted. The anisotropy (not shown) is very similar to that of the nonlinear model. Therefore, a linear combination of the nonlinear model and the Smagorinsky model does not significantly improve the predicted conditional means. A problem for this mixed model is that the nonlinear model predicts the total SGS stress, but the Smagorinsky model predicts only the deviatoric part. This suggests that a combination of the deviatoric part of the nonlinear model and the Smagorinsky model might be useful. Therefore, the mixed model is rewritten as:

$$\tau_{ij}^{mix} = \frac{1}{12}\Delta^2 \left\{ \frac{\partial u_i^r}{\partial x_k}\frac{\partial u_j^r}{\partial x_k} - \frac{1}{3}\frac{\partial u_m^r}{\partial x_k}\frac{\partial u_m^r}{\partial x_k}\delta_{ij} \right\} - 2(C_s\Delta)^2(2S_{mn}S_{mn})^{1/2}S_{ij}. \tag{3.21}$$

The deviatoric mixed model not only predicts well the normal components of SGS stress, $\left\langle \tau_{11}^d|u_1^r, u_3^r\right\rangle$ and $\left\langle \tau_{22}^d|u_2^r, u_3^r\right\rangle$, and their production rates, $\left\langle P_{11}^d|u_1^r, u_3^r\right\rangle$ and $\left\langle P_{22}^d|u_2^r, u_3^r\right\rangle$, but also predicts well $\left\langle \tau_{33}^d|u_1^r, u_3^r\right\rangle$ (Figure 3.21a) and $\left\langle P_{33}^d|u_1^r, u_3^r\right\rangle$ (Figure 3.21b), which are under-predicted by the original mixed model. The SGS shear stress production $\left\langle P_{13}^{mix}|u_1^r, u_3^r\right\rangle$ (Figure 3.21c) is also better predicted than that in Figure 3.20(b). Unfortunately, $\langle \tau_{13}|\mathbf{u}^r\rangle$ (identical to the mixed model prediction shown in Figure 3.20a) remains to be improved, which is a very important component for LES in the surface layer. The predicted anisotropy (Figure 3.18c) using the deviatoric mixed model is stronger than measurements, but is improved over that of the nonlinear model. The mixed model over-predicts the (intrinsic) anisotropy, but under-predicts $\langle \tau_{13}|u_1^r, u_3^r\rangle$, suggesting that the directions of the principal axes of $\langle \tau_{ij}|u_1^r, u_3^r\rangle$ are not predicted well. This is in contrast to the Smagorinsky model which under-predicts both. It is also experimented by changing the ratio of the two model coefficients (strictly speaking, the coefficient for the nonlinear part is fixed by the filter type) with little effect on the anisotropy.

It is interesting to note that another type of cancelation between the Smagorinsky model and the similarity model ([24]) was observed by Liu *et al.* (1999) [85] in rapidly strained homogeneous turbulence. There, the under-prediction by the Smagorinsky model and the over-prediction by the similarity model of the mean spectral energy transfer rate during straining were partially canceled when a mixed model was used. Therefore, it appears that various kinds of opposing trends of the Smagorinsky model and the similarity (and nonlinear) model can be partially canceled by using a mixed model.

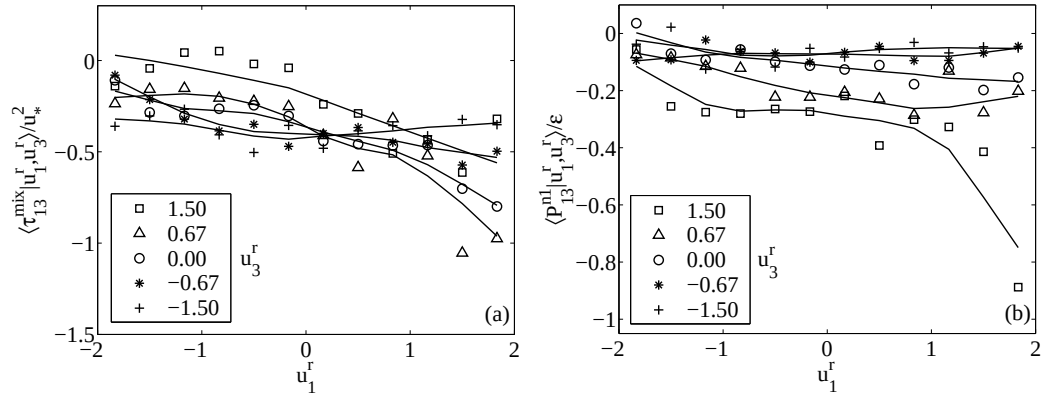

Figure 3.20 Predicted conditional shear SGS stress $\langle \tau_{13} | u_1^r, u_3^r \rangle$ and the conditional production $\langle P_{13} | u_1^r, u_3^r \rangle$ using mixed model conditional on the resolvable-scale velocity.

3.3.4 Kosović's nonlinear model

Kosović (1997) [67] proposed another nonlinear model:

$$\tau_{ij}^{n2} = -(C_s\Delta)^2 \Big\{ 2(2S_{mn}S_{mn})^{1/2} S_{ij} + C_1 (S_{ik}S_{kj} - \frac{1}{3} S_{mn}S_{mn}\delta_{ij}) + C_2 (S_{ik}\Omega_{kj} - \Omega_{ik}S_{kj}) \Big\}. \tag{3.22}$$

where C_s, C_1 and C_2 are model constants, which are determined here by matching the mean energy transfer rate, i.e. letting $\langle P_{ii}^d \rangle = \langle P_{ii}^{n2} \rangle$ while maintaining the ratios of their original values in Kosović [67]. The first part of this model is essentially the Smagorinsky model. By setting $C_2 = 0$, this model is essentially the deviatoric mixed model. A comparison between the results of this model (results not shown) and the deviatoric mixed model shows that the latter predicts $\langle \tau_{13} | u_1^r, u_3^r \rangle$ (Figure 3.22) better, but the rest of the components of the conditional SGS stress and the conditional SGS stress production are less well predicted. Therefore, this nonlinear model has a somewhat more balanced overall performance. Like the Smagorinsky model, this nonlinear model under-predicts the magnitude of the conditional SGS stress (by approximately 50%) when the mean energy transfer is matched. It is probably because the Smagorinsky model over-predicts the correlation between the SGS stress and the strain rate. The level of anisotropy of $\langle \tau_{ij} | u_1^r, u_3^r \rangle$ (Figure 3.18*d*) is also under-predicted, but the prediction is improved over that of the Smagorinsky model.

3.4 Effects of SGS model deficiencies on LES results

The measured conditional SGS stress and the SGS stress production and the model predictions can be used to identify model deficiencies that cause inaccuracies in LES results. Previous studies have shown that the Smagorinsky model over-predicts the mean shear and the streamwise

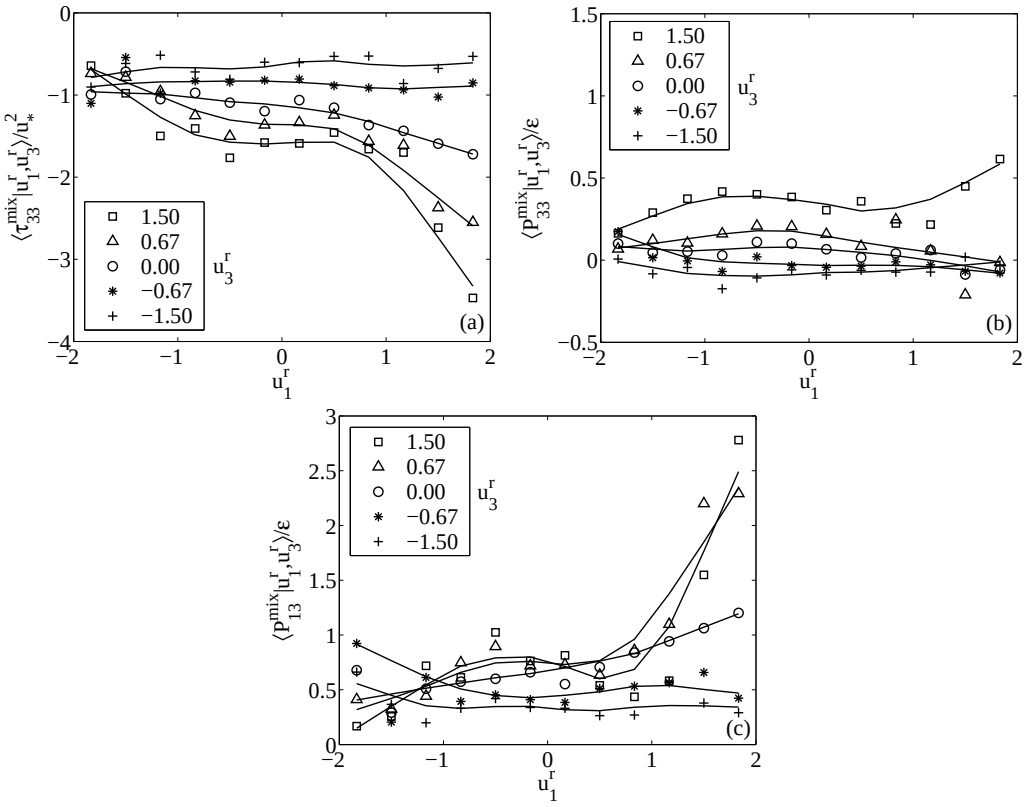

Figure 3.21 Predicted conditional SGS stress and conditional SGS stress production using the deviatoric mixed model conditional on the resolvable-scale velocity. Note that the predicted $\langle \tau_{13} | u_1^r, u_3^r \rangle$ is identical to that of the mixed model.

velocity variance near the surface ([8, 10]). It is argued that these inaccuracies are at least partly due to the under-prediction of the anisotropy of the SGS stress and its variations in the near-wall region. In the atmospheric boundary layer (ABL) the vertical shear stress component is determined by the geostrophic conditions and the mean shear ([86, 9]), which are a combination of the large-scale pressure gradient and the Coriolis force, therefore a simulation tends to adjust itself to satisfy these conditions. Because the anisotropy of the SGS stress (Figure 3.13) is under-predicted, the simulation must generate a larger strain rate to produce the correct SGS shear stress, thereby over-predicting the mean shear. In addition, the larger strain rate will cause over-prediction of the production of the streamwise velocity variance, $-\langle u_1^{r\prime} u_3^{r\prime} \rangle \frac{\partial U_1}{\partial x_3}$, therefore the streamwise velocity variance itself, where $u_i^{r\prime}$ is the fluctuation of u_i^r. Furthermore, the conditional variations of the anisotropy (the SGS shear stress) are also severely under-predicted, further reducing the transfer of the streamwise velocity variance to the subgrid-scales.

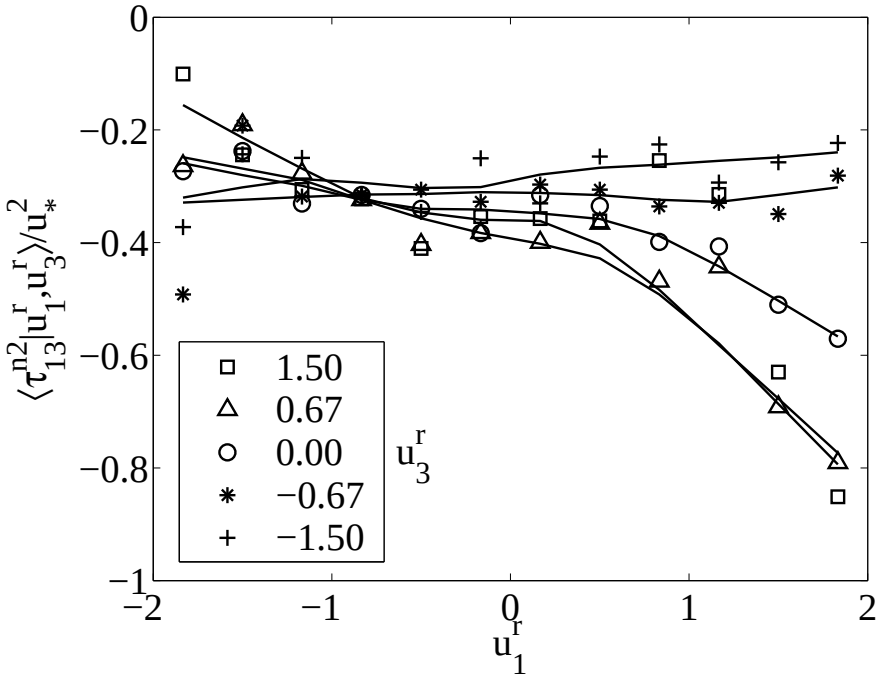

Figure 3.22 Predicted conditional shear SGS stress $\langle \tau_{13} | u_1^r, u_3^r \rangle$ using Kosović's nonlinear model conditional on the resolvable-scale velocity, which is improved over the mixed model.

The stochastic backscatter model of Mason and Thomson (1992) [8] introduces additional energy (on average) into the resolvable scales through random forcing, at the same time increasing the dissipation by eddy viscosity to maintain the energy balance. In doing so, the model is able to predict τ_{13} and anisotropy better without generating an excessive strain rate. In the split model of Sullivan *et al.* (1994) [10], an increasing part of τ_{13} is produced by the mean shear as the surface is approached; therefore the results are less affected by the inability of the Smagorinsky model to predict the anisotropy. The nonlinear model of Kosović [67] is also capable of producing a higher level of anisotropy (Figure 3.18*d*) and gives improved LES results. Therefore, it appears that the anisotropy of the SGS stress is important for the correct prediction of the mean shear and the streamwise velocity variance.

Another important surface-layer statistic is the vertical velocity skewness, which is underpredicted by LES using the Smagorinsky model ([87, 88]). This can be examined by considering the conditional SGS stress $\langle \tau_{33} | u_3^r \rangle$ and the SGS stress production $\langle P_{33} | u_3^r \rangle$, which appear in the

equation for the resolvable-scale vertical velocity PDF

$$\frac{\partial f_{u_3^r}}{\partial t} + v_3 \frac{\partial f_{u_3^r}}{\partial x_3} = \frac{\partial^2}{\partial v_3 \partial x_3} \left\{ \langle \tau_{33} |\, u_3^r = v_3 \rangle\, f_{u_3^r} \right\} + \frac{\partial^2}{\partial v_3 \partial v_3} \left\{ -\frac{1}{2} \langle P_{33} |\, u_3^r = v_3 \rangle\, f_{u_3^r} \right\} + \frac{\partial^2}{\partial v_3 \partial x_3} \left\{ \langle p^r |\, u_3^r = v_3 \rangle\, f_{u_3^r} \right\} + \frac{\partial^2}{\partial v_3 \partial v_3} \left\{ \left\langle p^r \frac{\partial u_3^r}{\partial x_3} \middle|\, u_3^r = v_3 \right\rangle f_{u_3^r} \right\} - \frac{g}{\Theta} \frac{\partial}{\partial v_3} \left\{ \langle \theta^r |\, u_3^r = v_3 \rangle\, f_{u_3^r}, \right\} \tag{3.23}$$

where $f_{u_3^r} = \langle \delta(u_3^r - v_3) \rangle$. The mixed transport terms due to the conditional SGS stress and the resolvable-scale pressure are expected to diminish with the filter scale, whereas the terms due to the conditional pressure-strain correlation and the conditional SGS stress production are expected to be invariant for inertial-range filter scales.

The pressure-strain correlation is associated with return to isotropy and partially counters the production. Therefore, the dominant term in the equation is expected to be the conditional SGS stress production. In a quasi-stationary and horizontally homogeneous ABL there is a balance primarily among advection, transport due to conditional pressure-strain correlation, and transport due to the conditional SGS stress production. Sabelnikov (1998) [40] analysed the PDF equation for scalar fluctuations generated by a constant mean scalar gradient and stationary isotropic turbulence and provided a self-similar relationship between the scalar PDF and the conditional scalar dissipation, which plays a similar role to P_{33} in equation (3.23). He showed that for a conditional dissipation independent of the scalar value, the scalar PDF is Gaussian. If the conditional dissipation increases with the scalar fluctuations, the PDF is super-Gaussian and vice versa. Because of the similarities between equation (3.23) and the scalar PDF transport equation, these trends are expected to hold qualitatively for equation (3.23). Therefore, there exists a direct link between the resolvable-scale vertical velocity PDF and $\langle P_{33} | u_3^r \rangle$ for a stationary ABL. Physically, to maintain a longer (or higher) tail of the PDF, the SGS turbulence must extract more energy from the resolvable scales when the velocity fluctuations are large. Figure 3.17(b) shows that the measured $\langle P_{33} | \mathbf{u}^r \rangle$ increases with u_3^r, therefore is asymmetric with respect to u_3^r. Consequently, the positive side of $f_{u_3^r}$ is higher than the negative side, resulting in a positive skewness. On the other hand, the prediction of the Smagorinsky model is much less dependent on u_3^r, and consequently will result in a smaller skewness. Therefore, the under-prediction of the vertical velocity skewness is probably due to the inability of the model to predict the asymmetry in $\langle P_{33} | u_3^r \rangle$. The specific model deficiencies identified here can be used to guide development of improved SGS models that will correctly predict these statistics. The analyses in this section and Section 3.2 can serve as examples for studying aspects of SGS turbulence and SGS models that are important for specific applications.

It is noted that previous *a priori* tests, especially those correlating the modeled to the true SGS stress, have provided little information about how SGS models will perform in a simulation. For example, the Smagorinsky model has very low correlation coefficients with the true SGS stress, but performs quite well in LES of isotropic turbulence while the similarity model correlates well with the true stress, but may cause simulations to become unstable. The difficulty in interpreting *a priori* test results and model performance in simulations is partly because there is no equation relating the tests results to LES statistics. In addition, owing to the chaotic nature of the LES equations, a high (unless perfect) correlation between the modeled and true SGS stress cannot guarantee accurate LES statistics. Another problem of these *a priori* tests is that they focused solely on the SGS stress whereas equation (3.4) shows that the SGS stress production rate is also important. In the case of homogeneous turbulence, the influence of the conditional SGS stress vanishes. In such flows, the conditional mean SGS energy transfer rate (near the mean velocity) plays an dominant role in determining the lower-order LES statistics. Therefore, the Smagorinsky, whose coefficient is determined by matching the inertial-range energy transfer rate to the theoretical values, performs quite well in LES of homogeneous turbulence with a well-resolved energy-containing range despite the low correlation with the true SGS stress. On the other hand, the similarity model under-predicts the (mean and conditional) energy transfer rate, therefore does not perform well (in fact might not be used alone) despite its relatively high correlation with the true SGS stress. In inhomogeneous flows, both the conditional SGS stress and the conditional SGS stress production rate are important. The mixed model makes use of the abilities of the Smagorinsky model to predict the mean energy transfer and of the similarity model to predict the SGS stress, resulting in improved performance. Therefore, *a priori* tests based on the JPDF equation differ fundamentally from the traditional tests and can provide valuable information about model performance.

3.5 Further analyses of $\langle \tau_{ij} | \mathbf{u}^r \rangle$ and $\langle P_{ij} | \mathbf{u}^r \rangle$

The results in the present study for the conditional SGS stress $\langle \tau_{ij} | \mathbf{u}^r \rangle$ and conditional SGS stress production rate $\langle P_{ij} | \mathbf{u}^r \rangle$ show that there are similarities between their trends. The deviatoric parts of $\langle \tau_{ij} | \mathbf{u}^r \rangle$ and $\langle P_{ij} | \mathbf{u}^r \rangle$ (not shown) also have similar dependence on $\mathbf{u}^r$. Wyngaard (1992) [9] showed that the Reynolds shear stress budget in the unstable surface layer is generally in local balance among shear production, buoyancy production, and pressure destruction, whereas turbulent transport is negligible. The (slow) pressure destruction term is usually modeled using Rotta (1951)'s

[89] "return-to-isotropy" model,

$$\frac{1}{\rho_0}\left\langle u_i\frac{\partial p}{\partial x_j}+u_j\frac{\partial p}{\partial x_i}\right\rangle \sim \frac{\langle u_iu_j\rangle-\frac{1}{3}\langle u_ku_k\rangle\delta_{ij}}{t_l} \tag{3.24}$$

where t_l is a time scale, which is of the order of the integral time scale. Therefore, it may be expected some similarities between $\langle u_iu_j\rangle$ and the combination of the shear and buoyancy production. Wyngaard (2004) [58] suggests that the balance between the SGS stress and the production can be given as

$$\frac{\tau_{ij}^{mod}}{t_\Delta}=P_{ij}^a \tag{3.25}$$

where t_Δ is a turbulent time scale and $P_{ij}^a = P_{ij}-\frac{1}{3}P_{kk}\delta_{ij}$ is the anisotropic part of the SGS stress production tensor. Because P_{ij}^a contains τ_{ij}, this relationship could potentially be used as an algebraic SGS model. To investigate this potential, the geometric alignment and eigenvalue relationship between $\left\langle\tau_{ij}^d|\mathbf{u}^r\right\rangle$ and $\left\langle P_{ij}^a|\mathbf{u}^r\right\rangle$ is studied. The effects of advection $u_k^r\frac{\partial\tau_{ij}^d}{\partial x_k}$ and buoyancy can also be analyzed by adding corresponding terms to the right-hand side of (3.25).

The eigenvalues of the conditional SGS stress tensor, $\left\langle\tau_{ij}^d|\mathbf{u}^r\right\rangle$, are denoted as α_τ,β_τ and γ_τ, ordered such that $\alpha_\tau\geq\beta_\tau\geq\gamma_\tau$, and the corresponding unit eigenvectors as $\vec{\alpha}_\tau,\vec{\beta}_\tau$ and $\vec{\gamma}_\tau$. Similarly, the eigenvalues of the conditional SGS stress production tensor, $\left\langle P_{ij}^a|\mathbf{u}^r\right\rangle$, are denoted as α_P,β_P and γ_P, ordered such that $\alpha_P\geq\beta_P\geq\gamma_P$, and the corresponding unit eigenvectors as $\vec{\alpha}_P,\vec{\beta}_P$ and $\vec{\gamma}_P$. In order to characterize the geometric alignment between the eigenvectors of $\left\langle\tau_{ij}^d|\mathbf{u}^r\right\rangle$ and $\left\langle P_{ij}^a|\mathbf{u}^r\right\rangle$, three angles, θ,ϕ and ξ, are defined as $\theta=\cos^{-1}(|\vec{\gamma}_P\cdot\vec{\gamma}_\tau|)$ (the angle between $\vec{\gamma}_P$ and $\vec{\gamma}_\tau$), $\phi=\cos^{-1}(|\vec{\beta}_P\cdot\vec{\beta}_\tau|)$, and $\xi=\cos^{-1}(|\vec{\alpha}_P\cdot\vec{\alpha}_\tau|)$.

The geometric alignment results for $\left\langle\tau_{ij}^d|\mathbf{u}^r\right\rangle$ and $\left\langle P_{ij}^a|\mathbf{u}^r\right\rangle$ are shown in Figure 3.23. For, $\left\langle\tau_{ij}^d|u_1^r\right\rangle$ and $\left\langle P_{ij}^a|u_1^r\right\rangle$, the values of θ,ϕ and ξ are generally less than 10° and weakly depend on u_1^r, indicating very good alignment. Figure 3.23(b) shows that $\left\langle\tau_{ij}^d|u_3^r\right\rangle$ and $\left\langle P_{ij}^a|u_3^r\right\rangle$ are aligned well when u_3^r is positive but are less well aligned when u_3^r is negative. Because $\langle\tau_{ij}|\mathbf{u}^r\rangle$ is much less anisotropic and $\left\langle\tau_{ij}^d|u_3^r\right\rangle$ and $\left\langle P_{ij}^a|u_3^r\right\rangle$ are small when u_3^r has large negative values, the alignment angles are less well defined.

The effects of advection and buoyancy on the conditional SGS stress are also examined by including these terms in the alignment calculation. The alignment results for $\left\langle\tau_{ij}^d|\mathbf{u}^r\right\rangle$ and $\left\langle P_{ij}^a+A_{ij}^a|\mathbf{u}^r\right\rangle$ and $\left\langle P_{ij}^a+P_{Bij}^a|\mathbf{u}^r\right\rangle$ are also computed, where A_{ij}^a is the advection term of τ_{ij}^d and $P_{Bij}^a=P_{Bij}-\frac{1}{3}P_{Bkk}\delta_{ij}$. The trends and the magnitudes of the alignment angles (not shown) are very close to those shown Figure 3.23. Therefore, introducing the advection term and the buoyancy production generally has a negligible effect on the geometric alignment.

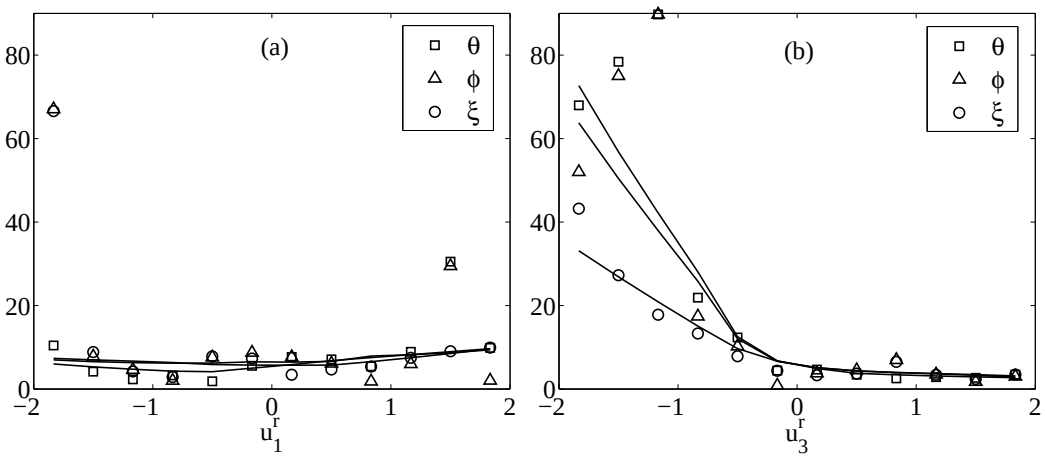

Figure 3.23 Geometric alignment of the measured conditional SGS stress and the conditional SGS stress production conditional on (a), u_1^r and (b), u_3^r. The alignment angles are small for positive u_3^r and increases for negative u_3^r but depends weakly on u_1^r.

The eigenvalues of $\langle \tau_{ij}^d | u_1^r \rangle$ and $\langle \tau_{ij}^d | u_3^r \rangle$ conditional on u_1^r and u_3^r are shown in Figure 3.24. The eigenvalues α_τ and γ_τ generally depend on u_1^r and u_3^r, and the magnitudes generally increase with u_1^r and u_3^r, indicating that the SGS turbulence is more anisotropic when both u_1^r and u_3^r are positive. The magnitude of α_β is generally small and weakly depends on u_1^r and u_3^r. In order to characterize the eigenvalue relationship between $\langle \tau_{ij}^d | \mathbf{u}^r \rangle$ and $\langle P_{ij}^a | \mathbf{u}^r \rangle$, the ratio of α_τ/α_P and γ_τ/γ_P conditional on u_1^r and u_3^r are plotted in Figures 3.25(a) and 3.25(b), respectively. The ratio of eigenvalue β_τ and β_P is not shown because both of them are small. The ratios α_τ/α_P and γ_τ/γ_P depend both on u_1^r and u_3^r, and the dependence on u_1^r is generally weaker than on u_3^r. The eigenvalue ratios of $\langle \tau_{ij}^d | \mathbf{u}^r \rangle$ and $\langle P_{ij}^a + A_{ij}^a | \mathbf{u}^r \rangle$ are also computed (not shown). The results are similar to those in Figure 3.25(a, b) because the magnitude of the advection is small. The eigenvalue ratios of $\langle \tau_{ij}^d | \mathbf{u}^r \rangle$ and $\langle P_{ij}^a + P_{Bij}^a | \mathbf{u}^r \rangle$ conditional on u_1^r are shown in Figure 3.25(c) and are not significantly different from those in Figure 3.25(a) which depend on u_1^r. The results of $\langle P_{ij}^a + P_{Bij}^a + A_{ij}^a | \mathbf{u}^r \rangle$ are close to the results of $\langle P_{ij}^a + P_{Bij}^a | \mathbf{u}^r \rangle$ (not shown). The effects of buoyancy production are somewhat surprising considering that plays an important role in the production of τ_{13} and τ_{33}.

The overall similarity between $\langle \tau_{ij}^d | \mathbf{u}^r \rangle$ and $\langle P_{ij}^a | \mathbf{u}^r \rangle$ can be quantified using their contraction,

$$\langle \tau_{ij}^d | \mathbf{u}^r \rangle : \langle P_{ij}^a | \mathbf{u}^r \rangle = \frac{\langle \tau_{ij}^d | \mathbf{u}^r \rangle \langle P_{ij}^a | \mathbf{u}^r \rangle}{| \langle \tau_{ij}^d | \mathbf{u}^r \rangle | | \langle P_{ij}^a | \mathbf{u}^r \rangle |}. \tag{3.26}$$

If the two tensors are perfectly aligned and their eigenvalues are proportional, the contraction has the value of one. The results in Figure 3.26(a) show that the $\langle \tau_{ij}^d | u_1^r \rangle : \langle P_{ij}^a | u_1^r \rangle$ is close to one and

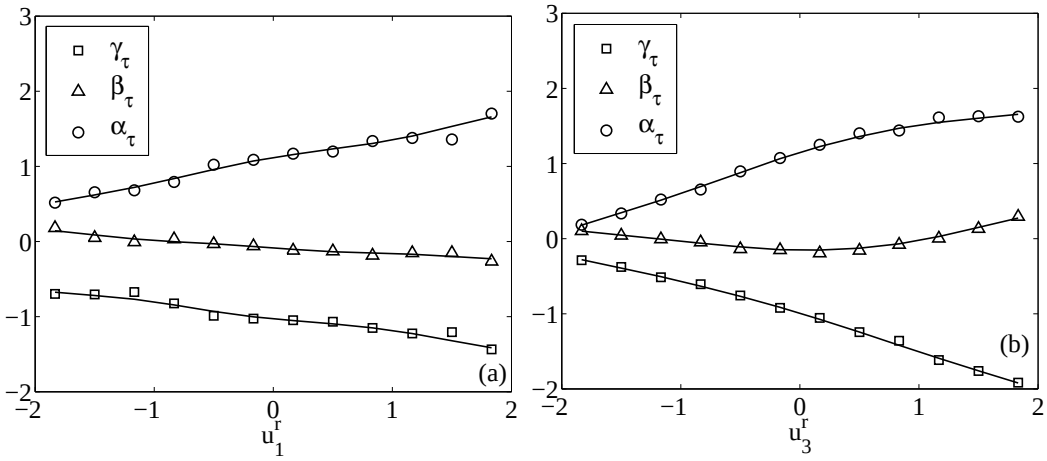

Figure 3.24 Eigenvalues of the conditional SGS stress conditional on (a), u_1^r and (b), u_3^r. The magnitudes of the eigenvalues increase with the resolvable-scale velocity.

weakly depends on u_1^r. The values in Figure 3.26(b) are also close to one and weakly depend on u_3^r when u_3^r is positive, but decrease with increasing magnitude of u_3^r when u_3^r is negative. Again, for negative u_3^r the eigenvalues of $\langle \tau_{ij}^d | u_3^r \rangle$ and $\langle P_{ij}^a | u_3^r \rangle$ are generally small and $\langle \tau_{ij}^d | u_3^r \rangle$ is less anisotropic, thus the alignment results are less well defined. The results also show that including the advection term has little effect on the contraction. However, including the buoyancy production rate causes the contraction to decrease and results in a stronger dependence on u_3^r. From a modeling point of view, because both $\langle \tau_{ij}^d | \mathbf{u}^r \rangle$ and $\langle P_{ij}^a | \mathbf{u}^r \rangle$ are small for negative u_3^r, it is probably more important to model correctly their magnitudes than their orientations.

3.6 Summary

In the present study, field measurements data taken in the convective atmospheric boundary layer are used to analyse the subgrid-scale turbulence. The necessary conditions for LES to predict correctly the one-point resolvable-scale velocity JPDF are that the SGS model reproduces the conditional means of the SGS stress and the SGS stress production rate. The conditions highlight the importance of the conditional energy transfer from the resolvable to the subgrid scales and the production rate of SGS shear stress.

Analyses of the conditional SGS stress and the conditional SGS stress production using the field data show that they are closely related to the surface-layer dynamics. Specifically, the updrafts generated by buoyancy, the downdrafts associated with the large-scale convective eddies, the mean

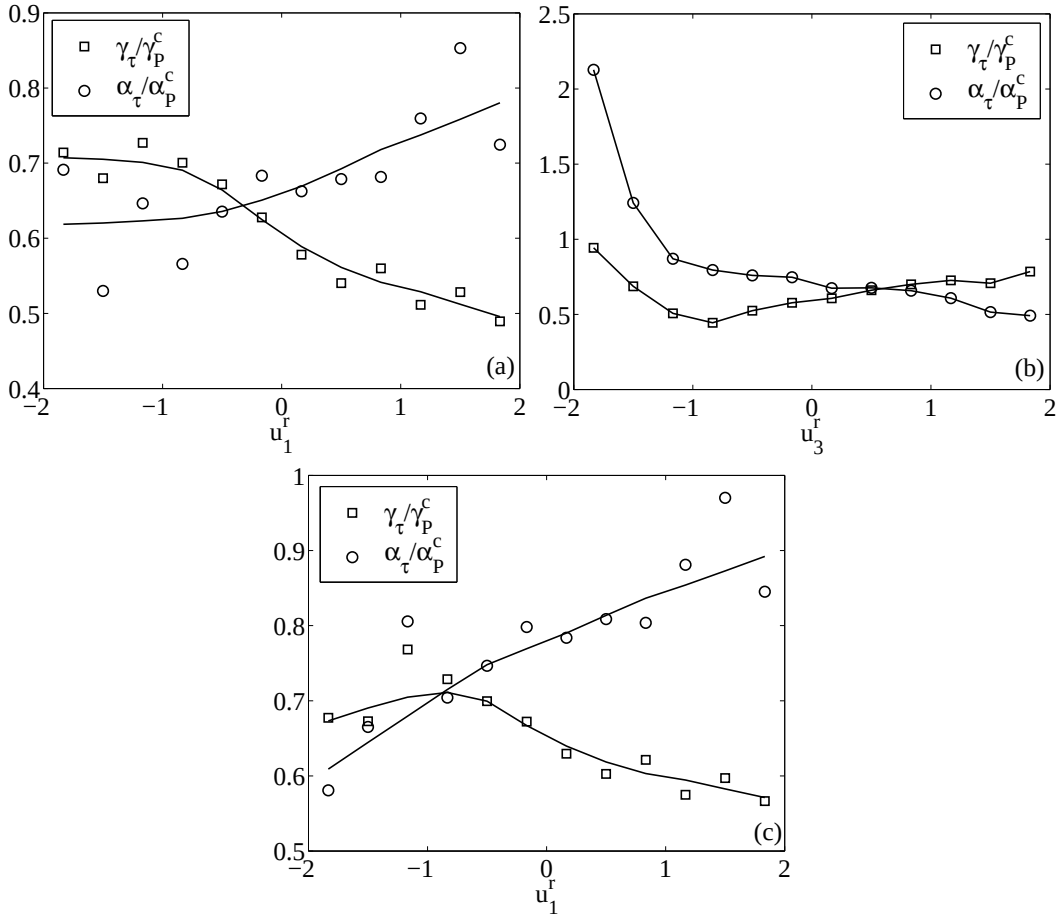

Figure 3.25 Ratios of the eigenvalues of the conditional SGS stress and the conditional SGS stress production conditional on (a), u_1^r and (b), u_3^r. The buoyancy production is included in (c).

shear, and the length scale inhomogeneity play important roles in the behaviors of $\langle \tau_{ij} | \mathbf{u}^r \rangle$ and $\langle P_{ij} | \mathbf{u}^r \rangle$.

The results show that when u_3^r is positive (updrafts), the subgrid-scale eddies move upward and are on average stretched in the vertical direction owing to shear and buoyancy acceleration. Under such conditions, all three components of the normal SGS stress gain energy through the spectral transfer. However, τ_{33} loses energy to τ_{11} (and τ_{22}) through inter-component exchange, resulting in anisotropy in the SGS stress. These processes are enhanced with increasing u_3^r owing to stronger vertical shear and buoyancy acceleration as well as the advection effects. While $\langle P_{33} | u_1^r, u_3^r \rangle$ generally depends weakly on u_1^r, $\langle P_{11} | u_1^r, u_3^r \rangle$ depends on u_1^r, because a larger u_1^r causes stronger vertical shear, further increasing the level of anisotropy. For negative u_3^r, the subgrid-scale eddies associated with the returning flow of large convective eddies move downward and are on average

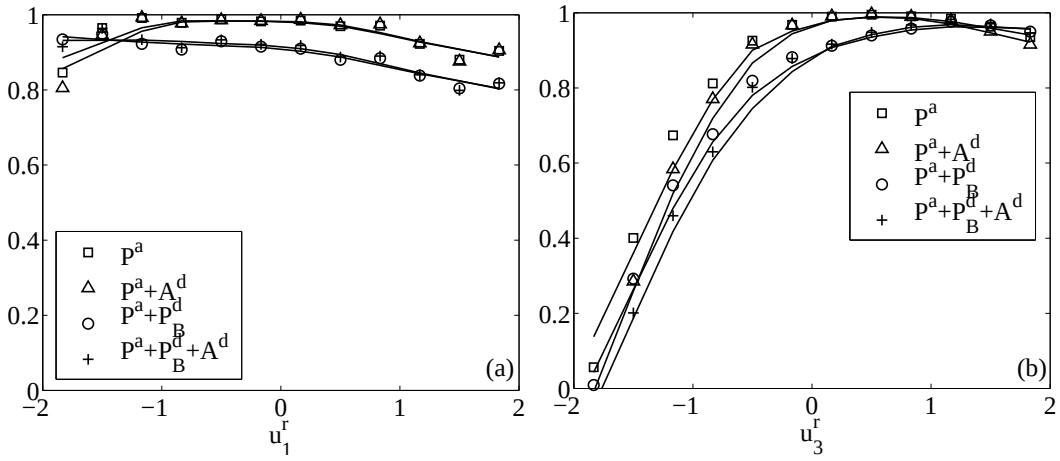

Figure 3.26 Contraction of the conditional SGS stress and the conditional SGS stress production conditional on (a), u_1^r and (b), u_3^r. The effects of advection and buoyancy production are also included and are generally small.

compressed in the vertical direction owing to the presence of the ground. The spectral transfer is negative (conditional backscatter) under such conditions. However, τ_{33} gains energy from τ_{11} (and τ_{22}) through inter-component exchange. These processes are also somewhat enhanced by increasing the magnitude of (negative) u_3^r, resulting in nearly isotropic SGS stress. These processes depend weakly on u_1^r because the vertical shear is weakened by the returning flow.

Representation of the conditional SGS stress in the Lumley triangle also shows similar trends for anisotropy. In general, the anisotropy is weak for negative u_3^r and is much stronger for positive u_3^r. For positive and negative u_1^r values, $\langle \tau_{ij} | u_1^r, u_3^r \rangle$ is close to axisymmetric with one large and one small eigenvalue, respectively, perhaps reflecting the shear and buoyancy effects. The results for the SGS shear stress $\langle \tau_{13} | u_1^r, u_3^r \rangle$ and the production term $\langle P_{13} | u_1^r, u_3^r \rangle$ are consistent with the dependence of the anisotropy on u_1^r and u_3^r. The magnitude of $\langle P_{13} | u_1^r, u_3^r \rangle$ depends on u_1^r and is enhanced by positive u_3^r. Comparisons of the results for different array configurations (Δ/z and $-z/L$) show that both grid anisotropy and the stability parameter ($-z/L$) affect the anisotropy of the SGS stress. The anisotropy of $\langle \tau_{ij} | \mathbf{u}^r \rangle$ is argued to be important for correctly predicting the mean velocity profile and the streamwise velocity variance. The results also show that there is significant similarity between $\langle \tau_{ij} | \mathbf{u}^r \rangle$ and $\langle P_{ij} | \mathbf{u}^r \rangle$ when u_3^r is positive. This is further evidenced by the small angles between their eigenvectors (less than 10°) and high values of the normalized tensor contraction (> 0.9).

Systematic tests of several current SGS models are performed. The Smagorinsky model can predict well neither the conditional mean of SGS stress nor its production. It can predict quite

well the trends of some shear stress components, but not the normal components, and can predict the trends of some normal components of conditional SGS stress production, but not the shear components. The magnitudes of these components are generally poorly predicted. The level of anisotropy is also severely under-predicted.

The nonlinear model ([82]) can predict reasonably well the trends of some normal stress components, but not the shear components, and can predict the trends of some normal components and shear components of the conditional SGS stress production rate. It over-predicts the conditional backscatter. Unlike the Smagorinsky model, the nonlinear model over-predicts the level of anisotropy. The mixed Smagorinsky-nonlinear model does not show significant improvement. The deviatoric part of the mixed model has an improved performance. It can predict most components of the conditional SGS stress and the conditional SGS stress production quite well. Unfortunately, $\langle \tau_{13} | \mathbf{u}^r \rangle$ is poorly predicted, which is very important for LES in the surface layer. Although the anisotropy is over-predicted, it is closer to the measurements than the mixed model and the nonlinear model.

The predicted $\langle \tau_{13} | \mathbf{u}^r \rangle$ using Kosović's nonlinear model is improved over of the deviatoric mixed model, but the rest of the components of the conditional SGS stress and the conditional SGS stress production are less well predicted. It also under-predicts the magnitude of the conditional SGS stress when the mean energy transfer is matched. The level of anisotropy is also under-predicted compared with measurements, but the prediction is improved over that of the Smagorinsky model.

Using the measured $\langle \tau_{ij} | \mathbf{u}^r \rangle$ and $\langle P_{ij} | \mathbf{u}^r \rangle$ and their model predictions, the deficiencies in current LES results, such as the over-predictions of the mean velocity profile and the streamwise velocity variance, and the under-prediction of the vertical velocity skewness are linked to the inability of the SGS models to predict $\langle \tau_{ij} | \mathbf{u}^r \rangle$ and $\langle P_{ij} | \mathbf{u}^r \rangle$ correctly. Specifically, the former is related to the under-prediction of the anisotropy of $\langle \tau_{ij} | \mathbf{u}^r \rangle$ and the latter is due to the under-prediction of the dependence of $\langle P_{33} | \mathbf{u}^r \rangle$ on u_3^r and the asymmetry in the dependence.

The analyses of the conditional SGS stress and the conditional SGS stress production rate can serve as an important guide in developing improved SGS models. In particular, the understanding gained on the characteristics of the SGS stress and its production and the deficiencies identified of SGS models in predicting these characteristics can be used to improve specific aspects of LES results that are crucial to a given application. It is emphasized that although the testing of the SGS models performed in the present study is *a priori* in nature, the linkage between the modeled terms and resolvable-scale velocity JPDF is strong because the analyses use the JPDF equation. Therefore, the test results can be used to identify the possible causes for LES deficiencies. Nonetheless, it would

be very useful to carry out *a posteriori* testing of SGS models by comparing model predictions of $\langle \tau_{ij} | \mathbf{u}^r \rangle$ and $\langle P_{ij} | \mathbf{u}^r \rangle$ from actual LES with measurements.

CHAPTER 4

On the subgrid-scale fluxes and their production rates in a convective atmospheric boundary layer

In this chapter, the subgrid-scale (SGS) scalar flux in the atmospheric surface layer is studied using field measurements data. When the filter scale is in the inertial range, the energy-containing scales are well resolved and most of the turbulent stress is contained in the resolvable scales. The effects of subgrid scales are generally considered to be limited to extracting energy from the resolvable scales at the correct rate ([1, 27, 61]). Thus, the LES results are to some extent insensitive to the subgrid-scale model employed ([6, 21]).

However, in LES of high-Reynolds-number turbulent boundary layers, such as the atmospheric boundary layer (ABL), the filter scale in the near-wall region is inevitably in the energy-containing scales ([62, 21, 32, 48, 49]). This causes the near-wall results to depend heavily on the SGS model ([49]). Therefore, the deficiencies of SGS models are likely to result in inaccuracies in the LES statistics in the near-wall region. For example, the standard Smagorinsky model over-predicts the mean scalar gradient and the mean scalar variance, but under-predicts the mean vertical scalar flux in the LES of the unstable ABL ([8, 10]). Therefore, an important question in improving SGS models is how the SGS turbulence and SGS models affect the resolvable-scale statistics under these conditions.

Previous studies of SGS turbulence have generally focused on the energy transfer rate from the resolvable to the subgrid scales (e.g., [61, 27]). However, a limitation of such studies is that they do not provide information on how the SGS turbulence affects the resolvable-scale statistics. *a priori* and *a posteriori* tests of SGS models (e.g., [22, 23, 24, 6, 25, 26, 8, 27, 28, 29, 30, 21, 31, 32, 33, 19, 34, 35, 36]) are also very limited in their ability to relate SGS model to the resolvable-scale statistics. For *a priori* tests, it is difficult to infer the effects of model performance on LES results.

For *a posteriori* tests, it is difficult to relate the deficiencies of LES results to specific model behaviors ([90]).

To better understand the effects of SGS turbulence and SGS models on the resolvable-scale statistics, a systematic approach was employed ([38, 91, 90]), which is based on the transport equations of the resolvable-scale velocity and velocity-scalar joint probability density function (JPDF). This approach has several advantages over traditional methods for testing SGS models. First, it deals with the resolvable-scale statistics, whose accurate predictions are generally the primary objective of LES. By contrast, traditional methods often compare instantaneous SGS variables which are very difficult interpret. Second, unlike the filtered Navier-Stokes equations and the scalar transport equation, the JPDF transport equation is not chaotic and previous analytical results of similar equations ([70, 40]) can be used to understand the behavior of SGS turbulence and SGS models ([90]). It is noted that the JPDF equations can be used to study the SGS turbulence and to perform both statistical *a priori* and *a posteriori* tests of SGS models. Chen and Tong (2006) [90] emphasized such *a priori* tests provide a strong linkage between the modeled SGS terms and the resolvable-scale velocity JPDF, and therefore, are qualitatively different from the traditional *a priori* tests based on correlations of the measured and modeled SGS variables.

Chen and Tong (2006) [90] used this approach to study the SGS turbulence in the surface layer of the ABL and identified several deficiencies of the SGS models that affects the LES statistics. They argued that the over-predictions of the mean shear and streamwise velocity variance near the surface by the Smagorinsky model are partly due to the under-prediction of the anisotropy of the SGS stress and its variations in the near-wall region. They also pointed out that the under-prediction of the vertical velocity skewness is likely due to the inability of the Smagorinsky model to predict the asymmetry in the production rate of the vertical normal component of the SGS stress. These analyses based on the JPDF equation provide important knowledge for improving SGS model.

The present work studies the influence of the SGS scalar flux and the SGS stress on the resolvable-scale velocity-scalar JPDF using the JPDF transport equation, which can be derived following the method given by Pope (1985) ([39]). Differentiating the definition of the JPDF:

$$f = \left\langle \delta[\theta^r - \psi] \prod_{i=1}^{3} \delta[u_i^r - v_i] \right\rangle, \tag{4.1}$$

we obtain

$$\frac{\partial f}{\partial t} = -\frac{\partial}{\partial v_i} \left\{ \left\langle \frac{\partial u_i^r}{\partial t} | \mathbf{u^r} = \mathbf{v}, \theta^r = \psi \right\rangle f \right\} - \frac{\partial}{\partial \psi} \left\{ \left\langle \frac{\partial \theta^r}{\partial t} | \mathbf{u^r} = \mathbf{v}, \theta^r = \psi \right\rangle f \right\}, \tag{4.2}$$

where δ is the Dirac delta function, and $\mathbf{v}$ and ψ are the sample-space variables for the resolvable-scale velocity $\mathbf{u}^r$ and the resolvable-scale scalar θ^r (a superscript r denotes a resolvable-scale variable), respectively, and the angle brackets denote an ensemble mean. Substituting the time derivatives, $\frac{\partial u_i^r}{\partial t}$ and $\frac{\partial \theta^r}{\partial t}$, in equation (4.2) with the right-hand side of the equation for the resolvable-scale velocity:

$$\frac{\partial u_i^r}{\partial t} = -\frac{\partial u_j^r u_i^r}{\partial x_j} - \frac{\partial \tau_{ij}}{\partial x_j} - \frac{\partial p^r}{\partial x_i} + \frac{g}{\Theta}\theta^r \delta_{i3} + \nu \frac{\partial^2 u_i^r}{\partial x_j \partial x_j}, \tag{4.3}$$

where $\tau_{ij} = (u_i u_j)^r - u_i^r u_j^r$, p^r, Θ, θ, and ν are the SGS stress (the Leonard stress $L_{ij} = (u_i^r u_j^r)^r - u_i^r u_j^r$ has been included in τ_{ij}), the filtered pressure, the mean potential temperature, the fluctuation potential temperature, and the kinematic viscosity, respectively, and the filtered resolvable-scale scalar equation:

$$\frac{\partial \theta^r}{\partial t} = -\frac{\partial \theta^r u_i^r}{\partial x_i} - \frac{\partial F_i}{\partial x_i} + \Gamma \frac{\partial^2 \theta^r}{\partial x_i^2}, \tag{4.4}$$

where $F_i = (u_i \theta)^r - u_i^r \theta^r$ and Γ are the SGS scalar flux and the molecular diffusivity, respectively, we have

$$\begin{aligned}\frac{\partial f}{\partial t} + v_j \frac{\partial f}{\partial x_j} = {} & \frac{\partial}{\partial v_i}\left\{\left\langle \frac{\partial \tau_{ij}}{\partial x_j} | \mathbf{u^r} = \mathbf{v}, \theta^r = \psi \right\rangle f\right\} + \frac{\partial}{\partial v_i}\left\{\left\langle \frac{\partial p^r}{\partial x_i} | \mathbf{u^r} = \mathbf{v}, \theta^r = \psi \right\rangle f\right\} \\ & - \frac{g}{\Theta}\frac{\partial}{\partial v_3}\left\{\langle \theta^r | \mathbf{u^r} = \mathbf{v}, \theta^r = \psi \rangle f\right\} + \frac{\partial}{\partial \psi}\left\{\left\langle \frac{\partial F_i}{\partial x_i} | \mathbf{u^r} = \mathbf{v}, \theta^r = \psi \right\rangle f\right\}. \end{aligned} \tag{4.5}$$

The two terms on the left-hand side are the time rate of change and the advection in physical space. The first three terms on the right-hand side are transport in velocity space of the JPDF by the SGS stress divergence, the resolvable-scale pressure gradient, and the buoyancy force, respectively. The last term is transport in scalar space by the SGS scalar flux divergence. The viscous force and scalar diffusion terms are small and are omitted at high Reynolds numbers and high Peclet numbers.

Because SGS turbulence is often studied by analyzing the SGS stress and flux rather than their divergences, an alternative form of the equation was given by Chen *et al.* (2005) [91]:

$$\begin{aligned}\frac{\partial f}{\partial t} + v_j \frac{\partial f}{\partial x_j} = {} & \frac{\partial^2}{\partial v_i \partial x_j}\left\{\langle \tau_{ij} | \mathbf{u^r} = \mathbf{v}, \theta^r = \psi \rangle f\right\} + \frac{\partial^2}{\partial v_i \partial v_j}\left\{\left\langle -\frac{1}{2} P_{ij} | \mathbf{u^r} = \mathbf{v}, \theta^r = \psi \right\rangle f\right\} \\ & + \frac{\partial^2}{\partial \psi \partial x_i}\left\{\langle F_i | \mathbf{u^r} = \mathbf{v}, \theta^r = \psi \rangle f\right\} + \frac{\partial^2}{\partial \psi \partial v_i}\left\{\langle P_{Fi} | \mathbf{u^r} = \mathbf{v}, \theta^r = \psi \rangle f\right\} \\ & + \frac{\partial^2}{\partial \psi \partial \psi}\left\{\langle P_\theta | \mathbf{u^r} = \mathbf{v}, \theta^r = \psi \rangle f\right\} + \frac{\partial^2}{\partial v_i \partial x_i}\left\{\langle p^r | \mathbf{u^r} = \mathbf{v}, \theta^r = \psi \rangle f\right\} \\ & + \frac{\partial^2}{\partial v_i \partial v_k}\left\{\left\langle p^r \frac{\partial u_k^r}{\partial x_i} | \mathbf{u^r} = \mathbf{v}, \theta^r = \psi \right\rangle f\right\} + \frac{\partial^2}{\partial v_i \partial \psi}\left\{\left\langle p^r \frac{\partial \theta^r}{\partial x_i} | \mathbf{u^r} = \mathbf{v}, \theta^r = \psi \right\rangle f\right\} \\ & - \frac{g}{\Theta}\frac{\partial}{\partial v_3}\left\{\langle \theta^r | \mathbf{u^r} = \mathbf{v}, \theta^r = \psi \rangle f\right\}, \end{aligned} \tag{4.6}$$

where $P_{ij} = -\left\{\tau_{ik}\frac{\partial u_j^r}{\partial x_k} + \tau_{jk}\frac{\partial u_i^r}{\partial x_k}\right\}, P_{Fi} = -\left\{\tau_{ik}\frac{\partial \theta^r}{\partial x_k} + F_k\frac{\partial u_i^r}{\partial x_k}\right\}$, and $P_\theta = -F_i\frac{\partial \theta^r}{\partial x_i}$ are the SGS stress production rate, the SGS scalar flux production rate, and the SGS scalar variance production rate, respectively. The terms on the right-hand side now are transport and mixed transport in velocity, physical, and scalar spaces due to the SGS stress, the SGS stress production rate, the SGS scalar flux, the SGS scalar flux production rate, the SGS scalar variance production rate, the resolvable-scale pressure, the pressure-strain correlation, the pressure-scalar-gradient correlation, and the buoyancy force, respectively. Therefore, the necessary conditions for LES to correctly predict the resolvable-scale velocity-scalar JPDF are that the conditional SGS stress, the conditional SGS scalar flux, the conditional SGS stress production rate, the conditional SGS scalar flux production rate, the conditional SGS scalar variance production rate are reproduced by the SGS models ([91]). The functional form of these conditional SGS statistics and their dependence on the surface-layer dynamics are therefore of great importance for understanding the influence of the SGS turbulence and SGS models on the resolvable-scale statistics.

These conditions were used to study the dependencies of the resolvable-scale velocity-scalar JPDF on the SGS turbulence in a turbulent jet ([91]). The results show that the conditional SGS scalar flux and the conditional SGS scalar flux production rate have a strong dependence on the resolvable-scale velocity and scalar, indicating strong flow history effects. Chen and Tong (2006) [90] investigated the SGS velocity field in the surface layer of the ABL and showed that the behaviors of the conditional SGS stress and the conditional SGS stress production rate are closely related to the surface dynamics, i.e., updrafts generated by buoyancy force, downdrafts associated with the large-scale convective eddies, the mean shear, and the length scale inhomogeneity in the vertical direction. In addition, they found that the conditional SGS stress and the conditional SGS stress production rate have similar trends, and their eigenvectors are generally well aligned with the normalized tensorial contraction being close to one, thereby indicating the potential of modeling the conditional SGS stress using its production rate.

In the present work the effects of the SGS motions on the resolvable-scale velocity-scalar JPDF in unstable atmospheric surface layer are investigated using measurement data. The field program and the array filter technique for measuring resolvable- and subgrid- scale variables are given in Section 4.1. Section 4.2 examines the measured conditional SGS statistics and the SGS model predictions. The conclusions are given in Section 4.3.

Table 4.1 Surface layer parameters for array 1 ($\Delta/z = 3.88$) under unstable conditions. The primary array height z_p is used for z.

Data#	$\langle u \rangle$ (ms^{-1})	$-z/L$	u_* (ms^{-1})	ϵ ($\mathrm{m}^2\mathrm{s}^{-3}$)	H ($\mathrm{K} \cdot \mathrm{ms}^{-1}$)	χ_T ($\mathrm{K}^2\mathrm{s}^{-1}$)	Duration (min)
a	1.42	0.34	0.15	0.003	0.02	0.001	35
b	3.56	0.22	0.33	0.031	0.17	0.026	30
c	3.65	0.21	0.36	0.039	0.20	0.035	83
d	3.25	0.24	0.36	0.041	0.24	0.048	33

Table 4.2 Surface layer parameters for the other arrays under unstable conditions. The primary array height z_p is used for z.

Array	Δ/z ($\approx$)	$\langle u \rangle$ (ms^{-1})	$-z/L$	u_* (ms^{-1})	ϵ ($\mathrm{m}^2\mathrm{s}^{-3}$)	H ($\mathrm{K\ m\ s}^{-1}$)	χ_T ($\mathrm{K}^2\mathrm{s}^{-1}$)	Total duration (min)
2	2.00	3.09	0.36	0.30	0.020	0.15	0.017	257
3	1.00	4.22	0.60	0.34	0.018	0.19	0.009	591
4	0.48	2.73	0.35	0.30	0.021	0.15	0.017	60

4.1 Measurement Data

Measurement data used in this chapter is the same as that in Chapter 3. Field measurements and data process procedures are thoroughly described in Chapter 3. The surface layer parameters for the data sets collected using the four arrays are given in Tables 3.1, 4.1, and 4.2.

The results in Section 3.3 show that the SGS stress for array 1 which has the largest Δ/z, is the most anisotropic and most difficult for SGS models to predict, therefore, similar to Chapter 3, the discussions of results are focused on array 1. In present work, the unstable surface layer is studied. Data sections that are quasi-stationary are generally 30-90 minutes in length. To achieve reasonable statistical convergence, the results of selected data sections collected under similar stability conditions are combined using each array configuration as done in Chapter 3. Therefore, the results for each data set are normalized using its parameters, then weight-averaged according to the number of conditional samples in each bin. In addition, similar to the conclusion in Chapter 3, the data size is sufficient for obtaining reliable statistics for the analyses.

4.2 Results

Similar to Chen and Tong (2006) [90] discussions are focused on results obtained using data from array 1. The stability parameter $-z/L$ has an average value of 0.24. Top-hat filters in both the streamwise and crossstream directions are used to obtain the resolvable-scale and subgrid-scale variables with a filter size $\Delta = 3.88z$, which is in the energy-containing range. The results for the other array configurations, i.e. different Δ/z, and $-z/L$ (Table 4.2), are also obtained. The results

Table 4.3 Measured Reynolds scalar flux and mean SGS scalar flux for the four arrays

Array	$\langle u_1'\theta'\rangle/H$	$\langle u_2'\theta'\rangle/H$	$\langle F_1\rangle/H$	$\langle F_2\rangle/H$	$\langle F_3\rangle/H$
1	-1.70	-0.23	-0.96	-0.00	0.70
2	-1.20	0.04	-0.62	0.02	0.56
3	-0.85	0.35	-0.26	0.01	0.33
4	-1.16	-0.21	-0.10	0.01	0.18

are generally similar to those for array 1 and will not be discussed. Table 4.3 gives the normalized Reynolds scalar flux and the ratios of the mean SGS scalar flux components to the vertical mean scalar flux. Array 1 has the largest fraction of the vertical SGS scalar flux and thus is the most challenging case for modeling. The measured and modeled SGS scalar flux components are given in Table 4.4 and discussed in Section 4.2.7

The results are normalized using the surface layer parameters. The conditional SGS stress, $\langle \tau_{ij}|\mathbf{u}^r, \theta^r\rangle$, and the conditional SGS stress production rate, $\langle P_{ij}|\mathbf{u^r}, \theta^r\rangle$, are normalized by the friction velocity, u_*^2, and the estimated energy dissipation rate, $\epsilon = \theta_\epsilon \frac{u_*^3}{k_a z}$, respectively, where $\theta_\epsilon = 1 - z/L$ for $z/L \leq 0$, as suggested by Kaimal *et al.* (1972) [62]. The conditional SGS scalar flux, $\langle F_i|\mathbf{u^r}, \theta^r\rangle$, and the conditional SGS scalar flux production rate, $\langle P_{Fi}|\mathbf{u^r}, \theta^r\rangle$, are normalized by the mean vertical heat flux, $H = \langle \theta' u_3'\rangle$, and $\frac{-T_* u_*^2}{z}$, respectively, where prime denotes fluctuations and $T_* = -\frac{H}{u_*}$ is the scale for temperature fluctuations. The conditional SGS variance spectral transfer rate, $\langle P_\theta|\mathbf{u^r}, \theta^r\rangle$, is normalized by the estimated scalar variance transfer rate, $\chi_T = \theta_h \frac{T_*^2 u_*}{k_a z}$, where $\theta_h = 0.74 \times (1 - 9z/L)^{-1/2}$ for $z/L \leq 0$, as suggested by Businger *et al.* (1971) [92].

4.2.1 SGS scalar flux and its production rate

The results for the conditional SGS scalar flux components $\langle F_1|\mathbf{u}^r, \theta^r\rangle$, $\langle F_2|\mathbf{u}^r, \theta^r\rangle$, and $\langle F_3|\mathbf{u}^r, \theta^r\rangle$ are shown in Figure 4.1. For convenience the sample-space variables $\mathbf{v}$ and ψ are omitted from the conditional means here and hereafter. In addition, only the fluctuation parts of $\mathbf{u}^r$ and θ, which are normalized by their respective r.m.s. values, are plotted.

The results show that $\langle F_1|\mathbf{u}^r, \theta^r\rangle$ and $\langle F_3|\mathbf{u}^r, \theta^r\rangle$ depend strongly on u_1^r and u_3^r for positive and small θ^r fluctuations, and the dependence is weaker for negative θ^r fluctuations. $\langle F_2|\mathbf{u}^r, \theta^r\rangle$ also depends on $|u_2^r|$ and u_3^r for positive and small θ^r fluctuations, and the dependence is weaker for negative θ^r fluctuations. $\langle F_1|\mathbf{u}^r, \theta^r\rangle$ generally has large values, because the large temperature fluctuations are highly correlated with the streak structure in the surface layer. The trends of the SGS scalar production rates $\langle P_{F1}|\mathbf{u}^r, \theta^r\rangle$, $\langle P_{F2}|\mathbf{u}^r, \theta^r\rangle$ and $\langle P_{F3}|\mathbf{u}^r, \theta^r\rangle$ (Figure 4.2) are generally similar to those of $\langle F_1|\mathbf{u}^r, \theta^r\rangle$, $\langle F_2|\mathbf{u}^r, \theta^r\rangle$, and $\langle F_3|\mathbf{u}^r, \theta^r\rangle$, respectively, for positive and small θ^r fluctuations,

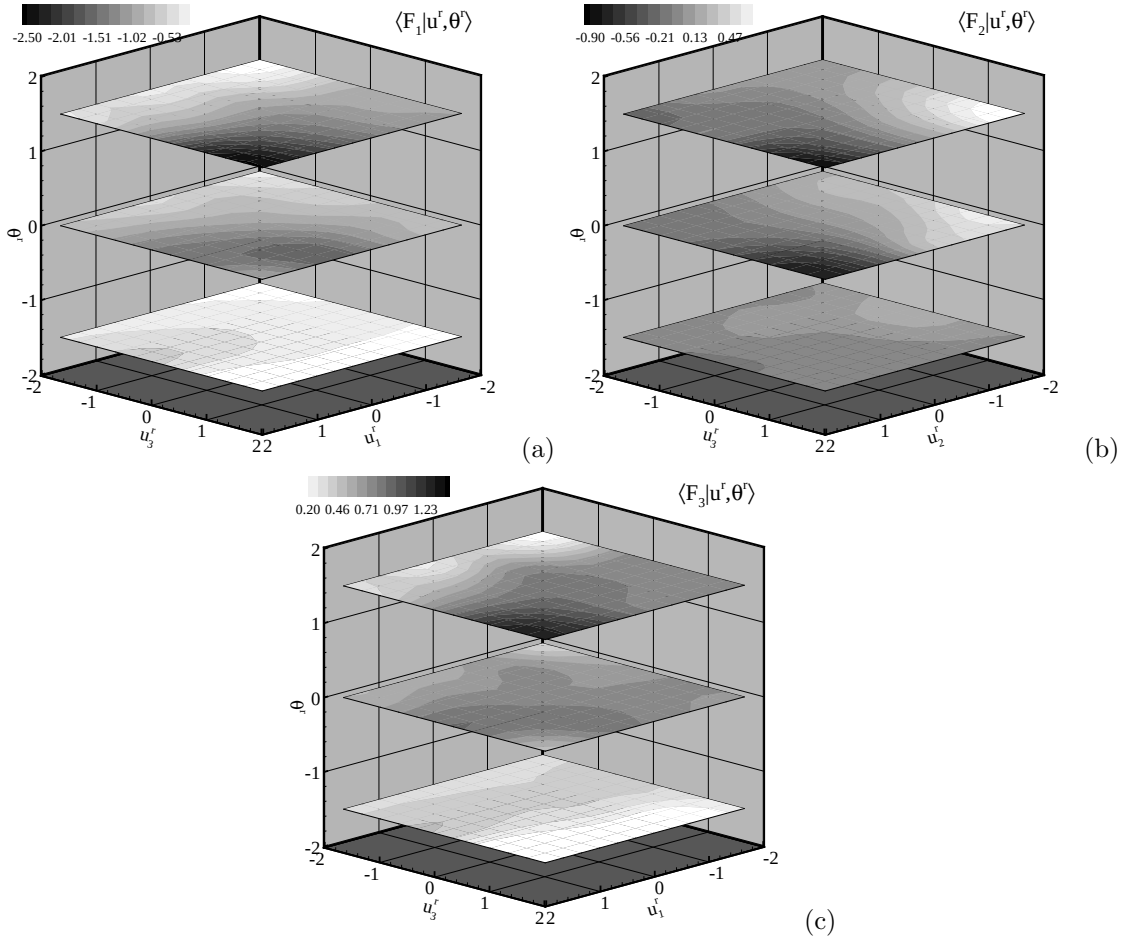

Figure 4.1 Conditional means of the SGS scalar flux. The dependencies on resolvable-scale velocity are strong for positive θ^r and are weak for negative θ^r.

indicating the dominant influence of the SGS scalar flux production rate on the evolution of the SGS scalar flux. The dependence on the resolvable-scale velocity for negative θ^r fluctuations is weak.

To better understand the connections between the conditional SGS scalar flux and its production rate, $\langle P_{F1}|\mathbf{u}^r,\theta^r\rangle$ is expanded as

$$\langle P_{F1}|\mathbf{u}^r,\theta^r\rangle = -\left\langle F_1\frac{\partial u_1^r}{\partial x_1} + F_2\frac{\partial u_1^r}{\partial x_2} + F_3\frac{\partial u_1^r}{\partial x_3} + \tau_{11}\frac{\partial \theta^r}{\partial x_1} + \tau_{12}\frac{\partial \theta^r}{\partial x_2} + \tau_{13}\frac{\partial \theta^r}{\partial x_3}|\mathbf{u}^r,\theta^r\right\rangle. \tag{4.7}$$

The first three terms on the right-hand are the production rate due to the interactions between the SGS scalar flux components and the resolvable-scale velocity gradient components and the last three terms are the production due to the interactions between SGS stress and the resolvable-scale scalar gradient. The results show that the leading components in $\langle P_{F1}|\mathbf{u}^r,\theta^r\rangle$ are $\left\langle -F_3\frac{\partial u_1^r}{\partial x_3}|\mathbf{u}^r,\theta^r\right\rangle$ and $\left\langle -\tau_{13}\frac{\partial \theta^r}{\partial x_3}|\mathbf{u}^r,\theta^r\right\rangle$, which have similar trends and magnitudes on which the discussion is focused in the following. The rest of terms are relatively small because the horizontal derivatives of u_1^r and θ^r are relatively small compared to their vertical derivatives. Similarly, $\langle P_{F3}|\mathbf{u}^r,\theta^r\rangle$ can be expanded

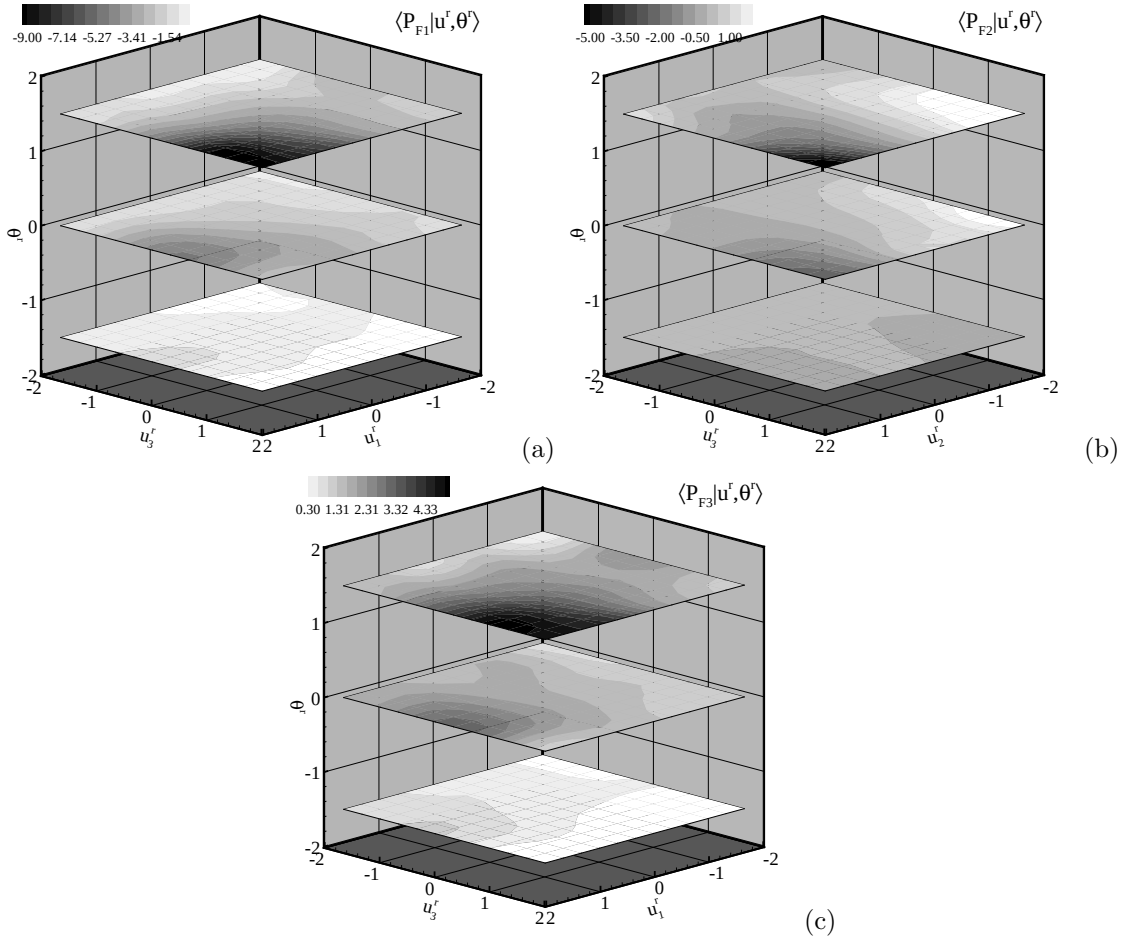

Figure 4.2 Conditional means of the SGS scalar flux production rate.

as:

$$\langle P_{F3}|\mathbf{u}^r,\theta^r\rangle = -\left\langle F_1\frac{\partial u_3^r}{\partial x_1} + F_2\frac{\partial u_3^r}{\partial x_2} + F_3\frac{\partial u_3^r}{\partial x_3} + \tau_{31}\frac{\partial \theta^r}{\partial x_1} + \tau_{32}\frac{\partial \theta^r}{\partial x_2} + \tau_{33}\frac{\partial \theta^r}{\partial x_3}|\mathbf{u}^r,\theta^r\right\rangle \tag{4.8}$$

The terms on the right-hand side of equation 4.8 are similar to those in equation 4.7. The dominant component in $\langle P_{F3}|\mathbf{u}^r,\theta^r\rangle$ is $\left\langle -\tau_{33}\frac{\partial\theta^r}{\partial x_3}|\mathbf{u}^r,\theta^r\right\rangle$. This is because the derivatives of u_3^r and θ^r in the horizontal directions are relatively small. Therefore, the attention is focused on $\left\langle -\tau_{33}\frac{\partial\theta^r}{\partial x_3}|\mathbf{u}^r,\theta^r\right\rangle$.

The trends for $\langle P_{F1}|\mathbf{u}^r,\theta^r\rangle$ and $\langle P_{F3}|\mathbf{u}^r,\theta^r\rangle$ are now discussed. For positive θ^r fluctuations, the eddies associated with updrafts generally come from the region near the ground, and contain large magnitudes of the vertical SGS flux and the SGS stress. They also likely to have experienced strong shear and vertical temperature gradient. Therefore, both F_3, τ_{33}, $\partial u_1^r/\partial x_3$ have large positive values while τ_{13} and $\partial\theta^r/\partial x_3$ have large negative values, resulting in negative $\left\langle -F_3\frac{\partial u_1^r}{\partial x_3}|\mathbf{u}^r,\theta^r\right\rangle$ and $\left\langle -\tau_{13}\frac{\partial\theta^r}{\partial x_3}|\mathbf{u}^r,\theta^r\right\rangle$, and positive $\left\langle -\tau_{33}\frac{\partial\theta^r}{\partial x_3}|\mathbf{u}^r,\theta^r\right\rangle$. Because both the vertical shear, flux, and temperature gradient are enhanced by positive values of u_1^r and u_3^r, the magnitudes of $\langle P_{F1}|\mathbf{u}^r,\theta^r\rangle$

and $\langle P_{F3}|\mathbf{u}^r, \theta^r\rangle$ increase with u_1^r and u_3^r. For small θ^r fluctuations, the eddies are generally well mixed, and therefore, tend to be more symmetric in the vertical direction, which is reflected by the symmetry of $\partial u_1^r/\partial x_3$ and $\partial\theta^r/\partial x_3$ in respect to u_3^r. Consequently, the magnitudes of $\langle P_{F1}|\mathbf{u}^r, \theta^r\rangle$ and $\langle P_{F3}|\mathbf{u}^r, \theta^r\rangle$ increase with u_1^r and $|u_3^r|$. For negative θ^r fluctuations, the eddies associated with downdrafts generally come from the mixed layer region, and contain relatively small SGS fluxes (Figure 4.1(c)). Therefore, the magnitudes of $\langle P_{F1}|\mathbf{u}^r, \theta^r\rangle$ and $\langle P_{F3}|\mathbf{u}^r, \theta^r\rangle$ are small and have weak dependencies on the resolvable-scale velocity.

Comparing the three cases of different θ^r values, the location of peak values of the conditional SGS scalar flux production rate appears to shift toward positive u_3^r for positive θ^r fluctuations, and toward negative u_3^r for negative θ^r fluctuations. This is probably because $\langle \partial u_1^r/\partial x_3|\mathbf{u}^r, \theta^r\rangle$ and $\langle \partial\theta^r/\partial x_3|\mathbf{u}^r, \theta^r\rangle$ (not shown) have similar trends, which indicates that the local gradients are enhanced by both updrafts with high temperature (positive θ^r fluctuations) and downdrafts with low temperature (negative θ^r fluctuations).

Chen and Tong (2006) [90] observed that the conditional SGS stress and the conditional SGS stress production rate also have similar trends for positive u_3^r, which they argued to be the result of the approximate balance between the SGS stress production and the pressure destruction and the fact that the pressure destruction term can be modeled as τ_{ij}/t_Δ where t_Δ is a time scale. The similar trends between the conditional SGS scalar flux and the conditional SGS scalar flux production rate for positive θ^r fluctuations also reflects the consistency with balance between the production rate and pressure destruction and the use of the SGS scalar flux and a time scale to model the pressure destruction. The differences between the trends of the conditional SGS scalar flux and the conditional SGS scalar flux production rate for small and negative θ fluctuations are probably because the production rates are small and no longer balance the pressure destruction.

The dominant components in $\langle P_{F1}|\mathbf{u}^r, \theta^r\rangle$ contains a slow term $\left\langle -F_3\frac{\partial u_1^r}{\partial x_3}|\mathbf{u}^r, \theta^r\right\rangle$, in which F_3 influences $\langle P_{F1}|\mathbf{u}^r, \theta^r\rangle$ through the interaction with $\partial u_1^r/\partial x_3$. However F_1 does not direct affect $\langle P_{F3}|\mathbf{u}^r, \theta^r\rangle$, which is dominated by $\left\langle \tau_{33}\frac{\partial\theta^r}{\partial x_3}|\mathbf{u}^r, \theta^r\right\rangle$. Consequently, accurate modeling of the vertical SGS scalar flux component may be more important than that of the horizontal SGS scalar flux component, and poor predictions of the vertical SGS scalar flux component by a SGS model may result in the inaccuracies in the horizontal SGS scalar flux in a LES. In addition, because $\left\langle -\tau_{13}\frac{\partial\theta^r}{\partial x_3}|\mathbf{u}^r, \theta^r\right\rangle$ affects $\langle P_{F1}|\mathbf{u}^r, \theta^r\rangle$ due to the dominant vertical derivative of resolvable-scale scalar, under-predictions of the condition SGS shear stress components by a SGS model may also result in the inaccuracies in the resolvable-scale horizontal scalar flux in a LES.

4.2.2 SGS scalar variance production rate

The SGS scalar variance production rate $\langle P_\theta|\mathbf{u}^r,\theta^r\rangle$ (Figure 4.3) generally increase with u_1^r and u_3^r and the dependence is strong for positive θ^r fluctuations and weak for negative θ^r fluctuations. For small θ^r fluctuations, the dependence of $\langle P_\theta|\mathbf{u}^r,\theta^r\rangle$ on u_3^r is symmetric and increases with $|u_3^r|$. The dominant component of $\langle P_\theta|\mathbf{u}^r,\theta^r\rangle$ is $\left\langle F_3\frac{\partial\theta^r}{x_3}|\mathbf{u}^r,\theta^r\right\rangle$. Because both F_3 and $\partial\theta^r/\partial x_3$ increase with u_1^r and u_3^r for positive θ^r, so does $\langle P_\theta|\mathbf{u}^r,\theta^r\rangle$. The symmetric dependence of $\langle P_\theta|\mathbf{u}^r,\theta^r\rangle$ on u_3^r is due to the symmetric dependence of $\partial\theta^r/\partial x_3$ on u_3^r. The asymmetry with respect to θ^r is likely to result in a positive skewness for θ^r.

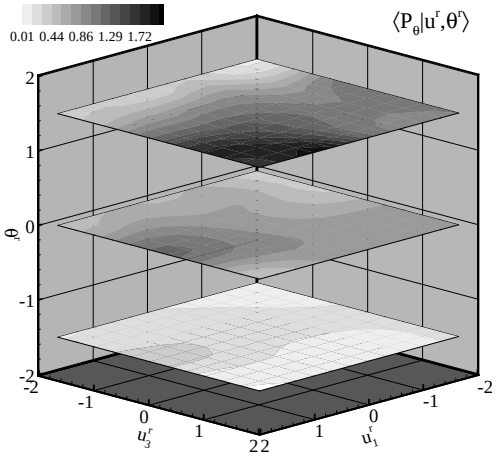

Figure 4.3 Conditional mean of the SGS scalar variance production rate.

4.2.3 Alignment of SGS scalar flux and its production rate

Chen and Tong (2006) [90] observed that the deviatoric part of $\langle\tau_{ij}|\mathbf{u^r}\rangle$ and $\langle P_{ij}|\mathbf{u^r}\rangle$ have similar trends, and the eigenvectors of $\langle\tau_{ij}|\mathbf{u^r}\rangle$ and $\langle P_{ij}|\mathbf{u^r}\rangle$ are well aligned with the normalized tensorial contraction being close to unity for positive u_3^r, indicating the balance between the production rate and pressure destruction and the validity of using the SGS stress and a time scale for modeling the pressure destruction. The results in section 4.2.1 also show that $\langle F_i|\mathbf{u}^r,\theta^r\rangle$ and $\langle P_{Fi}|\mathbf{u}^r,\theta^r\rangle$ have similar trends. To investigate the relationship between $\langle F_i|\mathbf{u}^r,\theta^r\rangle$ and $\langle P_{Fi}|\mathbf{u}^r,\theta^r\rangle$, the alignment angle between $\langle F_i|\mathbf{u}^r,\theta^r\rangle$ and $\langle P_{Fi}|\mathbf{u}^r,\theta^r\rangle$ is computed, which is given by

$$\alpha=\cos^{-1}\left(\frac{|\langle F_i|\mathbf{u}^r,\theta^r\rangle\cdot\langle P_{Fi}|\mathbf{u}^r,\theta^r\rangle|}{\|\langle F_i|\mathbf{u}^r,\theta^r\rangle\|\cdot\|\langle P_{Fi}|\mathbf{u}^r,\theta^r\rangle\|}\right) \tag{4.9}$$

Figure 4.4 shows that $\langle F_i|\mathbf{u}^r,\theta^r\rangle$ and $\langle P_{Fi}|\mathbf{u}^r,\theta^r\rangle$ are generally well aligned with the alignment angle α is generally less than 10° for positive and small θ^r fluctuations. For negative θ^r fluctuations, the alignment angle is small for positive u_3^r and larger (but still less than 30°) for

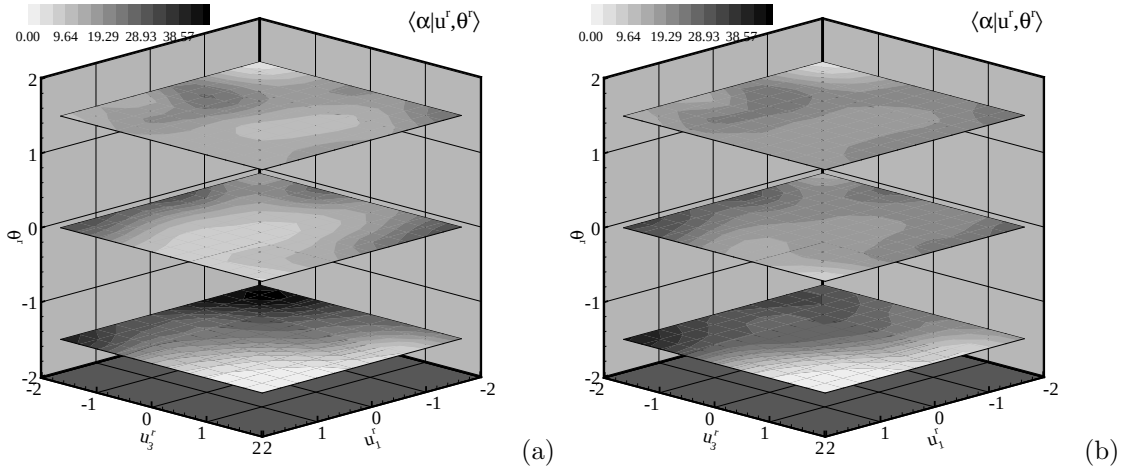

Figure 4.4 Geometric alignment of the measured conditional SGS scalar flux and the conditional SGS stress production rate. (a) the alignment angles are small for positive u_3^r and θ^r and increases for negative u_3^r and θ^r; (b) the effects of buoyancy is included, and the alignment angles are similar to (a).

negative u_3^r. This trend is similar to the alignment property between the conditional SGS stress and its production rate ([90]). This is probably because $\langle P_{Fi}|\mathbf{u}^r, \theta^r\rangle$ is small and might no longer be a dominant term in the SGS flux transport equation, and therefore not in balance with the pressure destruction. Another possibility is that the pressure destruction cannot be modeled as the SGS flux and a time scale under these condition. In order to study the effects of buoyancy force on the alignment property, the buoyancy production term ($P_{FB} = \frac{g}{\Theta}[(\theta^2)^r - (\theta^r)^2]$) is also included in the SGS scalar flux production rate. The alignment angle (Figure 4.4(b)) increase slightly, indicating that buoyancy does not significantly alter the alignment property. These results are consistent with the similarity between the conditional SGS scalar flux and the conditional SGS scalar flux production rate, suggesting the balance between the production rate and pressure destruction and the validity of using the SGS scalar flux and a time scale for modeling the pressure destruction for positive θ^r fluctuations.

4.2.4 SGS stress and its production rate

The normalized conditional SGS stress components $\langle \tau_{11}|\mathbf{u}^r, \theta^r\rangle$ and $\langle \tau_{33}|\mathbf{u}^r, \theta^r\rangle$ are given in Figure 4.5. The results show that similar to the SGS scalar flux $\langle \tau_{11}|\mathbf{u}^r, \theta^r\rangle$ and $\langle \tau_{33}|\mathbf{u}^r, \theta^r\rangle$ generally increase with u_1^r and u_3^r. The dependencies are strong for positive θ^r fluctuations and are weak for negative θ^r fluctuations.

The conditional SGS stress production rate $\langle P_{11}|\mathbf{u}^r, \theta^r\rangle$ (Figure 4.6 (a)) has a similar trend to $\langle \tau_{11}|\mathbf{u}^r, \theta^r\rangle$ (Figure 4.5(a)), suggesting that there is a local conditional equilibrium between the

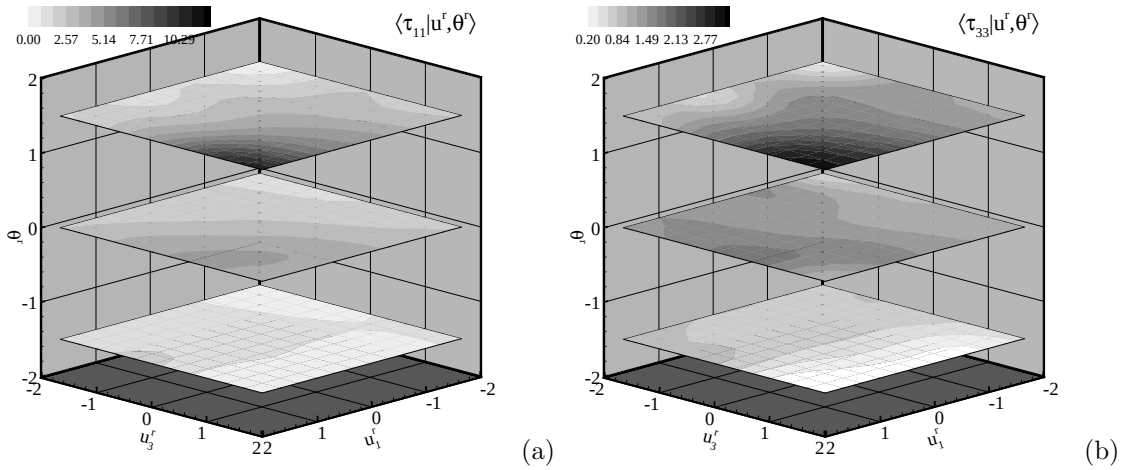

Figure 4.5 Conditional means of the normal components of the SGS stress. The dependencies are strong for positive θ^r and are weak for negative θ^r.

SGS stress production rate and the pressure destruction. However, the trend of $\langle P_{33}|\mathbf{u}^r, \theta^r\rangle$ (Figure 4.6(b)) is different from $\langle \tau_{33}|\mathbf{u}^r, \theta^r\rangle$ (Figure 4.5(b)) because the buoyancy production rate dominates the evolution of $\langle \tau_{33}|\mathbf{u}^r, \theta^r\rangle$, consistent with the previous results ([90]).

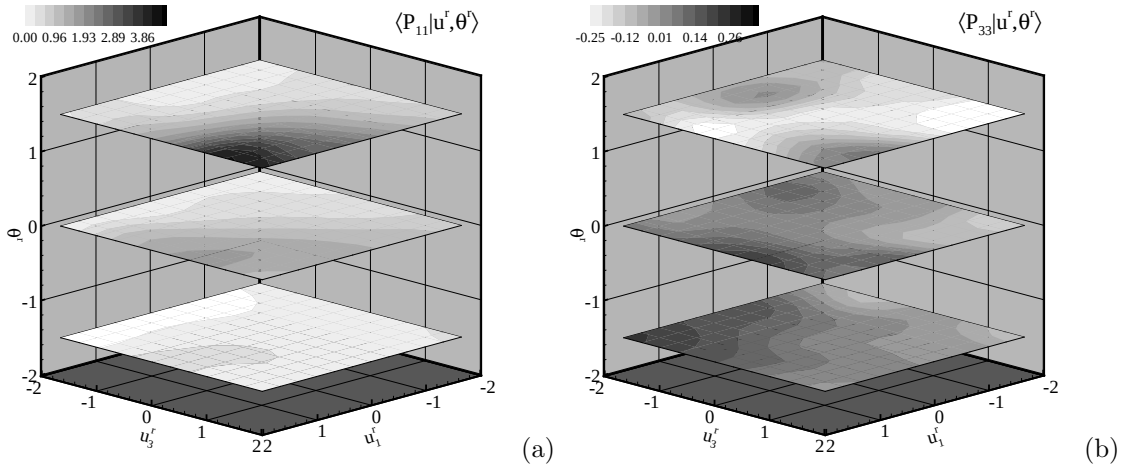

Figure 4.6 Conditional means of the normal components of the SGS stress production rates.

The dependence of $\langle P_{33}|\mathbf{u}^r, \theta^r\rangle$ on the resolvable-scale velocity decreases with θ^r fluctuations. For positive θ^r fluctuations, $\langle P_{33}|\mathbf{u}^r, \theta^r\rangle$ has negative values, indicating that τ_{33} loses energy to τ_{11} and τ_{22} and there is conditional backscatter. For negative θ^r fluctuations, $\langle P_{33}|\mathbf{u}^r, \theta^r\rangle$ is positive, indicating that τ_{33} gains energy. Previous study ([90]) has shown that under-prediction of the dependence of $\langle P_{33}|\mathbf{u}^r, \theta^r\rangle$ on u_3^r will cause the same for the vertical velocity skewness. This will be further examined along with SGS models in Section 4.2.7.

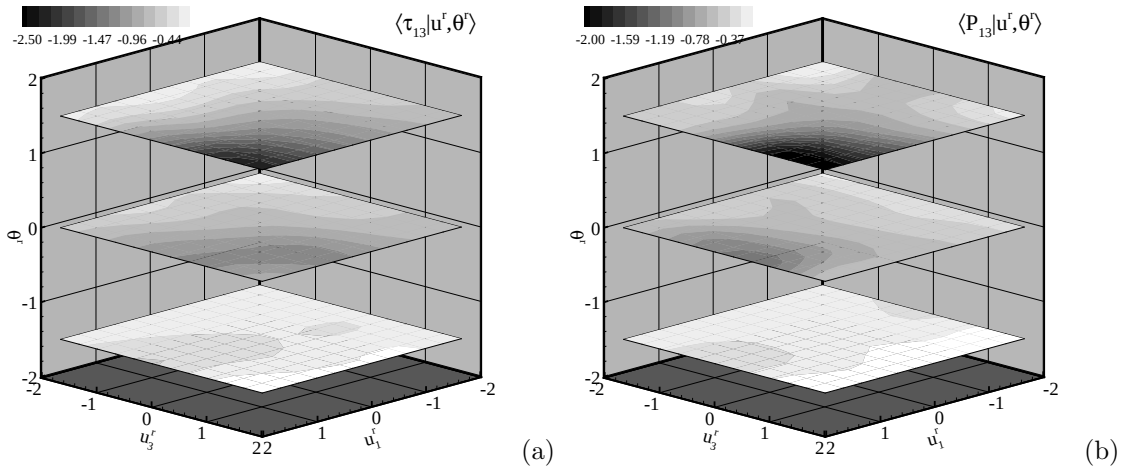

Figure 4.7 Conditional means of the shear components of the SGS stress and the shear production rate.

The conditional shear stress component $\langle \tau_{13} | \mathbf{u}^r, \theta^r \rangle$ (Figure 4.7(a)) has similar trend to τ_{11}. $\langle P_{13} | \mathbf{u}^r, \theta^r \rangle$ (Figure 4.7(b)) has a similar trend, again indicating the conditional quasi-equilibrium. Previous study ([90]) has shown that under-predictions of the trend and magnitude of the τ_{13} cause over-predictions of the mean streamwise velocity gradient near the surface, and that the correct prediction of $\langle \tau_{13} | \mathbf{u}^r \rangle$ is very important for predicting the horizontal velocity variance profile.

The dependence of $\langle \tau_{ij} | \mathbf{u}^r, \theta^r \rangle$ on θ^r is partly due to the flow history effect. The velocity field is not affected by a passive scalar. The dependence of the conditional SGS stress and conditional SGS stress production rate on the resolvable-scale scalar reflects the different flow histories that the SGS eddies with the same resolvable-scale velocity but different resolvable-scale scalar values have experienced ([91]). The temperature in the ABL is generally not passive, therefore, the dependence is probably partly due to the flow history and partly due to the buoyancy effects.

4.2.5 Anisotropy of the conditional SGS stress

An important property of the SGS stress is its level of anisotropy. The level of anisotropy of the conditional SGS stress can be characterized by the representation in the Lumley triangle ([81]). The dependence of the anisotropy on the resolvable-scale velocity (Lumley triangle for $\langle \tau_{ij} | \mathbf{u}^r \rangle$) Chen and Tong (2006) [90] shows that the anisotropy is weak for negative u_3^r and is much stronger for positive u_3^r. For positive and negative u_1^r values, $\langle \tau_{ij} | \mathbf{u}^r \rangle$ is close to axisymmetric with one large and one small eigenvalue, respectively, probably reflecting the shear and buoyancy effects. Here the dependence of the anisotropy on the resolvable-scale scalar is studied. The normalized anisotropy tensor for $\langle \tau_{ij} | \mathbf{u}^r, \theta^r \rangle$, $\frac{\langle \tau_{ij} | \mathbf{u}^r, \theta^r \rangle}{\langle \tau_{kk} | \mathbf{u}^r, \theta^r \rangle} - \frac{1}{3}\delta_{ij}$, can be determined by two variables ξ and η defined in terms

of its invariants ([37])

$$6\eta^2 = -2II = \frac{\left\langle \tau_{ij}^d | \mathbf{u}^r, \theta^r \right\rangle \left\langle \tau_{ij}^d | \mathbf{u}^r, \theta^r \right\rangle}{\left\langle \tau_{kk} | \mathbf{u}^r, \theta^r \right\rangle^2} \tag{4.10}$$

and

$$6\xi^3 = 3III = \frac{\left\langle \tau_{ij}^d | \mathbf{u}^r, \theta^r \right\rangle \left\langle \tau_{jk}^d | \mathbf{u}^r, \theta^r \right\rangle \left\langle \tau_{ki}^d | \mathbf{u}^r, \theta^r \right\rangle}{\left\langle \tau_{kk} | \mathbf{u}^r, \theta^r \right\rangle^3}, \tag{4.11}$$

where $\tau_{ij}^d = \tau_{ij} - \tau_{kk}\delta_{ij}/3$ is the deviatoric part of the SGS stress, and II and III are the second and third invariants of the anisotropy tensor respectively. If $\langle \tau_{ij} | \mathbf{u}^r, \theta^r \rangle$ is isotropic, both ξ and η are zero. (The first invariant or trace of $\left\langle \tau_{ij}^d | \mathbf{u}^r, \theta^r \right\rangle$ is always zero by definition). The representation for the conditional SGS stress results are shown in Figure 4.8. The arrows represent the conditional velocity vector (see [90] for more details). The results show that there is a clear dependence of the anisotropy on the resolvable-scale scalar. For positive and small θ^r fluctuations, $\langle \tau_{ij} | u_1^r, u_3^r, \theta^r \rangle$ is quite anisotropic and close to the results for $\langle \tau_{ij} | u_1^r, u_3^r \rangle$ (without conditioning on θ^r), consistent with the trends of $\langle \tau_{ij} | \mathbf{u}^r, \theta^r \rangle$ in Section 4.2.4. The points representing the anisotropy are not far from $\eta = -\xi$ and $\eta = \xi$ indicating that $\langle \tau_{ij} | u_1^r, u_3^r, \theta^r \rangle$ is close to axisymmetric with either one small eigenvalue or one large eigenvalue. One difference between the results for small θ^r fluctuations and for positive θ^r fluctuations is that there are more points close to $\eta = \xi$ than that of $\eta = -\xi$, indicating that the SGS eddies are more likely to contain SGS stress that is close to axisymmetric with one large eigenvalue. This is probably because the compression and shear effects are weakened as these eddies are likely to has gone through a strong mixing process.

For negative θ^r fluctuations, there are more points representing the anisotropy close to the origin than for positive and small θ^r fluctuations, indicating a slightly less anisotropic SGS stress. In addition, some points with $u_3^r < 0$ are close to the axisymmetric with one small eigenvalue ($\eta = -\xi$) due to the compression effect, and some points with $u_3^r > 0$ are close to the axisymmetric with one large eigenvalue ($\eta = \xi$) due to the weakened shear effect.

The results discussed above are for $\Delta/z = 3.88$ and $-z/L = 0.24$ (array 1). The level of the anisotropy of $\langle \tau_{ij} | u_1^r, u_3^r, \theta^r \rangle$ for different array configurations are shown in Figure 4.9. For positive temperature fluctuations, the results for $\langle \tau_{ij} | u_1^r, u_3^r, \theta^r \rangle$ is similar to the results $\langle \tau_{ij} | u_1^r, u_3^r \rangle$ (without conditional on θ^r) which was discussed by Chen and Tong (2006) [90]. The results of $\langle \tau_{ij} | u_1^r, u_3^r, \theta^r > 0 \rangle$ for different array configurations are qualitatively similar to those for array 1, with the dependence on u_3^r generally stronger and the dependence on u_1^r generally weaker. A comparison of the level of anisotropy for array 2 and array 4 (fixing $-z/L$ and reducing Δ/z from 2.00 for array 2 to 0.48 for array 4), the results for array 4 has fewer points for the axisymmetric SGS stress with one small eigenvalue ($\eta = -\xi$) than that of array 2. This is because the compression

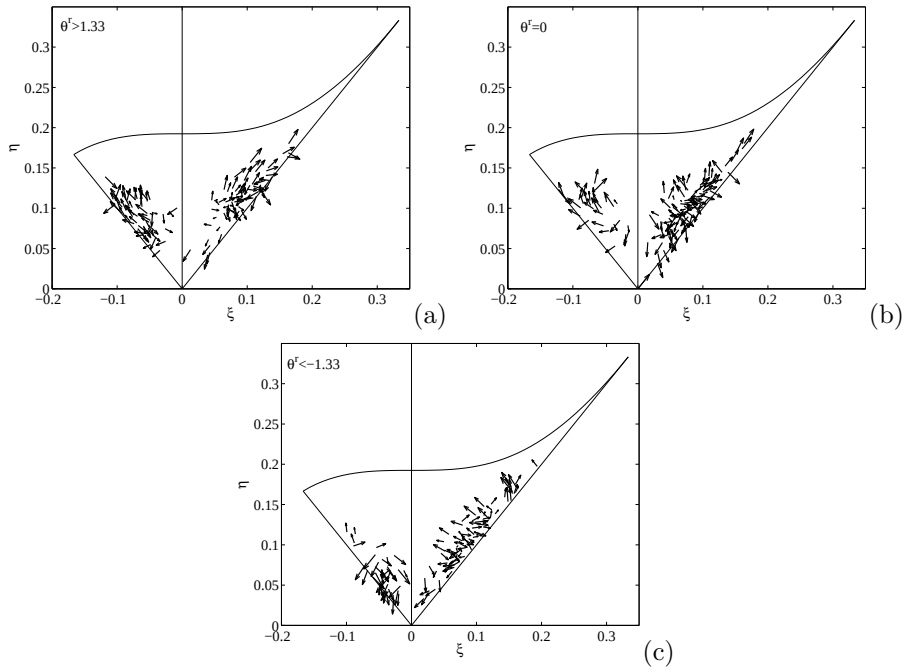

Figure 4.8 Lumley triangle representation of the conditional SGS stress. The arrows represent the conditional vector (u_1^r, u_3^r). (a) for positive θ^r, $\langle \tau_{ij} | u_1^r, u_3^r, \theta^r \rangle$ is quite anisotropic and close to the results for $\langle \tau_{ij} | u_1^r, u_3^r \rangle$ (without conditioning on θ^r); (b) for small θ^r, the results are similar to the (a); (c) for negative θ^r, the conditional SGS stress is less anisotropy.

effects associated with the returning flow of large convective eddies for array 4 are weaker than those of for array 2. A comparison of the levels of anisotropy for array 2 ($\Delta/z = 2.00, -z/L = 0.36$) and array 3 ($\Delta/z = 1.00, -z/L = 0.60$) shows that $\langle \tau_{ij} | u_1^r, u_3^r \rangle$ for array 3 is less anisotropic than that for array 2, and has very few points near the line of axisymmetric SGS stress with one small eigenvalue ($\eta = -\xi$). This is because the enhanced buoyancy due to larger z/L and weakened shear and compression effects due to smaller Δ/z. The level of the anisotropy of $\langle \tau_{ij} | u_1^r, u_3^r, \theta^r \rangle$ for small temperature fluctuations (not shown) is similar to the results for positive temperature fluctuations. For negative temperature fluctuations, the level of anisotropy for different arrays is generally more isotropy and less different, which is due to weaker buoyancy effect. Among the four arrays, array 1 has the largest Δ/z and the smallest $-z/L$, and consequently has the highest level of anisotropy and the strongest compression effects associated with the returning flow of large convective eddies. Therefore, it is expected that the SGS stress and its production rate for array 1 are the most challenging to predict by SGS models. Anisotropic grids (refined in the vertical direction), which are often used near the surface to match the flow interior with the surface (e.g., [21]), therefore are of importance.

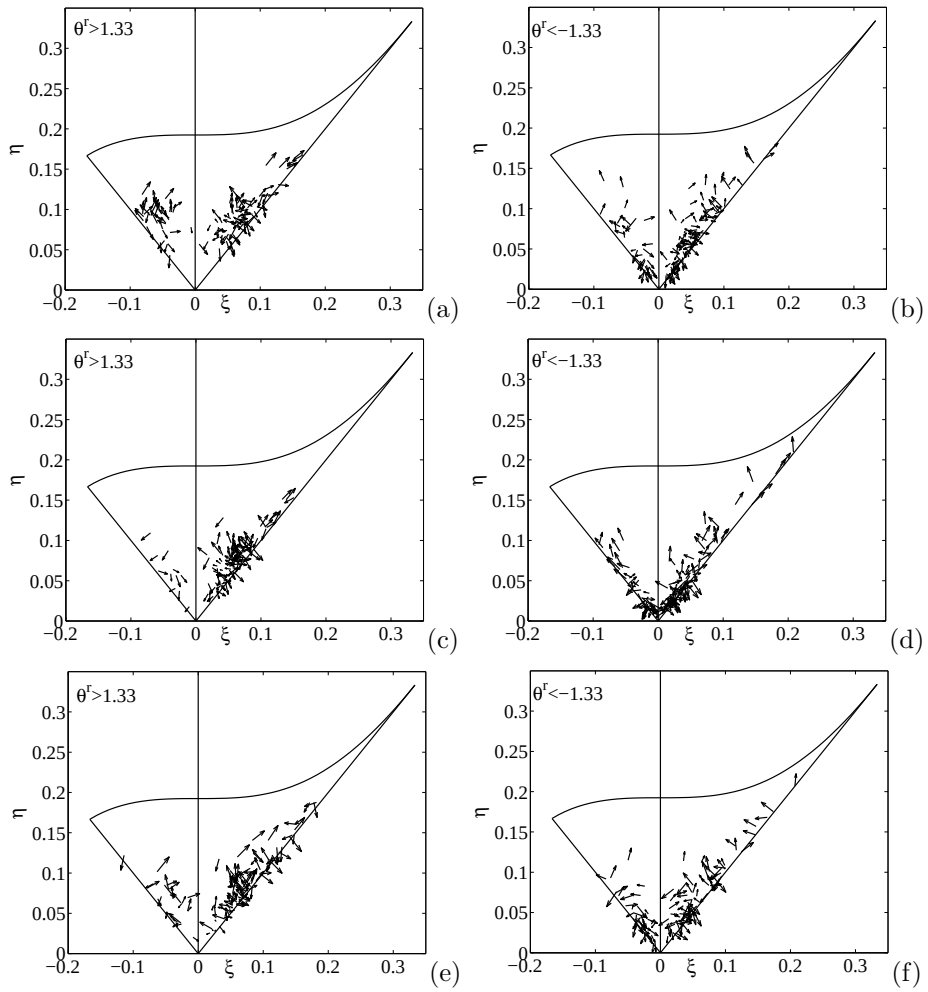

Figure 4.9 The Lumley triangle representation of the conditional SGS stress from other array configurations: (a-b) array 2 ($\Delta/z = 2.00, -z/L = 0.36$); (c-d) array 3 ($\Delta/z = 1.00, -z/L = 0.60$); (e-f), array 4 ($\Delta/z = 0.48, -z/L = 0.35$). The arrows represent the conditioning vector (u_1^r, u_3^r)**.**

4.2.6 Alignment between the conditional SGS stress and its production rate

The geometric alignment of $\left\langle \tau_{ij}^d | \mathbf{u}^r, \theta^r \right\rangle$ and $\left\langle P_{ij}^a | \mathbf{u}^r, \theta^r \right\rangle$ can be characterized by the angles between their eigenvectors. The alignment between $\left\langle \tau_{ij}^d | \mathbf{u}^r \right\rangle$ and $\left\langle P_{ij}^a | \mathbf{u}^r \right\rangle$ ($P_{ij}^a = P_{ij} - P_{kk}\delta_{ij}/3$) were first studied by Chen and Tong (2006) [90] with the finding that $\left\langle \tau_{ij}^d | u_3^r \right\rangle$ and $\left\langle P_{ij}^a | u_3^r \right\rangle$ are well aligned for positive u_3^r with the alignment angles are less than 10° but are less well aligned for negative u_3^r. Here the dependence of the alignment between the conditional SGS stress and its production rate on temperature fluctuations are further examined. The alignment angles are defined in the same way as those in Chen and Tong (2006) [90]. The eigenvalues of the conditional SGS stress tensor, $\left\langle \tau_{ij}^d | \mathbf{u}^r, \theta^r \right\rangle$, are denoted as α_τ, β_τ and γ_τ, ordered such that $\alpha_\tau \geq \beta_\tau \geq \gamma_\tau$, and the corresponding unit eigenvectors as $\vec{\alpha}_\tau, \vec{\beta}_\tau$ and $\vec{\gamma}_\tau$. Similarly, the eigenvalues of the conditional SGS stress production

tensor, $\left\langle P_{ij}^a | \mathbf{u}^r, \theta^r \right\rangle$, are denoted as α_P, β_P and γ_P, ordered such that $\alpha_P \geq \beta_P \geq \gamma_P$, and the corresponding unit eigenvectors as $\vec{\alpha}_P, \vec{\beta}_P$ and $\vec{\gamma}_P$. Three alignment angles, ψ, ϕ and ξ, are defined as $\psi = \cos^{-1}(|\vec{\gamma}_P \cdot \vec{\gamma}_\tau|)$ (the angle between $\vec{\gamma}_P$ and $\vec{\gamma}_\tau$), $\phi = \cos^{-1}(|\vec{\beta}_P \cdot \vec{\beta}_\tau|)$, and $\xi = \cos^{-1}(|\vec{\alpha}_P \cdot \vec{\alpha}_\tau|)$.

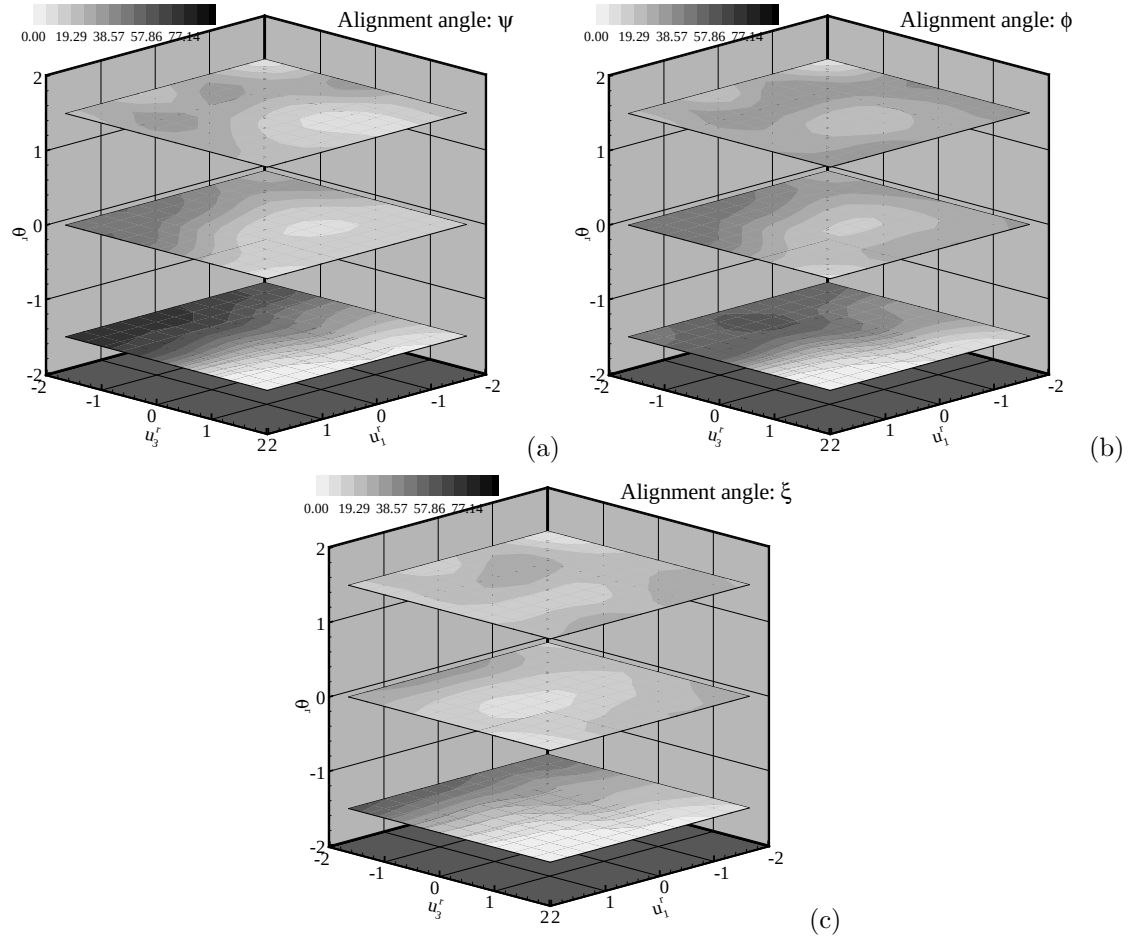

Figure 4.10 Geometric alignment of conditional SGS stress and its production rate. The alignment angles are small for positive θ^r and increases for negative θ^r and u_3^r.

The results for the alignment angles are given in Figure 4.10. The results show that $\left\langle \tau_{ij}^d | \mathbf{u}^r, \theta^r \right\rangle$ and $\left\langle P_{ij}^a | \mathbf{u}^r, \theta^r \right\rangle$ are generally well aligned for positive u_3^r and is less well aligned for negative u_3^r, but that the alignment angles weakly depend on u_1^r, which is similar to the results of Chen and Tong (2006) [90]. Alignment angles are smaller for positive θ^r fluctuations and larger for negative θ^r fluctuations.

The results for the Lumley triangle (Figure 4.8) show that SGS stress is more anisotropic for $u_3^r > 0$, therefore, there is likely a strong trend to return to isotropy, and therefore the pressure destruction can be predicted well by τ_{ij}/t_Δ hence the better alignment where t_Δ is a time scale. In addition, the updrafts with higher temperature ($\theta^r > 0$) generally experience stronger shear and

Table 4.4 Modeled mean SGS scalar flux for array 1

	$\langle F_1 \rangle / H$	$\langle F_2 \rangle / H$	$\langle F_3 \rangle / H$
F_i^{smg}	-0.003	-0.003	0.51
F_i^{nl}	-1.31	0.03	0.13
F_i^{mix}	-1.31	0.03	0.54

temperature gradients near ground with large production rate with the production and pressure destruction as the dominant terms in the SGS stress transport equation, approximately balancing each other. Therefore, the SGS stress and its production rate are well aligned. For $u_3^r < 0$, The Lumley triangle shows that the SGS stress is less anisotropic. Therefore the tendency to return to isotropy may be weaker, resulting in poor alignment. Another possible explanation for the poor alignment is that the production rate is small and is no longer a dominant term to balance the pressure destruction. However, it is not clear which term in the SGS stress transport equation causes the imbalance, although Chen and Tong (2006) [90] showed that the vertical advection term is not the cause.

4.2.7 SGS scalar flux model

The results discussed in the previous parts of this section provide a basis for studying the effects of SGS models on LES statistics. Here the model predictions of $\langle F_i | \mathbf{u}^r, \theta^r \rangle$, $\langle P_{Fi} | \mathbf{u}^r, \theta^r \rangle$ and $\langle P_\theta | \mathbf{u}^r, \theta^r \rangle$ are examined using the Smagorinsky model, the nonlinear model, and the mixed model, and compare them to the experimental results. The mean values of the measured and modeled mean SGS scalar flux components are given in Table 4.4.

In order to compute the modeled SGS scalar flux production rate P_{Fi}, the modeled SGS stress is needed. In this work, the modeled SGS stress is computed using the same procedure given in Chen and Tong (2006) [90]. Previous study ([90]) shows that the conditional mean of the normal components are severely under-predicted by the Smagorinsky model and slightly over-predicted by the nonlinear model. The trends of the shear components are generally well predicted by the Smagorinsky model and are poorly predicted by the nonlinear model. The magnitudes of the shear components are generally under-predicted by a factor of two using the Smagorinsky model. The mixed model can predict normal components well but not the shear component. These results are important for understanding the trends and magnitudes of the conditional mean of the SGS scalar flux production rate discussed in the following.

The Smagorinsky model

The Smagorinsky model is given by Smagorinsky (1963) [60] and Lilly (1967) [1].

$$F_i^{smg} = -Pr_T^{-1}(C_S\Delta)^2(2S_{mn}S_{mn})^{1/2}\frac{\partial\theta^r}{\partial x_i} \tag{4.12}$$

where $C_s = 0.154$ is the Smagorinsky constant for a box filter and Pr_T is the SGS turbulent Prandtl number, and S_{ij} is the resolvable-scale velocity strain rate. In this work, $Pr_T^{-1}C_s^2$ is determined by matching the mean SGS scalar variance production rate.

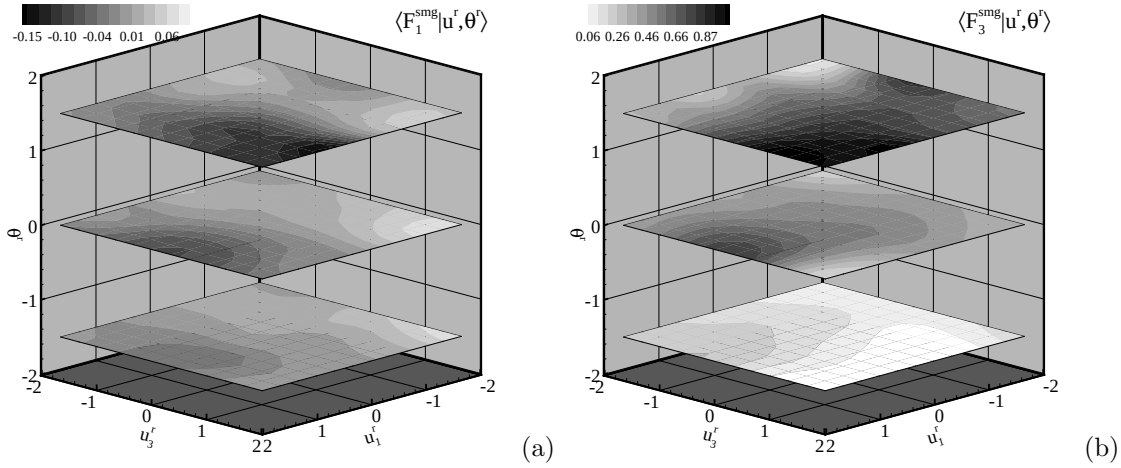

Figure 4.11 Predicted conditional SGS scalar flux using the Smagorinsky model. The trend of $\langle F_3|\mathbf{u}^r,\theta^r\rangle$ is well predicted.

Tables 4.3 and 4.4 show that the mean horizontal SGS scalar flux is severely under-predicted and the mean vertical SGS scalar flux is under-predicted by approximately 30 percent. The predicted conditional means using the Smagorinsky model are shown in Figure 4.11 and 4.12. Figures 4.11(a) and 4.1(a) shows that the horizontal SGS scalar flux, $\langle F_1|\mathbf{u}^r,\theta^r\rangle$ is under-predicted, because the model uses only the horizontal scalar gradient $\partial\theta^r/\partial x_1$, which is very small. The sign of $\langle F_1|\mathbf{u}^r,\theta^r\rangle$ is also not predicted correctly. As discussed in Section 4.2.1 the conditional production of F_1 is dominated by $\left\langle F_3\frac{\partial u_1^r}{\partial x_3}|\mathbf{u}^r,\theta^r\right\rangle$ and $\left\langle \tau_{13}\frac{\partial\theta^r}{\partial x_3}|\mathbf{u}^r,\theta^r\right\rangle$. However, these gradients do not appear in the model; therefore the model cannot account for the dominant production mechanisms and consequently cannot predict the flux correctly. The results demonstrate the importance of including the effects of the dominant vertical gradient in the modeling of $\langle F_1|\mathbf{u}^r,\theta^r\rangle$.

Figures 4.11(b) and 4.1(c) shows that the magnitude of the vertical SGS scalar flux $\langle F_3|\mathbf{u}^r,\theta^r\rangle$ is better predicted than that of $\langle F_1|\mathbf{u}^r,\theta^r\rangle$. The trends of $\langle F_3|\mathbf{u}^r,\theta^r\rangle$ are generally well predicted for

positive θ^r fluctuations. The trends for small θ^r fluctuations are somewhat less well predicted. Because $\langle F_3^{smg}|\mathbf{u}^r,\theta^r\rangle$ uses the gradients $\partial\theta^r/\partial x_3$ which is in the dominant term in P_{F3}, it is generally much better predicted than $\langle F_1^{smg}|\mathbf{u}^r,\theta^r\rangle$

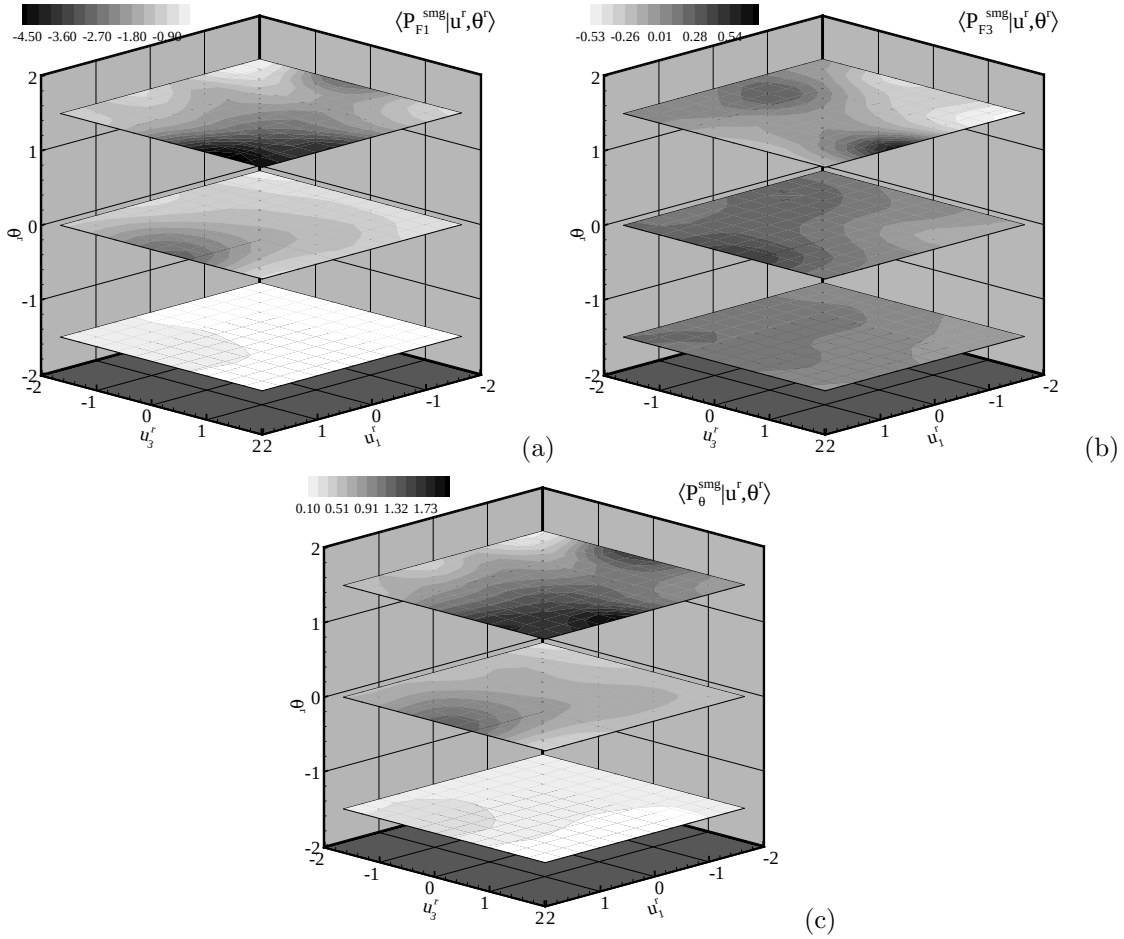

Figure 4.12 Predicted conditional SGS scalar flux production rate and SGS scalar variance production rate using the Smagorinsky model. The trend of $\langle P_{F1}|\mathbf{u}^r,\theta^r\rangle$ is well predicted.

The trend of $\langle P_{F1}|\mathbf{u}^r,\theta^r\rangle$ is generally well predicted (Figures 4.12(a) and 4.2(a)). $\langle P_{F1}^{smg}|\mathbf{u}^r,\theta^r\rangle$ $(=-\left\langle\tau_{1k}^{smg}\frac{\partial\theta^r}{\partial x_k}+F_k^{smg}\frac{\partial u_1^r}{\partial x_k}|\mathbf{u}^r,\theta^r\right\rangle)$ is dominated by the term $-\left\langle F_3^{smg}\frac{\partial u_1^r}{\partial x_3}+\tau_{13}^{smg}\frac{\partial\theta^r}{\partial x_3}|\mathbf{u}^r,\theta^r\right\rangle$. Therefore, the well predicted trend of $\langle P_{F1}|\mathbf{u}^r,\theta^r\rangle$ is largely due to the well predicted trends of τ_{13} and F_3. However, the magnitude is under-predicted approximately by a factor of two due to the under-prediction of the magnitude of τ_{13} ([90]) and F_3. The trend and magnitude of $\langle P_{F3}|\mathbf{u}^r,\theta^r\rangle$ in Figure 4.12(b) are poorly predicted. As discussed in Section 4.2.1 $\langle P_{F3}^{smg}|\mathbf{u}^r,\theta^r\rangle$ $(=-\left\langle\tau_{3k}^{smg}\frac{\partial\theta^r}{\partial x_k}+F_k^{smg}\frac{\partial u_3^r}{\partial x_k}|\mathbf{u}^r,\theta^r\right\rangle)$ is dominated by the term $\left\langle-\tau_{33}^{smg}\frac{\partial\theta^r}{\partial x_3}|\mathbf{u}^r,\theta^r\right\rangle$. Therefore, the poor prediction of $\langle P_{F3}|\mathbf{u}^r,\theta^r\rangle$ is due to the poor prediction of τ_{33} by the Smagorinsky model ([90]). The trend and magnitude of $\langle P_\theta|\mathbf{u}^r,\theta^r\rangle$ in Figure 4.12(c) are generally well predicted, which is likely to lead to well predicted skewness of

θ^r. The dominant term of $\langle P_\theta^{smg}|\mathbf{u}^r,\theta^r\rangle$ is $\left\langle F_3^{smg}\frac{\partial\theta^r}{\partial x_3}|\mathbf{u}^r,\theta^r\right\rangle$, therefore, the well predicted trend (the magnitude is matched) is due to the well predicted trend of F_3.

The results for the SGS production rates show that when the conditional means of the SGS stress and/or flux components that appear in a SGS production rate are well predicted by a SGS model, the conditional mean of the SGS production rate is also well predicted. This suggests that the correlations between the conditional fluctuations of the SGS stress (flux) and the resolvable-scale gradients are of less importance. Consequently, it appears to be sufficient to focus on the conditional means.

The nonlinear model

The nonlinear model ([82, 22]) is essentially the first order approximation of the similarity model [24] and is given by:

$$F_i^{nl} = \frac{1}{12}\Delta^2\frac{\partial\theta^r}{\partial x_k}\frac{\partial u_i^r}{\partial x_k}. \tag{4.13}$$

The predictions of the nonlinear model are shown in Figures 4.13 and 4.14. In general, the nonlinear model predicts the overall trends and the magnitudes better than the Smagorinsky model. The trends for small θ^r fluctuations are under-predicted but the magnitude is slightly over-predicted.

The mean horizontal SGS scalar flux is over-predicted by approximately 35 percent and the mean vertical SGS scalar flux is under-predicted by approximately 80 percent. The predicted magnitude of $\langle F_1|\mathbf{u}^r,\theta^r\rangle$ using the nonlinear model is better than that of the Smagorinsky model. The better prediction can be understood as following: data (not shown) indicate that the nonlinear model component $F_1^{nl} = \frac{\partial\theta^r}{\partial x_k}\frac{\partial u_1^r}{\partial x_k}$ is dominated by the term $\frac{\partial\theta^r}{\partial x_3}\frac{\partial u_1^r}{\partial x_3}$, which can be rewritten in terms of the Smagorinsky-model-like terms as

$$F_1^{nl} \sim \frac{\partial\theta^r}{\partial x_3}\frac{\partial u_1^r}{\partial x_3} \propto F_3^{smg}\frac{\partial u_1^r}{\partial x_3} + \tau_{13}^{smg}\frac{\partial\theta^r}{\partial x_3}. \tag{4.14}$$

The previous section shows that τ_{13} and F_3 are well predicted by the Smagorinsky model. Therefore, the term $F_3^{smg}\frac{\partial u_1^r}{\partial x_3} + \tau_{13}^{smg}\frac{\partial\theta^r}{\partial x_3}$ in equation (15) is effectively the Smagorinsky model prediction of $\langle P_{F1}|\mathbf{u}^r,\theta^r\rangle$. Figures 4.1(a), 4.2(a), and 4.4(a) have shown that the conditional SGS flux and the conditional flux production rate have similar trends, which is likely a result of the balance between the SGS flux production rate and the pressure destruction and the fact that the latter can be quite well predicted by the SGS flux and a SGS time scale. Therefore, $\langle F_1|\mathbf{u}^r,\theta^r\rangle$ is better predicted by the nonlinear model.

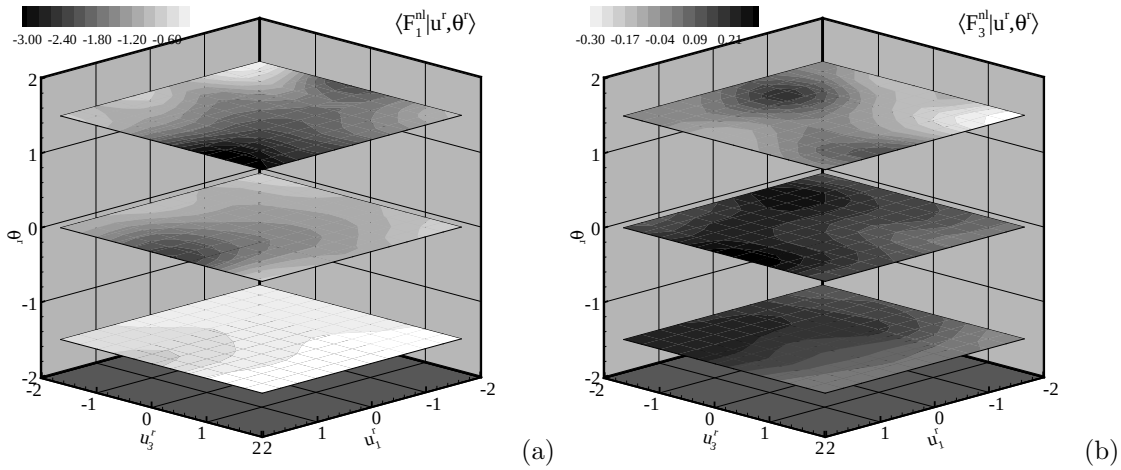

Figure 4.13 Predicted conditional SGS scalar flux using the nonlinear model. The trend of $\langle F_1|\mathbf{u}^r,\theta^r\rangle$ is well predicted.

The trend of $\langle F_3|\mathbf{u}^r,\theta^r\rangle$ is under-predicted. Furthermore, $\left\langle F_3^{nl}|\mathbf{u}^r,\theta^r\right\rangle$ has some spurious negative values and the magnitudes for positive values are under-predicted. The dominant component of F_3^{nl} is $\frac{\partial\theta^r}{\partial x_3}\frac{\partial u_3^r}{\partial x_3}$, which can be rewritten as

$$F_3^{nl} \sim \frac{\partial\theta^r}{\partial x_3}\frac{\partial u_3^r}{\partial x_3} \propto \tau_{33}^{smg}\frac{\partial\theta^r}{\partial x_3}. \tag{4.15}$$

Because τ_{33} is poorly modeled by the Smagorinsky model, $\frac{\partial\theta^r}{\partial x_3}\frac{\partial u_3^r}{\partial x_3}$ is not a good model for the dominant term of P_{F3}. Therefore, $\langle F_3|\mathbf{u}^r,\theta^r\rangle$ is poorly modeled by the nonlinear model.

The above analysis of the nonlinear model using the Smagorinsky model and the surface layer SGS dynamics provides a physical explanation of the performance of the nonlinear model. Here a similar analysis of the nonlinear SGS stress model is also provided. The normal component of the nonlinear model τ_{11}^{nl} can be rewritten as $\tau_{11}^{nl} \sim \frac{\partial u_1^r}{\partial x_1}\frac{\partial u_1^r}{\partial x_1} + \frac{\partial u_1^r}{\partial x_2}\frac{\partial u_1^r}{\partial x_2} + \frac{\partial u_1^r}{\partial x_3}\frac{\partial u_1^r}{\partial x_3} \propto \tau_{11}^{smg}\frac{\partial u_1^r}{\partial x_1} + \tau_{12}^{smg}\frac{\partial u_1^r}{\partial x_2} + \tau_{13}^{smg}\frac{\partial u_1^r}{\partial x_3}$. Because the trend of τ_{13} is well predicted by the Smagorinsky model, $\tau_{13}^{smg}\frac{\partial u_1^r}{\partial x_3}$ is a good model for the dominant term in P_{11}, therefore, τ_{11} is well predicted. Similarly, the dominant term in τ_{33}^{nl}, $\frac{\partial u_3^r}{\partial x_3}\frac{\partial u_3^r}{\partial x_3}$, can be written as $\tau_{33}^{smg}\frac{\partial u_3^r}{\partial x_3}$. Because τ_{33} is poorly predicted by the Smagorinsky model, so is τ_{33} by the nonlinear model.

These model predictions can also be used to analyze predictions of $\langle P_{ij}|\mathbf{u}^r,\theta^r\rangle$. The magnitude and the trend of $\langle P_{F1}|\mathbf{u}^r,\theta^r\rangle$ for positive θ^r fluctuations are not well predicted (Figure 4.14(a)). This is due to the poor predictions of F_3 and τ_{13}, which are in the dominant terms in $\langle P_{F1}|\mathbf{u}^r,\theta^r\rangle$ $(-\left\langle F_3\frac{\partial u_1^r}{\partial x_3} + \tau_{13}\frac{\partial\theta^r}{\partial x_3}|\mathbf{u}^r,\theta^r\right\rangle)$. The magnitude of $\langle P_{F3}|\mathbf{u}^r,\theta^r\rangle$ (Figure 4.14(b)) is under-predicted, while the trend for positive θ^r fluctuations is better predicted than that for small and negative θ^r fluctuations. This is due to the well predicted trend of τ_{33}, which is in the dominant term of

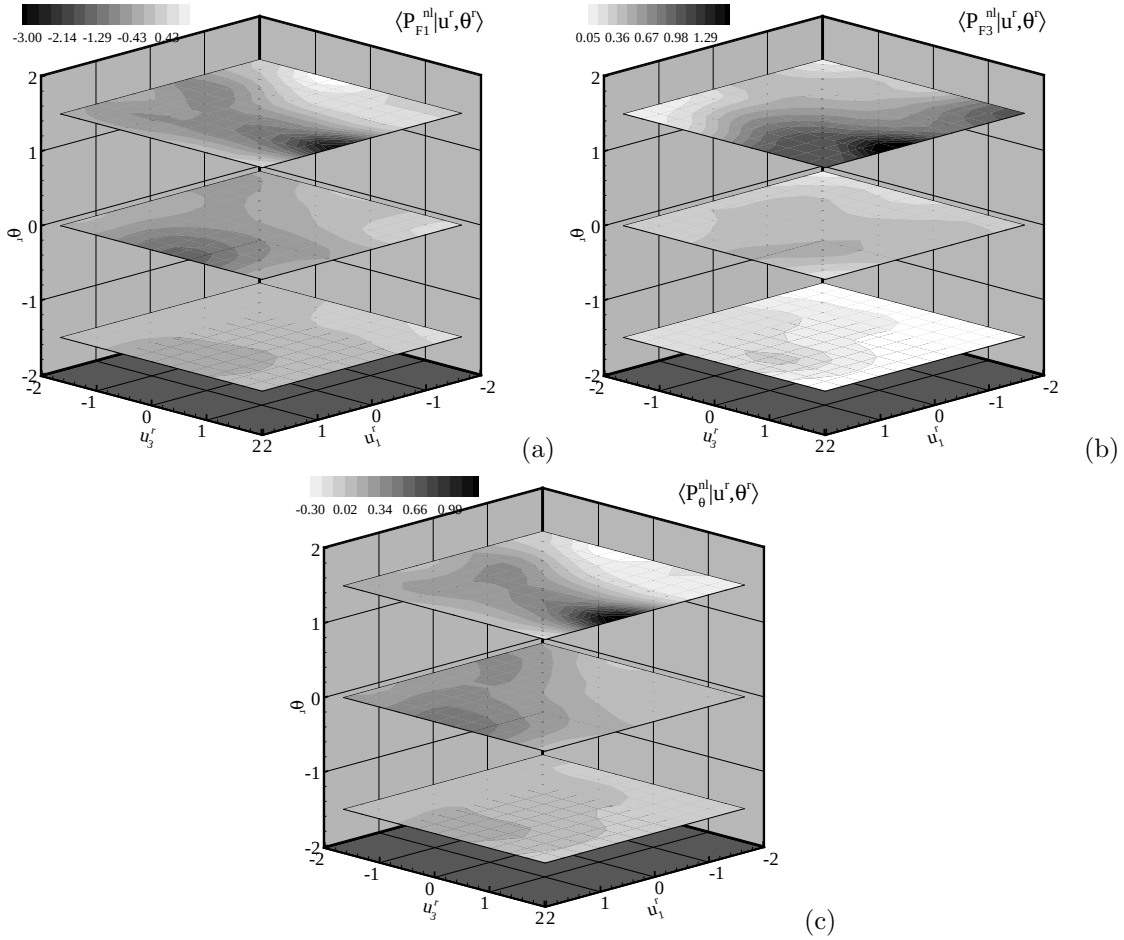

Figure 4.14 Predicted conditional SGS scalar flux production rate and the scalar variance production rate using the nonlinear model.

$\langle P_{F3}|\mathbf{u}^r,\theta^r\rangle$ ($\left\langle -\tau_{33}\frac{\partial\theta^r}{\partial x_3}|\mathbf{u}^r,\theta^r\right\rangle$). The magnitude of $\langle P_\theta|\mathbf{u}^r,\theta^r\rangle$ is well predicted, whereas the trend is not as well predicted as the Smagorinsky model. This is due to the poor prediction of F_3, which is in the dominant term of $\langle P_\theta|\mathbf{u}^r,\theta^r\rangle$ ($\left\langle F_3\frac{\partial\theta^r}{\partial x_3}|\mathbf{u}^r,\theta^r\right\rangle$).

The mixed model

The previous results show that the Smagorinsky model can predict quite well $\langle F_3|\mathbf{u}^r,\theta^r\rangle$, but not $\langle F_1|\mathbf{u}^r,\theta^r\rangle$, and the nonlinear model can predict quite well $\langle F_1|\mathbf{u}^r,\theta^r\rangle$, but not $\langle F_3|\mathbf{u}^r,\theta^r\rangle$. Therefore, a mixed model combining these two models, as done for SGS stress ([22, 30]),

$$F_i^{mix}=\frac{1}{12}\Delta^2\frac{\partial\theta^r}{\partial x_k}\frac{\partial u_i^r}{\partial x_k}-Pr_T^{-1}(C_S\Delta)^2(2S_{mn}S_{mn})^{1/2}\frac{\partial\theta^r}{\partial x_i}, \tag{4.16}$$

can potentially provide improved predictions.

The mean horizontal SGS scalar flux is over-predicted by approximately 35 percent and the mean vertical SGS scalar flux is under-predicted by approximately 23 percent. The results of the

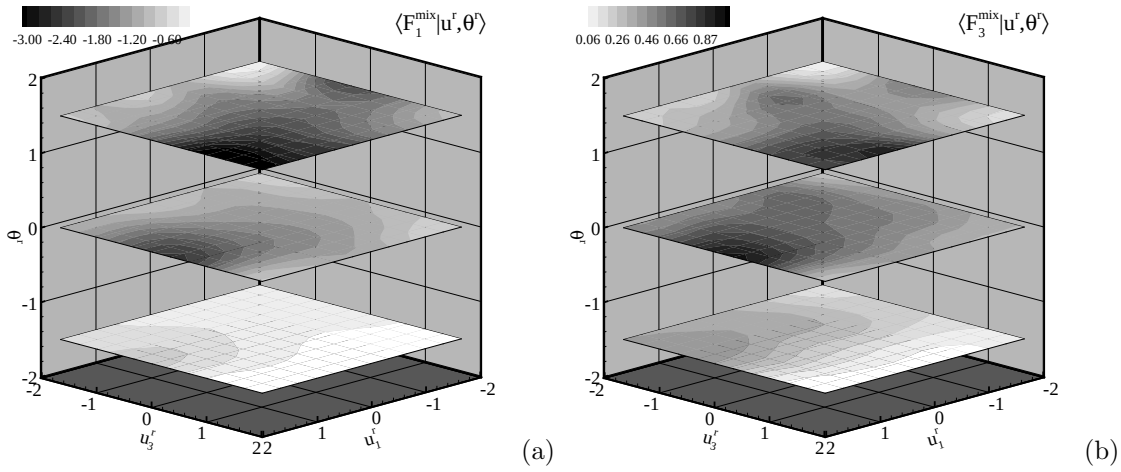

Figure 4.15 Predicted conditional SGS scalar flux using the mixed model.

conditional means for the mixed model are shown in Figure 4.15 and 4.16. The predicted magnitude and trend of $\langle F_1|\mathbf{u}^r,\theta^r\rangle$ are close to, but not quite as good as the predictions of the nonlinear model due to the under-predicted magnitude of $\langle F_1|\mathbf{u}^r,\theta^r\rangle$ by the Smagorinsky part of the model. The predicted trend of $\langle F_3|\mathbf{u}^r,\theta^r\rangle$ is in between the predictions of the Smagorinsky model and the nonlinear models, because the magnitude of $\left\langle F_3^{nl}|\mathbf{u}^r,\theta^r\right\rangle$ is comparable to that of $\langle F_3^{smg}|\mathbf{u}^r,\theta^r\rangle$.

The magnitude and trend of $\left\langle P_{F1}^{mix}|\mathbf{u}^r,\theta^r\right\rangle$ are close to the predictions of the nonlinear model with improved magnitude. This is because the mixed model predictions of F_3 and τ_{13} are better than the nonlinear model, but not as good as the Smagorinsky model. The magnitude of $\left\langle P_{F3}^{mix}|\mathbf{u}^r,\theta^r\right\rangle$ is close to the predictions of the nonlinear model, because the magnitude of $\langle P_{F3}^{smg}|\mathbf{u}^r,\theta^r\rangle$ is smaller than that of $\left\langle P_{F3}^{nl}|\mathbf{u}^r,\theta^r\right\rangle$. The trend of $\left\langle P_{\theta}^{mix}|\mathbf{u}^r,\theta^r\right\rangle$ is in between those of $\left\langle P_{\theta}^{nl}|\mathbf{u}^r,\theta^r\right\rangle$ and $\langle P_{\theta}^{smg}|\mathbf{u}^r,\theta^r\rangle$. Therefore, the prediction of $\langle P_\theta|\mathbf{u}^r,\theta^r\rangle$ using the mixed model is not as good as that of the Smagorinsky model but better than that of the nonlinear model. Therefore, the mixed model offers a compromise between the Smagorinsky model and the nonlinear model.

4.2.8 Potential effects of SGS models on the resolvable-scale statistics

The conditional SGS fluxes and their production rates discussed above evolve the resolvable-scale velocity-scalar JPDF through equation (4.6). Deviations of SGS model predictions from their true values will lead to inaccuracies in the predicted JPDF. Chen and Tong (2006) [90] discussed the potential effects of the modeled SGS stress and their prediction rates on the resolvable-scale velocity JPDF. Here the velocity-scalar JPDF is focused.

The results in previous sections show that the conditional horizontal scalar flux production rate is dominated by $\left\langle -F_3\frac{\partial u_1^r}{\partial x_3}|\mathbf{u}^r,\theta^r\right\rangle$ and $\left\langle -\tau_{13}\frac{\partial \theta^r}{\partial x_3}|\mathbf{u}^r,\theta^r\right\rangle$, and the conditional vertical scalar flux

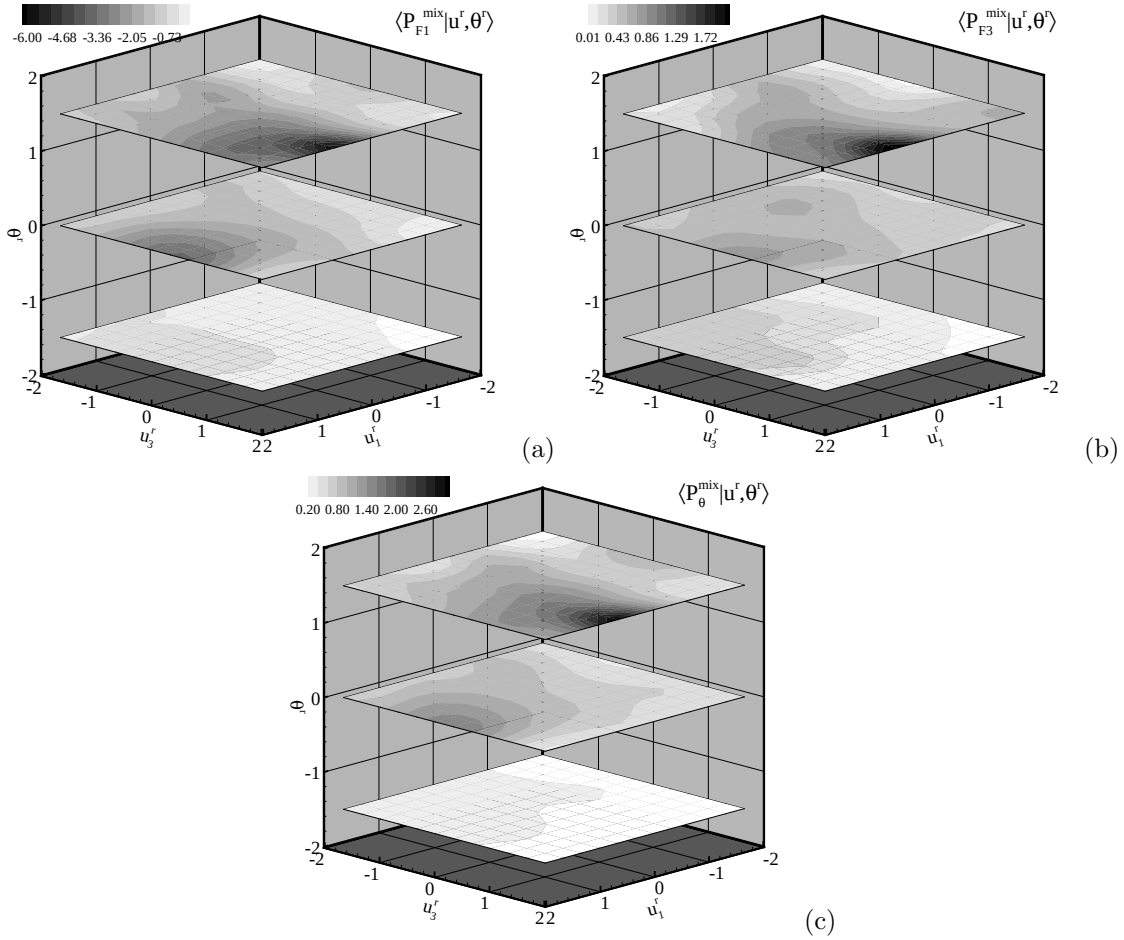

Figure 4.16 Predicted conditional SGS scalar flux production rate and SGS scalar variance production rate using the mixed model.

production rate is dominated by $\left\langle -\tau_{33}\frac{\partial\theta^r}{\partial x_3}|\mathbf{u}^r,\theta^r\right\rangle$. Therefore, correct predictions of F_3,τ_{13} and τ_{33} are very important for reproducing the resolvable-scale velocity-scalar JPDF. It is emphasized that τ_{13} and τ_{33} not only affect the resolvable-scale velocity statistics, but also the resolvable-scale scalar and velocity-scalar joint statistics.

The Smagorinsky model under-predicts the conditional horizontal SGS scalar flux but predicts well the trend of the conditional vertical SGS scalar flux. The under-prediction of the conditional horizontal SGS scalar flux directly affects the scalar PDF, and therefore the velocity-scalar JPDF. The model also under-predicts the conditional τ_{33} ([90]). Because τ_{33} appears in the dominant term of the conditional vertical scalar flux production rate, $\tau_{33}\frac{\partial\theta^r}{\partial x_3}$, the under-prediction of the conditional τ_{33} causes under-prediction of the conditional vertical scalar flux production rate, which in turn results in under-prediction of the resolvable-scale vertical scalar flux (velocity-temperature

correlation). With a constant heat flux boundary condition, the mean scalar gradient will be over-predicted because the LES fields have to adjust themselves to carry the correct heat flux at the boundary. The improved mean scalar profile using the split model ([8]) and stochastic model ([10]) may be partly because these models provide improved τ_{13} and τ_{33}, which is important for predicting the scalar flux production rate.

The nonlinear model can predict quite well the conditional horizontal SGS scalar flux but not the vertical SGS flux. Again due to the constant heat flux boundary condition the under-prediction of the vertical SGS scalar flux causes over-prediction of the mean scalar gradient. The under-predictions of the conditional F_3 and τ_{13} also cause under-prediction of the conditional P_{F1}, which results in under-prediction of the horizontal resolvable-scale scalar flux.

These potential SGS models effects indicate that for LES to reproduce a resolvable-scale statistics, all the relevant conditional SGS stress, flux, and SGS production rates must be correctly predicted. An example in which this condition is not satisfied is the poor prediction of the conditional τ_{33} by the Smagorinsky model, which can lead to incorrect predictions of the conditional P_{F3} and hence the resolvable-scale vertical scalar flux even when F_3 is quite well predicted. Previous efforts to improve SGS models generally focused on the model predictions of the SGS stress and flux. The results here show that in addition to the SGS stress and flux, the predictions of the SGS production rates must also be improved.

The statistical *a priori* tests in Chen and Tong (2006) [90] and in the present work using the JPDF equation method, which differ qualitatively from the traditional *a priori* analyses, demonstrate the importance of modeling the conditional SGS stress, flux, and SGS production rate for correctly reproducing LES statistics. To evaluate the model performance in actual simulations, *a posteriori* test must be conducted. LES data of high-Reynolds number convective atmospheric boundary layers have been begun being used to obtain these conditional statistics. Like the *a priori* tests, such *a posteriori* tests are also qualitatively different from the traditional ones. For traditional *a posteriori* tests, the mean, variance, spectra profile and other. flow parameters are compared with experiment measurements. A major limitation of the traditional tests is that it is difficult to relate the deficiencies of LES results to specific aspects of the model behaviors. This is partly because the SGS stress evolves LES fields through dynamic equations, which are chaotic with many degrees of freedom, making it difficult to relate the properties of the solutions to the behaviors of the SGS terms in the equation. By contrast, the *a posteriori* tests examine the conditional means, which evolve directly the resolvable-scale velocity and scalar statistics through the JPDF equation, which is not chaotic. Therefore, it provides a more direct link between the resolvable-scale statistics and

the SGS models. The conditional means of SGS stress, scalar flux, and their production rate are compared with the *a prior* test results here and in Chen and Tong (2006) [90]. The results, which will be published separately from the present work, show a high level of consistency between the *a priori* and *a posteriori* tests, providing future support for PDF equation-based approach for studying SGS turbulence and SGS models.

4.3 Summary

In the present study, Field measurements data taken in a convective atmospheric boundary layer was used to analyze the SGS statistics that evolve the resolvable-scale velocity-scalar JPDF. These statistics must be correctly modeled for LES to reproduce the JPDF. The results show that the statistics, including the conditional SGS scalar flux, its production rate, and the SGS scalar variance production rate conditional on the resolvable-scale velocity and scalar, depend strongly on the resolvable-scale velocity and scalar and the dependence is closely related to the surface layer dynamics. Therefore, SGS model predictions of these SGS statistics can potentially have strong effects on LES statistics.

Analyses show that the dependence is generally strong for positive resolvable-scale temperature fluctuations and is weak for negative fluctuations. For positive θ^r fluctuations, eddies associated with updrafts generally come from the near ground region, which contain large magnitudes of vertical SGS flux and SGS stress, and experience strong shear and vertical temperature gradient, resulting in large SGS flux production rates. For small θ^r fluctuations, eddies are generally well mixed, therefore, the results tend to be more symmetric with respect to u_3^r. For negative θ^r fluctuations, eddies associated with downdrafts generally come from the mixed layer region, which carry relatively small fluxes, resulting small magnitudes and weak dependence of the conditional SGS scalar flux production rates on the resolvable-scale velocity. Therefore, it may be more important (and more difficult) to model correctly the strong dependence for positive θ^r fluctuations. In addition, the dependence of the SGS stress and its production rate on the resolvable-scale temperature suggests that it may be beneficial to model such dependencies to account for flow-history effects.

The vertical SGS scalar flux is shown to have a "slow" effect on the horizontal SGS scalar production rate. The horizontal SGS scalar flux does not influence directly the vertical SGS scalar flux production rate but nonetheless affects the resolvable-scale scalar PDF. It is argued that the dependencies of the SGS stress and its production rate on the resolvable-scale temperature fluctuations are partly due to the flow history effect.

The conditional SGS scalar flux and the conditional SGS scalar flux production rate have similar trends and are generally well aligned for positive θ^r fluctuations with the alignment angle being generally less than 10°. This is consistent with the balance between the production rate and pressure destruction and the validity of using the SGS scalar flux and a time scale for the pressure destruction. The similarities and the dynamic connections between the conditional scalar flux and its production rate provide the potential of using the conditional scalar flux production rate to model the scalar flux in convective ABLs.

The Lumley triangle representation of the conditional SGS stress shows that the anisotropy of $\langle \tau_{ij} | u_1^r, u_3^r, \theta^r \rangle$ for positive temperature fluctuations is quite strong and is close to the that for $\langle \tau_{ij} | u_1^r, u_3^r \rangle$ (without conditioning on θ^r). The conditional SGS stress are not far from being axisymmetric with either one small or large eigenvalue. For small θ^r fluctuations, the results are somewhat similar to the results for positive θ^r fluctuations. For negative θ^r fluctuations, the conditional SGS stress is less anisotropic. The conditional SGS stress and its production are generally well aligned for positive θ^r fluctuations and are less well aligned for negative θ^r, consistent with the results on the Lumley triangle and the possible quasi-equilibrium between the SGS stress production and pressure destruction.

Statistical *a priori* tests using these conditional statistics show that the Smagorinsky model under-predicts the conditional horizontal scalar flux but it predicts quite well the conditional vertical SGS scalar flux because it uses the dominant vertical scalar gradients. The model also predicts quite well the trends of the conditional horizontal scalar flux production rate, because the conditional τ_{13} and F_3 are quite well predicted. However, it predicts poorly the conditional vertical SGS scalar flux production rate due to its poor prediction of τ_{33}. The conditional scalar variance production rate are well predicted because the trend of F_3 is well predicted, which may lead to good prediction of the resolvable-scale scalar skewness.

The nonlinear model predicts quite well the conditional horizontal SGS scalar flux. Both the conditional horizontal and vertical SGS scalar flux production rates are under-predicted. Predictions of the SGS flux using the nonlinear model are found to be closely related to the predictions of the Smagorinsky model and the quasi-equilibrium between the production and pressure destruction. The analysis of the nonlinear model using the Smagorinsky model and the surface layer dynamics provides a physical explanation of the performance of the nonlinear model. A similar analyse of the nonlinear SGS stress model are also performed.

Analyses of the SGS models show that the current SGS models have varying level of performance in predicting different SGS components. Often the poor prediction of one SGS flux component

affects the prediction of the production rate of another SGS flux component, thereby resulting in errors in the LES statistics that depend on the production rate. Therefore, efforts to improve SGS models need to ensure that all the relevant SGS fluxes related to the LES statistics of interests or of importance to the intended applications are correctly predicted.

CHAPTER 5

A new *a posteriori* test for subgrid-scale stress models

In this chapter, a new *a posteriori* test is employed to study SGS model performance. Large eddy simulation (LES) computes the large, or resolvable scales of turbulent flows, and models the effects of the small, or subgrid (SGS) scales. In the ideal situation, the filter scale is in the inertial range, the energy-containing scales are well resolved and most of the turbulent stresses is carried by the resolvable scales. Under such conditions the LES result is to some extent insensitive to the subgrid-scale model employed ([6, 21]).

However, in LES of many important flows, such as in the near-wall region of a high-Reynolds-number turbulent boundary layer, the filter scale is inevitably in the energy-containing scales because the latter scale with the distance from the surface ([62, 21, 32, 48, 49]). Consequently, a significant portion of the turbulent stress must be carried by the SGS model, thereby causing strong dependence of the results on the SGS model ([49]). The deficiencies in the SGS model are therefore likely to lead to errors in LES results in the near-wall region. For example, LES of the unstable ABL using the Smagorinsky model over-predicts the mean shear and the streamwise velocity variance ([6, 21, 10, 63]) in the surface layer, and at the same time under-predicts the vertical velocity skewness. These deficiencies in LES results has been argued to be related to the Smagorinsky model's being too dissipative ([21, 10]). Various methods for improving LES results have been developed, including stochastic backscatter ([65, 66, 8]), the split model of Schumann ([65, 10]), a nonlinear model ([67]), and the scale-dependent dynamic Smagorinsky model ([64]). The improvements achieved by these methods demonstrated the importance of incorporating surface-layer SGS physics into SGS models and of systematically understanding the effects of model behaviors on LES results. Therefore, an important question in improving SGS models is how the SGS turbulence and SGS models affect the resolvable-scale statistics under these conditions.

Traditional *a priori* and *a posteriori* tests of SGS models (e.g., [22, 23, 24, 6, 25, 26, 8, 27, 28, 29, 30, 21, 31, 32, 33, 19, 34, 35, 36]), although have contributed greatly to understanding of the

current SGS models, provide little information regarding the relationship between SGS models and LES results (statistics). For *a priori* tests it is difficult to predict the effects of model behaviors on LES results. For example, the correlation between the modeled and measured SGS stress components provides little information about model performance in a simulation. For *a posteriori* tests it is difficult to relate deficiencies of LES results (e.g., the mean velocity and Reynolds stress profiles) to specific aspects of the model behaviors.

To better understand the relationship between SGS models and LES statistics, as well as that between the SGS turbulence and the resolvable-scale statistics, a systematic *a priori* test approach was developed ([38, 91, 90]) using the transport equations of the resolvable-scale velocity and velocity-scalar joint probability density function (JPDF). This approach analyzes the SGS dynamic terms that evolves the JPDF, which contains all single-point velocity statistics, through the JPDF equation, thereby making it possible to relate models test results to LES statistics, i.e., model performance in simulations.

Chen and Tong (2006) [90] used this approach to study the SGS turbulence in the surface layer of the atmospheric boundary layer and identified several deficiencies of the SGS models that affects the LES statistics. The Smagorinsky model, the nonlinear model, the mixed model, and the Kosović's nonlinear model were tested using the JPDF equation method in a convective atmospheric surface layer in their study, which differ qualitatively from the traditional *a priori* analyses. They found that none of these models can predict both conditional SGS stress and conditional SGS stress production rate correctly at the same time. The Smagorinsky and the Kosović's nonlinear model under-predict the anisotropy and the variations of the anisotropy whereas the nonlinear model and the mixed model over-predict both, which are considered to be important for predicting the mean shear and the streamwise velocity variance profile. The under-prediction of the vertical velocity skewness is argued to be related to the inability to predict the asymmetry in $\langle P_{33}|u_3^r\rangle$. Therefore, such *a priori* analyses using PDF equation can provide important guidance for developing SGS models. To evaluate the model performance in actual simulations, these conditional statistics need to be examined in actual LES.

In the present work, a new *a posteriori* test is developed based on the transport equations of the resolvable-scale velocity JPDF to study the subgrid-scale (SGS) stress using the LES data in the atmospheric surface layer. The resolvable-scale velocity JPDF equation was given by Chen and

Tong (2006) [90]:

$$\begin{aligned}\frac{\partial f}{\partial t}+v_j\frac{\partial f}{\partial x_j} &= \frac{\partial^2}{\partial v_i\partial x_j}\left\{\langle\tau_{ij}|\mathbf{u}^r=\mathbf{v}\rangle f\right\}+\frac{\partial^2}{\partial v_i\partial v_j}\left\{\left\langle-\frac{1}{2}P_{ij}|\mathbf{u}^r=\mathbf{v}\right\rangle f\right\}\\ &+ \frac{\partial^2}{\partial v_i\partial x_i}\left\{\langle p^r|\mathbf{u}^r=\mathbf{v}\rangle f\right\}+\frac{\partial^2}{\partial v_i\partial v_j}\left\{\left\langle p^r\frac{\partial u_j^r}{\partial x_i}|\mathbf{u}^r=\mathbf{v}\right\rangle f\right\}\\ &- \frac{g}{\Theta}\frac{\partial}{\partial v_3}\left\{\langle\theta^r|\mathbf{u}^r=\mathbf{v}\rangle f\right\}. \qquad (5.1)\end{aligned}$$

where

$$\tau_{ij}=(u_iu_j)^r-u_i^ru_j^r$$

is the SGS stress (the Leonard stress $L_{ij}=(u_i^ru_j^r)^r-u_i^ru_j^r$ has been included in τ_{ij}), a superscript r denotes a resolvable-scale variable, Θ and θ are the mean and fluctuation potential temperatures, respectively.

The left-hand side of the equation is the time derivative and the advection in physical space. The right-hand side represents mixed transport in physical and velocity spaces by the conditional SGS stress and the resolvable-scale pressure and transport in velocity space by the conditional SGS stress production rate, $\left\langle-\frac{1}{2}P_{ij}|\mathbf{u}^r=\mathbf{v}\right\rangle$, the conditional resolvable-scale pressure-strain correlation, and the conditional buoyancy force, where

$$P_{ij}=-\left\{\tau_{ik}\frac{\partial u_j^r}{\partial x_k}+\tau_{jk}\frac{\partial u_i^r}{\partial x_k}\right\}$$

Equation (1) shows that the SGS stress directly affects the resolvable-scale velocity JPDF through the conditional SGS stress and the conditional SGS stress production and indirectly through the pressure terms. Therefore, the necessary conditions for LES to correctly predict the velocity JPDF are that the conditional means of SGS stress and SGS stress production rate must be reproduced by the SGS model ([38]). Therefore, equation (1) provides a link between the SGS stress and the resolvable-scale velocity JPDF and can be used to study the effects of the SGS stress on the JPDF in *a posteriori* tests. In the test the conditional means of LES-generated the SGS stress and its production rate are compared to measurements (or DNS).

It is noted that the *a posteriori* tests performed here are qualitatively different from the traditional tests, in which the mean, variance, spectra and other profiles of other flow parameters are compared with experiment measurements. (Direct comparisons between the instantaneous LES-generated SGS stress and measurements as done in traditional *a priori* tests are not possible because LES fields are not correlated to the true turbulence fields). A major limitation of such *a posteriori* tests is that it is difficult to relate the deficiencies of LES results to specific aspects of the model

behaviors. This is because the SGS stress evolves LES fields through dynamic equations, which are chaotic with many degrees of freedom, making it difficult to relate the properties of the solutions to the behaviors of the SGS terms in the LES equations. By contrast, this *a posteriori* tests examine the conditional means, which evolve directly the resolvable-scale velocity and scalar statistics through the JPDF equation. Therefore, it provides a more direct link between the resolvable-scale statistics and the SGS models. In addition, traditional *a posteriori* tests results generally cannot be directly related to *a priori* tests results, partly because the former often deal with statistics and the latter deal with instantaneous SGS stress. The JPDF equation based *a posteriori* tests, on the other hand, analyze the same JPDF equation as the (s *a priori* tests, making it possible to directly evaluate the consistency of model performance in the two types of tests.

In LES employing certain SGS models, such as the Smagorinsky model, only the deviatoric part of the SGS stress, $\tau_{ij}^d = \tau_{ij} - \frac{1}{3}\tau_{kk}\delta_{ij}$, is modeled. Therefore, it is also useful to examine the corresponding production term P_{ij}^d defined as

$$P_{ij}^d = -\left\{\tau_{ik}^d \frac{\partial u_j^r}{\partial x_k} + \tau_{jk}^d \frac{\partial u_i^r}{\partial x_k}\right\}. \tag{5.2}$$

Thus, P_{ij} can be written as

$$P_{ij} = P_{ij}^d - \frac{2}{3}\tau_{kk}S_{ij}, \tag{5.3}$$

where S_{ij} is the resolvable-scale strain rate tensor. Equation (3) shows that the normal components of P_{ij} contain the energy transfer from the resolvable to the subgrid scales, $P_{\alpha\alpha}^d$ $(\alpha = 1, 2, 3)$, and the redistribution among three normal components of the SGS stress (inter-component exchange), $-\frac{2}{3}\tau_{kk}S_{\alpha\alpha}$, respectively. The shear components of P_{ij} contain the production of SGS shear stress in anisotropic turbulence owing to both straining and rotation by the resolvable-scale velocity field, P_{ij}^d, and the production of shear stress due to straining of isotropic SGS turbulence, $-\frac{2}{3}\tau_{kk}S_{ij}, (i \neq j)$. Therefore the decomposition in (3) is useful for further understanding the physics of P_{ij} ([90]). They found that the results of $\langle\tau_{ij}|\mathbf{u}^r\rangle$ and $\langle P_{ij}|\mathbf{u}^r\rangle$ closely related to the surface-layer dynamics. Specifically, the updrafts generated by buoyancy, the downdrafts associated with the large-scale convective eddies, the mean shear, and the length scale inhomogeneity play important roles in the behaviors of $\langle\tau_{ij}|\mathbf{u}^r\rangle$ and $\langle P_{ij}|\mathbf{u}^r\rangle$. They found that $\langle P_{11}|\mathbf{u}^r\rangle$ is dominated by $-2\left\langle \tau_{13}\frac{\partial u_1^r}{\partial x_3}\middle|\, \mathbf{u}^r\right\rangle$, and secondarily dominated by $-2\left\langle \tau_{11}\frac{\partial u_1^r}{\partial x_1}\middle|\, \mathbf{u}^r\right\rangle$ due to the dominated shear $\partial u_1^r/\partial x_3$. Similarly, $\langle P_{33}|\mathbf{u}^r\rangle$ is dominated by $-2\left\langle \tau_{33}\frac{\partial u_3^r}{\partial x_3}\middle|\, \mathbf{u}^r\right\rangle$, and $\langle P_{13}|\mathbf{u}^r\rangle$ is dominated by $-\left\langle \tau_{33}\frac{\partial u_1^r}{\partial x_3}\middle|\, \mathbf{u}^r\right\rangle$. Therefore, the evolution of $\langle\tau_{11}|\mathbf{u}^r\rangle$ is primarily influenced by the conditional SGS shear stress $\langle\tau_{13}|\mathbf{u}^r\rangle$ (dominant term in $\langle P_{11}|\mathbf{u}^r\rangle$), and secondarily influenced by $\langle\tau_{11}|\mathbf{u}^r\rangle$. Similarly the evolution of $\langle\tau_{22}|\mathbf{u}^r\rangle$ is

Table 5.1 LES simulation parameters

Case	$L_x, L_y \times L_z$	$N_x, N_y \times N_z$	Q_*	U_g	u_*	$-z_i/L$
Sullivan 1994	10000×2000	250×128	0.1	20.0	0.66	5.63
Otte 2001 (Smag)	2500×999	144×160	0.2	15.0	0.66	6.04
Otte 2001(Kosović)	2500×1000	140×160	0.2	15.0	0.65	5.57

influenced by $\langle \tau_{23} | \mathbf{u}^r \rangle$ and $\langle \tau_{22} | \mathbf{u}^r \rangle$. The evolution of $\langle \tau_{33} | \mathbf{u}^r \rangle$ is influenced by $\langle \tau_{33} | \mathbf{u}^r \rangle$, and the evolution of $\langle \tau_{13} | \mathbf{u}^r \rangle$ is influenced by $\langle \tau_{33} | \mathbf{u}^r \rangle$ as well. This dynamics relation can be used to analyze the trend of the conditional SGS stress production rate predicted by SGS models, and analyze the dynamics between the scalar flux and its production rate (Chapter 4). In this chapter, this method is adopted to analyze the means and conditional means of the SGS stress and its production rate of the LES.

In this chapter, a new *a posteriori* test is employed to study SGS model performance using LES data. The rest of the paper is organized as follows. Section 5.1 outlines the large-eddy simulation and field measurement. The means and conditional means of SGS stress and its production rate of LES results are compared with the measurements and *a priori* test results in Section 5.2 and 5.3, followed by conclusions.

5.1 LES and field measurements

In this chapter, the LES data of atmospheric boundary layers are obtained by using the Smagorinsky model ([60, 83]), the split model (also called two-part eddy-viscosity model) ([10]), and the Kosović model ([67], Otte and Wyngaard 2001). The LES data using the Smagorinsky model and the Kosović model are described by Otte and Wyngaard 2001. The data using the split model are described by Sullivan *et al.* (1994) [10]. The split model was used by Sullivan *et al.* (1994) [10], which preserves the usual SGS turbulent kinetic energy eddy-viscosity model formulation, but includes a mean flow contribution and a reduced contribution from turbulent fluctuation near surface layer. Previous *a priori* study ([90]) showed that the conditional statistics of the split model are similar to that of the standard Smagorinsky model, but with smaller magnitudes and mean offsets. The parameters for the simulations are given in Table 5.1. The simulation results are compared with both the *a priori* test results and the results from measurement data (HATS) in Chen and Tong (2006) [90]).

The Smagorinsky model is given by Smagorinsky (1963), Lilly (1967), and Moeng (1984) [60, 1, 83].

$$\tau_{ij}^{smg} = -2\nu_t S_{ij} = -2C_k \Delta e^{1/2} S_{ij}, \tag{5.4}$$

where $C_k = 0.1$ is the Smagorinsky constant ([83]), e is the SGS turbulent kinetic energy, S_{ij} is the resolvable-scale strain rate, and Δ is the filter size.

The split model is given by Sullivan *et al.* (1994) [10].

$$\tau_{ij}^{split} = -2\nu_t \gamma S_{ij} - 2\nu_T \langle S_{ij} \rangle, \tag{5.5}$$

where γ is the isotropy factor, and ν_T is the mean field eddy-viscosity. These two factors changes with height to match the similarity theory at the first grid point and provide anisotropy in the SGS motion near the wall. In present study, the second grid point data are chose to compute the mean and the conditional mean statistics. The corresponding isotropy factor $\gamma = 0.61$.

Kosović (1997) [67] proposed a nonlinear model:

$$\tau_{ij}^{kos} = -2\nu_t S_{ij} - (C_s \Delta)^2 \left\{ C_1 (S_{ik} S_{kj} - \frac{1}{3} S_{mn} S_{mn} \delta_{ij}) + C_2 (S_{ik} \Omega_{kj} - \Omega_{ik} S_{kj}) \right\}, \tag{5.6}$$

where C_s, C_1 and C_2 are model constants.

The conditional statistics of the LES are compared with the results obtained using the field measurement (HATS). The field measurements for this study, named the horizontal array turbulence study, or HATS field program, were conducted at a field site 5.6 km east-northeast of Kettleman City, California, in the summer of 2000 as a collaboration primarily among the National Center for Atmospheric Research, Johns Hopkins University and Penn State University (CT was part of the Penn State group). Horst *et al.* (2004) [75] describe the field site and the data collection procedures in detail.

The field measurement design is based on the transverse array technique proposed, studied, and first used by the Penn State group ([76, 77, 48, 49]) for surface-layer measurements in the ABL. The technique uses horizontal sensor arrays to perform two-dimensional filtering to obtain resolvable- and subgrid-scale variables. Two arrays are vertically spaced to obtain vertical derivatives. The primary horizontal array consists of nine equally spaced sonic anemometers (Campbell Scientific SAT3) and the secondary array has five sonics at a second height. The arrays are aligned perpendicular to the prevailing wind direction.

The filter operation in the streamwise direction is performed by invoking Taylor's hypothesis. Filtering in the transverse direction is realized by averaging the output of the signals from the sensor array ([48]). In the present study, the arrays are used to approximate top-hat filters, which are the most compact type in physical space. Because derivatives are computed using finite differencing, which is effectively a top-hat filter, top-hat filters provide consistency among the resolvable-scale velocity and its derivatives.

Four different array configurations are employed in the HATS program. The filter (grid) aspect ratio (Δ/z, where z as the height of the primary array) ranges from 0.48 to 3.88, allowing the effects of grid anisotropy to be examined. Chen and Tong (2006) [90] focused on the unstable data case of array 1, because it has the largest $\Delta/z = 3.88$, the most anisotropic and most difficult for SGS models to predict. In the present work, the unstable data case of array 2 are chose, because its aspect ratio $\Delta/z = 2.0$ is closer to that of the LES data ($\Delta/z = 2.14$ for Sullivan 1994 runs and $\Delta/z = 1.92$ for Otte 2001 runs). Comparisons between model predictions and measurements only require the relative magnitude of the results and the conditional means obtained from array 2 has no quantitatively different from the conditional means obtained from array 1, therefore, the results in Chen and Tong (2006) [90] are still applicable to present study.

Due to the complexity of the variables of interest and of the conditional sampling procedure, a precise level of statistical uncertainty are not able to be provided. However, by monitoring the statistical scatter while increasing the data size, it is concluded that reasonable statistical convergence is achieved [90]. In addition, comparisons between model predictions and measurements only require the relative magnitude of the results and are less affected by the uncertainty. Therefore, the data size is sufficient for obtaining reliable statistics for the analyses.

The results for the mean SGS stress $\langle \tau_{ij} \rangle$ and the conditional SGS stress $\langle \tau_{ij} | \mathbf{u}^r \rangle$ are normalized by the friction velocity u_*^2. The results for the mean $\langle P_{ij} \rangle$ and the conditional SGS stress production $\langle P_{ij} | \mathbf{u}^r \rangle$ is normalized by the estimated energy dissipation rate $\epsilon = \phi_\epsilon \frac{u_*^3}{k_a z}$, where $\phi_\epsilon = 1 - z/L$ for $z/L \leq 0$ as suggested by Kaimal *et al.* (1972) [62].

5.2 Unconditional statistics

The mean horizontal resolvable-scale velocity vertical gradient ($\Phi_m = \frac{\partial u}{\partial z} \frac{k_a z}{u_*}$), the (total) velocity variances profiles, and the vertical resolvable-scale velocity skewness of the simulation are shown in Figures 5.1 and 5.2, respectively. The LES profiles obtained using the split model and the Kosović model are closer to measurements ([90]) than those using the Smagorinsky model.

Table 5.2 Mean statistics of the HATS (array 2), *a priori* test, and LES results (at the second grid-point height).

	HATS	*a priori*			LES		
		Smag	Split	Kosović	Smag	Split	Kosović
$\langle u_1' u_1' \rangle / u_*^2$	12.12				5.08	5.79	4.80
$\langle u_2' u_2' \rangle / u_*^2$	13.19				4.52	5.15	4.47
$\langle u_3' u_3' \rangle / u_*^2$	1.86				1.43	1.20	0.89
$\langle -u_1' u_3' \rangle / u_*^2$	1.00				0.84	0.98	0.82
$\langle u_1^{r\prime} u_1^{r\prime} \rangle / u_*^2$	9.78				3.76	4.96	3.39
$\langle u_2^{r\prime} u_2^{r\prime} \rangle / u_*^2$	11.40				3.20	4.31	3.16
$\langle u_3^{r\prime} u_3^{r\prime} \rangle / u_*^2$	0.44				0.12	0.38	0.25
$\langle -u_1^{r\prime} u_3^{r\prime} \rangle / u_*^2$	0.46				0.39	0.71	0.52
$\langle \tau_{11}^d \rangle / u_*^2$	0.55	0.01	0.01	0.32	0.01	0.00	0.29
$\langle \tau_{22}^d \rangle / u_*^2$	-0.08	0.01	0.03	0.05	0.01	0.01	0.19
$\langle \tau_{33}^d \rangle / u_*^2$	-0.44	0.01	0.01	-0.33	-0.01	-0.01	-0.48
$\langle -\tau_{13} \rangle / u_*^2$	0.57	0.23	0.38	0.23	0.44	0.28	0.29
$\langle \tau_{kk}/3 \rangle / u_*^2$	1.87				1.32	0.83	1.12
$\langle P_{11} \rangle / \epsilon$	0.87	0.67	0.75	0.69	1.13	0.80	0.64
$\langle P_{22} \rangle / \epsilon$	0.29	0.44	0.42	0.46	0.18	0.27	0.32
$\langle P_{33} \rangle / \epsilon$	0.07	0.09	0.08	0.03	-0.04	0.00	0.02
$\langle -P_{13} \rangle / \epsilon$	0.63	0.90	0.90	0.53	1.34	0.60	0.32
$\langle P_{11}^d \rangle / \epsilon$	0.80	0.59	0.67	0.62	1.10	0.79	0.60
$\langle P_{22}^d \rangle / \epsilon$	0.19	0.34	0.32	0.36	0.15	0.24	0.30
$\langle P_{33}^d \rangle / \epsilon$	0.11	0.12	0.11	0.07	0.04	0.06	0.09
$\langle P_{13}^d \rangle / \epsilon$	0.22	-0.05	-0.05	0.32	0.00	0.02	0.43

Table 5.2 shows that the measured Reynolds (mean total) stress components $\langle u_1' u_1' \rangle$ and $\langle u_2' u_2' \rangle$ (where $'$ denotes the fluctuations) have larger values than the other components, so are the measured mean resolvable-scale stress components $\langle u_1^{r\prime} u_1^{r\prime} \rangle$ and $\langle u_2^{r\prime} u_2^{r\prime} \rangle$. This feature is generally captured by the all simulations. The smaller LES values for the normal components may be related to the difference in z_i/L for LES and measurements.

The mean SGS stress normal components, $\langle \tau_{11}^d \rangle$ and $\langle \tau_{33}^d \rangle$, have larger magnitude than $\langle \tau_{22}^d \rangle$. This features is not captured by the Smagorinsky model and the split model in both the *a priori* and *a posteriori* tests. The Kosović model capture this trend much better, but slightly over-predicts $\langle \tau_{22}^d \rangle$ and $\langle \tau_{33}^d \rangle$. The mean SGS shear stress are under-predicted by all the models in both *a priori* and *a posteriori* tests.

The mean SGS stress production rate $\langle P_{11} \rangle, \langle P_{22} \rangle$, and $\langle P_{13} \rangle$ have large magnitudes than the other components, which are generally captured by the models both in *a priori* and *a posteriori* tests. However, none of the models captures well the relative magnitudes among those components.

The large magnitudes of $\langle P_{11}^d \rangle$ and $\langle P_{22}^d \rangle$ are generally captured by those models, but their ratio is less well captured. $\langle P_{13}^d \rangle$ is under-predicted by both the Smagorinsky model and the split model in both *a priori* and *a posteriori* test, which is due to the under-prediction of the $\langle \tau_{33}^d \rangle$.

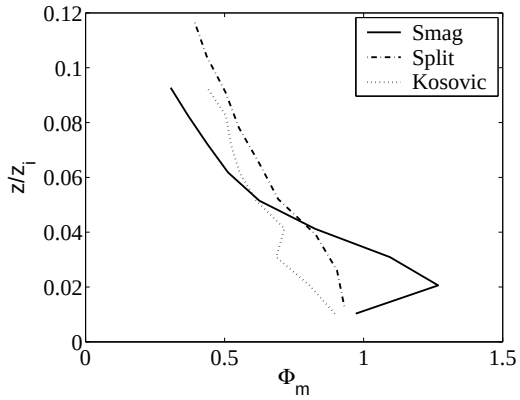

Figure 5.1 LES results of the mean horizontal resolvable-scale velocity vertical gradient profile in the surface layer.

However, it is over-predicted by the Kosović model in both *a priori* test and in LES, which is due to the over-prediction of the $\langle \tau_{33}^d \rangle$. $\langle P_{33}^d \rangle$ is well predicted in *a priori* test by both the Smagorinsky model and the split model but less well captured in the LES, which is probably due to the LES not reproducing correctly the correlation between τ_{33}^d and $\partial u_3^r / \partial x_3$ (the dominant term in $\langle P_{33}^d \rangle$).

In order to quantitatively measure the relationships among SGS components, their eigenvalue structures are examined using the Lumley triangle ([81]). For example, the normalized mean SGS stress tensor for $\langle \tau_{ij} \rangle$,

$$\langle \tau_{ij}^d \rangle / \langle \tau_{kk} \rangle = \langle \tau_{ij} \rangle / \langle \tau_{kk} \rangle - \frac{1}{3}\delta_{ij}, \tag{5.7}$$

can be determined by two variables ξ and η defined in terms of its invariants ([37])

$$6\eta^2 = -2II = \langle \tau_{ij}^d \rangle \langle \tau_{ij}^d \rangle / \langle \tau_{kk} \rangle^2, \tag{5.8}$$

$$6\xi^3 = 3III = \langle \tau_{ij}^d \rangle \langle \tau_{jk}^d \rangle \langle \tau_{ki}^d \rangle / \langle \tau_{kk} \rangle^3, \tag{5.9}$$

where II and III are the second and third invariants of the anisotropy tensor. If $\langle \tau_{ij} \rangle$ is isotropic, both ξ and η are zero (the first invariant or trace of $\langle \tau_{ij}^d \rangle$ is always zero by definition).

The Lumley triangle representation for the measured Reynolds stress and the resolvable-scale stress (Figure 5.3(a)) shows that both are close to axisymmetric with two large eigenvalues ($\eta = -\xi$). On the other hand, the mean SGS stress is close to axisymmetric with one large eigenvalue ($\eta = \xi$) in the surface layer. This difference is because the influence of large-scale convective eddies, which results in the large value of σ_u and σ_v. The filter near the boundary removes the effects of large-scale eddies, resulting in a structure close to axisymmetric with one large eigenvalue. As the filter size increases, the eigenvalue structure of the mean SGS stress would change from

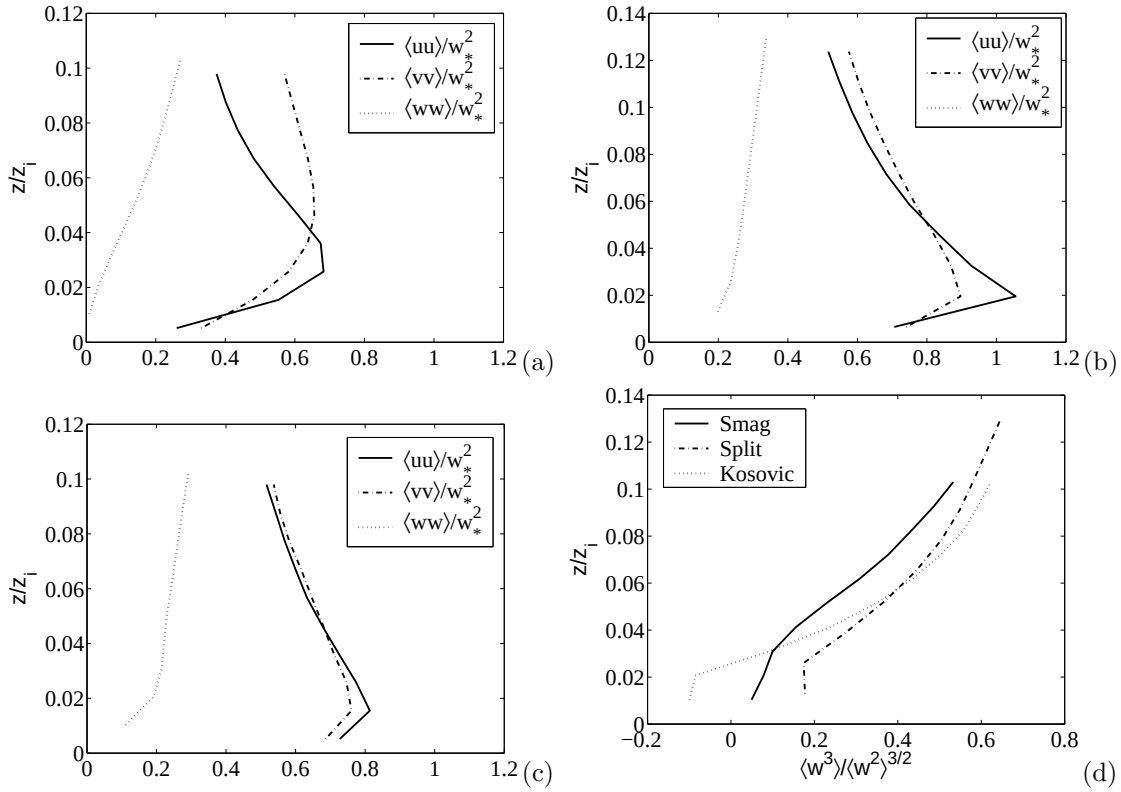

Figure 5.2 LES results of the (total) velocity variance and the vertical resolvable-scale velocity skewness profiles in the surface layer: a) the Smagorinsky model; b) the split model; c) the Kosović model; d) the vertical resolvable-scale velocity skewness.

being axisymmetric with one large eigenvalue structure to axisymmetric with two large eigenvalue structure. The eigenvalue structure of the modeled mean SGS stress using these models (*a priori* tests), also shown in Figure 5.3(a), are less anisotropic than the measurements. The slightly higher level of anisotropy of the Kosović model than that of the Smagorinsky model was also observed in *a priori* test ([90]). The higher level of anisotropy of the split model than that of the Smagorinsky model is due to the contribution from the mean part of the modeled τ_{13} component.

In order to examine the influence of the modeled mean SGS stress on the resolved stress coming from scales close to the filter scale, the band-passed stress is computed using a bandpass filter ($\langle \tau_{ij}^b \rangle = \langle (u_i^r - u_i^{nr})(u_j^r - u_j^{nr}) \rangle$ where nr denotes a second low-pass filter of width n times larger than the LES filter size). Figure 5.3(b) shows the LES results for several second filter widths ranging from 2 grid spaces to 34 grid spaces. The measured mean band-passed stress for $n = 2$ (Figure 5.3(a)) is axisymmetric with one large eigenvalue structure. As the width increases, i.e., large scales are included, the structure moves closer to the mean resolvable-scale stress structure.

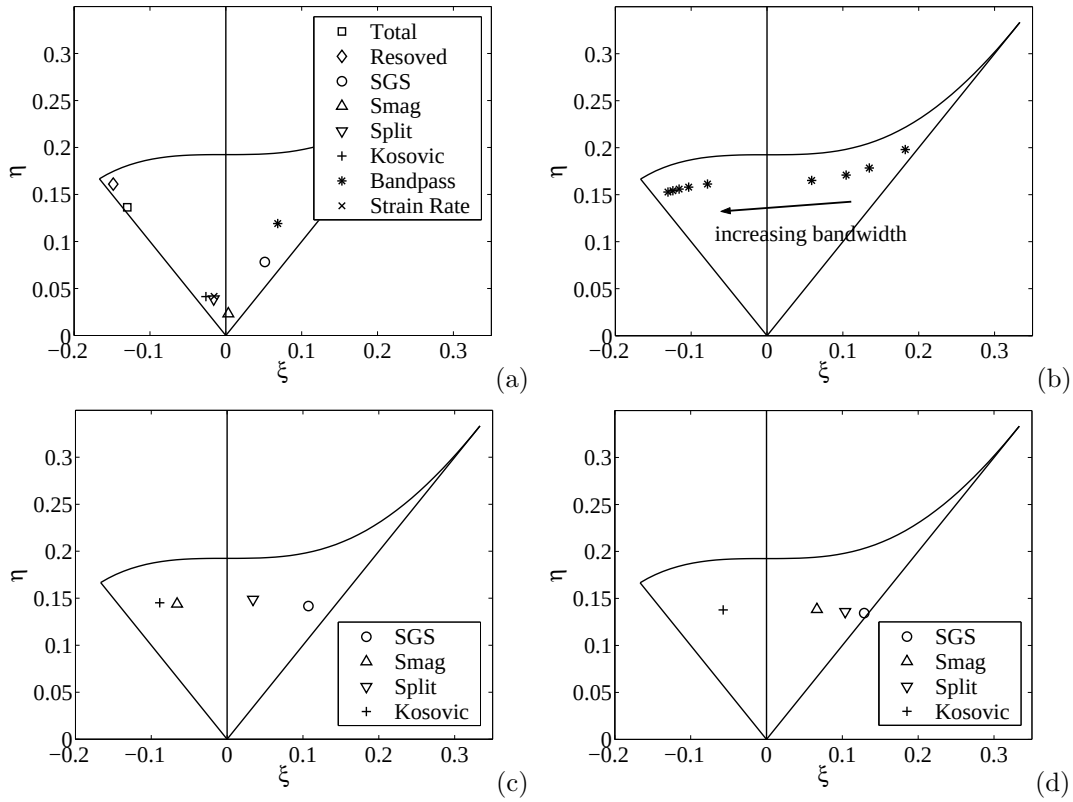

Figure 5.3 Lumley triangle representation of: a) the measured Reynolds stress, mean resolvable-scale stress, mean SGS stress, mean band-passed stress with a second filter size twice that of the first filter, and the modeled (*a priori* test) mean SGS stress. The strain rate is also given for reference; b) the LES results of the mean band-passed stress using the Kosović model. The bandwidth increases from 2 grid spaces to 34 grid spaces by each step increment 4; c) the measured mean SGS stress production rate; d) the measured $\langle P_{ij}^d \rangle$.

These results indicate that the SGS stress influence strongly the structure near the filter scale but not the large-scales.

Chen *et al.* (2003) [38] found that while the influence of SGS stress decreases with decreasing filter scale, the SGS stress production rate has persistent influences on the resolvable-scale velocity JPDF. Thus, it is important for the SGS models to predict the structure of the mean SGS stress production rate well. Though the SGS stress production rate does not satisfy the Cauchy-Schwarz inequality and its ξ and η values are not confined to the Lumley triangle, it is nonetheless useful to present its structure using Lumley triangle. an arbitrary factor is used to normalize the production rate such that the ξ and η values fall within the Lumley triangle. Therefore, $\xi > 0$ still represents a structure close to axisymmetric with one large eigenvalue, $\xi < 0$ represents a structure close to axisymmetric with two large eigenvalue, and the origin represent an isotropy structure. However,

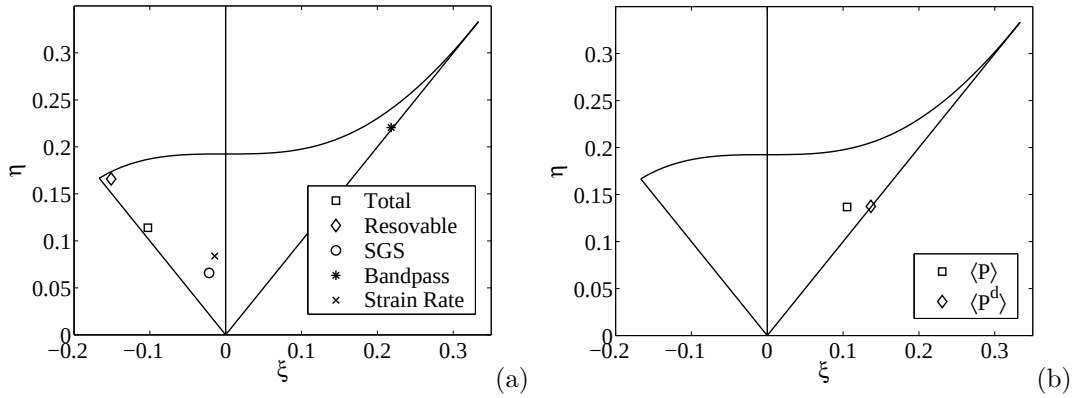

Figure 5.4 LES results (*a posteriori* test) of the Lumley triangle representation of: a) the mean SGS stress; b) the mean SGS stress production rate using the Smagorinsky model.

the distance from the origin does not represent the level of anisotropy as is the case for the SGS stress. Figure 5.3(c) and (d) show the Lumley triangle representation of the measured $\langle P_{ij} \rangle$ and $\left\langle P_{ij}^d \right\rangle$, respectively. Figure 5.3(c) shows that $\langle P_{ij} \rangle$ has a similar structure to the mean SGS stress because they are on the same radical line starting from origin, consistent with the good alignment and tensorial contraction between the conditional SGS stress and its production rate ([90]). Figure 5.3(d) shows that $\left\langle P_{ij}^d \right\rangle$ has similar structure to that of $\langle P_{ij} \rangle$, but is closer to axisymmetric with one large eigenvalue ($\eta = \xi$). This indicates that including the production due to straining of isotropic part of the SGS stress moves the SGS stress production rate structure to axisymmetric with two large eigenvalue structure. Note that in *a priori* tests the SGS stress τ_{ij} for the SGS models is obtained by adding the measured $\tau_{kk}/3$ into the modeled τ_{ij}^d to compute modeled P_{ij}. Therefore, the eigenvalue structure of the mean SGS stress production rate is influenced by the relative ratio between the measured $\tau_{kk}/3$ and the modeled τ_{ij}^d. By varying the percentage of τ_{kk}, it is found that the eigenvalue structure of the mean SGS stress production rate moves closer to the axisymmetric with two large eigenvalue structure when the percentage of τ_{kk} increasing.

The Lumley triangle representation for the Reynolds stress, the mean resolvable-scale stress, and the mean SGS stress obtained in LES using the Smagorinsky model, the split model, and the Kosović model are showed in Figure 5.4(a), 5.5(a), and 5.6(a), respectively. The structure of the Reynolds stress and the mean resolvable-scale stress are well predicted using the split model and the Kosović model. The predicted level of anisotropy of the Reynolds stress using the Smagorinsky model is slightly lower than the measurements, but the resolvable-scale mean stress is slightly higher than

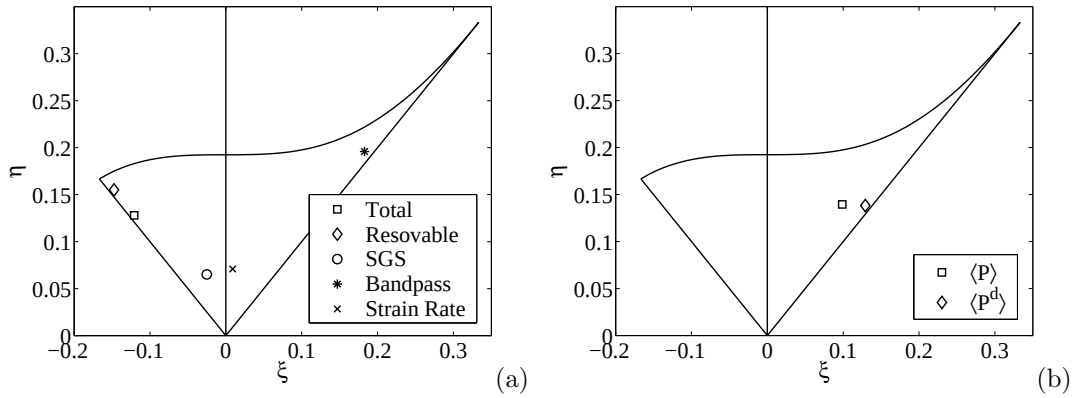

Figure 5.5 LES results (*a posteriori* test) of the Lumley triangle representation of: a) the mean SGS stress; b) the mean SGS stress production rate using the split model.

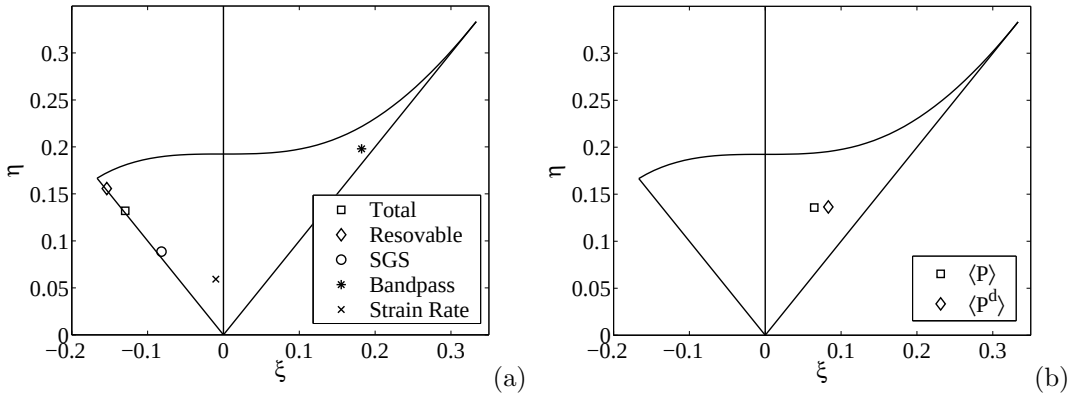

Figure 5.6 LES results (*a posteriori* test) of the Lumley triangle representation of: a) the mean SGS stress; b) the mean SGS stress production rate using the Kosović model.

the measurements, which comes from the over-prediction of the magnitude of $\langle u_3' u_3' \rangle$ and the under-prediction the magnitude of $\langle u_3^r u_3^r \rangle$ by the Smagorinsky model. The mean band-passed stress from these simulations is close to axisymmetric with one large eigenvalue, similar to the measurements.

The Lumley triangle representation for the LES mean SGS stress using the Kosović model is close to axisymmetric with two large eigenvalue. The LES mean SGS stress using the Smagorinsky model and the split model have similar eigenvalue structures: close to axisymmetric with two large eigenvalues. Their eigenvalue structures are different from the measured mean SGS stress eigenvalue structure, but similar to the *a priori* test results (Figure 5.3(a)).

While the LES mean SGS stress eigenvalue structure is different from the measurements, the Reynolds, mean resolvable-scale, and the mean band-passed stress eigenvalue structures are generally well predicted. These predictions can be understood by examining the first two terms on

the right-hand-side of equation (1): in a horizontally homogenous atmospheric boundary layer, the derivatives in horizontal direction vanish, and the SGS stress influences the resolvable-scale JPDF through $\langle \tau_{13} | \mathbf{u}^r \rangle$, $\langle \tau_{23} | \mathbf{u}^r \rangle$, and $\langle \tau_{33} | \mathbf{u}^r \rangle$. Therefore, the over-prediction the magnitude of $\langle \tau_{22} \rangle$ by the Kosović model does not influence strongly the eigenvalue structure of the Reynolds, mean resolvable-scale, and the mean band-passed stress. However, it may cause inaccuracies in flow that are not horizontally homogenous. The slight inaccuracies in the LES eigenvalue structures of the Reynolds stress and the mean resolvable-scale stress using the Smagorinsky model come from the inaccuracies of $\langle u_3' u_3' \rangle$ and $\langle {u^r}_3' {u^r}_3' \rangle$, which is probably due to the inaccuracies of the $\langle \tau_{33} \rangle$ (the dominant term in $\langle P_{33} \rangle$). The improvement of the LES results using the split model over the Smagorinsky model probably is because the increased anisotropy through $\langle \tau_{13} \rangle$, which partially compensates the effects of the under-prediction of the τ_{33}.

From equation (1), it is also seen that the SGS stress production rate influence the resolvable-scale statistics regardless of homogeneity ([38]). The Lumley triangle representation of $\langle P_{ij} \rangle$ from LES is close to axisymmetric with one large eigenvalue (Figure 5.4(b), 5.5(b), and 5.6(b)), which are similar to the measurements shown in Figure 5.3(c). The Lumley triangle representation of $\left\langle P_{ij}^d \right\rangle$ is also axisymmetric with one large eigenvalue, which are similar to the measurements and the *a priori* test results (Figure 5.3(d)), except the Kosović model, which over-predicts the magnitude of P_{22} due to the over-predicted magnitude of τ_{22}. These results are consistent to the above analysis that the SGS stress production rate is important. In addition, the Lumley triangle representation of the properly normalized mean LES strain rate (normalized by $\sqrt{\langle \tau_{kk} \rangle / 2}/(0.1\Delta)$) are also generally well predicted by all models (Figure 5.3(a), 5.4(a), 5.5(a) and 5.6(a)).

5.3 Conditional statistics

The results for the conditional normal SGS stress components are plotted against the horizontal resolvable-scale velocity, u_1^r, for different values of the vertical resolvable-scale velocity, u_3^r (Figure 5.7). Only the fluctuation parts of $\mathbf{u}^r$ components normalized by their respective r.m.s. values is plotted.

The measurement results of the conditional SGS stress and its production rate are shown in Figures 5.7 and 5.8. The trends and the magnitudes of the conditional SGS stress and its production generally depend on the resolvable-scale velocity and increase with the resolvable-scale velocity. One exception is $\langle P_{33} | \mathbf{u}^r \rangle$ which weakly depends on u_1^r, similar to the results in Chen and Tong (2006) [90]. The Lumley triangle representation, the eigenvalue geometric alignment, eigenvalue, and the

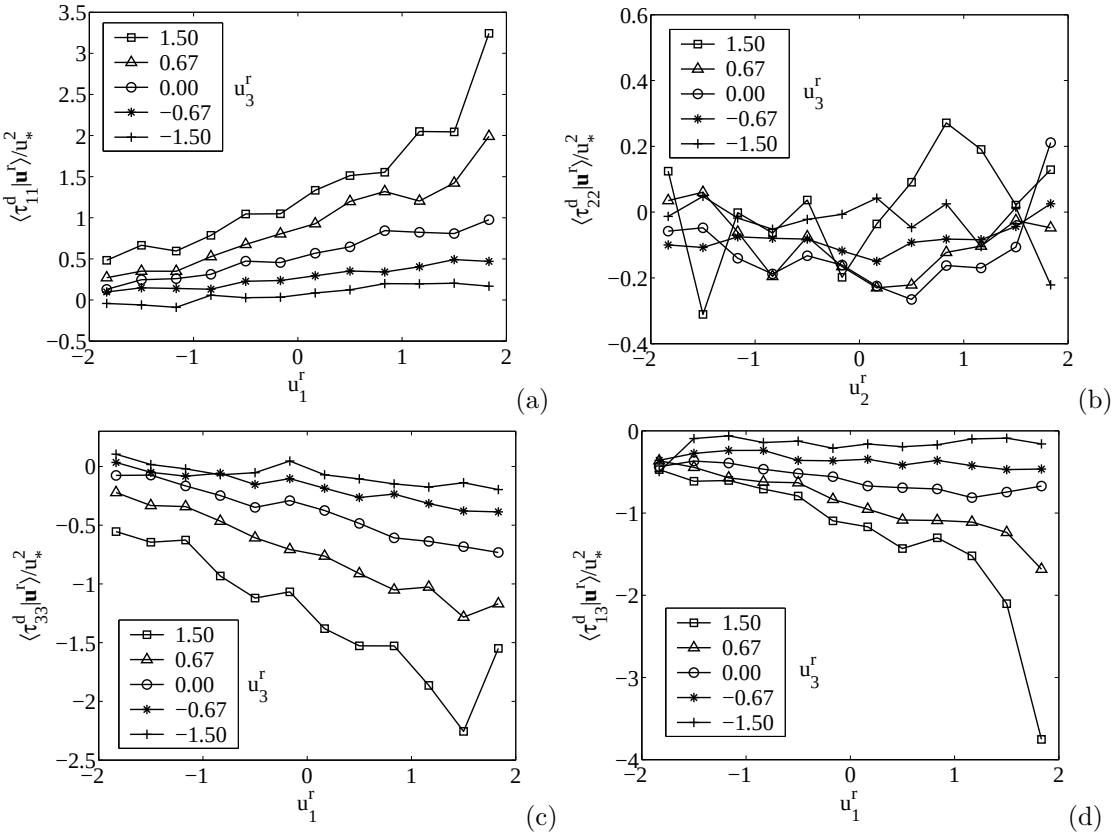

Figure 5.7 Conditional means of the measured deviatoric SGS stress components conditional on the resolvable-scale velocity components. The dependence on the horizontal velocity components is generally stronger for position u_3^r.

eigenvalue ratio of the conditional SGS stress and its production rate are shown in Figure 5.9(a) and 5.10 respectively. These results are similar to those for array 1 discussed in detail in Chen and Tong (2006) [90].

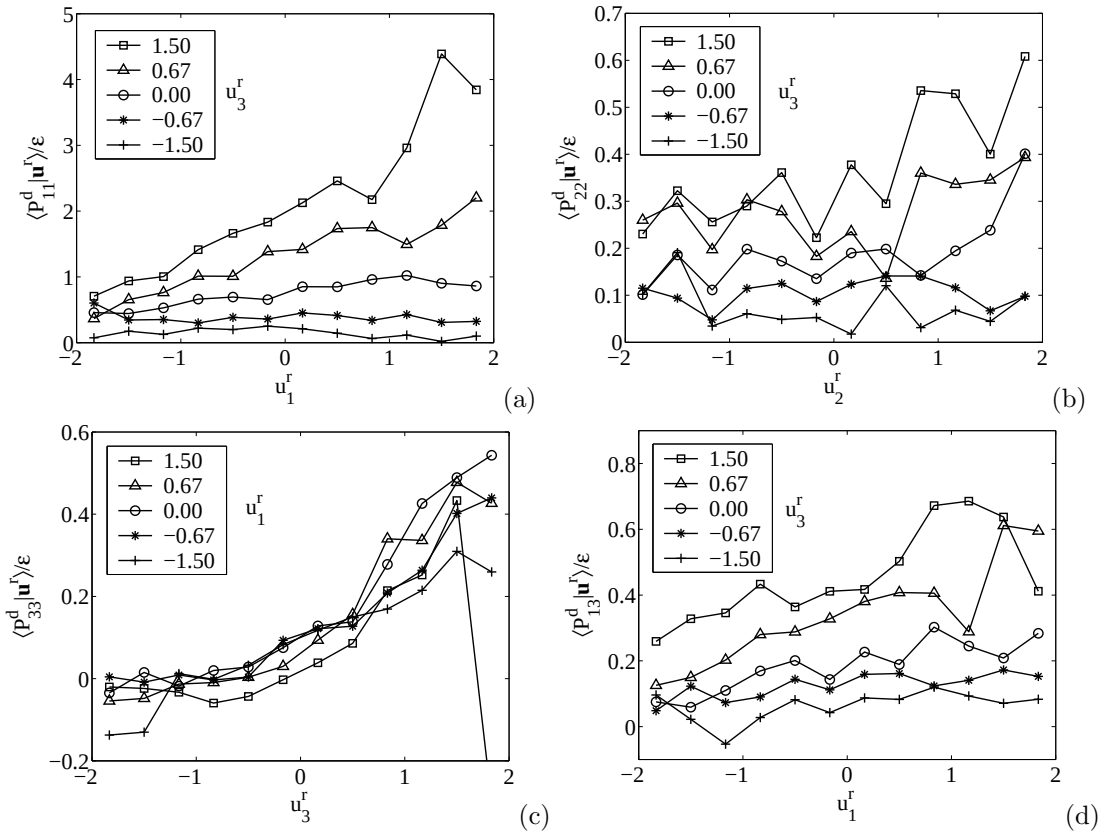

Figure 5.8 Conditional means of the measured SGS stress production rate components conditional on the resolvable-scale velocity components.

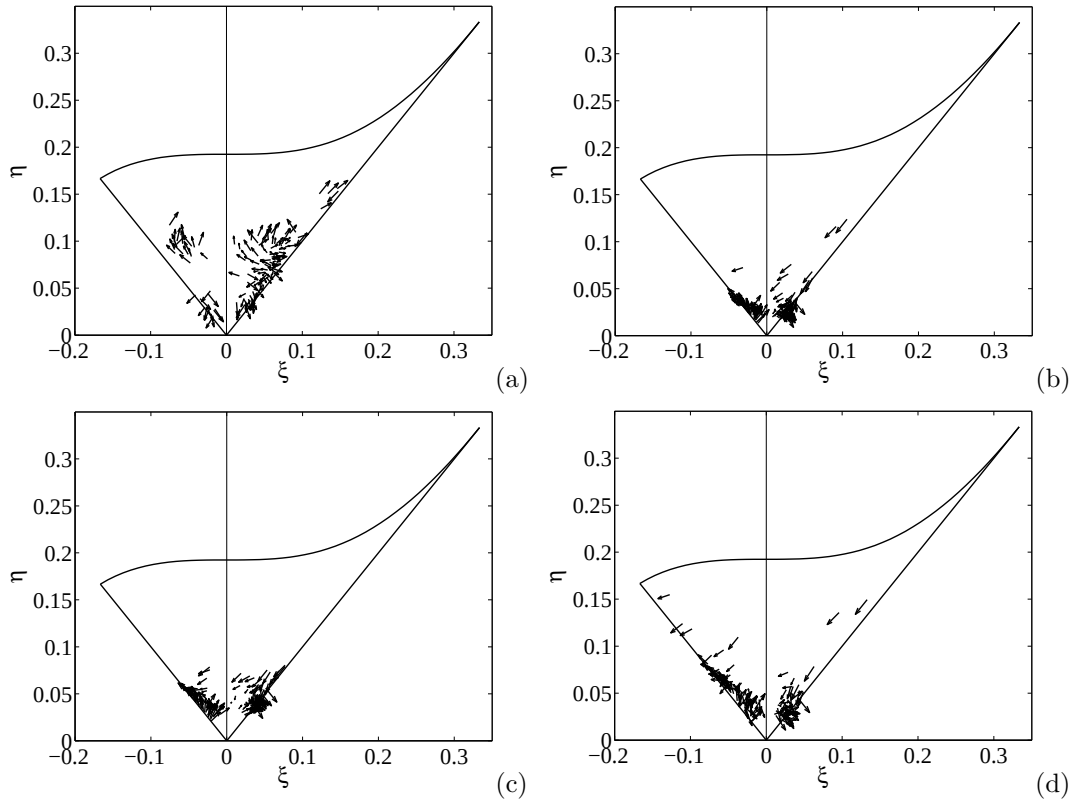

Figure 5.9 Lumley triangle representation of the measured and modeled (*a priori* test) conditional SGS stress: a) the measurement; b) the Smagorinsky model; c) the split model; d) the Kosović model. The arrows represent the conditioning vector (u_1^r, u_3^r).

The *a priori* test results for the Smagorinsky model are shown in Figures 5.11 and 5.12. The model can predict well neither the conditional mean of SGS stress nor its production. It can predict quite well the trends of some shear stress components, but not the normal components, and can predict the trends of some normal components of conditional SGS stress production, but not the shear components. The magnitudes of these components are generally poorly predicted. The level of anisotropy is also severely under-predicted (Figure 5.9(b)). These results are similar to those discussed in Chen and Tong (2006) [90]. The *a priori* test results for the split model are generally similar to that of the Smagorinsky model except $\langle \tau_{13} | \mathbf{u}^r \rangle$ (Figure 5.13) because the contribution from the mean part is generally small except for the shear stress. Figure 5.13 shows that the variation of $\langle \tau_{13}^{split} | \mathbf{u}^r \rangle$ is smaller but the magnitude is larger than that of the Smagorinsky model due to the contribution from the mean part, which results in a higher level of anisotropy (Figure 5.9(c)).

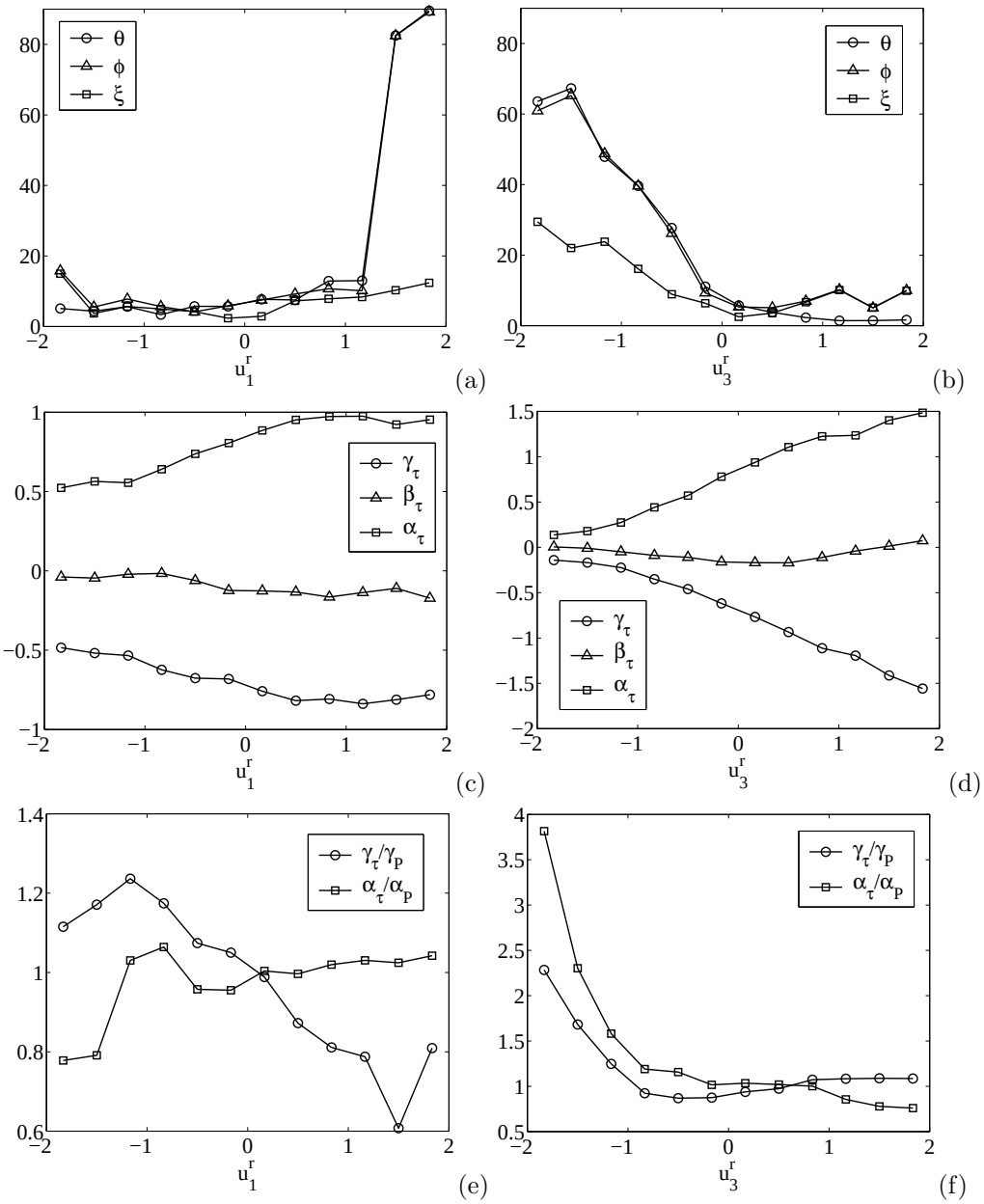

Figure 5.10 The measured geometric alignment angles and eigenvalues of the conditional SGS stress and its production rate: (a-b) the geometric alignment angles; (c-d) the eigenvalues of the conditional SGS stress; (e-f) the eigenvalue ratios of the conditional SGS stress to its production rate.

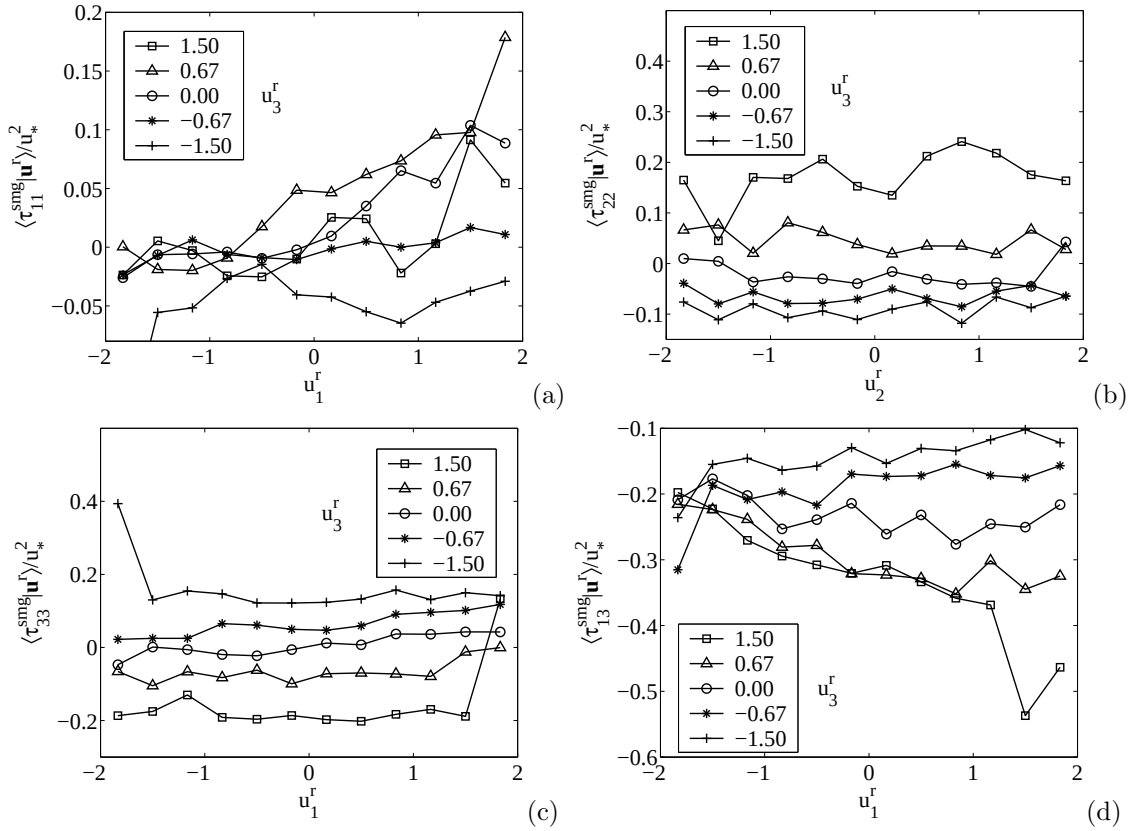

Figure 5.11 Predicted conditional SGS stress (*a priori* test) using the Smagorinsky model. Only the trend of $\langle \tau_{13} | \mathbf{u}^r \rangle$ is predicted reasonably well.

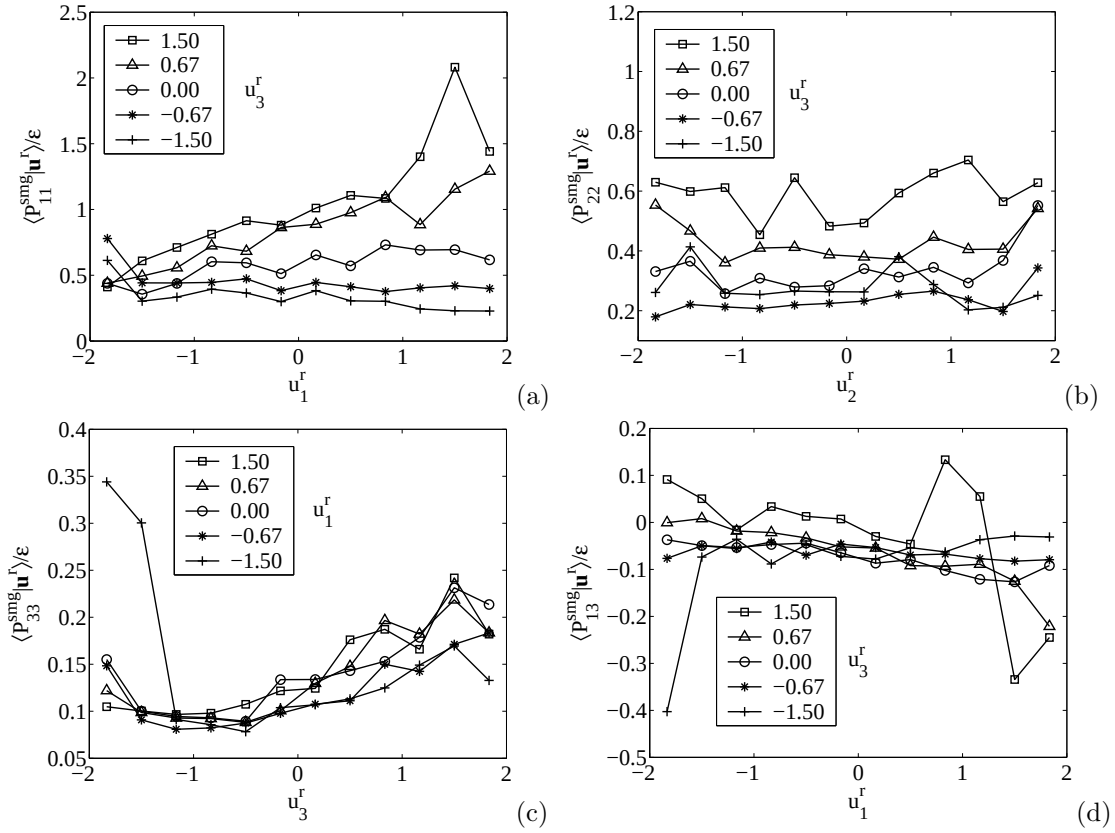

Figure 5.12 Predicted conditional SGS stress production rate (*a priori* test) using the Smagorinsky model.

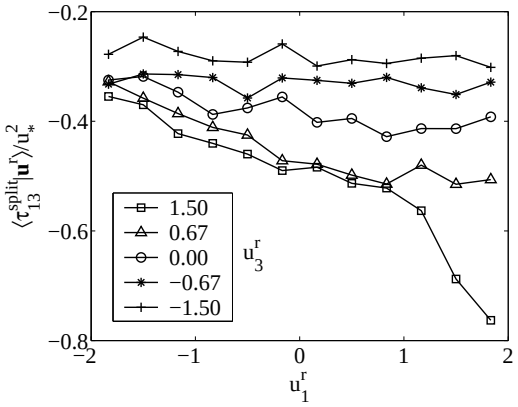

Figure 5.13 Predicted conditional SGS shear stress (*a priori* test) using the split model. The variations of the predicted $\langle\tau_{13}|\mathbf{u}^r\rangle$ are smaller but the magnitude is larger than that of the Smagorinsky model due to the contribution from the mean part.

The results of the Kosović model (Figures 5.14-5.15) show that it has better overall performance than the Smagorinsky model and the split model. Chen and Tong (2006) [90] showed that it has the best overall performance among the models tested. However, it under-predicts the magnitude of the conditional SGS stress when the mean energy transfer is matched. The level of anisotropy (Figure 5.9(d)) is also under-predicted compared with measurements, but the prediction is improved over that of the Smagorinsky model.

In the following the *a posteriori* test (LES) results of these SGS models are presented and compared with the measurements and the *a priori* test results discussed above (Figure 5.7-5.15).

5.3.1 Smagorinsky model

The LES results for $\langle\tau_{ij}^{smg}|\mathbf{u}^r\rangle$ and $\langle P_{ij}^{smg}|\mathbf{u}^r\rangle$ are shown in Figures 5.16 and 5.17, respectively. The magnitudes of both $\langle\tau_{ij}^{d}|\mathbf{u}^r\rangle$ and $\langle P_{ij}^{d}|\mathbf{u}^r\rangle$ are generally under-predicted. The magnitudes and trends of these conditional means are generally similar to that of the *a priori* test results using the measurements (HATS) data ([90]).

Figure 5.16(a) shows that the trends of $\langle\tau_{11}^{d}|\mathbf{u}^r\rangle$ are generally well predicted. However, similar to the *a priori* test results, the magnitudes are severely under-predicted. The trends and magnitudes of $\langle\tau_{22}^{d}|\mathbf{u}^r\rangle$ (Figure 5.16(b)) are generally well predicted. The dependence of $\langle\tau_{33}^{d}|\mathbf{u}^r\rangle$ (Figure 5.16(c)) on u_1^r and the magnitude are under-predicted. Figure 5.16(d) shows that the trend of $\langle\tau_{13}|\mathbf{u}^r\rangle$ on u_3^r is reasonably well predicted, but the magnitude is under-predicted. Similarly, the magnitude $\langle\tau_{23}^{d}|\mathbf{u}^r\rangle$ are generally under-predicted. These results are similar to the *a priori* test results (Figure 5.11). The under-prediction of $\langle\tau_{13}|\mathbf{u}^r\rangle$ in both *a priori* and *a posteriori* tests

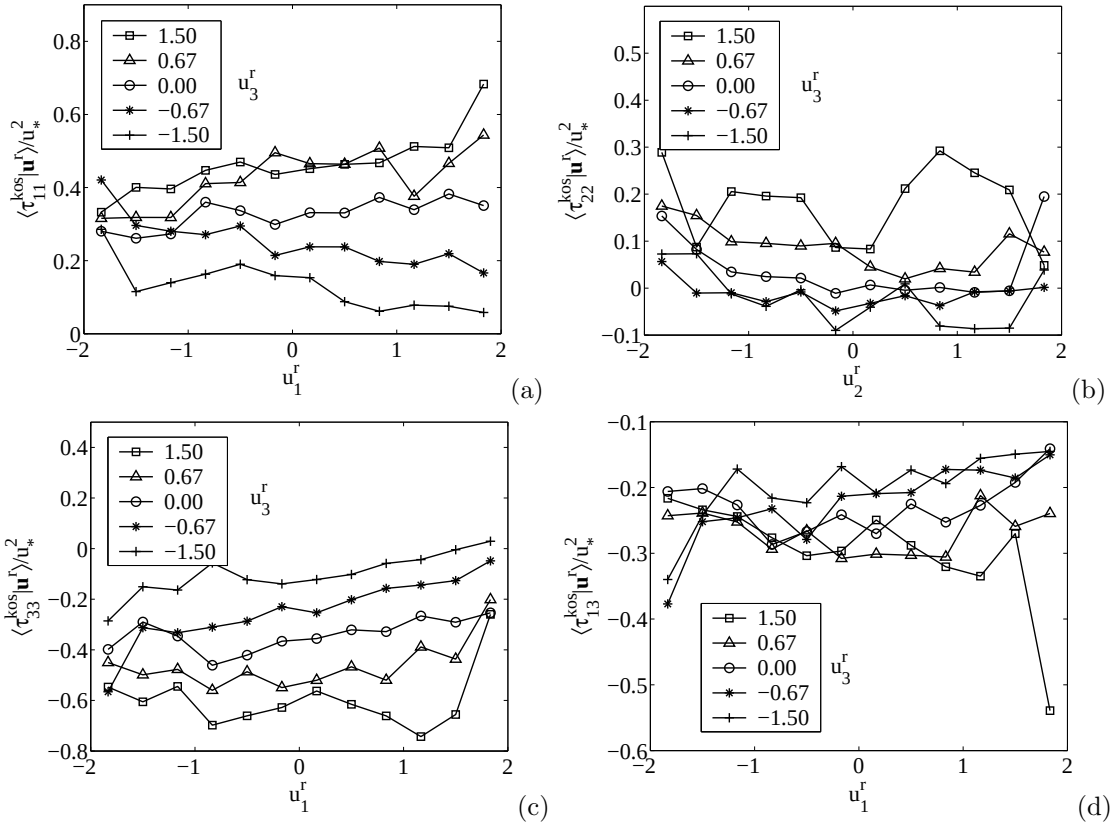

Figure 5.14 Predicted conditional SGS stress (*a priori* test) using the Kosović model.

provides strong support to the argument that it causes the over-prediction of the vertical derivative of the streamwise velocity.

The magnitude of $\left\langle P_{11}^d | \mathbf{u}^r \right\rangle$ (Figure 5.17(a)) is generally under-predicted, and the dependence on u_3^r is reasonably well predicted. The under-prediction of the magnitude is due to its under-prediction of the magnitude of τ_{11}^d and τ_{13} ($\left\langle P_{11}^d | \mathbf{u}^r \right\rangle = \left\langle -\tau_{1j}^d \frac{\partial u_1^r}{\partial x_j} | \mathbf{u}^r \right\rangle$). The magnitude of $\left\langle P_{33}^d | \mathbf{u}^r \right\rangle$ (Figure 5.17(c)) and its asymmetric dependence on u_3^r is not well captured, which is due to the under-prediction of τ_{33} because $\left\langle P_{33}^d | \mathbf{u}^r \right\rangle$ is dominated by $\left\langle -\tau_{33}^d \frac{\partial u_3^r}{\partial x_3} | \mathbf{u}^r \right\rangle$ ([90]). The trends and magnitudes of $\left\langle P_{13}^d | \mathbf{u}^r \right\rangle$ (Figure 5.17(d)) on u_1^r are slightly under-predicted. Again, this is due to the model prediction of $\langle \tau_{33} | \mathbf{u}^r \rangle$. These results are similar to the *a priori* tests with the exception that the *a posteriori* results for $\left\langle P_{13}^d | \mathbf{u}^r \right\rangle$ are somewhat better than that of the *a priori* test results. The poor predictions of $\left\langle P_{33}^d | \mathbf{u}^r \right\rangle$, in particular its asymmetric dependence on u_3^r in both *a priori* and *a posteriori* tests confirm the argument that it is the cause for the under prediction of the vertical velocity skewness in the surface layer.

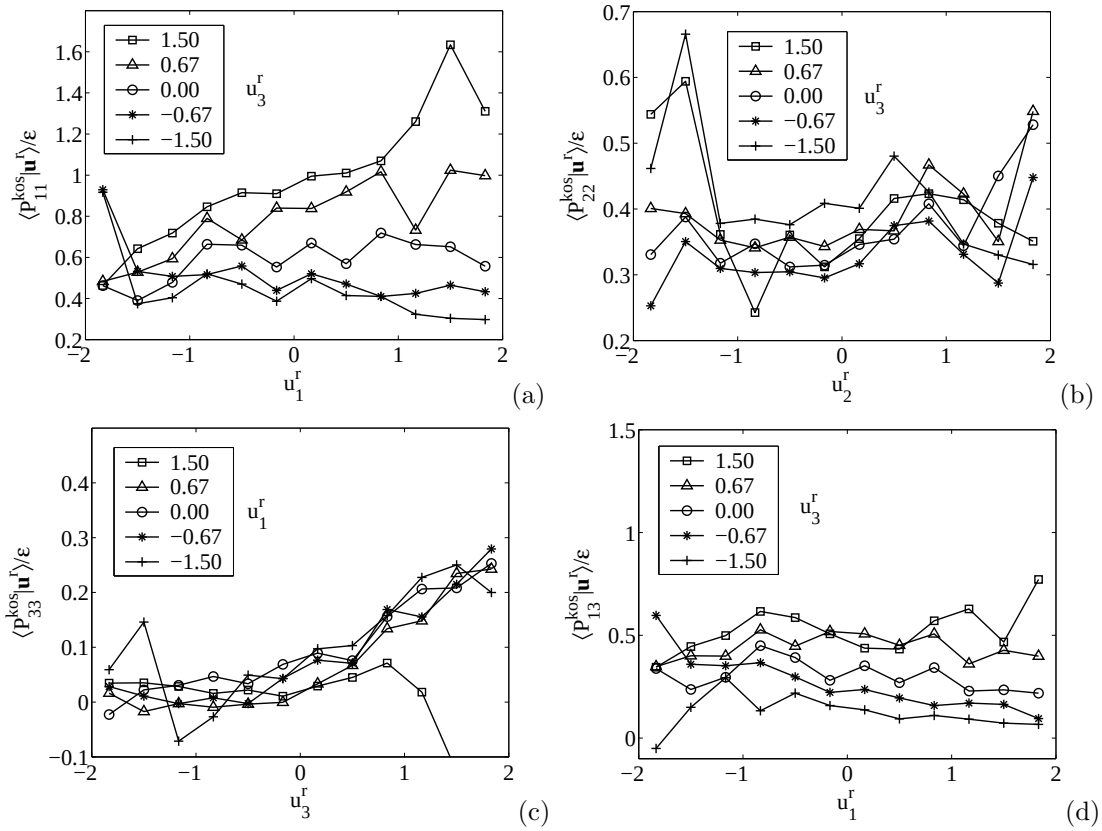

Figure 5.15 Predicted conditional SGS stress production rate (*a priori* test) using the Kosović model.

Chen and Tong (2006) [90] found that the level of anisotropy of the conditional SGS stress is very important for both understanding the surface layer dynamics and SGS modeling. The level of anisotropy of the conditional SGS stress can also be characterized by the representation in the Lumley triangle ([81]). The Lumley triangle for the conditional SGS stress can be obtained in the way similar to that for the mean SGS stress in Section 5.2 as done in Chen and Tong (2006) [90].

Measurements ([90]) show that the anisotropy is weak for negative u_3^r and is much stronger for positive u_3^r. For positive and negative u_1^r values, $\langle \tau_{ij}|\mathbf{u}^r\rangle$ is close to axisymmetric with one large and one small eigenvalue, respectively, probably reflecting the shear and buoyancy effects.

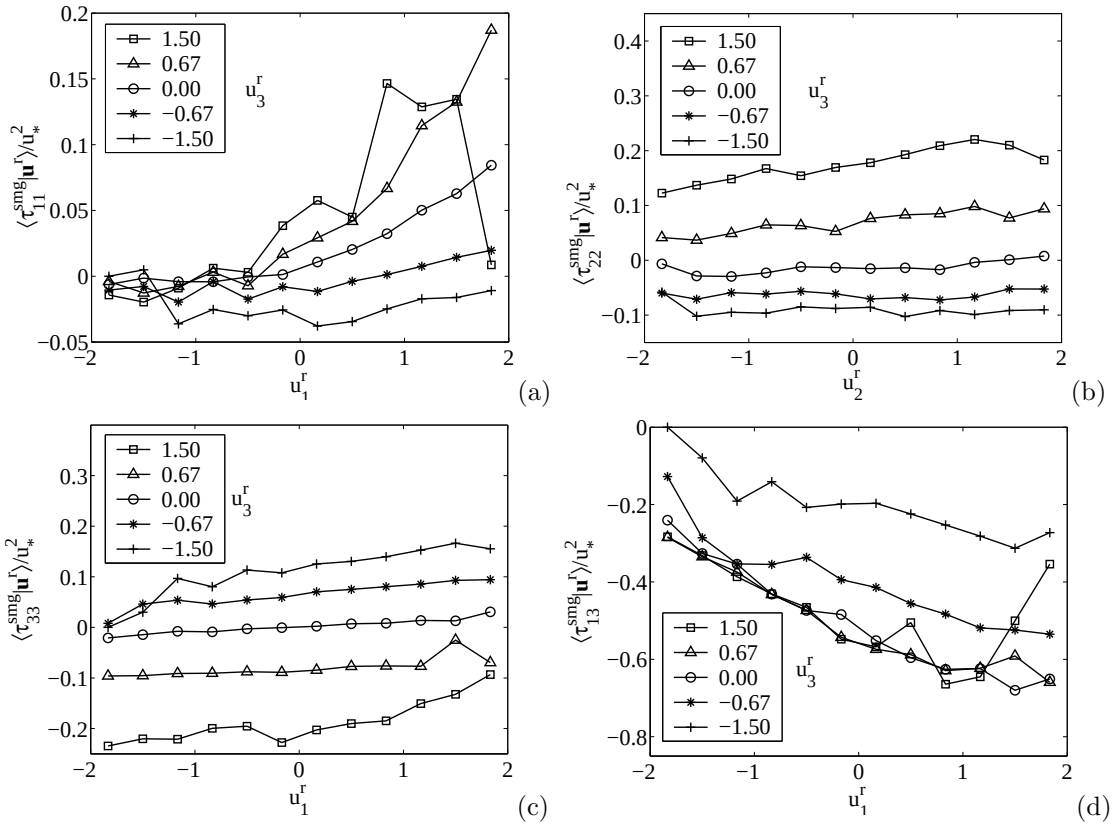

Figure 5.16 LES results (*a posteriori* test) of the conditional SGS stress using the Smagorinsky model.

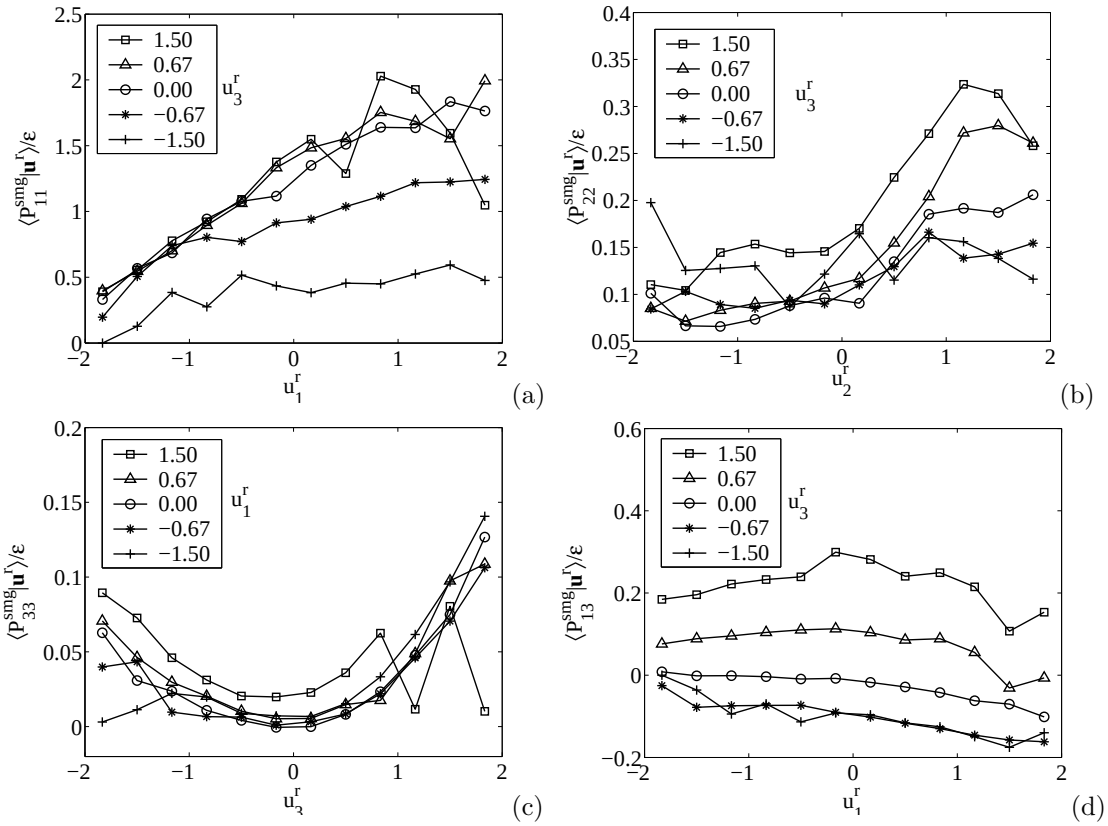

Figure 5.17 LES results (*a posteriori* test) of the conditional SGS stress production rate using the Smagorinsky model.

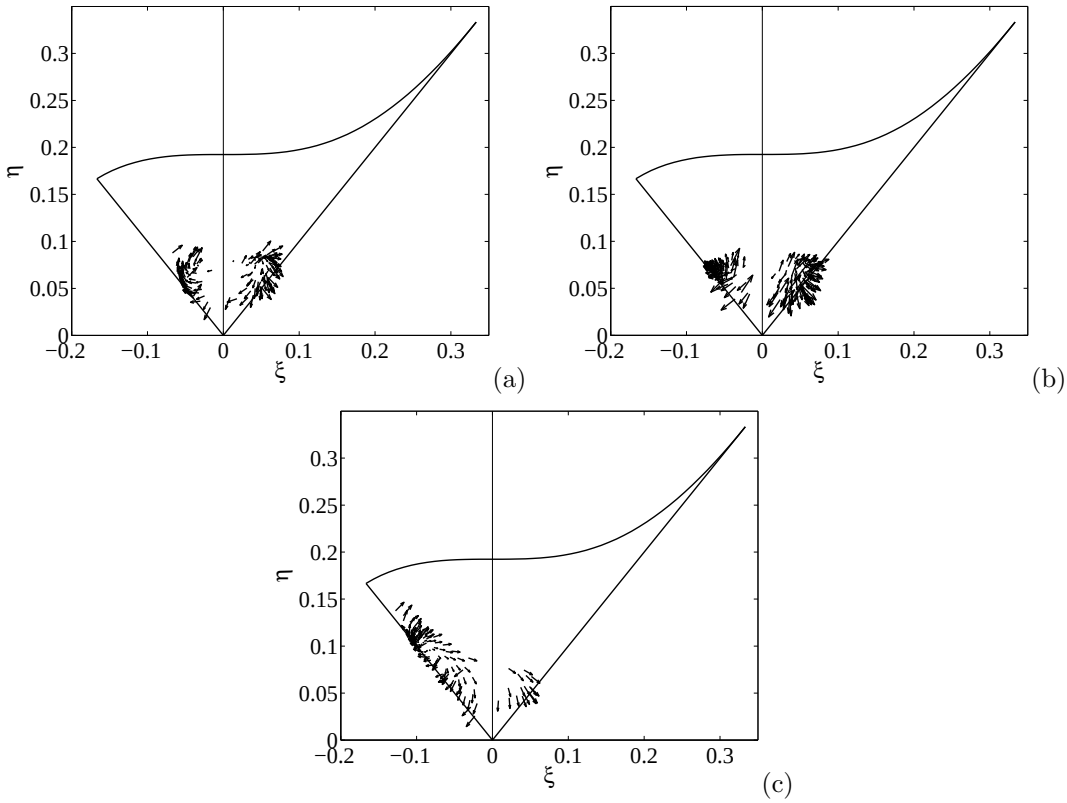

Figure 5.18 LES results (*a posteriori* test) of the Lumley triangle representation of the conditional SGS stress using: a) the Smagorinsky model; b) the split model; c) the Kosović model.

The level of anisotropy of the conditional SGS stress in LES represented in the Lumley triangle are shown in Figure 5.18(a). Similar to the *a priori* test results, the data points are close to the origin, indicating the under-prediction of the level of the anisotropy. The qualitatively dependence of the eigenvalue structure on the resolvable-scale velocity is not correctly predicted. The underpediction of the anisotropy is probably due to the similar reason that it was under-predicted in *a priori* test: the strong correlation between the modeled SGS stress and the strain rate forces reduction of the magnitude of the anisotropic (deviatoric) SGS stress to maintain the correct energy transfer.

To study the eigenvalue structure relationships between the conditional SGS stress and its production rate, the geometric alignment between $\left\langle \tau_{ij}^d | \mathbf{u}^r \right\rangle$ and $\left\langle P_{ij}^a | \mathbf{u}^r \right\rangle$ (where $P_{ij}^a = P_{ij} - P_{kk}\delta_{ij}/3$) are examined, which is characterized by the angle of their eigenvectors.

The alignment between $\langle \tau_{ij}^d | \mathbf{u}^r \rangle$ and $\langle P_{ij}^a | \mathbf{u}^r \rangle$ were studied by Chen and Tong (2006) [90]. They found that $\langle \tau_{ij}^d | u_1^r \rangle$ and $\langle P_{ij}^a | u_1^r \rangle$ are generally well aligned. The alignment angle is less than 10°

and weakly depend on u_1^r. $\langle \tau_{ij}^d | u_3^r \rangle$ and $\langle P_{ij}^a | u_3^r \rangle$ are well aligned for positive u_3^r and less well aligned for negative u_3^r. The definition of the geometric alignment was given in Chen and Tong (2006) [90], and are simply repeated here. The eigenvalues of the conditional SGS stress tensor, $\langle \tau_{ij}^d | \mathbf{u}^r, \rangle$, are denoted as α_τ, β_τ and γ_τ, ordered such that $\alpha_\tau \geq \beta_\tau \geq \gamma_\tau$, and the corresponding unit eigenvectors as $\vec{\alpha}_\tau, \vec{\beta}_\tau$ and $\vec{\gamma}_\tau$. Similarly, the eigenvalues of the conditional SGS stress production tensor, $\langle P_{ij}^a | \mathbf{u}^r \rangle$, are denoted as α_P, β_P and γ_P, ordered such that $\alpha_P \geq \beta_P \geq \gamma_P$, and the corresponding unit eigenvectors as $\vec{\alpha}_P, \vec{\beta}_P$ and $\vec{\gamma}_P$. In order to characterize the geometric alignment between the eigenvectors of $\langle \tau_{ij}^d | \mathbf{u}^r \rangle$ and $\langle P_{ij}^a | \mathbf{u}^r \rangle$, three angles, θ, ϕ and ξ, are defined as $\theta = \cos^{-1}(|\vec{\gamma}_P \cdot \vec{\gamma}_\tau|)$ (the angle between $\vec{\gamma}_P$ and $\vec{\gamma}_\tau$), $\phi = \cos^{-1}(|\vec{\beta}_P \cdot \vec{\beta}_\tau|)$, and $\xi = \cos^{-1}(|\vec{\alpha}_P \cdot \vec{\alpha}_\tau|)$.

The geometric alignment between $\left\langle \tau_{ij}^d | \mathbf{u}^r \right\rangle$ and $\left\langle P_{ij}^a | \mathbf{u}^r \right\rangle$ (in Figure 5.19(a-b)) are generally well predicted in LES for u_1^r and $u_3^r > 0$, but is not predicted correctly for $u_3^r < 0$. The generally good alignment for $u_3^r > 0$ indicates that the LES reproduces the quasi-equilibrium dynamics between the SGS stress production and destruction mechanism in surface layer. But for $u_3^r < 0$, the LES still predicts this quasi-equilibrium while the surface layer is not.

The trends of the eigenvalue of $\left\langle \tau_{ij}^d | u_1^r \right\rangle$ (Figure 5.19(c-d)) are generally well predicted. The dependence of the eigenvalues on u_3^r are generally less well predicted. The magnitudes are generally under-predicted, which is consistent with the results for $\left\langle \tau_{ij}^d | \mathbf{u}^r \right\rangle$. The trends and the magnitude of the eigenvalue ratio of $\left\langle \tau_{ij}^d | u_1^r \right\rangle$ to $\left\langle P_{ij}^a | u_1^r \right\rangle$ (Figure 5.19(e-f)) are not predicted correctly.

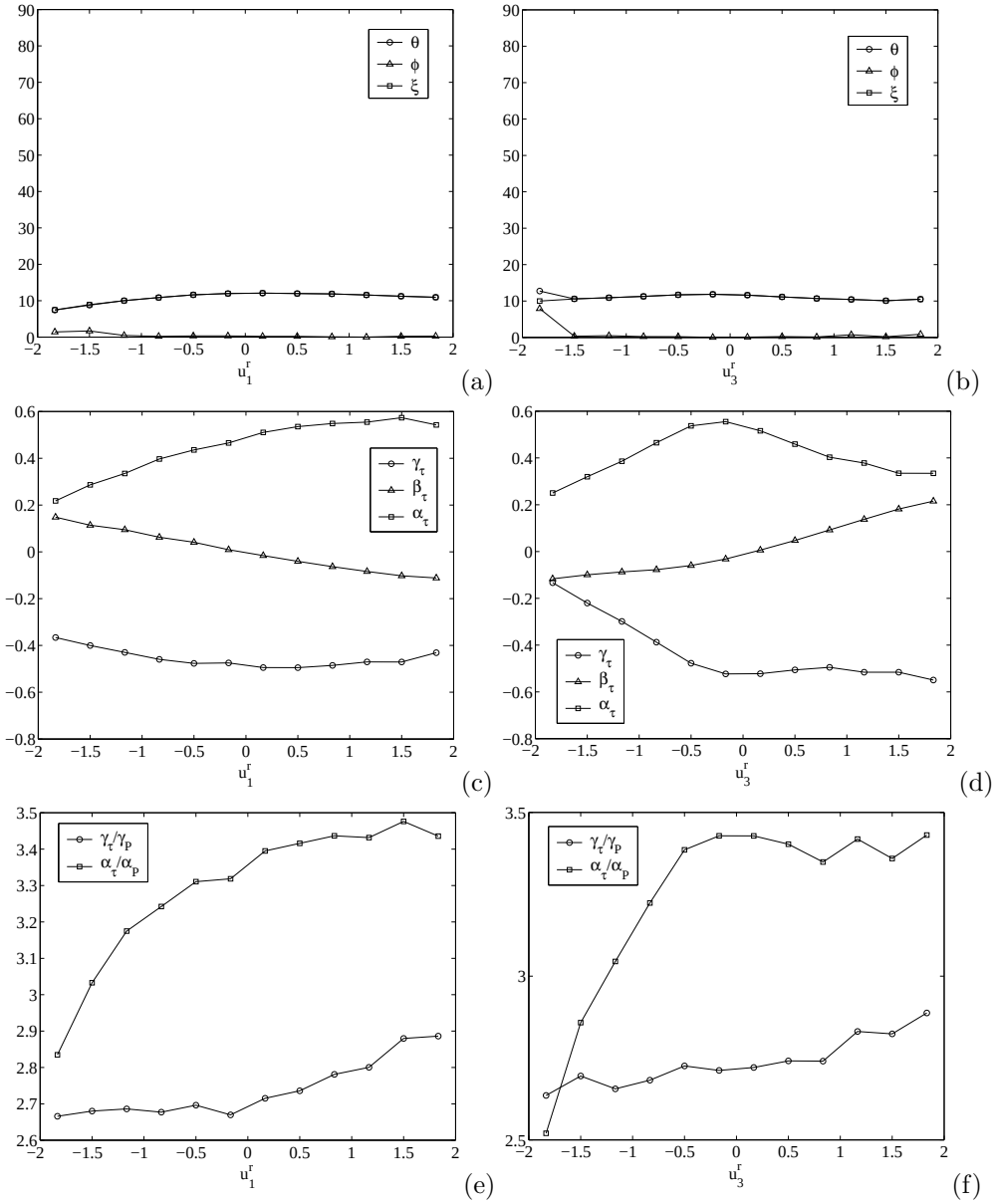

Figure 5.19 LES results (*a posteriori* test) of the geometric alignment angles and eigenvalues of the conditional SGS stress and its production rates: (a-b) the geometric alignment angles; (c-d) the eigenvalues of the conditional SGS stress; (e-f) the eigenvalue ratios of the conditional SGS stress to its production rate using the Smagorinsky model.

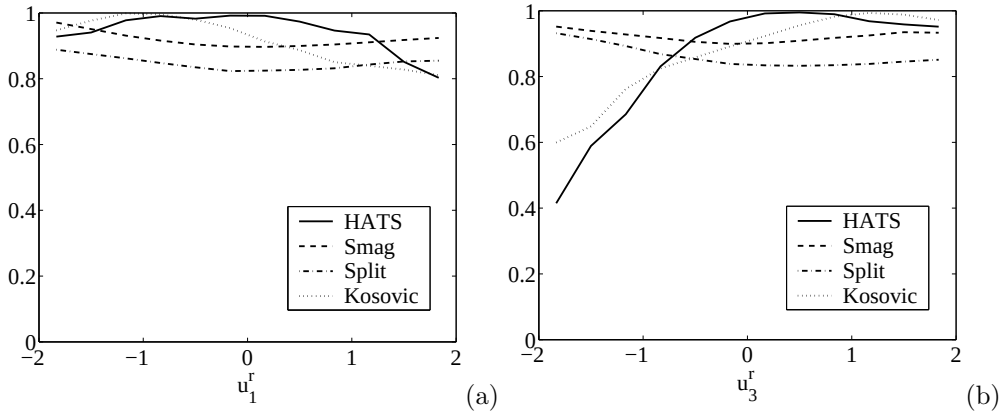

Figure 5.20 Contraction of the conditional SGS stress and its production rate from the LES (*a posteriori* test) and the measurements (*a priori* test).

The overall similarity between $\langle \tau_{ij}^d | \mathbf{u}^r \rangle$ and $\langle P_{ij}^a | \mathbf{u}^r \rangle$ can be quantified using their contraction, $\langle \tau_{ij}^d | \mathbf{u}^r \rangle \langle P_{ij}^a | \mathbf{u}^r \rangle = \frac{\langle \tau_{ij}^d | \mathbf{u}^r \rangle \langle P_{ij}^a | \mathbf{u}^r \rangle}{|\langle \tau_{ij}^d | \mathbf{u}^r \rangle| |\langle P_{ij}^a | \mathbf{u}^r \rangle|}$. If the two tensors are perfectly aligned and their eigenvalues are proportional, the contraction has the value of one. The magnitudes and the trends of the contraction (Figure 5.20) are predicted well for $u_3^r > 0$, but not for $u_3^r < 0$. This is consistent with the above eigenvalue alignment and eigenvalue results. These results are similar to the *a priori* tests (not shown).

These results of the conditional SGS stress and its production and their geometric alignment are generally similar to the *a priori* test results, indicating that the LES correctly reproduced the conditional resolvable-scale strain rate. The deviation of $\left\langle P_{13}^d | \mathbf{u}^r \right\rangle$ in LES from the *a priori* test results indicates that the LES does not correctly reproduce the resolvable-scale stress and strain rate correlation. The consistency between the *a posteriori* test results and the *a priori* test results suggest that analyzing the conditional SGS stress and its production rate are a highly capable approach for identifying specific model deficiencies and for evaluating SGS model performance in simulations.

5.3.2 Split model

Table 5.2 shows that the LES results for the mean SGS stresses using the split model are the same as those of the Smagorinsky model except the mean SGS shear stress component $\langle \tau_{13} \rangle$. The LES results for the conditional means for the two models are also similar except $\left\langle \tau_{13}^d | \mathbf{u}^r \right\rangle$ (Figure 5.21(a)). The dependence of $\left\langle \tau_{13}^d | \mathbf{u}^r \right\rangle$ for the split model on u_1^r is under-predicted. The magnitude is also under-predicted and is smaller than that of the Smagorinsky model. The deviation of the *a*

posteriori test (LES) results from *a priori* tests and measurements indicates that the dependencies of flow statistics on the resolvable-scale velocity are not correctly reproduced.

While the LES mean SGS stress using the split model are generally similar to that of the Smagorinsky model except the mean shear SGS stress component $\langle \tau_{13} \rangle$, the LES mean SGS stress production rate is different from that of the Smagorinsky model. The magnitudes of the conditional SGS stress production are different from that of the Smagorinsky model. This finding provides further support the importance of the SGS stress production rate ([38]). $\left\langle P_{11}^{split} | \mathbf{u}^r \right\rangle$ (Figure 5.21(b)) has a similar trend to that of the Smagorinsky model (Figure 5.17(a)), but with smaller magnitude due to the smaller magnitude of the predicted τ_{13}^d. The magnitude of $\left\langle P_{33}^{split} | \mathbf{u}^r \right\rangle$ (Figure 5.21(d)) is slightly smaller than that of the Smagorinsky model. The magnitude of $\left\langle P_{13}^{split} | \mathbf{u}^r \right\rangle$ (Figure 5.21(e)) on u_1^r is also slightly smaller than that of the Smagorinsky model.

The Lumley triangle representation of the conditional SGS stress are shown in Figure 5.18(b). Similar to the *a priori* test results, the data points are close to the origin, indicating under-prediction of the level of the anisotropy. The trends and magnitude of the geometric alignment (not shown) between the conditional SGS stress and its production rate are generally similar to that of the Smagorinsky model except the alignment angle θ and ξ are about five degrees larger. The generally good tensorial alignment indicates that the simulation reproduces the quasi-equilibrium dynamics between the SGS stress production and destruction rates in the surface layer for $u_3^r > 0$. However, the model over-predicts the alignment for $u_3^r < 0$ when the surface layer is probably not in quasi-equilibrium.

The trend of the eigenvalue of and eigenvalue ratios (not shown) are also similar to those of the Smagorinsky model, but with slightly smaller values. The trend of the tensorial contraction (Figure 5.20) is also similar to that of the Smagorinsky model, but with sightly larger magnitudes.

These results of the conditional SGS stress and its production as well as their geometric alignment are similar to the *a priori* test results, not qualitatively different from that of the Smagorinsky model. Therefore, in spite of the improved mean LES profiles using the split model, the conditionals means are still similar to that of the LES using the Smagorinsky model. Consequently, the improvement resolvable-scale velocity JPDF over the Smagorinsky model may be limited.

5.3.3 Kosović model

The trends for $\left\langle \tau_{ij}^d | \mathbf{u}^r \right\rangle$ (Figure 5.22) and $\left\langle P_{ij}^d | \mathbf{u}^r \right\rangle$ (Figure 5.23) are generally well predicted in LES using the Kosović model. The magnitudes of $\left\langle \tau_{ij}^d | \mathbf{u}^r \right\rangle$ is generally under-predicted. The magnitudes of $\left\langle P_{ij}^d | \mathbf{u}^r \right\rangle$ is generally better predicted.

The trends of $\left\langle \tau_{11}^d | \mathbf{u}^r \right\rangle$ are generally well predicted, but the magnitudes are under-predicted, similar to the *a priori* test results ([90]). The trends and magnitudes of $\left\langle \tau_{22}^d | \mathbf{u}^r \right\rangle$ are well predicted. The magnitude of $\left\langle \tau_{33}^d | \mathbf{u}^r \right\rangle$ is slightly under-predicted. The trends of $\left\langle \tau_{33}^d | \mathbf{u}^r \right\rangle$ are generally well predicted, but the dependence on u_3^r is over-predicted, which is due to the over-prediction of the dependence on u_3^r of the conditional vertical gradient of the vertical resolvable-scale velocity $\langle \partial u_3^r / \partial x_3 \rangle$. The magnitude of $\left\langle \tau_{13}^d | \mathbf{u}^r \right\rangle$ is under-predicted by a factor of 2. The dependence of $\left\langle \tau_{13}^d | \mathbf{u}^r \right\rangle$ on u_1^r is generally well predicted, but the dependence on u_3^r is under-predicted. Both the trends and the magnitudes of $\left\langle \tau_{23}^d | \mathbf{u}^r \right\rangle$ are under-predicted.

The magnitudes of $\left\langle P_{11}^d | \mathbf{u}^r \right\rangle$ are under-predicted by a factor of 2, which is due to the under-prediction of the magnitudes of the conditional SGS shear stress $\langle \tau_{13} | \mathbf{u}^r \rangle$. The trend of $\left\langle P_{11}^d | \mathbf{u}^r \right\rangle$ is generally well predicted. The magnitude $\left\langle P_{33}^d | \mathbf{u}^r \right\rangle$ is generally well predicted. The dependence on u_3^r is over-predicted because the dependence of $\left\langle \tau_{33}^d | \mathbf{u}^r \right\rangle$ is over-predicted on u_3^r, which is the dominant term of $\left\langle P_{33}^d | \mathbf{u}^r \right\rangle$.

The magnitudes and trends of $\left\langle P_{13}^d | \mathbf{u}^r \right\rangle$ are well predicted, but the dependence on u_3^r is over-predicted, which is due to the over-prediction the dependence on u_3^r of τ_{33}. These results of the conditional SGS stress and its production are similar to the *a priori* test results.

The Lumley triangle representation of the conditional SGS stress, shown in Figure 5.18(c), is different from the measurements but similar the *a priori* test results. There are more data points close to $\eta = -\xi$ (axisymmetric with two large eigenvalue) than to $\eta = \xi$ (axisymmetric with one large eigenvalue). This result comes from the over-prediction of the magnitude of $\left\langle \tau_{22}^d | \mathbf{u}^r \right\rangle$. Again, the over-prediction of the magnitude of $\left\langle \tau_{22}^d | \mathbf{u}^r \right\rangle$ is expected to have little consequence on the resolvable-scale statistics in horizontally homogenous boundary layer, but may results in large inaccuracies in other flows where τ_{22} is important.

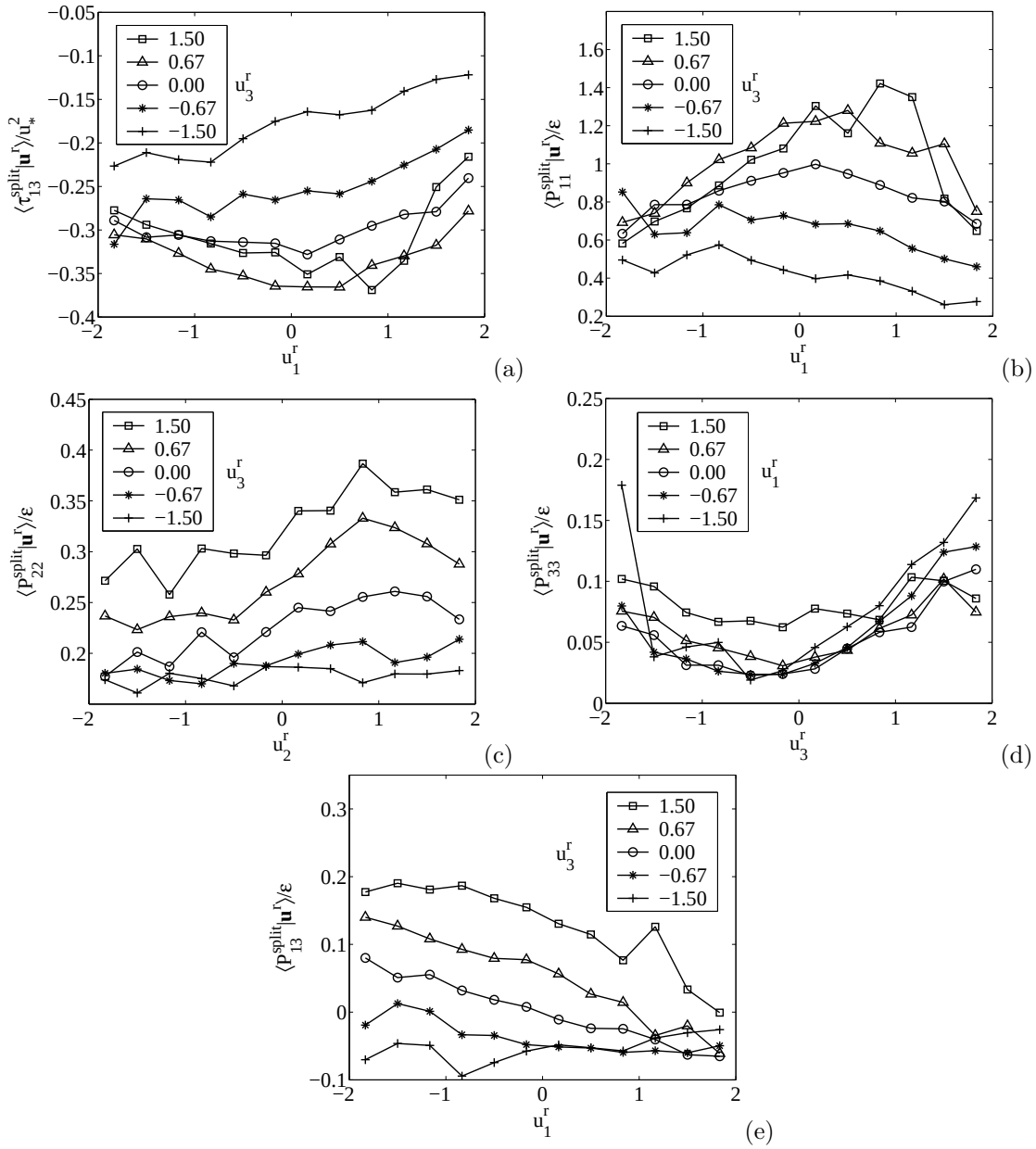

Figure 5.21 LES results (*a posteriori* test) of the conditional SGS stress and its production rate using the split model.

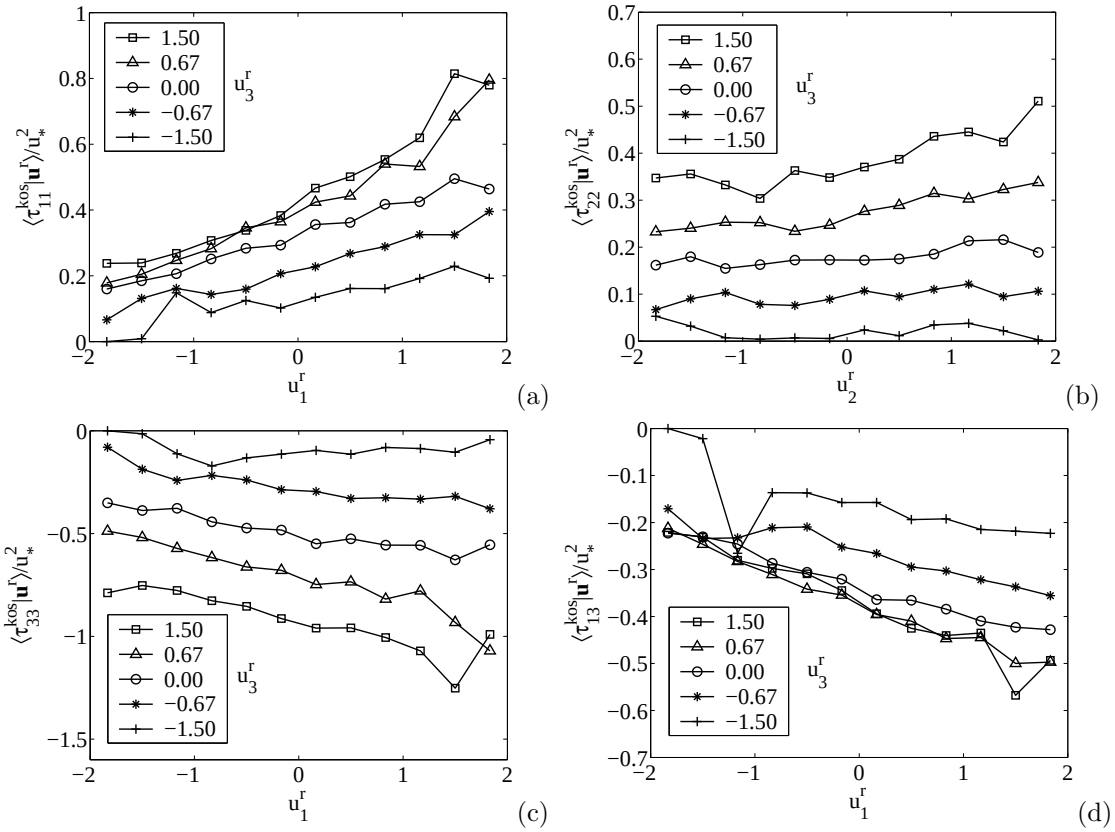

Figure 5.22 LES results (*a posteriori* test) of the conditional SGS stress using the Kosović model.

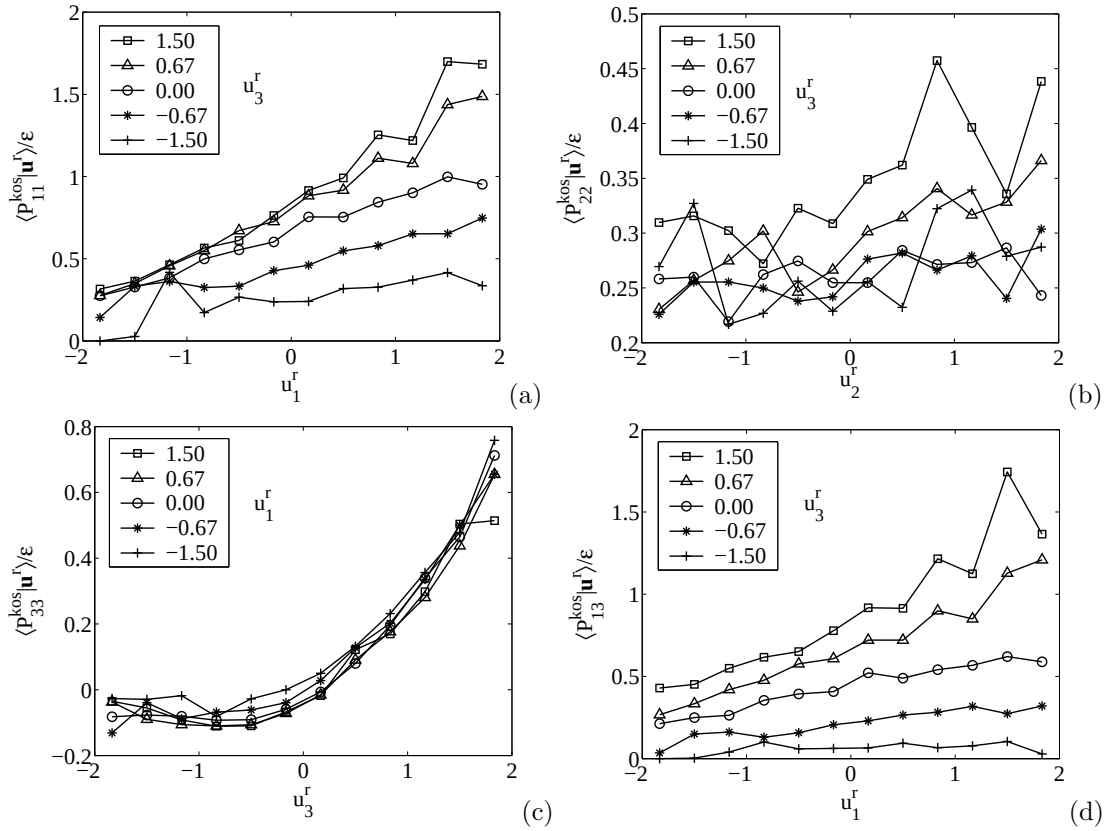

Figure 5.23 LES results (*a posteriori* test) of the conditional SGS stress production rate using the Kosović model.

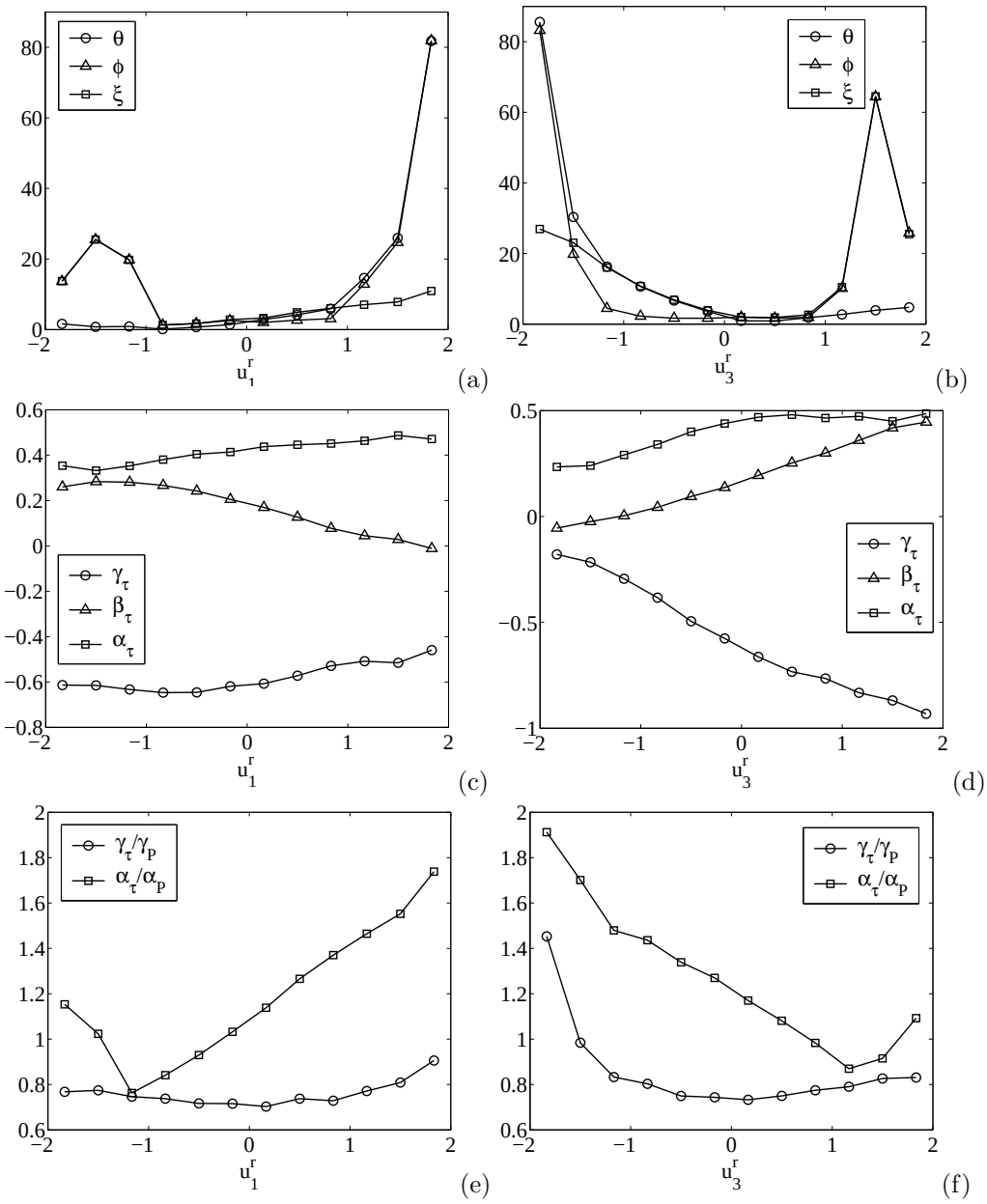

Figure 5.24 LES results (*a posteriori* test) of the geometric alignment angles and eigenvalues of the conditional SGS stress and its production rate: (a-b) the geometric alignment angles; (c-d) the eigenvalues of the conditional SGS stress; (e-f) the eigenvalue ratios of the conditional SGS stress to its production rate using the Kosović model.

The trends of the geometric alignment between $\langle \tau_{ij}^d | \mathbf{u}^r \rangle$ and $\langle P_{ij}^a | \mathbf{u}^r \rangle$ are shown in Figure 5.24(a) and (b). The alignment is generally well predicted for u_1^r and $u_3^r > 0$. The dependence for $u_3^r < 0$ is not well predicted, but shows some improvements over the Smagorinsky model and the split model.

The dependence of the eigenvalue of $\langle \tau_{ij}^d | \mathbf{u}^r \rangle$ (Figure 5.24(c) and (d)) are generally well predicted. But its magnitudes are under-predicted. The trends and the magnitudes of the eigenvalue ratios (Figure 5.24(e) and (f)) are not predicted correctly. The magnitudes and the trends of the contraction between $\langle \tau_{ij}^d | u_1^r \rangle$ and $\langle P_{ij}^a | u_1^r \rangle$ are shown in Figure 5.20, which are very close to the measurement results and show improvement over the Smagorinsky model and the split model. These results of the geometric alignment between the conditional SGS stress and its production are similar to the *a priori* test results.

5.4 Summary

In this study a new *a posteriori* test is developed and employed to study SGS model performance. The approach compares the conditional means of the LES-generated SGS stress and the conditional stress production rate conditional on the resolvable-scale velocity, which must be reproduced by the SGS model for large eddy simulation (LES) to correctly predict the one-point resolvable-scale velocity joint probability density function, with measurements.

The measurement results for the Lumley triangle representation show that the Reynolds stress and the mean resolvable-scale stress are close to axisymmetric with two large eigenvalue, whereas the mean SGS stress is close to axisymmetric with one large eigenvalue in surface layer. This is because the influence of large-scale eddies. The filter near the boundary removes the effect of large-scale eddies, resulting in a structure close to axisymmetric with one large eigenvalue. The Lumley triangle representation of the mean SGS stress production rate shows that it has a similar structure to the mean SGS stress consistent to the good alignment and tensorial contraction between the conditional SGS stress and its production rate ([90]).

The LES results of the Lumley triangle representation for the Reynolds stress and the mean resolvable-scale stress are well predicted using the split model and the Kosović model. The predicted level of anisotropy of the Reynolds stress using the Smagorinsky model is slightly lower than the measurements, but the resolvable-scale mean stress is slightly higher than the measurements. The Lumley triangle representation for the LES mean SGS stress of all models are close to axisymmetric

with two large eigenvalue, different from the measured mean SGS stress eigenvalue structure, but similar to the *a priori* test results.

The LES results for the magnitudes of the both conditional SGS stress and its production rate are generally under-predicted using the Smagorinsky model. The LES can reproduce the trends of some shear stress components but not the normal components, and can reproduce the trends of some normal components of the conditional SGS stress production rate, but not the shear components. These *a posteriori* test results are generally similar to that of the *a priori* test results ([90]).

Anisotropy of the conditional SGS stress as shown in the Lumley triangle using the Smagorinsky model is under-predicted in LES, similar to the *a priori* test results. The geometric alignment, eigenvalues, eigenvalue ratios, and contraction of the conditional SGS stress and its production rate are generally reproduced in LES using the Smagorinsky model for $u_3^\tau > 0$, but not for $u_3^\tau < 0$, which are similar to the *a priori* tests.

The LES results of the conditional SGS stress and its production as well as their geometric alignment using the split model are similar to the *a priori* test results, and are not qualitatively different from that of the Smagorinsky model. Therefore, in spite of the improved mean LES profiles using the split model, the conditionals means are still similar to that of the LES using the Smagorinsky model. Consequently, the improvement of the resolvable-scale velocity JPDF over the Smagorinsky model may be limited.

The LES results of the conditional SGS stress and its production, their geometric alignment, eigenvalues, and contraction using the Kosović model are similar to the *a priori* test results and show improvement over the Smagorinsky model.

The *a posteriori* test results discussed are generally consistent with the *a priori* test results. The model strength and deficiencies observed here are also similar to those identified in previous statistical *a priori* tests analyzing the conditional statistics. The consistency is partly because both types of tests analyze the SGS terms in the velocity JPDF equation. By contrast the traditional *a priori* test have not direct relationship to *a posteriori* tests because the former compare the instantaneous modeled and measured SGS stress and the latter compare the LES and measured statistics profiles. More importantly, the consistency provides strong support to the approach of analyzing the conditional SGS stress and its production rate in the JPDF equation to test SGS models and to understand SGS physics, which is capable of identifying specific model deficiencies and of evaluating SGS model performance in simulations.

CHAPTER 6

Conclusions

In this work, the effects of the subgrid-scale (SGS) turbulence on the resolvable-scale statistics as well as the effects of SGS models on large-eddy simulation (LES) are studied. It is shown that the SGS turbulence evolves the resolvable-scale joint probability density function (JPDF) through the conditional means of the SGS stress, the SGS scalar flux, and their production rate, which must be reproduced by the SGS model for LES to predict correctly the one-point resolvable-scale statistics, a primary goal of LES. This necessary condition is used as the basis for studying SGS physics and for testing SGS models. Theoretical predictions, measurements data obtained in a turbulent jet and in a convective atmospheric surface layer, and large-eddy simulation data of convective atmospheric boundary layers are combined to investigate the effects of filter size, the dependence of the SGS turbulence on the flow dynamics, and SGS models performance using new *a priori* and *a posteriori* tests developed in this research.

For inertial-range filter scales, the issue of the influences of the SGS stress and the SGS scalar flux on the resolvable-scale velocity-scalar JPDF are examined. The filter-scale dependencies of the mean production rates are predicted using Lumley's assumption. The results using the data obtained in a slightly heated turbulent jet show that the conditional SGS flux and the conditional SGS flux production rates are found to strongly depend on the resolvable-scale velocity and scalar and have similar functional forms for eddies that are likely in quasi-equilibrium. This is also observed in the atmospheric surface layer, suggesting that the similarity exists whenever SGS eddies are in quasi-equilibrium regardless of the larger-scale flow geometry. It is also found that the dependencies on the resolvable-scale velocity have qualitatively different forms for positive and negative resolvable-scale scalar fluctuations, indicating strong flow history effects.

The measured mean SGS scalar flux, the mean SGS scalar flux production rate, and the mean SGS shear stress production rate are generally consistent with the predictions based on Lumley's assumption, which is consistent with Kolmogorov's hypothesis, suggesting that the SGS flux, its production rate, and the SGS shear stress production have diminishing effects on the lower-order resolvable-scale velocity-scalar statistics. However, it is found that the conditional SGS scalar flux

and SGS scalar flux production rate fall-off much slower with the filter scale than the mean SGS scalar flux and SGS scalar flux production rate, a behavior similar to the conditional SGS shear stress production rate Chen *et al.* (2003) [38]. The slower fall-offs of these conditional statistics suggest that they have non-diminishing influences on the JPDF and the high-order statistics of the resolvable-scale velocity and scalar, such as turbulent transport and scalar PDF.

The Smagorinsky model predictions of the filter-scale dependencies of the mean SGS fluxes and the mean SGS flux production rate are consistent with predictions and experimental results; therefore, the models are likely to have diminishing effects on lower-order LES statistics (e.g. mean and r.m.s.). The model predictions of the conditional SGS flux decrease faster with the filter scale than measurements whereas the conditional SGS flux production does not decrease. Therefore, models are likely to have effects on the high-order LES statistics even for inertial-range filter scales but in ways different from that of the SGS turbulence.

For energy-containing filter scales, field measurements data take in the convective atmospheric boundary layer are used to analyse the effects of the subgrid-scale stress and its production rate on the resolvable-scale velocity JPDF. Analyses of the conditional SGS stress and the conditional SGS stress production using the field data show that they are closely related to the surface-layer dynamics. Specifically, the updrafts generated by buoyancy, the downdrafts associated with the large-scale convective eddies, the mean shear, and the length scale inhomogeneity play important roles in the behaviors of the conditional SGS stress and its production rate.

The results show that when the resolvable-scale vertical velocity (u_3^r) is positive (updrafts), the subgrid-scale eddies move upward and are on average stretched in the vertical direction owing to shear and buoyancy acceleration. Under such conditions, the spectral transfer and inter-component exchange among the normal SGS stress components result in forward energy transfer and anisotropy in the SGS stress. For negative u_3^r, the subgrid-scale eddies associated with the returning flow of large convective eddies move downward and are on average compressed in the vertical direction owing to the presence of the ground. The spectral transfer and inter-component exchange result in conditional backscatter and nearly isotropic SGS stress.

Representation of the conditional SGS stress in the Lumley triangle also shows similar trends for anisotropy. The results also show that the conditional SGS stress and its production rate have similar trends and are generally well aligned.

Statistic *a priori* tests of several current SGS models are performed. None of those models are able to predict correctly the trends of both the conditional SGS stress and its production rate. The Smagorinsky and Kosović's nonlinear model under-predict the anisotropy and the variations of

the anisotropy, whereas the other nonlinear model ([82]) and the mixed model over-predict both. However, Kosović's nonlinear model shows a better overall performance than the Smagorinsky, the nonlinear model, and the mixed model.

Using the measured conditional SGS stress and its production rate and their model predictions, the deficiencies in current LES results, such as the over-predictions of the mean velocity profile and the streamwise velocity variance, and the under-prediction of the vertical velocity skewness are linked to the inability of the SGS models to predict the conditional SGS stress and its production rate correctly. Specifically, the former is related to the under-prediction of the anisotropy of the conditional SGS stress and the latter is due to the under-prediction of the dependence of $\langle P_{33}|\mathbf{u}^r\rangle$ on u_3^r and the asymmetry in the dependence.

To further study the effects of the SGS turbulence on the resolvable-scale velocity-scalar statistics for energy-containing filter scales, field measurements data taken in a convective atmospheric boundary layer are used to analyze the SGS statistics that evolve the resolvable-scale velocity-scalar JPDF. The results show that the conditional SGS scalar flux, its production rate, and the SGS scalar variance production rate conditional on the resolvable-scale velocity and scalar, depend strongly on the resolvable-scale velocity and scalar and the dependence is closely related to the surface layer dynamics. Therefore, SGS model predictions of these SGS statistics can potentially have strong effects on LES statistics.

Analyses show that the dependence is generally strong for positive resolvable-scale temperature fluctuations and is weak for negative fluctuations. For positive temperature fluctuations, eddies associated with updrafts generally come from the near ground region, which contain large magnitudes of vertical SGS flux and SGS stress, and experience strong shear and vertical temperature gradient, resulting in large SGS flux production rates. For negative temperature fluctuations, eddies associated with downdrafts generally come from the mixed layer region, which carry relatively small fluxes, resulting small magnitudes and weak dependence of the conditional SGS scalar flux production rates on the resolvable-scale velocity.

Examination of the SGS flux production rates show that the vertical SGS scalar flux influences the horizontal SGS scalar production rate, however the horizontal SGS scalar flux does not influence directly the vertical SGS scalar flux production rate but nonetheless affects the resolvable-scale scalar PDF. Therefore, correct modeling of the conditional vertical scalar flux components is crucial. Furthermore, The conditional SGS scalar flux and the conditional SGS scalar flux production rate have similar trends and are generally well aligned. The similarities and the dynamic

connections between the conditional scalar flux and its production rate indicate the potential of using the conditional scalar flux production rate to model the scalar flux in convective ABLs.

Statistical *a priori* tests using these conditional statistics show that the Smagorinsky model can predict well the conditional vertical scalar flux and the conditional horizontal scalar flux production rate. The nonlinear model can predict well the conditional horizontal scalar flux. Predictions of the SGS flux using the nonlinear model are found to be closely related to the predictions of the Smagorinsky model and the quasi-equilibrium between the production and pressure destruction. Analyses of the nonlinear model using the Smagorinsky model and the surface layer dynamics provide a physical explanation of the performance of the nonlinear model. A similar analyse of the nonlinear SGS stress model are also performed.

To understand the model performance in LES, a new *a posteriori* test is developed and employed to study SGS model performance. The approach compares the conditional means of the LES-generated SGS stress and the conditional stress production rate with measurements.

The measurement results for the Lumley triangle representation show that the Reynolds stress and the mean resolvable-scale stress are close to axisymmetric with two large eigenvalue, whereas the mean SGS stress is close to axisymmetric with one large eigenvalue in surface layer. The Lumley triangle representation of the mean SGS stress production rate shows that it has a similar structure to the mean SGS stress, consistent with the good alignment and tensorial contraction between the conditional SGS stress and its production rate ([90]).

The LES results of the Lumley triangle representation for the Reynolds stress and the mean resolvable-scale stress are well predicted using the split model and the Kosović model but are less well predicted using the Smagorinsky model. The Lumley triangle representation for the LES mean SGS stress of all models are inconsistent with the measured mean SGS stress eigenvalue structure, but similar to the *a priori* test results.

The magnitudes of the both conditional SGS stress and its production rate are generally under-predicted in LES using the Smagorinsky model. The LES cannot reproduce the trends of the conditional SGS stress and its production rate well at same time. These *a posteriori* test results are generally similar to that of the *a priori* test results ([90]). The Lumley triangle representation and geometric alignments using the Smagorinsky model are also similar to the *a priori* test results. The LES results of the conditional SGS stress and its production rate using the split model are similar to the *a priori* test results, and are not qualitatively different from that of the Smagorinsky model. Therefore, in spite of the improved mean LES profiles using the split model, the conditionals means are still similar to that of the LES using the Smagorinsky model. The LES results of the conditional

SGS stress and its production rate using the Kosović model are similar to the *a priori* test results and show improvement over the Smagorinsky model.

The results obtained in this research have strong implications on SGS modeling. Analyses show that for the inertial-range filter scales SGS predictions of the mean statistics support the premise of LES at the level of lower-order statistics. However, in applications where higher-order statistics (e.g. turbulent transport and scalar PDF) are important, SGS predictions of these conditional statistics should be an essential part of model tests. For the energy-containing filter scales the current SGS models have varying level of performance in predicting different SGS components. As a results, the poor prediction of one SGS component often affects the prediction of the production rate of another SGS component, thereby resulting in errors in the LES statistics. Therefore, efforts to improve SGS models need to ensure that all the relevant SGS fluxes related to the LES statistics of interests or of importance to the intended applications are correct predicted. Given the strong dependence of the conditional statistics on the flow dynamics, it may be necessary to incorporate some aspects of the dynamics to correctly predict these conditional statistics.

The *a posteriori* test results are generally consistent with the *a priori* test results. The model strength and deficiencies observed here are also similar to those identified in previous statistical *a priori* tests analyzing the conditional statistics. The consistency is partly because both types of tests analyze the SGS terms in the velocity JPDF equation. By contrast the traditional *a priori* test have not direct relationship to *a posteriori* tests. The consistency provides strong support to the approach of analyzing the conditional SGS stress and its production rate in the JPDF equation to test SGS models and to understand SGS physics, which is capable of identifying specific model deficiencies and of evaluating SGS model performance in simulations.

To further understand the SGS scalar flux model performance in LES, this new *a posteriori* test can be extended to study the resolvable-scale velocity-scalar JPDF equation. The conditional means of the SGS fluxes and their production rate conditioning on the resolvable-scale velocity and scalar need to be examined using LES data. Analytical results used to investigate the relationship between the SGS terms and the JPDF equation in Chapter 3 is important for identifying the deficiencies of SGS models. This provides impetus for further analytical understanding of the JPDF equations, which will greatly benefit the evaluation and development of improved SGS models.

REFERENCES

1. Lilly, D. K., The representation of small-scale turbulence in numerical simulation experiments, *In Proc. IBM Scientific Computing Symp. Environ. Sci.*, p. 195 (1967).

2. Deardorff, J. W., A numerical study of three-dimensional turbulent channel flow at large Reynolds numbers, *J. Fluid Mech.*, **41**:453 – 480 (1970).

3. Deardorff, J. W., Numerical investigation of neutral and unstable planetary boundary layers, *J. Atmos. Sci.*, **29**:91 – 115 (1972).

4. Moeng, C.-H. and Wyngaard, J. C., Statistics of conservative scalars in the convective boundary layer, *J. Atmos. Sci.*, **41**:3161 – 3169 (1984).

5. Schmidt, H. and Schumann, U., Coherent structure of the convective boundary layer derived from large-eddy simulations, *J. Fluid Mech.*, **200**:511 – 562 (1989).

6. Nieuwstadt, F. T. M. and de Valk, P. J. P. M. M., A large eddy simulation of of buoyant and non-buoyant plume dispersion in the atmospheric boundary layer, *Atmos. Environ.*, **21**:2573 – 2587 (1987).

7. Germano, M., Piomelli, U., Moin, P., and Cabot, W. H., A dynamic subgrid-scale eddy viscosity model, *Phys. Fluids A*, **3**:1760–1765 (1991).

8. Mason, P. J. and Thomson, D. J., Stochastic backscatter in large-eddy simulation of boundary layers, *J. Fluid. Mech.*, **242**:51 – 78 (1992).

9. Wyngaard, J. C., Atmosperic turbulence, *Annu. Rev. Fluid Mech.*, **24**:205 – 233 (1992).

10. Sullivan, P. P., McWilliams, J. C., and Moeng, C.-H., A subgrid-scale model for large-eddy simulation of planetary boundary-layer flows, *Boundary-Layer Met.*, **71**:247 – 276 (1994).

11. Lesieur, M. and Métais, O., New Trends in Large Eddy Simulations of Turbulence, *Ann. Rev. Fluid Mech.*, **28**:45–82 (1996).

12. Meneveau, C. and Katz, J., Scale-invariance and turbulence models for large-eddy simulation, *Annu. Rev. Fluid Mech.*, **32**:1–32 (2000).

13. Rogallo, R. S. and Moin, P., Numerical Simulation of turbulent flows, *Annu. Rev. Fluid Mech.*, **16**:99–137 (1984).

14. Zang, Y., Street, R. L., and Koseff, A dynamic mixed subgrid-scale model and its application to turbulent recirculating flows, *Phys. Fluids A*, **5**:3186–3196 (1993).

15. Meneveau, C., Lund, T. S., and Cabot, W. H., A Lagrangian dynamics subgrid-scale model of turbulence, *J. Fluid Mech.*, **319**:353–385 (1996).

16. Horiuti, K., A new dynamic two-parameter mixed model for large-eddy simulation, *Phys. Fluids*, **9**:3443–3464 (1997).

17. Domaradzki, J. A. and Saiki, E. M., A subgrid-scale model based on the estimation of unresolved scales of turbulence, *Phys. Fluids*, **9**:2148 (1997).

18. Vreman, B., Geurts, B., and Kuerten, H., Large-Eddy Simulation of the Turbulent Mixing Layer, *J. Fluid Mech.*, **339**:357–390 (1997).

19. Sarghini, F., Piomelli, U., and Balaras, E., Scale-similar models for large-eddy simulations, *Phys. Fluids*, **11**:1596–1607 (1999).

20. Hughes, T. J. R., Mazzei, L., Oberai, A. A., and Wray, A. A., The multiscale formulation of large eddy simulation: Decay of homogeneous isotripic turbulence, *Phys. Fluids*, **13**:505–512 (2001).

21. Mason, P. J., Large-eddy simulation: A critical review of the technique, *Quart. J. Roy. Meteor. Soc.*, **120**:1–26 (1994).

22. Clark, R. A., Ferziger, J. H., and Reynolds, W. C., Evaluation of subgrid-models using an accurately simulated turbulent flow, *J. Fluid Mech.*, **91**:1–16 (1979).

23. McMillan, O. J. and Ferziger, J. H., Direct testing of subgrid-scale models, *Am. Inst. Aeronaut. Astronaut. J.*, **17**:1340 – 1346 (1979).

24. Bardina, J., Ferziger, J. H., and Reynolds, W. C., Improved Subgrid Scale Models for Large Eddy Simulation, *AIAA Paper 80-1357*, (1980).

25. Piomelli, U., Moin, P., and Ferziger, J. H., Model consistency in large eddy simulation of turbulent channel flows, *Phys. Fluid*, **31**:1884 – 1891 (1988).

26. Lund, T. S. and Novikov, E. A., Parametrization of subgrid-scale stress by the velocity gradient tensor, *Annual Research Briefs - Center for Turbulence Research*, pp. 27 – 43 (1992).

27. Domaradzki, J. A., Liu, W., and Brachet, M. E., An analysis of subgrid-scale interactions in numerically simulated isotropic turbulence, *Phys. Fluids A*, **5**:1747 – 1759 (1993).

28. Piomelli, U., High Reynolds-number calculations using the dynamic subgrid-scale stress model, *Phys. Fluid A*, **5**:1484 – 1490 (1993).

29. Härtel, C., Kleiser, L., Unger, F., and Friedrich, R., Subgrid-scale energy-transfer in the near-wall region of turbulent flow, *Phys. Fluid*, **6**:3130 – 3143 (1994).

30. Liu, S., Meneveau, C., and Katz, J., On the Properties of Similarity Subgrid-Scale Models as Deduced from Measurements in a Turbulent Jet, *J. Fluid Mech.*, **275**:83–119 (1994).

31. Meneveau, C., Statistics of turbulence subgrid-scale stress: Necessary conditions and experimental tests, *Phys. Fluids*, **6**:815 (1994).

32. Peltier, L. J., Wyngaard, J. C., Khanna, S., and Brasseur, J., Spectra in the unstable surface layer, *J. Atmos. Sci.*, **53**:49 – 61 (1996).

33. Juneja, A. and Brasseur, J. G., Characteristics of subgrid-resolved-scale dynamics in anisotropic turbulence, with application to rough-wall boundary layers, *Phys. Fluid*, **11**:3054 – 3068 (1999).

34. Tao, B., Katz, J., and Meneveau, C., Geometry and scale relationships in high Reynolds number turbulence determined from three-dimensional holographic velocimetry, *Phys. Fluids*, **12**:941 – 944 (2000).

35. Porté-Agel, F., Parlange, M. B., Meneveau, C., and Eichinger, W. E., A priori field study of the subgrid-scale heat fluxes and dissipation in the atmospheric surface layer, *J. Atmos. Sci.*, **58**:2673–2698 (2001).

36. Sullivan, P. P., Horst, T. W., Lenschow, D. H., Moeng, C.-H., and Weil, J. C., Structure of subfilter-scale fluxes in the atmospheric surface layer with application to large-eddy simulation modeling, *J. Fluid Mech.*, **482**:101 – 139 (2003).

37. Pope, S. B., *Turbulent Flows*, Cambridge University press, Cambridge, England, 2000.

38. Chen, Q., Zhang, H., Wang, D., and Tong, C., Subgrid-scale stress and its production rate: conditions for the resolvable-scale velocity probability density function, *J. Turbulence*, **4**:027 (2003).

39. Pope, S. B., PDF methods for turbulent reacting flows, *Prog. Eng. Combust. Sci*, **11**:119–192 (1985).

40. Sabelnikov, V. A., Asymptotic solution of the equation for the probability distribution of a passive scalar in grid turbulence with a uniform mean scalar gradient, *Phys. Fluids*, **10**:753 – 755 (1998).

41. Adrian, R. J., Stochastic estimation of sub-grid scale motions, *Appl. Mech. Rev.*, **43**:S214 – S218 (1990).

42. He, G.-w., Wang, M., and Lele, S. K., Evaluation of subgrid-scale models in terms of time correlations, in *Proceedings of summer program*, pp. 73 – 78, Center for Turbulence Research, Stanford University, 2002.

43. He, G.-w., Wang, M., and Lele, S. K., On the computation of space-time correlations by large-eddy simulation, *Phys. Fluids*, **16**:3859 – 3867 (2004).

44. Lumley, J., Similarity and the turbulent energy spectrum, *Phys. Fluids*, **10**:855 – 858 (1967).

45. Wygnanski, I. and Fiedler, H., Some measurements in the self-preserving jet, *J. Fluid Mech.*, **38**:577 (1969).

46. Panchapakesan, N. R. and Lumley, J. L., Turbulence measurements in axisymmetric jet of air and helium. Part 1. air jet, *J. Fluid Mech.*, **246**:197 (1993).

47. Hussein, H. J., Capp, S. P., and George, W. K., Velocity measurements in a high-Reynolds-number, momentum-conserving, axisymmetric, turbulent jet, *J. Fluid Mech.*, **258**:31 (1994).

48. Tong, C., Wyngaard, J. C., Khanna, S., and Brasseur, J. G., Resolvable- and subgrid-scale measurement in the atmospheric surface layer: technique and issues, *J. Atmos. Sci.*, **55**:3114–3126 (1998).

49. Tong, C., Wyngaard, J. C., and Brasseur, J. G., Experimental study of subgrid-scale stress in the atmospheric surface layer, *J. Atmos. Sci.*, **56**:2277–2292 (1999).

50. Porté-Agel, F., Parlange, M. B., Meneveau, C., Eichinger, W. E., and Pahlow, M., Subgrid-scale dissipation in the atmospheric surface layer: Effects of stability and filter dimension, *J. Atmos. Sci.*, **57**:75–87 (2000).

51. Cerutti, S. and Meneveau, C., Statistics of filtered velocity in grid and wake turbulence, *Phys. Fluids*, **12**:1143–1165 (1999).

52. Cerutti, S., Meneveau, C., and Knio, O. M., Spectral and hyper eddy viscosity in high-Reynolds-number turbulence, *J. Fluid Mech.*, **421**:307–338 (2000).

53. Tong, C., Measurements of conserved scalar filtered density function in a turbulent jet, *Phys. Fluids*, **13**:2923–2937 (2001).

54. Wang, D. and Tong, C., Conditionally filtered scalar dissipation, scalar diffusion, and velocity in a turbulent jet, *Phys. Fluids*, **14**:2170–2185 (2002).

55. Rajagopalan, A. G. and Tong, C., Experimental investigation of scalar-scalar-dissipation filtered joint density function and its transport equation, *Phys. Fluids*, **15**:227–244 (2003).

56. Antonia, R. A., Browne, L. W. B., and Chambers, A. J., Determination of time constants of cold wires, *Rev. Sci. Instrum.*, **52**:1382 (1981).

57. Browne, L. W. B., Antonia, R. A., and Chua, L. P., Calibration of X-probes for turbulent flow measurements, *Exps. Fluids*, **7**:201–208 (1989).

58. Wyngaard, J. C., Toward Numerical Modeling in the "Terra Incognita", *J. Atmos. Sci.*, **61**:1861 – 1826 (2004).

59. Wyngaard, J., Cospectral similarity in the atmospheric surface layer, *Q.J.R. Meteorol. Soc.*, **98**:590 – 603 (1972).

60. Smagorinsky, J., General circulation experiments with the primitive equations: I. The basic equations, *Mon. Weather Rev.*, **91**:99 – 164 (1963).

61. Borue, V. and Orszag, S., Local energy flux and subgrid-scale statistics in three-dimensional turbulence, *J. Fluid Mech.*, **366**:1–31 (1998).

62. Kaimal, J. C., Wyngaard, J. C., Izumi, Y., and Coté, O. R., Spectral characteristic of surface-layer turbulence, *Q.J.R. Met. Soc.*, **98**:563 – 589 (1972).

63. Khanna, S. and Brasseur, J. G., Analysis of Monin-Obukhov similarity from large-eddy simulation, *J. Fluid Mech.*, **345**:251 – 286 (1997).

64. Porté-Agel, F., Meneveau, C., and Parlange, M., A scale-dependent dynamics model for large-eddy simulation: application to a neutral atmospheric buoyancy layer, *J. Fluid Mech.*, **415**:261 – 284 (2000).

65. Schumann, U., Subgrid scale model for finite difference simulations of turbulent flows in plane channels and annuli, *J. Comp. Physics*, **18**:376 – 404 (1975).

66. Leith, C. E., Stochastic backscatter in a subgrid-scale model: plane shear mixing layer, *Phys. Fluids A*, **2**:297 – 299 (1990).

67. Kosović, B., Subgrid-scale modelling for the large-eddy simulation of high-Reynolds-number boundary layer, *J. Fluid Mech.*, **336**:151 – 182 (1997).

68. Langford, J. A. and Moser, R. D., Optimal LES formulations for isotropic turbulence, *J. Fluid Mech.*, **398**:321–346 (1999).

69. Tong, C., Galilean invariance of velocity probability density function transport equation, *Phys. Fluids*, **15**:2073–2076 (2003).

70. Jaberi, F. A., Miller, R. S., and Givi, P., Conditional statistics in turbulent scalar mixing and reaction, *AIChE J.*, **42**:1149–1152 (1996).

71. Wyngaard, J. C., Coté, O. R., and Izumi, Y., Local free convection, similarity, and the budgets of shear stress and heat flux, *J. Atmos. Sci.*, **28**:1171 – 1182 (1971).

72. Pope, S. B., Ten questions concerning the large-eddy simulation of turbulent flows, *New J. Phys.*, **6**:1 – 24 (2004).

73. Gicquel, L. Y. M., Givi, P., Jaberi, F. A., and Pope, S. B., Velocity filtered density function for large eddy simulation of turbulent flows, *Phys. Fluids*, **14**:1196–1213 (2002).

74. Wang, D., Tong, C., and Pope, S. B., Experimental study of velocity filtered joint density function and its transport equation, *Phys. Fluids*, **16**:3599 – 3613 (2004).

75. Horst, T. W., Kleissl, J., Lenschow, D. H., Meneveau, C., Moeng, C.-H., Parlange, M. B., Sullivan, P. P., and Weil, J. C., HATS: Field observations to obtain spatially-filtered turbulence fields from transverse arrays of sonic anemometers in the atmosperic surface flux layer, *J. Atmos. Sci.*, **61**:1566 – 1581 (2004).

76. Edsall, R. M., Thomson, D. W., Wyngaard, J. C., and Peltier, L. J., A technique for measurement of resolvable-scale flux budgets, in *11th Symp. on Boundary Layers and Turbulence*, pp. 15 – 17, Amer. Meteor. Soc., Charlotte, NC, 1995.

77. Tong, C., Wyngaard, J. C., Khanna, S., and Brasseur, J. G., Resolvable- and subgrid-scale measurement in the atmospheric surface layer, in *12th Symp. on Boundary Layers and Turbulence*, pp. 221 – 222, Amer. Meteor. Soc., Vancouver, BC, Canada, 1997.

78. Kleissl, J., Meneveau, C., and Parlange, M., On the magnitude and variability of subgrid-scale eddy-diffusion coefficients in the atmospheric surface layer, *J. Atmos. Sci.*, **60**:2372 – 2388 (2003).

79. Lumley, J. L., Interpretation of time spectra measured in high-intensity shear flows, *Phys. Fluids*, **6**:1056 – 1062 (1965).

80. Piomelli, U., Yu, Y., and Adrian, R. J., Subgrid-scale energy transfer and near-wall turbulence structure, *Phys. Fluids*, **8**:215–224 (1996).

81. Lumley, J. L., Computational modeling of turbulent flows, *Adv. Appl. Mech.*, **18**:123 – 176 (1978).

82. Leonard, A., Energy cascade in large-eddy simulations of turbulent fluid flows., *Adv. in Geophys.*, **18**:237 – 248 (1974).

83. Moeng, C.-H., Large-eddy simulation model for the study of planetary boundary-layer turbulence, *J. Atmos. Sci.*, **41**:2052 – 62 (1984).

84. Shaw, R. and Schumann, U., Large-eddy simulation of turbulent flow above and within a forest, *Boundary Layer Meteoro.*, **61**:47 – 64 (1992).

85. Liu, S., Katz, J., and Meneveau, C., Evolution and modeling of subgrid scales during rapid distortion of turbulence, *J. Fluid Mech.*, **387**:281–320 (1999).

86. Panofsky, H. A. and Dutton, J., *Atmospheric Turbulence*, Wiley-Interscience, 1984.

87. Moeng, C.-H. and Rotunno, R., Vertical-velocity skewness in the buoyancy-driven boundary-layer, *J. Atmos. Sci.*, **47**:1149 – 1162 (1990).

88. Lemone, M. A., Some observations of vertical velocity skewness in the convective planetary boundary-layer, *J. Atmos. Sci.*, **47**:1163 – 1169 (1990).

89. Rotta, J. C., Statistische Theorie nichthomogener Turbulenz, *Z. Phys.*, **129**:547 – 572 (1951).

90. Chen, Q. and Tong, C., Investigation of the subgrid-scale stress and its production rate in a convective atmospheric boundary layer using measurement data, *J. Fluid Mech.*, **547**:65 – 104 (2006).

91. Chen, Q., Wang, D., Zhang, H., and Tong, C., Effects of subgrid-scale turbulence on resolvable-scale velocity-scalar statistics, *J. Turbulence*, **6**:36 (2005).

92. Businger, J., Wyngaard, J., Izumi, Y., and Bradley, E., Flux-profile relationship in the atmospheric boundary layer, *J. of Atmospheric Sciences*, **28**:181 – 189 (1971).